

1994

Shell-side condensation of HFC-134a and HCFC-123 on enhanced-tube bundles

Joseph B. Huber
Iowa State University

Follow this and additional works at: <https://lib.dr.iastate.edu/rtd>

 Part of the [Mechanical Engineering Commons](#)

Recommended Citation

Huber, Joseph B., "Shell-side condensation of HFC-134a and HCFC-123 on enhanced-tube bundles " (1994). *Retrospective Theses and Dissertations*. 10482.
<https://lib.dr.iastate.edu/rtd/10482>

This Dissertation is brought to you for free and open access by the Iowa State University Capstones, Theses and Dissertations at Iowa State University Digital Repository. It has been accepted for inclusion in Retrospective Theses and Dissertations by an authorized administrator of Iowa State University Digital Repository. For more information, please contact digirep@iastate.edu.

INFORMATION TO USERS

This manuscript has been reproduced from the microfilm master. UMI films the text directly from the original or copy submitted. Thus, some thesis and dissertation copies are in typewriter face, while others may be from any type of computer printer.

The quality of this reproduction is dependent upon the quality of the copy submitted. Broken or indistinct print, colored or poor quality illustrations and photographs, print bleedthrough, substandard margins, and improper alignment can adversely affect reproduction.

In the unlikely event that the author did not send UMI a complete manuscript and there are missing pages, these will be noted. Also, if unauthorized copyright material had to be removed, a note will indicate the deletion.

Oversize materials (e.g., maps, drawings, charts) are reproduced by sectioning the original, beginning at the upper left-hand corner and continuing from left to right in equal sections with small overlaps. Each original is also photographed in one exposure and is included in reduced form at the back of the book.

Photographs included in the original manuscript have been reproduced xerographically in this copy. Higher quality 6" x 9" black and white photographic prints are available for any photographs or illustrations appearing in this copy for an additional charge. Contact UMI directly to order.



University Microfilms International
A Bell & Howell Information Company
300 North Zeeb Road, Ann Arbor, MI 48106-1346 USA
313-761-4700 800-521-0600

Order Number 9503567

**Shell-side condensation of HFC-134a and HCFC-123 on
enhanced-tube bundles**

Huber, Joseph B., Ph.D.

Iowa State University, 1994

U·M·I

300 N. Zeeb Rd.
Ann Arbor, MI 48106

Shell-side condensation of HFC-134a and HCFC-123
on enhanced-tube bundles

by

Joseph B. Huber

A Dissertation Submitted to the
Graduate Faculty in Partial Fulfillment of the
Requirements for the Degree of
DOCTOR OF PHILOSOPHY

Department: Mechanical Engineering
Major: Mechanical Engineering

Approved:

Signature was redacted for privacy.

In Charge of Major Work

Signature was redacted for privacy.

For the Major Department

Signature was redacted for privacy.

For the Graduate College

Iowa State University
Ames, Iowa
1994

TABLE OF CONTENTS

NOMENCLATURE	xvii
ACKNOWLEDGEMENTS	xxii
CHAPTER 1. INTRODUCTION	1
Scope of Research Project	2
Organization of Dissertation	3
CHAPTER 2. THEORETICAL ANALYSIS	5
Introduction	5
Classical Nusselt Analysis for Smooth Tubes	6
Single tubes	6
Tube bundles	8
Analysis of Finned Tubes	10
Single finned tubes	11
Tube bundles	17
Analysis of Other Enhanced Geometries	21
Boundary Layer Analysis	22
Forced Convection Analysis	25
Summary	27
CHAPTER 3. EXPERIMENTAL APPARATUS	31
Test Section	33

Tube Bundles	33
Refrigerant Loop	38
Water Loop	40
Glycol Chiller	40
Data Acquisition System	41
CHAPTER 4. EXPERIMENTAL PROCEDURE	44
Determination of the Water-side Heat Transfer Coefficient	44
Rig Operation	49
Data Reduction	51
Uncertainty of the Shell-side Heat Transfer Coefficients	53
Experimental uncertainty	53
Statistical uncertainty	54
Adaptation of Theoretical Models to the Current Study	54
The Pearson-Withers (P-W) correlation	55
The Webb-Murawski (W-M) correlation	55
CHAPTER 5. HFC-134a SHELL-SIDE CONDENSATION RESULTS	57
Results for the 26-fpi Geometry	58
Average bundle heat transfer coefficient results	58
Average row heat transfer coefficient results	59
Comparison to the P-W and W-M correlations	63
Results for the 40-fpi Geometry	65
Average bundle heat transfer coefficient results	65
Average row heat transfer coefficient results	66
Comparison to P-W and W-M correlations	70
Results for the Tu-Cii Geometry	71

Average bundle heat transfer coefficient results	71
Average row heat transfer coefficient results	74
Comparison to P-W and W-M correlations	77
Results for G-SC Geometry	77
Average bundle heat transfer coefficient results	77
Average row heat transfer coefficients results	79
Comparison to P-W and W-M correlations	82
Comparison of HFC-134a and CFC-12 Heat Transfer Coefficients	83
Comparison of average bundle heat transfer coefficients	83
Comparison of average row heat transfer coefficients	88
Comparison of Bundle Geometries	91
Summary	93
CHAPTER 6. HCFC-123 SHELL-SIDE CONDENSATION RESULTS	94
Results for the 26-fpi Geometry	95
Average bundle heat transfer coefficient results	95
Average row heat transfer coefficient results	98
Comparison to the P-W and W-M correlations	101
Results for the 40-fpi Geometry	102
Average bundle heat transfer coefficient results	102
Average row heat transfer coefficient results	105
Comparison to P-W and W-M correlations	107
Results for Tu-Cii Geometry	108
Average bundle heat transfer coefficient results	108
Average row heat transfer coefficient results	111
Comparison of HCFC-123 and HFC-134a for the Tu-Cii geometry	113

Comparison to P-W and W-M correlations	115
Results for G-SC Geometry	116
Average bundle heat transfer coefficient results	116
Average row heat transfer coefficients results	119
Comparison of HCFC-123 and HFC-134a for the G-SC geometry	121
Comparison to P-W and W-M correlations	122
Comparison of HCFC-123 and CFC-11 Heat Transfer Coefficients	122
Comparison of average bundle heat transfer coefficients	122
Comparison of average row heat transfer coefficients	126
Comparison of Bundle Geometries	126
Summary	129
CHAPTER 7. DESIGN CORRELATIONS FOR HFC-134a AND HCFC-123	132
Form of the Correlation Used to Fit the Experimental Data	132
Comparison of Correlation to Experimental Data	134
Limitations on the Present Correlation	140
CHAPTER 8. CONCLUSIONS	143
Summary of HFC-134a Data	143
Summary of HCFC-123 Data	144
BIBLIOGRAPHY	146
APPENDIX A. DERIVATION OF UNCERTAINTY ANALYSIS EQUATIONS	150
APPENDIX B. TABULATED HFC-134a CONDENSATION DATA	156
APPENDIX C. TABULATED CFC-12 CONDENSATION DATA	165
APPENDIX D. TABULATED HCFC-123 CONDENSATION DATA	174
APPENDIX E. TABULATED CFC-11 CONDENSATION DATA	183

LIST OF TABLES

Table 2.1:	Constants for the Webb and Murawski (1990) condensation model	22
Table 2.2:	Deviation of the Sparrow and Gregg (1959) and the Chen (1961) analysis from the Nusselt theory	24
Table 2.3:	Chronological listing of notable works in involving the theoretical and empirical analysis of condensation on tubes	28
Table 3.1:	Tube geometry specifications	34
Table 3.2:	Water-side heat transfer enhancement specifications for the different tube geometries	36
Table 3.3:	Uncertainties in the measured parameters	42
Table 5.1:	Property comparison for HFC-134a, CFC-12, and CFC-113 at 35°C	87
Table 6.1:	Property comparison for HCFC-123, CFC-11, and CFC-113 at 35°C	123
Table 7.1:	Constants for Equation 7.1	135
Table B.1:	Refrigerant-side data for the 26-fpi geometry	157
Table B.2:	Water-side data for the 26-fpi geometry	157
Table B.3:	Row data for the 26-fpi geometry	158
Table B.4:	Shell-side heat transfer coefficients and uncertainties for the 26-fpi geometry	158
Table B.5:	Refrigerant-side data for the 40-fpi geometry	159

Table B.6:	Water-side data for the 40-fpi geometry	159
Table B.7:	Row data for the 40-fpi geometry	160
Table B.8:	Shell-side heat transfer coefficients and uncertainties for the 40-fpi geometry	160
Table B.9:	Refrigerant-side data for the Tu-Cii geometry	161
Table B.10:	Water-side data for the Tu-Cii geometry	161
Table B.11:	Row data for the Tu-Cii geometry	162
Table B.12:	Shell-side heat transfer coefficients and uncertainties for the Tu-Cii geometry	162
Table B.13:	Refrigerant-side data for the G-SC geometry	163
Table B.14:	Water-side data for the G-SC geometry	163
Table B.15:	Row data for the G-SC geometry	164
Table B.16:	Shell-side heat transfer coefficients and uncertainties for the G-SC geometry	164
Table C.1:	Refrigerant-side data for the 26-fpi geometry	166
Table C.2:	Water-side data for the 26-fpi geometry	166
Table C.3:	Row data for the 26-fpi geometry	167
Table C.4:	Shell-side heat transfer coefficients and uncertainties for the 26-fpi geometry	167
Table C.5:	Refrigerant-side data for the 40-fpi geometry	168
Table C.6:	Water-side data for the 40-fpi geometry	168
Table C.7:	Row data for the 40-fpi geometry	169
Table C.8:	Shell-side heat transfer coefficients and uncertainties for the 40-fpi geometry	169
Table C.9:	Refrigerant-side data for the Tu-Cii geometry	170

Table C.10:	Water-side data for the Tu-Cii geometry	170
Table C.11:	Row data for the Tu-Cii geometry	171
Table C.12:	Shell-side heat transfer coefficients and uncertainties for the Tu-Cii geometry	171
Table C.13:	Refrigerant-side data for the G-SC geometry	172
Table C.14:	Water-side data for the G-SC geometry	172
Table C.15:	Row data for the G-SC geometry	173
Table C.16:	Shell-side heat transfer coefficients and uncertainties for the G-SC geometry	173
Table D.1:	Refrigerant-side data for the 26-fpi geometry	175
Table D.2:	Water-side data for the 26-fpi geometry	175
Table D.3:	Row data for the 26-fpi geometry	176
Table D.4:	Shell-side heat transfer coefficients and uncertainties for the 26-fpi geometry	176
Table D.5:	Refrigerant-side data for the 40-fpi geometry	177
Table D.6:	Water-side data for the 40-fpi geometry	177
Table D.7:	Row data for the 40-fpi geometry	178
Table D.8:	Shell-side heat transfer coefficients and uncertainties for the 40-fpi geometry	178
Table D.9:	Refrigerant-side data for the Tu-Cii geometry	179
Table D.10:	Water-side data for the Tu-Cii geometry	179
Table D.11:	Row data for the Tu-Cii geometry	180
Table D.12:	Shell-side heat transfer coefficients and uncertainties for the Tu-Cii geometry	180
Table D.13:	Refrigerant-side data for the G-SC geometry	181

Table D.14:	Water-side data for the G-SC geometry	181
Table D.15:	Row data for the G-SC geometry	182
Table D.16:	Shell-side heat transfer coefficients and uncertainties for the G-SC geometry	182
Table E.1:	Refrigerant-side data for the 26-fpi geometry	184
Table E.2:	Water-side data for the 26-fpi geometry	184
Table E.3:	Row data for the 26-fpi geometry	185
Table E.4:	Shell-side heat transfer coefficients and uncertainties for the 26-fpi geometry	185
Table E.5:	Refrigerant-side data for the 40-fpi geometry	186
Table E.6:	Water-side data for the 40-fpi geometry	186
Table E.7:	Row data for the 40-fpi geometry	187
Table E.8:	Shell-side heat transfer coefficients and uncertainties for the 40-fpi geometry	187
Table E.9:	Refrigerant-side data for the Tu-Cii geometry	188
Table E.10:	Water-side data for the Tu-Cii geometry	188
Table E.11:	Row data for the Tu-Cii geometry	189
Table E.12:	Shell-side heat transfer coefficients and uncertainties for the Tu-Cii geometry	189
Table E.13:	Refrigerant-side data for the G-SC geometry	190
Table E.14:	Water-side data for the G-SC geometry	190
Table E.15:	Row data for the G-SC geometry	191
Table E.16:	Shell-side heat transfer coefficients and uncertainties for the G-SC geometry	191

LIST OF FIGURES

Figure 2.1:	Schematic of different condensate flow patterns: (a) Nusselt condensation, (b) staggered bundle flow, (c) turbulent dripping, (d) horizontal vapor flow with shear (Marto, 1991)	11
Figure 2.2:	Schematic of condensate flooding on a finned tube (Marto, 1991)	12
Figure 3.1:	Schematic of experimental test facility	32
Figure 3.2:	Photograph of tube geometries	35
Figure 3.3:	Schematic of tube-sheet	35
Figure 4.1:	Water-side STC data for the 26-fpi and 40-fpi geometries	48
Figure 4.2:	Water-side STC data for the Tu-Cii and G-SC geometries	48
Figure 5.1:	Average shell-side bundle heat transfer coefficient vs. heat flux for the condensation of HFC-134a on the 26-fpi geometry	59
Figure 5.2:	Average shell-side bundle heat transfer coefficient vs. LMTD for the condensation of HFC-134a on the 26-fpi geometry	60
Figure 5.3:	Average shell-side bundle heat transfer coefficient vs. condensation temperature difference for the condensation of HFC-134a on the 26-fpi geometry	60
Figure 5.4:	Average shell-side row heat transfer coefficient vs. row number for the condensation of HFC-134a on the 26-fpi geometry	61

Figure 5.5:	Average shell-side row heat transfer coefficient vs. row number for the condensation of HFC-134a on the 26-fpi geometry	64
Figure 5.6:	Average shell-side bundle heat transfer coefficient vs. heat flux for the condensation of HFC-134a on the 40-fpi geometry	65
Figure 5.7:	Average shell-side bundle heat transfer coefficient vs. LMTD for the condensation of HFC-134a on the 40-fpi geometry	67
Figure 5.8:	Average shell-side bundle heat transfer coefficient vs. condensation temperature difference for the condensation of HFC-134a on the 40-fpi geometry	67
Figure 5.9:	Average shell-side row heat transfer coefficient vs. row number for the condensation of HFC-134a on the 40-fpi geometry	68
Figure 5.10:	Average shell-side row heat transfer coefficient vs. row number for the condensation of HFC-134a on the 40-fpi geometry	70
Figure 5.11:	Average shell-side bundle heat transfer coefficient vs. heat flux for the condensation of HFC-134a on the Tu-Cii geometry	71
Figure 5.12:	Average shell-side bundle heat transfer coefficient vs. LMTD for the condensation of HFC-134a on the Tu-Cii geometry	73
Figure 5.13:	Average shell-side bundle heat transfer coefficient vs. condensation temperature difference for the condensation of HFC-134a on the Tu-Cii geometry	73
Figure 5.14:	Average shell-side row heat transfer coefficient vs. row number for the condensation of HFC-134a on the Tu-Cii geometry	75
Figure 5.15:	Average shell-side row heat transfer coefficient vs. row number for the condensation of HFC-134a on the Tu-Cii geometry	76

Figure 5.16:	Average shell-side bundle heat transfer coefficient vs. heat flux for the condensation of HFC-134a on the G-SC geometry	78
Figure 5.17:	Average shell-side bundle heat transfer coefficient vs. LMTD for the condensation of HFC-134a on the G-SC geometry	80
Figure 5.18:	Average shell-side bundle heat transfer coefficient vs. condensation temperature difference for the condensation of HFC-134a on the G-SC geometry	80
Figure 5.19:	Average shell-side row heat transfer coefficient vs. row number for the condensation of HFC-134a on the G-SC geometry	81
Figure 5.20:	Average shell-side row heat transfer coefficient vs. row number for the condensation of HFC-134a on the G-SC geometry	83
Figure 5.21:	Comparison of the HFC-134a and CFC-12 average shell-side bundle heat transfer coefficients for the 26-fpi geometry	84
Figure 5.22:	Comparison of the HFC-134a and CFC-12 average shell-side bundle heat transfer coefficients for the 40-fpi geometry	84
Figure 5.23:	Comparison of the HFC-134a and CFC-12 average shell-side bundle heat transfer coefficients for the Tu-Cii geometry	85
Figure 5.24:	Comparison of the HFC-134a and CFC-12 average shell-side bundle heat transfer coefficients for the G-SC geometry	85
Figure 5.25:	Comparison of the HFC-134a and CFC-12 average shell-side row heat transfer coefficients for the 26-fpi geometry at a bundle load of 36 kW (123 000 Btu/hr)	89
Figure 5.26:	Comparison of the HFC-134a and CFC-12 average shell-side row heat transfer coefficients for the 40-fpi geometry at a bundle load of 36 kW (123 000 Btu/hr)	89

Figure 5.27:	Comparison of the HFC-134a and CFC-12 average shell-side row heat transfer coefficients for the Tu-Cii geometry at a bundle load of 36 kW (123 000 Btu/hr)	90
Figure 5.28:	Comparison of the HFC-134a and CFC-12 average shell-side row heat transfer coefficients for the G-SC geometry at a bundle load of 36 kW (123 000 Btu/hr)	90
Figure 5.29:	Comparison of the HFC-134a average shell-side bundle heat transfer coefficients for the four tube geometries	92
Figure 5.30:	Comparison of the CFC-12 average shell-side bundle heat transfer coefficients for the four tube geometries	92
Figure 6.1:	Average shell-side bundle heat transfer coefficient vs. heat flux for the condensation of HCFC-123 on the 26-fpi geometry	96
Figure 6.2:	Average shell-side bundle heat transfer coefficient vs. LMTD for the condensation of HCFC-123 on the 26-fpi geometry	97
Figure 6.3:	Average shell-side bundle heat transfer coefficient vs. condensation temperature difference for the condensation of HCFC-123 on the 26-fpi geometry	97
Figure 6.4:	Average shell-side row heat transfer coefficient vs. row number for the condensation of HCFC-123 on the 26-fpi geometry	99
Figure 6.5:	Average shell-side row heat transfer coefficient vs. row number for the condensation of HCFC-123 on the 26-fpi geometry	101
Figure 6.6:	Average shell-side bundle heat transfer coefficient vs. heat flux for the condensation of HCFC-123 on the 40-fpi geometry	103
Figure 6.7:	Average shell-side bundle heat transfer coefficient vs. LMTD for the condensation of HCFC-123 on the 40-fpi geometry	104

Figure 6.8:	Average shell-side bundle heat transfer coefficient vs. condensation temperature difference for the condensation of HCFC-123 on the 40-fpi geometry	104
Figure 6.9:	Average shell-side row heat transfer coefficient vs. row number for the condensation of HCFC-123 on the 40-fpi geometry	106
Figure 6.10:	Average shell-side row heat transfer coefficient vs. row number for the condensation of HCFC-123 on the 40-fpi geometry	107
Figure 6.11:	Average shell-side bundle heat transfer coefficient vs. heat flux for the condensation of HCFC-123 on the Tu-Cii geometry	109
Figure 6.12:	Average shell-side bundle heat transfer coefficient vs. LMTD for the condensation of HCFC-123 on the Tu-Cii geometry	110
Figure 6.13:	Average shell-side bundle heat transfer coefficient vs. condensation temperature difference for the condensation of HCFC-123 on the Tu-Cii geometry	110
Figure 6.14:	Average shell-side row heat transfer coefficient vs. row number for the condensation of HCFC-123 on the Tu-Cii geometry	112
Figure 6.15:	Average shell-side row heat transfer coefficient vs. row number for the condensation of HCFC-123 on the Tu-Cii geometry	114
Figure 6.16:	Average shell-side bundle heat transfer coefficient vs. heat flux for the condensation of HCFC-123 on the G-SC geometry	117
Figure 6.17:	Average shell-side bundle heat transfer coefficient vs. LMTD for the condensation of HCFC-123 on the G-SC geometry	118
Figure 6.18:	Average shell-side bundle heat transfer coefficient vs. condensation temperature difference for the condensation of HCFC-123 on the G-SC geometry	118

Figure 6.19: Average shell-side row heat transfer coefficient vs. row number for the condensation of HCFC-123 on the G-SC geometry 119

Figure 6.20: Average shell-side row heat transfer coefficient vs. row number for the condensation of HCFC-123 on the G-SC geometry 121

Figure 6.21: Comparison of the HCFC-123 and CFC-11 average shell-side bundle heat transfer coefficients for the 26-fpi geometry 124

Figure 6.22: Comparison of the HCFC-123 and CFC-11 average shell-side bundle heat transfer coefficients for the 40-fpi geometry 124

Figure 6.23: Comparison of the HCFC-123 and CFC-11 average shell-side bundle heat transfer coefficients for the Tu-Cii geometry 125

Figure 6.24: Comparison of the HCFC-123 and CFC-11 average shell-side bundle heat transfer coefficients for the G-SC geometry 125

Figure 6.25: Comparison of the HCFC-123 and CFC-11 average shell-side row heat transfer coefficients for the 26-fpi geometry at a bundle load of 36 kW (123 000 Btu/hr) 127

Figure 6.26: Comparison of the HCFC-123 and CFC-11 average shell-side row heat transfer coefficients for the 40-fpi geometry at a bundle load of 36 kW (123 000 Btu/hr) 127

Figure 6.27: Comparison of the HCFC-123 and CFC-11 average shell-side row heat transfer coefficients for the Tu-Cii geometry at a bundle load of 36 kW (123 000 Btu/hr) 128

Figure 6.28: Comparison of the HCFC-123 and CFC-11 average shell-side row heat transfer coefficients for the G-SC geometry at a bundle load of 36 kW (123 000 Btu/hr) 128

Figure 6.29:	Comparison of the HCFC-123 average shell-side bundle heat transfer coefficients for the four tube geometries	130
Figure 6.30:	Comparison of the CFC-11 average shell-side bundle heat transfer coefficients for the four tube geometries	130
Figure 7.1:	Actual and predicted average shell-side bundle heat transfer coefficients for the 26-fpi geometry	136
Figure 7.2:	Actual and predicted average shell-side bundle heat transfer coefficients for the 40-fpi geometry	136
Figure 7.3:	Actual and predicted average shell-side bundle heat transfer coefficients for the Tu-Cii geometry	137
Figure 7.4:	Actual and predicted average shell-side bundle heat transfer coefficients for the G-SC geometry	137
Figure 7.5:	Difference between the actual and predicted average shell-side bundle heat transfer coefficients for the 26-fpi geometry	138
Figure 7.6:	Difference between the actual and predicted average shell-side bundle heat transfer coefficients for the 40-fpi geometry	138
Figure 7.7:	Difference between the actual and predicted average shell-side bundle heat transfer coefficients for the Tu-Cii geometry	139
Figure 7.8:	Difference between the actual and predicted average shell-side bundle heat transfer coefficients for the G-SC geometry	139

NOMENCLATURE

Symbols

A	area
a	constant for Webb-Murawski correlation
a	leading constant for Equation 7.1
B_g	liquid retention parameter, defined by Equation 2.21
b	Re exponent for Equation 7.1
C_N	constant for Pearson-Withers correlation
C_p	specific heat
C_1	condensate retention constant used in Equation 2.19
c	Bo exponent for Equation 7.1
D	diameter
D_{eq}	equivalent diameter for finned tubes
d	Pr exponent for Equation 7.1
g	acceleration of gravity
h_o	average shell-side heat transfer coefficient
$h_{o,\sigma}$	average shell-side heat transfer coefficient corrected for surface tension effects
i	enthalpy
i_{fg}	enthalpy of vaporization

i'_{fg}	modified enthalpy of vaporization
k	thermal conductivity
L	tube length
\bar{L}	effective length of fin side, given by Equation 2.14
LMTD	log-mean temperature difference
m	inundation exponent
\dot{m}	mass flow rate
N	number of tubes in a vertical column
n	exponent for Webb-Murawski correlation
\bar{p}	pressure
p_f	fin pitch
q	heat transfer rate
q'	heat transfer rate per unit tube length
q''	heat transfer rate per unit surface area (heat flux)
r_c	thermal resistance due to surface tension
S_m	length of the convex surface over which the condensate film flows
T	temperature
t_b	fin thickness at base
\bar{v}	specific volume
w	uncertainty

Greek symbols

η	efficiency
Γ	flow rate of falling condensate per unit tube length

μ	viscosity
ϕ_f	flooding angle
ρ	density
σ	surface tension
θ_m	angle through which the normal to the condensation surface turns
θ'	derivative of non-dimensional temperature in the Sparrow and Gregg analysis
ζ	parameter that characterizes the aspect ratio of the fin cross-section

Subscripts

<i>act</i>	actual
<i>atm</i>	atmospheric
<i>B</i>	bundle
<i>C</i>	column
Chen	Chen analysis
<i>D</i>	based on diameter
<i>ef</i>	effective
<i>f</i>	liquid phase
<i>fl</i>	flooded region
<i>fn</i>	finned region
<i>fs</i>	fin sides
<i>ft</i>	fin tips
<i>g</i>	vapor phase
<i>H</i>	based on hydraulic diameter
<i>N</i>	row number

<i>Nu</i>	based on original Nusselt analysis
<i>o</i>	outer
<i>pre</i>	predicted
<i>R</i>	row
<i>r</i>	fin root, or refrigerant
S-G	Sparrow and Gregg analysis
<i>s</i>	tube surface
<i>sat</i>	saturation
<i>tw</i>	tube wall
<i>uf</i>	unfinned region
<i>w</i>	water
1	row 1

Dimensionless groups

F_d	forced convection parameter defined by Equation 2.39
G	forced convection parameter defined by Equation 2.43
H	natural convection parameter defined by Equation 2.34
J	natural convection parameter defined by Equation 2.35
K	flow pattern parameter, $\Gamma(g/\rho_f)^{1/4}/(2\sigma^{3/4})$
Λ_r	liquid retention parameter defined by Equation 2.20
Nu	Nusselt number, $(hD)/k$
P^*	forced convection parameter defined by Equation 2.42
Pr	Prandtl number, $(\mu C_p)/k$
Re	Reynolds number, $4\dot{m}/(D\mu)$
\tilde{Re}	two-phase Reynolds number, $(U_\infty \rho_f D)/\mu_f$

ACKNOWLEDGEMENTS

This work was sponsored by the American Society of Heating, Refrigerating, and Air-Conditioning Engineers as 676-RP. The advice and technical guidance of ASHRAE Technical Committee TC 8.5 (Liquid-to-Refrigerant Heat Exchangers) were greatly appreciated. I wish to thank the Project Monitoring Subcommittee, which was comprised of Keith Starner (project monitoring subcommittee chairman), Satish Oza, Fred Scheideman, and Petur Thors, for providing technical support over the course of this study. The tubes used in this study were supplied by Wolverine Tube, Inc., Decatur AL, and Wieland America, Buffalo Grove, IL. The spring-type turbulators were supplied by the Trane Company, La Crosse, WI.

I wish to sincerely thank to Dr. Michael Pate for serving as my major professor during the course of this study. His guidance and support were invaluable during my research and during the writing of this dissertation. Special thanks to Dr. Greg Maxwell, Dr. Ambar Mitra, Dr. Howard Shapiro, and Dr. Gene Takle for serving on my Program of Study Committee.

The support of the Iowa State University Department of Mechanical Engineering and the Iowa State University Engineering Research Institute is also greatly appreciated. I would like to thank Hap Steed, Gaylord Scandrett, and James Dautremont for their technical support during the construction and shake-down of the experimental test facility. Special thanks to Kerri Eggers for skillfully handling the mounds of paperwork generated by this project.

I would like to thank my colleagues in the Heat Transfer Laboratory for their support. Special thanks to Lance Rewerts, who worked in conjunction with me on 676-RP. The many discussions I have had with these colleagues have been invaluable to me. I greatly appreciate

the support of my parents, James and Darlene Huber, and my sister, Michelle Huber, for their continual support and encouragement.

Finally, thanks be to God, the creator and upholder of the universe, for guiding me through these many years of higher education. I pray that You will continue to guide me as I move on to a new stage of my life. I am also grateful to my many friends at Unity Christian Reformed Church in Ames. The friendliness, support, and opportunities that this institution has given me over the past seven years will never be forgotten.

CHAPTER 1. INTRODUCTION

For the past five decades, CFCs (chlorofluorocarbons) and HCFCs (hydrochlorofluorocarbons) have been the primary working fluids for the majority of the vapor-compression refrigeration devices in service. CFC-12 has been by far the most common refrigerant for devices such as household refrigerators and freezers, window air-conditioners, and automobile air-conditioners. CFC-11 is commonly used in large chiller units which produce chilled water for the cooling of large buildings. CFC-11 is also used as a secondary heat transfer fluid. The popularity of these two refrigerants stems from the fact that these substances are non-toxic, inexpensive to produce, easy to handle, and compatible with many common materials. These fluids were once thought to cause no harm to the atmosphere. However, CFCs have been found to destroy the Earth's protective ozone layer, and current mandates require that all new refrigeration equipment produced after 1996 must use an ozone-safe refrigerant.

HFC-134a is the current choice to replace CFC-12. HFC-134a has similar thermodynamic properties to those of CFC-12, is compatible with the materials commonly used in refrigeration equipment, is non-toxic, and has no ozone depletion potential. HFC-134a is already being used in some appliances, and several automobile and heavy equipment manufacturers have already switched to HFC-134a for air-conditioning use.

HCFC-123 is the interim choice to replace CFC-11. Since HCFC-123 has a small, but non-zero, ozone depletion potential, its use may be restricted in the future. HCFC-123 is one of the few fluids with thermodynamic properties similar to those of CFC-11. HCFC-123 is not without drawbacks however. HCFC-123 is not compatible with many of the elastomers

and plastics currently used in the refrigeration industry. The allowable exposure limit for HCFC-123 is 30 ppm, which is significantly lower than the allowable exposure limit for HFC-134a, which is 400 ppm. Despite the drawbacks, engineers have found suitable solutions to the compatibility and toxicity problems, and refrigeration units utilizing HCFC-123 are commercially available.

The purpose of the present study, which was sponsored by the American Society of Heating, Refrigerating and Air-Conditioning Engineers (ASHRAE), was to obtain experimental performance data for the condensation of HFC-134a and HCFC-123 on enhanced tube surfaces. ASHRAE commissioned this study to fill the current void in the shell-side condensation data base regarding HFC-134a and HCFC-123.

The data collected in this study will be used in several ways to aid engineers who design shell-and-tube condensers. First, the data will be used by the engineer to determine the condenser size necessary for a given condensing load. Secondly, the data will aid the designer in choosing a tube geometry for a particular refrigerant and heat flux. Thirdly, the data can be used to compare the performance of HFC-134a and HCFC-123 to CFC-12 and CFC-11 for a particular tube geometry and heat flux. These comparisons are necessary when engineers are involved in the re-design of present CFC-based equipment.

Scope of Research Project

The study described in this document was part of a larger ASHRAE research project 676-RP "Experimental determination of shell-side condenser bundle heat transfer design factors for Refrigerants R-123 and R-134a". The portion of 676-RP described herein was concerned with finding the effect of heat flux and tube geometry on the shell-side heat transfer coefficient.

Shell-side condensation heat transfer data were obtained for alternative refrigerants HFC-134a and HCFC-123. Data for conventional refrigerants CFC-12 and CFC-11 were also ob-

tained for comparison purposes. The tube bundles used in this study were constructed from 19.1 mm (0.75 in) o.d. 1024-fpm (26-fpi), 1575-fpm (40-fpi), Turbo C-II, and GEWA SC tubes. These four tube geometries are the most commonly used in shell-and-tube refrigerant condensers. The tube bundles tested are 5 columns wide by 5 rows deep and have a staggered tube arrangement with a horizontal pitch of 22.2 mm (0.875 in) and a vertical pitch of 19.1 mm (0.75 in). The data were obtained at a refrigerant saturation temperature of 35°C (95°F) over a nominal bundle heat flux range of 18 000 - 40 000 W/m² (5700 - 12 700 Btu/(hr·ft²

In vapor-compression systems, a small amount of lubricating oil is carried out of the refrigerant compressor by the refrigerant and circulates through the system. This circulating oil is known to affect the heat transfer characteristics of the condenser. The normal procedure when testing new refrigerants is to produce data for the general case of the pure refrigerant, and later examine the effect of oil concentration. Since no previous HFC-134a and HCFC-123 bundle condensation data existed, the scope of this project was limited to testing pure refrigerants only.

Organization of Dissertation

Chapter 2 presents an overview of the theoretical techniques used to analyze shell-side condensation. Chapter 3 describes the test facility used to obtain the experimental heat transfer data presented in this study. Chapter 4 explains the experimental procedures used to obtain the heat transfer data and the data reduction techniques used to calculate the shell-side heat transfer coefficients. Chapter 5 discusses the HFC-134a data and compares the HFC-134a data

to CFC-12 data, while Chapter 6 discusses the HCFC-123 data and compares the HCFC-123 data to the CFC-11 data. Chapter 7 presents a semi-empirical correlation for the average shell-side bundle heat transfer coefficients presented in Chapters 5 and 6. Chapter 8 gives conclusions based on the results of the present study.

CHAPTER 2. THEORETICAL ANALYSIS

Introduction

Condensation is defined as the removal of energy from a substance existing in the vapor phase in such a manner that the substance changes from the vapor phase into the liquid phase (Collier, 1981). Condensation can occur when the vapor is sufficiently cooled below its saturation temperature to the point that droplet nucleation occurs. *Homogeneous nucleation* occurs when the droplets form within the vapor. *Heterogeneous nucleation* occurs when the droplets form on particles entrained within the vapor, or when the droplets form on the walls of the system. This study is concerned with the condensation that takes place in shell-and-tube condensers, in which heterogeneous condensation of refrigerant vapors takes place on cooled horizontal surfaces of circular cross section.

Heterogeneous condensation on cooled surfaces occurs in one of two ways, depending on the condition of the surface on which the condensation occurs (Incropera and DeWitt, 1990). *Film condensation* occurs when a liquid film covers the entire condensing surface. The liquid film flows continuously from the surface because of gravitational effects. Film condensation generally occurs on clean surfaces. *Dropwise condensation* occurs when the liquid film is inhibited from completely wetting the condensing surface. The inhibition of wetting may be caused by the mechanical condition of the surface or by coating the surface with an appropriate substance. During dropwise condensation, microscopic condensate droplets, instead of a continuous liquid film, form and grow on the cooled surface. When the drops

become sufficiently large, gravity or aerodynamic drag forces pull the drops from the surface and new droplets form immediately.

Both the condensate film and condensate droplets form a resistance to heat transfer. However, the diameter of the droplets is significantly less than the thickness of the liquid film, and a falling drop exposes a new surface on which condensation can take place. Thus, dropwise heat transfer coefficients are orders of magnitude higher than filmwise coefficients. Unfortunately, dropwise condensation is difficult to maintain, especially when low surface tension fluids which readily wet the condensing surface are used. Because of the difficulty in promoting and maintaining dropwise condensation, shell-and-tube condensers are designed to operate in film-wise condensation mode. For this reason, the discussion in this chapter will concentrate on film condensation only.

Condensation heat transfer can also be classified in terms of natural convection and forced convection. The main difference between these two regimes is the effect of vapor velocity on the condensate layer. In forced convection, the vapor surrounding the tube is at a high velocity, causing a shear stress to exist between the vapor and the condensate. Also at high vapor velocities, vapor separation occurs, and the liquid layer thickens significantly after separation occurs.

Classical Nusselt Analysis for Smooth Tubes

Single tubes

The first attempt to solve the case of film condensation on vertical plates and horizontal tubes was performed by Nusselt in 1916. The approach used by Nusselt involved applying force balances and energy balances to a differential element of liquid in the condensate film. Nusselt made several assumptions in order to facilitate a solution (Nusselt, 1916):

- the liquid film is in laminar flow, and the flow is controlled by viscous and gravitational forces;
- the vapor is saturated;
- the liquid and the vapor have the same temperature, T_{sat} ;
- energy is transferred through the liquid film by conduction only;
- the temperature profile is linear through the liquid film;
- the liquid and the plate have the same temperature at their interface;
- the solid surface is isothermal;
- the liquid properties are not temperature dependent;
- the vapor does not exert normal or shear stresses on the liquid surface (ie. the vapor is stationary);
- the liquid has zero velocity at the plate surface;
- subcooling of the liquid is negligible.

The Nusselt analysis for the film condensation on the outside of a horizontal smooth tube leads to the following expression for the average heat transfer coefficient:

$$h_o = 0.725 \left[\frac{\rho_f(\rho_f - \rho_g)g_i k_f^3}{D\mu_f(T_{\text{sat}} - T_{s,o})} \right]^{1/4} \quad (2.1)$$

Rose (1988) states that the leading coefficient in the above equation should be 0.728; the value of 0.725 in the original Nusselt equation is in error due to small numerical inaccuracies in

Nusselt's work. Nusselt added a correction to account for subcooling of the condensate by using a modified enthalpy of vaporization:

$$i'_{fg} = i_{fg} + \frac{3}{8}C_{p,f}(T_{sat} - T_{s,o}) \quad (2.2)$$

To better match experimental data, Rohsenow et al. (1956) suggested that for $Pr > 0.5$ and $C_{p,f}(T_{sat} - T_{s,o})/i'_{fg} < 1.0$, the following modification to the enthalpy of vaporization be used:

$$i'_{fg} = i_{fg} + 0.68C_{p,f}(T_{sat} - T_{s,o}) \quad (2.3)$$

Tube bundles

Nusselt extended the single tube analysis to a vertical in-line column of horizontal tubes (Incropera and DeWitt, 1990). He assumed that all the condensate from a tube drains by gravity directly to the top of the tube below it. Nusselt assumed that the condensate drained as a smooth laminar continuous sheet. The effect is that the condensate layer thickens on the lower tubes and decreases the heat transfer coefficient. Assuming that the quantity $T_{sat} - T_{s,o}$ remains the same for each tube in the column, Nusselt determined that the average heat transfer coefficient for the entire column of tubes is given by

$$h_{o,C} = h_1 \cdot N^{-m} \quad (2.4)$$

where N is the number of tubes in the column, and $m = 1/4$. The average row coefficient for tube N is (Webb 1990)

$$h_N = h_1 \cdot (N^{1-m} - (N-1)^{1-m}) \quad (2.5)$$

By convention, the top tube (or row in the case of bundles) has $N = 1$, and N increases for each subsequent lower tube (or row). The Nusselt exponent is conservative, because the condensate actually drains in droplets or jets, depending on the surface tension of the liquid. Thus, the condensate layer on the lower tubes is not as thick as predicted by Nusselt.

Short and Brown (1951) were the first to experimentally establish the inundation effect on smooth tubes in a quiescent vapor. They condensed CFC-11 and water on a vertical bank of twenty tubes, and showed that Nusselt's analysis greatly overestimated the effect of inundation in actual tube banks. The Nusselt analysis overestimates the effect of inundation because the condensate tends to fall as discrete droplets and not as a continuous laminar sheet, as Nusselt originally assumed. Based on their data, Short and Brown proposed

$$\frac{h_{o,N}}{h_{o,1}} = 1.24N^{-1/4} \quad (2.6)$$

In addition, Short and Brown showed that the Nusselt equation for a single tube can alternately be written in terms of the condensate flow rate per length of tube, Γ :

$$\frac{h_{o,N}}{k_f} \left[\frac{\mu_f^2}{\rho_f(\rho_f - \rho_g)g} \right]^{1/3} = 1.51 \left(\frac{4\Gamma_N}{\mu_f} \right)^{-1/3} \quad (2.7)$$

The parameter Γ_N is the condensate flow rate from tube N . The fraction $4\Gamma_N/\mu_f$ is the condensate Reynolds number for the flow from tube N .

Kern (1958) improved on the Nusselt model by taking the actual flow patterns of the draining condensate into consideration. Assuming that 1) the liquid fell onto the lower banks of tubes in discrete droplets or columns, and 2) the falling liquid caused ripples in the film on the lower tubes, Kern proposed the following less conservative model:

$$\frac{h_{o,C}}{h_1} = N^{-1/6} \quad (2.8)$$

Kern's model was found to closely approximate the Short and Brown (1951) data, and is recommended as the current commercial design standard (Butterworth, 1977). Because experimental data have shown significant deviation from the Nusselt equation at high values of Γ_N/μ_f (where the flow changes from the laminar to turbulent regimes), Webb (1984b) has recommended that Equation 2.8 and Equation 2.6 should only be used for $Re_L < 200$, noting that the resulting predictions should be conservative.

Chen (1961) suggested that additional condensation occurs between the tubes because the liquid is subcooled. His correlation is

$$h_o = 0.728 \left[1 + 0.2 \frac{C_{p,f}(T_{sat} - T_{s,o})}{i_{fg}} \right] (N - 1) \left[\frac{\rho_f(\rho_f - \rho_g)g'_{fg}k_f^3}{D\mu_f(T_{sat} - T_{s,o})} \right]^{1/4} \quad (2.9)$$

All of the correlations described above were developed for in-line bundles. Eissenberg (Marto, 1988b), working with steam, proposed a model based on the assumption that in a staggered bundle, not all of the condensate falls directly down between tubes. Rather, because of local vapor flow between tubes, some of the condensate is diverted laterally and strikes the tubes on either side of the draining tube, as shown in Figure 2.1(b). As a result, the draining condensate strikes the tubes of the lower rows on their side rather than their tops, thus minimizing the liquid layer on the top of the tubes. The thinner liquid layer results in a smaller decrease in heat transfer performance as row number increases. The Eissenberg model is given by

$$h_{o,B} = h_1 \cdot (0.60 + 0.42N^{-1/4}) \quad (2.10)$$

This approach gave reasonable results for steam, although no data indicating its applicability to low viscosity fluids (such as refrigerants) were found.

Analysis of Finned Tubes

While the smooth tube analysis of the previous section provides a good theoretical basis for condensation study, most modern refrigerant condensers use tubes that have some type of enhanced surface. The first type of enhanced tube commercially used was the integral fin tube. The fins increase the heat transfer surface area, but also cause surface tension forces to become important.

During condensation, the condensate *floods*, or fills the space between between the fins on the lower portion of the tube. This phenomenon, which is shown schematically in

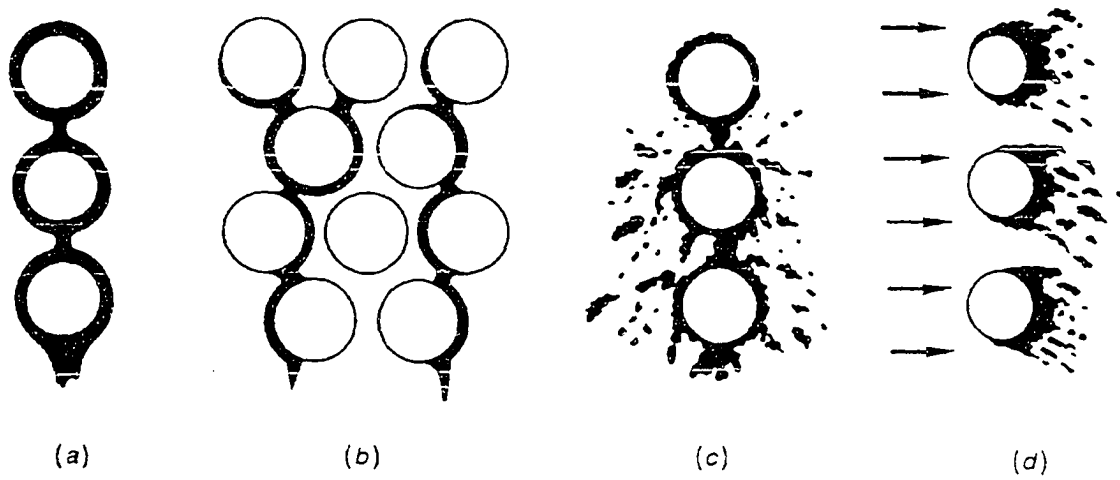


Figure 2.1: Schematic of different condensate flow patterns: (a) Nusselt condensation, (b) staggered bundle flow, (c) turbulent dripping, (d) horizontal vapor flow with shear (Marto, 1991)

Figure 2.2, is also known as *holdup*, or *liquid retention*. Flooding occurs as gravity pulls the condensate towards the bottom of the tube, and surface tension forces in the condensate cause the condensate to fill the spaces between the fins. The heat transfer is decreased in the flooded region because of the thick liquid layer. On the upper portion of the tube, surface tension tends to spread the liquid film, thus increasing heat transfer. If the spacing between the fins is decreased, more heat transfer area per unit length is added, but an increasing portion of the tube will be flooded, and at a critical fin spacing, the entire tube will be flooded. Thus, the fin spacing must be optimized for a given fluid.

Single finned tubes

Beatty and Katz model Beatty and Katz (1948) were the first to develop a heat transfer correlation for finned tube condensation. Their analysis was based on a Nusselt-type, gravity driven condensation model which treated the fins as a vertical plate and the inter-fin tube

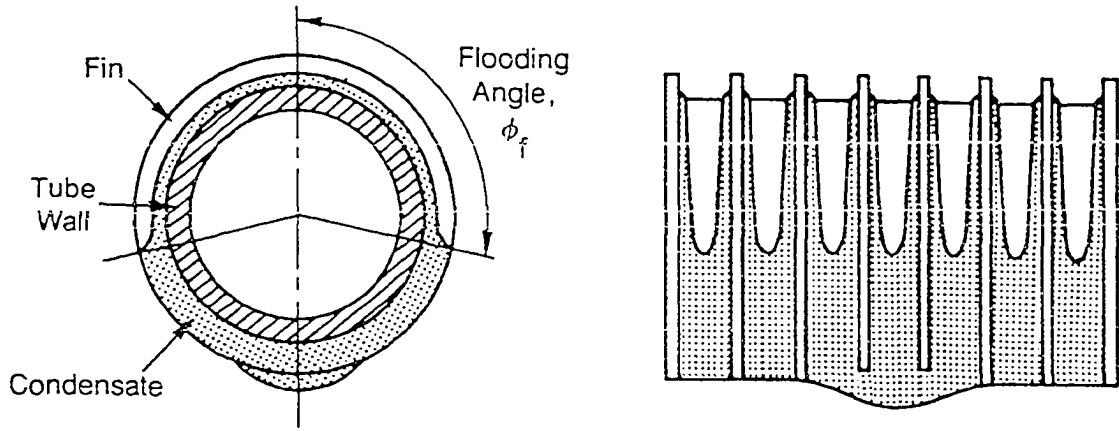


Figure 2.2: Schematic of condensate flooding on a finned tube (Marto, 1991)

spaces as a horizontal tube. The average heat transfer coefficient is given by

$$h_o = \eta_{fn} h_{fn} \frac{A_{fn}}{A_{ef}} + h_{uf} \frac{A_{uf}}{A_{ef}} \quad (2.11)$$

The tips of the fins, as well as all surface tension effects, were neglected. The final form of the Beatty-Katz correlation is

$$h_o = 0.689 \left[\frac{\rho_f^2 g_i f_f k_f^3}{\mu_f (\tau_{sai} - \tau_{s,o}) \Gamma_{cq}} \right]^{1/4} \quad (2.12)$$

where

$$\left[\frac{1}{D_{eq}} \right]^{1/4} = 1.30 \eta_{fn} \frac{A_{fn}}{A_{ef}} \frac{1}{\bar{L}^{1/4}} + \frac{A_{uf}}{A_{ef}} \frac{1}{D_r^{1/4}} \quad (2.13)$$

$$\bar{L} = \frac{\pi(D_o^2 - D_r^2)}{4D_o} \quad (2.14)$$

$$A_{ef} = \eta_{fn} A_{fn} + A_{uf} \quad (2.15)$$

The heat transfer coefficient is based on the actual outer surface area, which includes the surface area of the fins as well as the surface area of the exposed tube.

The original Beatty and Katz equation does not account for fin-tip heat transfer. The equivalent diameter can be corrected to account for heat transfer from the fin tips (Smirnov and Lukanov, 1972):

$$\left[\frac{1}{D_{eq}} \right]^{1/4} = 1.30 \eta_{fn} \frac{A_{fs}}{A_{ef}} \frac{1}{\bar{L}^{1/4}} + \frac{A_{ft}}{A_{ef}} \frac{1}{D_o^{1/4}} + \frac{A_{uf}}{A_{ef}} \frac{1}{D_r^{1/4}} \quad (2.16)$$

$$\bar{L} = \frac{\pi(D_o^2 - D_r^2)}{4D_o} \quad (2.17)$$

$$A_{ef} = \eta A_{fs} + \eta A_{ft} + A_{uf} \quad (2.18)$$

The Katz and Beatty correlation was obtained using tubes with 276 and 630 fins per meter (fpm) (7 and 16 fins per inch (fpi)) and HCFC-22 along with other low surface tension fluids where surface tension effects are minimal. Although this correlation is used quite successfully in the refrigeration industry, other investigators have attempted to include surface tension effects in the theoretical formulation, as will be shown in some of the models that follow.

HTRI model Ishihara and Palen (1982) describe the early HTRI methods of computing surface tension effects for finned tubes. A thermal resistance was computed for the condensate retained in the spaces between the fins:

$$r_c = C_1 [1 + \tanh(\Lambda_r - 2.5)]^2 \quad (2.19)$$

where

$$\Lambda_r = B_g \frac{\sigma}{\rho_f g} \quad (2.20)$$

$$B_g = p_f \left[\frac{4D_o - 2D_r + \frac{2}{p_f}}{\frac{\pi}{4}(D_o^2 - D_r^2)} \right] \quad (2.21)$$

C_1 is an experimentally determined condensation retention factor. The resistance of the retained condensate was assumed to reduce the heat transfer of the tube. The reduced heat transfer coefficient was computed from

$$h_{o,\sigma} = \frac{h_o}{1 + r_c h_o} \quad (2.22)$$

Gregorig model Gregorig (1954) realized that surface tension forces on a convex surface will cause the pressure of a liquid film covering the surface to be greater than the local vapor pressure, and that the opposite is true for concave surfaces. Gregorig was studying condensation on fluted tubes, which have alternating concave and convex surface regions, and found that the pressure gradient induced by surface tension was much greater than the pressure gradient induced by gravity. Thus, the pressure gradients set up by surface tension tend to drive the condensate off of the convex flutes and into the convex troughs, and the condensate film thickness is much thinner on the flutes than in the troughs.

Gregorig ignored gravitational effects and used numerical integration to solve the case of a constant film thickness on the convex flutes. He found that the increased heat transfer on the flutes (due to the thin film) far outweighed the decreased heat transfer in the troughs (due to the thick film), thus causing the fluted tube to have a heat transfer coefficient several times greater than that for the smooth tube.

Karkhu and Borovkov model Karkhu and Borovkov (1971) were the first to include the effects of surface tension in finned-tube analysis. The tube surface was divided into two regions. The first region was comprised of the fins, where the condensate was assumed to flow towards the fin root under the influence of surface tension only; gravity forces were neglected. The second region, which was comprised of the surface area between the fins, collected the condensate which drained from the fins. The heat transfer in the second region was ignored, because the film thickness (due to the draining condensate) was assumed to be large. To

account for flooding on the bottom of the tube, the flooding angle (ϕ_f) was assumed to be 150° , and the heat transfer from the fins in the flooded region was neglected. The resulting equations required a numerical solution. Karkhu and Borovkov found the agreement between their predicted heat transfer coefficient and experimental data to be within 5%.

Webb, Rudy, and Kedzierski model Webb et al. (1985) proposed a model which includes surface tension drainage on the fins, gravity drainage on the surface between the fins, and heat transfer in the flooded area of the tube. The average heat transfer coefficient is given by

$$h_o = \frac{\phi_f}{\pi} \left[\eta_{fn} h_{fn} \frac{A_{fn}}{A_{ef}} + h_{uf} \frac{A_{uf}}{A_{ef}} \right] + \left[1 - \frac{\phi_f}{\pi} \right] h_{fl} \quad (2.23)$$

Webb uses the less common condensate retention angle α , which is the complement of the flooding angle ϕ_f (ie. $\alpha = \pi - \phi_f$). Equation 2.23 has been modified to use the flooding angle ϕ_f .

To model the fin heat transfer, Webb chose a surface-tension dominated model and assumed that the fins had a convex surface profile. Webb used the method proposed by Adamek to calculate the condensate layer thickness and radius of curvature for the convex fin surfaces. The fin heat transfer coefficient is given by:

$$h_{fn} = 2.149 \frac{k_f}{S_m} \left[\frac{\sigma_i f_g \theta_m S_m \rho_f}{\mu_f k_f (T_{sat} - T_{s,o}) (\zeta + 2)^3} \frac{\zeta + 1}{(\zeta + 2)^3} \right]^{1/4} \quad (2.24)$$

This heat transfer coefficient is based on the nominal surface area of the tube, $A_o = \pi D_o L$, where D_o is outer diameter of the fins. The parameter ζ characterizes the aspect ratio of the fin cross section, and is iteratively determined so that the profile equation correctly predicts the thickness at the fin base. The parameter θ_m , which is the angle through which the convex surface turns, is visually determined for the tube of interest. The parameter S_m is the length of the convex surface over which the condensate film flows.

The heat transfer coefficient for the unflooded surface between the fins is given by

$$h_{uf} = 1.514 \left[\frac{\mu_f^2}{k_f^3 \rho_f^2 g} \text{Re}_{uf} \right]^{-1/3} \quad (2.25)$$

where

$$\text{Re}_{uf} = \frac{4\dot{m}_r}{\mu_f(p_f - t_b)} \quad (2.26)$$

The term \dot{m}_r is calculated iteratively and requires that h_{fn} be previously calculated. Equation 2.25 is the Nusselt equation for horizontal tubes written in terms of the condensate Reynolds number.

The heat transfer in the flooded region is characterized by a two dimensional conduction problem. Webb numerically solved the conduction equations for the condensation of CFC-11 for the 1024-fpm (26-fpi) geometry and found that the heat transfer in the finned region accounted for only 0.2% of the total heat transfer. For water (which has a higher thermal conductivity than CFC-11) condensing on 203-fpm (5-fpi) geometry, Webb estimated that only 1.6% of the heat transfer would occur in the flooded region. Therefore, Webb concluded that the heat transfer in the flooded region would be negligible for most practical cases. Webb compared this model to experimental data for the condensation of CFC-11 on several types of finned tubes, and found the predicted values to be within 20% of the experimental values.

Honda, Nozu, Uchima model The most comprehensive model to date has been developed by Honda et al. (1987), and is an extension of an earlier model (Honda and Nozu, 1984). Heat transfer from the fin tips, fin sides, and unfinned areas is considered, and the tube is divided into flooded and unflooded regions to account for significant differences in the heat transfer phenomenon for the thick and thin film regions. The model allows for wall temperature variations axially between the fins, as well as circumferentially around the tube. Gravity and surface tension effects are both considered. The calculation of the average heat

transfer coefficient requires an iterative solution involving roughly 15 equations. The values predicted by the Honda et al. (1987) model agreed with their experimental CFC-113 and methanol data to within 20%.

Tube bundles

Katz and Geist experiment Katz and Geist (1948) attempted to determine a row effect for finned tube bundles by using the Beatty and Katz (1948) single-tube correlation in conjunction with the Nusselt bundle model (Equations 2.4 and 2.5). They condensed CFC-12, acetone, n-butane, and water on a vertical column of six horizontal 590-fpm (15-fpi) tubes. Katz and Geist found that Equation 2.5 underpredicts the lower row heat transfer coefficients. For CFC-12, the ratio of the actual heat transfer coefficient to the predicted heat transfer coefficient for row 2 was 1.16, while the ratio was 1.55 for row 6. The underprediction was worse for acetone and n-butane. Marto (1988a) states that the Katz and Geist (1948) data can be better correlated by setting $m = 0.06$ in Equation 2.4.

Pearson and Withers model Pearson and Withers (1969) tested the Katz and Beatty correlation using HCFC-22 and the more modern fin configurations of 748 and 1024 fpm (19 and 26 fpi). The data were collected from two 60 tube condensers having a 24 mm (0.9375 in) triangular pitch. Pearson and Withers suggested that their data could be correlated by multiplying the right side of Equation 2.12 by a factor of

$$\frac{C_N}{N^{1/4}} \quad \text{where } C_N = 1.34 \text{ for the 1024-fpm} \\ C_N = 1.31 \text{ for the 748-fpm} \quad (2.27)$$

The value of N in this experiment was 4. At the time of this experiment, the 1024-fpm was just coming into use. Since Pearson and Withers found little difference between values

of C_N for the two fin types, they suggested that 748-fpm data for other working fluids could be extrapolated to the 1024-fpm geometry.

Pearson and Withers found the 1024-fpm geometry to have a 25% increase in condensing capacity over the 748-fpm geometry. The performance increase was attributed to the 25% increase in surface area per unit length of the 1024-fpm geometry over the 768-fpm geometry. Since the Pearson-Withers correlation is simply a modification of the Beatty-Katz correlation, the predicted heat transfer coefficients are based on the actual outer surface area, and are essentially the same for both tube types. The condensing capacity is determined by multiplying the heat transfer coefficient by the outer surface area. Since the 1024-fpm has a 25% greater surface area than the 748-fpm, its performance (as predicted by the Pearson-Withers correlation) will also be 25% greater.

Webb and Murawski experiment and model Webb and Murawski (1990) attempted to correlate the row effect found during the condensation of CFC-11 on several enhanced tubes, including a 1024-fpm (26-fpi) tube. The data were correlated in two ways: the exponent m was found for Equation 2.5, and the row coefficient was correlated as a function of Reynolds number (Re). The Reynolds number correlation is given by

$$h_{o,R} = aRe_L^{-n} \quad (2.28)$$

where

$$Re_L = \frac{4\Gamma}{\mu_f} \quad (2.29)$$

The parameter Γ is the total condensate mass flow rate per unit length from the bottom of the tube of interest, and includes the condensate draining from the above tubes. Thus, the Reynolds number increases with row number N , and subsequently $h_{o,R}$ drops. The heat transfer coefficients predicted by the Webb-Murawski model are based on the nominal surface

area. The nominal surface area is calculated from $\pi D_o L$, where D_o is the outer diameter of the finned section.

The average heat transfer coefficient for a tube bank of N rows is calculated by integrating Equation 2.28 over Re from row 1 to N . The result of this integration is

$$h_{o,B} = \frac{a}{(1-n)(Re_{L,N} - Re_{L,1})} \left[Re_{L,N}^{1-n} - Re_{L,1}^{1-n} \right] \quad (2.30)$$

The average heat transfer coefficient equation listed in the original Webb and Murawski paper is in error; the equation listed above is correct.

Webb and Murawski found that m varied with the condensation temperature difference $T_{sat} - T_{s,o}$. Therefore, Webb and Murawski prefer the Reynolds number correlation, since the constants a and n were independent of the condensation temperature difference, and the Reynolds number correlation can be used for any row, as long as \dot{m}_r is known.

For the 1024-fpm (26-fpi) geometry, Webb and Murawski found that $a = 13900 \text{ W}/(\text{m}^2 \cdot \text{K})$, and $n = 0.0$. Since $n = 0.0$ indicates that the heat transfer coefficient is independent of Reynolds number, the heat transfer coefficient does not depend on row number. This was attributed to channeling of the condensate by the fins, which prevented the liquid from spreading axially and covering more of the tube surface as the liquid drained from row to row. The other tubes in Webb and Murawski study all showed much less channeling of the condensate and hence had much larger row effects.

Honda, Nozu, and Takeda model The most detailed analysis of condensation on finned tube bundles was performed by Honda, Nozu, and Takeda (1989). This model considers two different flow pattern modes: column mode and sheet mode. Honda originally observed 4 flow modes (droplet mode, column mode, column and sheet mode, and sheet mode), but combined the droplet, column, and column and sheet modes together into one mode for simplicity. The transition between modes is specified by the parameter \bar{K} , where $\bar{K} =$

$\Gamma(g/\rho_f)^{1/4}/(2\sigma^{3/4})$. When $K \leq 0.42$, the column mode exists; the sheet mode exists when $K > 0.42$.

For column mode flow, the tube is divided into a region that is affected by the columnar drainage from the above tube, and a region that is not affected by columnar drainage. The affected and unaffected regions are divided into flooded and unflooded regions, as with the Honda single-tube model. The tube surface is further divided into thin film and thick film regions. The heat transfer rates in the unaffected region can be calculated from the Honda single-tube model. For the affected region, the single-tube model must be modified to account for the columnar dripping. This modification introduces a nonlinear equation which must be solved iteratively as well as a differential equation which must be solved numerically. The sheet mode is treated the same as columnar flow in the affected region, with the assumption that the condensate is distributed uniformly along the length of the tube.

The Honda model predicts the row-by-row data of Katz and Giest (1948) for CFC-12 and acetone with 5%, while the model predicts the Katz and Geist (1948) *n*-butane data to within 15%. Honda et al. ran several simulations for CFC-12 and steam condensation for a 15-row bundle. The model predicts that the heat transfer coefficient for CFC-12, which has small values of both surface tension and enthalpy of vaporization relative to steam, is strongly influenced by the fin spacing at the tip. Honda predicts the optimum value of CFC-12 fin spacing for the top bundle row to be 0.2 mm (0.00787 in), and 0.3 mm (0.0118 in) for bundle rows 2-15. The optimum fin thickness for CFC-12 is predicted to be 0.3 mm (0.0118 in). The fin height used by Honda in these calculations was 1.4 mm (0.55 in). Using the optimum values of fin spacing and fin thickness results in a tube that would have 1667 fpm (66 fpi). Because of the complexity involved in solving the Honda bundle model, simpler models such as the Pearson and Withers model are commonly used in industry.

Murata, Abe, and Hashizume model An analytical model for tubes with rectangular shaped fins was proposed by Murata et al. (1990). The fin surface was divided into a fin region, a connecting region, and a root region, where the condensate draining from the fin region collects. The tube surface was divided into flooded and unflooded regions. The heat transfer coefficient for the fin region was determined by using the method of Webb et al. (1985). The heat transfer coefficient for the the connecting region of the fin was found by integrating the thermal conductivity to condensate thickness ratio over the length of the connecting region. The heat transfer coefficient for the root region of the fin was found by assuming a one-dimensional condensate temperature profile and then solving the energy equation. The model neglects heat transfer in the flooded region of the tube.

The model of Murata et al. predicted their own single tube data very well, but underpredicted the performance of tubes in bundles. The discrepancy was attributed to the fact that the model neglected both the heat transfer in the flooded region of the tubes as well as the effect of splashing in the lower part of the bundle. Comparisons to other data were not included.

Analysis of Other Enhanced Geometries

Little work has been done on the theoretical analysis of enhancement types other than fins. Other common enhanced geometries include the GEWA SC, which has fins of a Y-shaped cross section, and the Turbo C-II, which has fins that have been mechanically knurled to produce a saw-tooth fin shape.

Webb and Murawski (1990), whose model was discussed in a previous section, also analyzed CFC-11 condensation for several enhanced tube geometries. They correlated their results with the equation

$$h_N = a \text{Re}_L^{-n} \quad (2.31)$$

The constants a and n for several enhanced tubes are shown in Table 2.1.

Table 2.1: Constants for the Webb and Murawski (1990) condensation model

geometry	a W/(m ² ·K)	n
26-fpi	13 900	0.000
GEWA SC	54 140	0.220
Turbo C	257 800	0.507
Tred-D	269 900	0.576
Modified Turbo C	113 300	0.446

Webb and Gee (1979) also proposed a spined-fin enhancement and did a preliminary analytical analysis. The spine cross section was 0.3 mm × 0.3 mm (0.012 in × 0.012 in) and the spine height was varied from 0.826 mm to 1.59 mm (0.0325 in to 0.0625 in). The theory behind the spine-fin geometry was that the three-dimensional spines give more surface area per unit volume of material than conventional circular fins, and thus a higher heat transfer coefficient for a given amount of tube material. The analysis showed that for equal values of $h_o A/L$, the spine fin would require 60% less material than normal circular-fin tubes. This tube was never commercially produced.

Boundary Layer Analysis

Another approach to solving the condensation heat transfer problem is to use a boundary layer approach. Such an analysis of film condensation begins by examining the case of two-dimensional condensation occurring on a vertical flat plate or single round tube. Two boundary layers are assumed to exist, namely a liquid condensate film next to the cooled plate and a vapor boundary layer next to the the condensate boundary layer. Continuity, momentum, and energy differential equations are written for the liquid boundary layer, while continuity and momentum equations are written for the vapor boundary layer. These differential equations and boundary conditions can be found in Rose (1988). The studies discussed in this section

deal with natural convection only.

Sparrow and Gregg (1959) first tried the approach described above for laminar, natural convection condensation. They neglected the vapor shear stress at the condensate-vapor interface. By transforming the governing differential equations with an appropriate similarity variable, Sparrow and Gregg found the following relationship for the surface heat transfer:

$$\frac{0.728\text{Nu}_o}{\text{Nu}_{o,Nu}} = (0.733)[- \theta'(0)] \left[\frac{C_p(T_{sat} - T_{s,o})/i_{fg}}{\text{Pr}} \right]^{1/4} \quad (2.32)$$

The parameter θ' is the derivative of non-dimensional temperature with respect to the similarity variable. Equation 2.32 requires a numerical solution. For values of $C_p(T_{sat} - T_{s,o})/i_{fg} < 0.01$, the results were very similar to the Nusselt theory. Table 2.2 lists deviations of the Sparrow-Gregg analysis from the Nusselt analysis for various combinations of $C_p(T_{sat} - T_{s,o})/i_{fg}$ and Pr_f .

Chen (1961) added the effect of vapor shear stress to the analysis. Chen used an approximation of the vapor shear stress so that solution of the vapor boundary layer equations was not necessary. Chen also performed an analysis for a column of tubes and modified the Nusselt column analysis by proposing that 1) additional condensation occurs between the tubes and 2) the condensate gains momentum as it falls from tube to tube. Chen correlated the results of his numerical solution with the equation

$$\frac{h_{o,N}}{h_{o,Nu,1}} = [1 + 0.2H(N - 1)] \left[\frac{1 + 0.68H + 0.02HJ}{1 + 0.95J - 0.15HJ} \right]^{1/4} \quad (2.33)$$

where

$$H = C_p(T_{sat} - T_{s,o})/i_{fg} \quad (2.34)$$

$$J = \frac{k_f(T_{sat} - T_{s,o})}{\mu_f i_{fg}} \quad (2.35)$$

Table 2.2: Deviation of the Sparrow and Gregg (1959) and the Chen (1961) analysis from the Nusselt theory

$C_p(T_{sat} - T_w)/i_{fg}$	Pr_f	$Nu_o/Nu_{o,Nu}$ (S-G)	$Nu_o/Nu_{o,Nu}$ (Chen)	$Nu_{o,S-G}/Nu_{o,Chen}$
0.01	0.003	0.88	0.71	1.24
0.01	0.008	0.95	-	-
0.01	0.01	-	0.84	-
0.01	1	1.01	0.92	1.10
0.01	10	1.01	1.00	1.01
0.01	100	1.01	1.00	1.01
0.10	0.003	0.58	0.42	1.38
0.10	0.008	0.71	-	-
0.10	0.01	-	0.58	-
0.10	0.03	0.88	0.71	1.24
0.10	1	1.02	1.00	1.02
0.10	10	1.04	1.00	1.04
0.10	100	1.04	1.10	0.95
1.00	1	1.10	1.00	1.10
1.00	10	1.14	1.15	0.99
1.00	100	1.15	1.17	0.98

For single tubes, Rose (1988) re-arranged Equation 2.33 to explicitly show the Pr dependence. These alternate forms of the Chen equations are

$$\frac{Nu_o}{Nu_{o,Nu}} = \left[\frac{1 + 0.68Pr_f J + 0.02Pr_f J^2}{1 + 0.85J - 0.15Pr_f J^2} \right]^{1/4} \quad (2.36)$$

$$\frac{Nu_o}{Nu_{o,Nu}} = \left[\frac{1 + 0.68H + \frac{0.02}{Pr_f} H^2}{1 + \frac{0.85}{Pr_f} H - \frac{0.15}{Pr_f} H^2} \right]^{1/4} \quad (2.37)$$

The deviation of the Chen analysis from the Nusselt theory is also given in Table 2.2. The ratio Nu_{S-G}/Nu_{Chen} shows the effect of vapor shear. Rose (1988) compares the results of Chen with the results of Sparrow and Gregg and concludes that surface shear effects are negligible at high Pr and small at low Prandtl numbers. Rose's conclusion is in agreement

with the values of Table 2.2.

Maekawa and Rose (Rose, 1988) confirmed that Chen's correlation matched his numerical solution to within 1%, and also gave a slightly more accurate and complicated expression for Chen's numerical results. Gaddis (1979) also used the boundary layer approach, and his numerical results are in good agreement with Chen (1961), and Maekawa and Rose (Rose, 1988). Rose (1988) suggests that these numerical studies appear to verify the validity of the simple Nusselt analysis for most practical purposes.

Forced Convection Analysis

Although forced convection condensation effects (vapor shear) is not the primary focus of this study, a brief overview of important works will be mentioned. A more detailed coverage of the development of forced convection theory from the boundary layer standpoint is provided by Rose (1988).

The first significant development of a forced convection boundary layer analysis was performed by Shekriladze and Gomelauroi (1966). Neglecting the pressure gradient in the condensate momentum balance, the condensate surface velocity, and the inertia and convection effects in the condensate film, the horizontal tube heat transfer is given by

$$\text{Nu}_o \bar{\text{Re}}^{-1/2} = 0.64[1 + (1 + 1.69 F_d)^{1/2}]^{1/2} \quad (2.38)$$

where

$$F_d = \frac{\mu_f^i f_f g^g D}{k_f (T_{sat} - T_{s,o}) U_\infty^2} \quad (2.39)$$

The value $\bar{\text{Re}}$ is defined as the two-phase Reynolds number and is based on the vapor velocity and the condensate properties, such that

$$\bar{\text{Re}} = \frac{U_\infty D \rho_f}{\mu_f} \quad (2.40)$$

Rose (1984) included the effect of the condensate film pressure gradient and suggested

$$\text{Nu}_o \bar{\text{Re}}^{-1/2} = \frac{0.64(1 + 1.81P^*)^{0.209}(1 + 1/G)^{1/3} + 0.728F_d^{1/2}}{(1 + 3.51F_d^{0.53} + F_d)^{1/4}} \quad (2.41)$$

where

$$P^* = \frac{\rho_g \mu_f^i f_g}{\rho_f k_f (T_{sat} - T_{s,o})} \quad (2.42)$$

$$G = \left[\frac{k_f (T_{sat} - T_{s,o})}{\mu_f^i f_g} \right] \cdot \left[\frac{\rho_f \mu_f}{\rho_g \mu_g} \right]^{1/2} \quad (2.43)$$

Rose suggests that Equation 2.43 will provide adequate results for most practical purposes.

Gaddis (1979) made a comprehensive study of forced convection condensation which did not contain any of the above mentioned simplifications. The added complications of condensate inertia, convection, and pressure gradient necessitate a numerical solution of the boundary layer equations. Using steam as the working fluid, Gaddis' model is in excellent agreement with the Nusselt analysis for the case of stagnant vapor. Gaddis' model predicts that the threshold at which vapor-shear becomes important increases with the vapor pressure of the working fluid. Using steam at a pressure of 0.1 atm as an example, vapor shear effects are noticeable at $\text{Re} = 300$, while at 10 atm vapor shear effects are first noticeable at $\text{Re} = 3000$.

Honda and Fujii (1984) carried out a detailed solution of horizontal tube condensation in which the heat transfer in the condensate film and the heat transfer in the wall were simultaneously considered. Although this model neglected condensate inertia, convection, and pressure gradient, the complexity added by the wall heat transfer necessitates a numerical solution. The results of the Honda-Fujii model are in excellent agreement with experimental CFC-113 data. The the circumferential variation in Nu as predicted by Honda and Fujii agreed with the results of Gaddis (1979) to within 3.7%. For CFC-113, the Honda analysis shows that significant deviation from the Nusselt theory begins at vapor velocities of 2 m/s (6.56 ft/s)

Summary

Table 2.3 gives a chronological listing of notable theoretical and empirical works concerning condensation on the outside of tubes. This table concentrates on works which are applicable to the refrigeration industry, such as general theoretical analyses and studies which concentrate on the surfaces and working fluids commonly used in the refrigeration industry. All of the works listed in Table 2.3 have been presented and discussed in this chapter.

A considerable amount of analysis has been performed on the condensation of steam. However, because of the significant differences between the properties of steam and refrigerants, as well as the fact that the surfaces used to condense steam are different than those used in the refrigeration industry, specific works pertaining to the condensation of steam are not listed or discussed here.

Table 2.3: Chronological listing of notable works in involving the theoretical and empirical analysis of condensation on tubes

Investigator	Year	configuration	Remarks
Nusselt	1916	single smooth tube	First to model condensation on a horizontal tube.
Nusselt	1916	single column of tubes	Related average heat transfer coefficient for a column of tubes to the heat transfer coefficient of the top tube in the column. Assumed tubes drained in a continuous laminar sheet.
Beatty, Katz	1948	single 7- and 16- fpi tube	First to present a correlation for condensation on finned tubes.
Katz, Geist	1948	bundle of 6 finned tubes	Studied condensation on a column of finned tubes.
Short, Brown	1951	smooth-tube bundle	Proposed that the Nusselt bundle model be modified by a factor of 1.24.
Gregorig	1954	single fluted tube	Realized that surface tension plays an important role in condensation on enhanced surfaces.
Rohsenow	1956	single smooth tube	Suggested an improved enthalpy of vaporization for the Nusselt model.
Kern	1958	column of smooth tubes	Proposed that condensate drains as discrete drops or columns.
Sparrow, Gregg	1959	single smooth tube	First to use boundary layer approach to solve condensation problems.
Chen	1961	single smooth tube	Added vapor shear stress effects to Sparrow and Gregg model.

Table 2.3 (Continued)

Investigator	Year	configuration	Remarks
Shekriladze, Gomelauri	1966	single smooth tube	Considered forced convection for a horizontal tube.
Pearson, Withers	1969	19- and 26-fpi bundles	First to correlate 26-fpi data with the Beatty- Katz model.
Eissenberg	1972	smooth-tube bundle	Examined row effect in a staggered tube bundle.
Karkhu, Borovkov	1971	single finned tube	First to include surface tension effects in a finned tube analysis.
Smirnov, Lukanov	1972	finned-tube bundle	Proposed a modified equivalent diameter for the Beatty-Katz equation which included the fin tip.
Butterworth	1977	smooth-tube bundle	Developed a correlation for combined vapor s- hear and inundation.
Gaddis	1979	single smooth tube	First comprehensive treatment of forced convection.
Gogonin, Dorokhov	1981	smooth and finned-tube bundles	Studied vapor velocity effects on the condensa- tion of CFC-21 in tube bundles.
Honda, Fujii	1984	single smooth tube	Considered heat transfer in the tube wall and condensate film simultaneously.

Table 2.3 (Continued)

Investigator	Year	configuration	Remarks
Rose	1984	single smooth tube	Considered pressure gradient effects in forced convection.
Webb et al.	1985	single finned tube	Accounted for differences in heat transfer between the finned, flooded, and unflooded regions of a tube.
Honda, Nozu	1987	single low-finned tube	Honda smooth tube model extended to finned tubes.
Honda et al.	1987	single low-finned tube	Previous Honda finned tube model is further generalized.
Maekawa, Rose	1988	single smooth tube	Followed Chen's methodology and proposed a more accurate correlation of numerical results.
Honda et al.	1989	bundle of low-finned tubes	Extension of previous model to include inundation effects.
Webb, Murawski	1990	column of enhanced tubes	Correlated row effect as a function of Re using CFC-11 data.
Murata et al.	1992	finned-tube bundle	Studied inundation effects on the condensation of HCFC-123 in tube bundles.

CHAPTER 3. EXPERIMENTAL APPARATUS

The experimental test facility used in this study measures shell-side condensation heat transfer coefficients for pure refrigerants. The test facility was designed so that it could be easily adapted to a variety of shell-side condensation studies. The ASHRAE 676-RP work statement required the test facility to conform to several requirements:

1. the test facility must be able to provide the data necessary to calculate the average bundle heat transfer coefficient as well as the average heat transfer coefficient for the middle tube of each row;
2. the average shell-side heat transfer coefficient must be measured without relying on tube-wall temperature measurements;
3. the test section must be capable of accommodating multiple tube bundles and multiple refrigerants;
4. the test facility must be able to accommodate a bundle tube loading of 2400 W per linear meter (2500 BTU/hr per linear foot);
5. The test section must be at least 309 mm (12 in) long and must accommodate a 5 column wide by 5 row deep tube bundle;
6. the temperature rise of the water passing through the test section must be greater than 1.11°C (2°F);

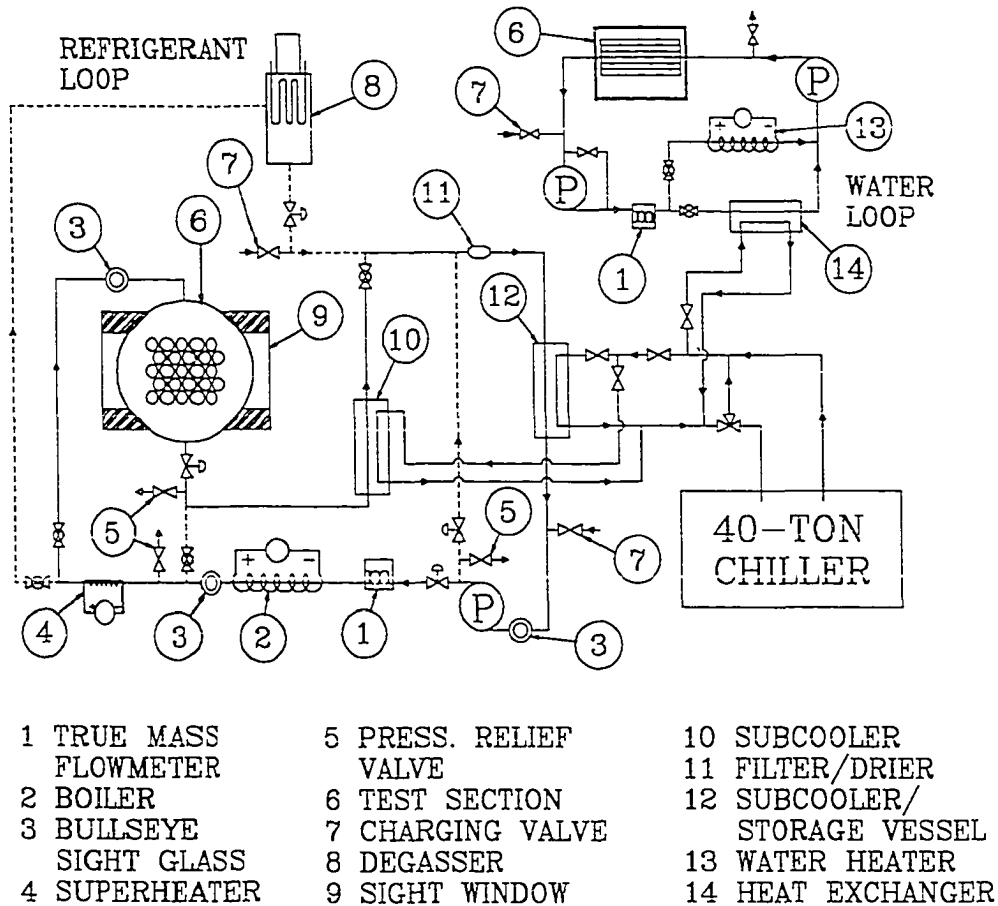


Figure 3.1: Schematic of experimental test facility

7. the refrigerant loop of the test section must not introduce any oil into the refrigerant;
8. the refrigerant loop must provide 35°C (95°F) saturated vapor for the test section.

The major components of the shell-side condensation test facility are the test section, the tube bundles, the refrigerant loop, the closed water loop, the glycol chiller, and the data acquisition system. A schematic diagram of the test facility is given in Figure 3.1. The various test facility components are discussed below.

Test Section

The test section was constructed from 203 mm (8 in) i.d. schedule 40 stainless steel pipe. The test section is 660 mm (26 in) long with 152 mm (6 in) high sight windows installed on each side to allow visual observation of the condensation phenomenon. Flanges were installed on each end of the test section to accommodate the installation of tube bundles and water boxes. The test section has 3 ports on the top side (two are used as vapor inlet ports and one is used for instrumentation) and 3 ports on the bottom side (one is used for the condensate outlet while the other two are presently unused). The test section also has two side auxiliary ports, one of which is connected to a pressure relief valve while the other is attached to a refrigerant charging valve.

During the initial portion of this study, a test section of 1270 mm (50 in) in length was used. However, the bundle tube loadings obtained with the longer test section were too low to satisfy the project requirements. In order to raise the bundle tube loading, the test section length was reduced to 660 mm (26 in). The latter 660-mm (26-in) test section was used throughout this study.

Tube Bundles

The tube bundles are 5 columns wide by 5 rows deep and were constructed from 2 different finned tube geometries and two different enhanced tube geometries. All tubes have a nominal o.d. of 19.1 mm (0.75 in) and are made from standard copper alloys. The finned geometries tested were the 26 fin per inch (fpi) (1024 fin per meter (fpm)) and the 40-fpi (1575-fpm). The 26-fpi has a standard fin height of 1.45 mm (0.057 in), while the 40-fpi is of the low fin variety and has a fin height of 0.86 mm (0.034 in). For a given nominal outer diameter, low-fin tubes typically have a larger inner diameter than tubes with standard height fins, and are used in cases where the smaller inner diameter of the standard fin-height tube

Table 3.1: Tube geometry specifications

tube	fin count fins/m	D_o nominal mm	D_i nominal mm	D_r mm	fin height mm	A_o nominal m^2/m	A_o actual m^2/m	A_i nominal m^2/m
26-fpi	1024	18.80	14.40	15.90	1.45	0.0588	0.193	0.0454
40-fpi	1575	18.87	15.70	17.10	0.86	0.0594	0.179	0.0493
Tu-Cii	–	18.90	15.54	17.07	0.91	0.0597	–	0.0488
G-SC	1024	18.94	14.17	16.82	1.06	0.0595	0.200	0.0445

tube	fin count fins/in	D_o nominal in	D_i nominal in	D_r in	fin height in	A_o nominal ft^2/ft	A_o actual ft^2/ft	A_i nominal ft^2/ft
26-fpi	26	0.739	0.568	0.625	0.057	0.193	0.634	0.149
40-fpi	40	0.743	0.622	0.675	0.034	0.195	0.586	0.163
Tu-Cii	–	0.744	0.612	0.672	0.036	0.196	–	0.160
G-SC	26	0.746	0.558	0.662	0.042	0.195	0.656	0.146

would cause an excessive pressure drop in the water passing through the tube. The bundles have a staggered tube arrangement with a horizontal pitch of 22.2 mm (0.875 in) and a vertical pitch of 19.1 mm (0.75 in).

The enhanced geometries tested were the Wolverine Turbo C-II (hereafter referred to as Tu-Cii), and the Wieland GEWA SC (hereafter referred to as G-SC). The G-SC is characterized by long, Y-shaped fins, while the Tu-Cii has short fins that have been roughened by mechanical working. The tube geometric specifications are given in Table 3.1. A photograph of the tube geometries tested in this study is shown in Figure 3.2, and a schematic of the tube-sheet (which shows the staggered pitch arrangement) is shown in Figure 3.3.

The tubes were manufactured with a spiral inner heat transfer enhancement in order to decrease the water-side heat transfer resistance. The water-side enhancements consists of several spiral ridges that run axially along the inner surface of the tube. The dimensions of the water-side enhancements for each tube are listed in Table 3.2. It should be mentioned that the measurement of heat transfer coefficients in this study focuses on the shell-side only.

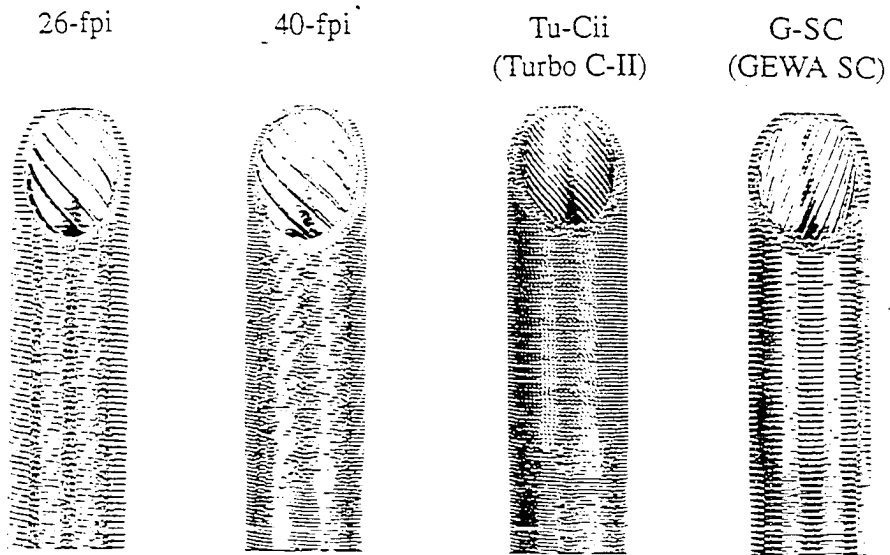


Figure 3.2: Photograph of tube geometries

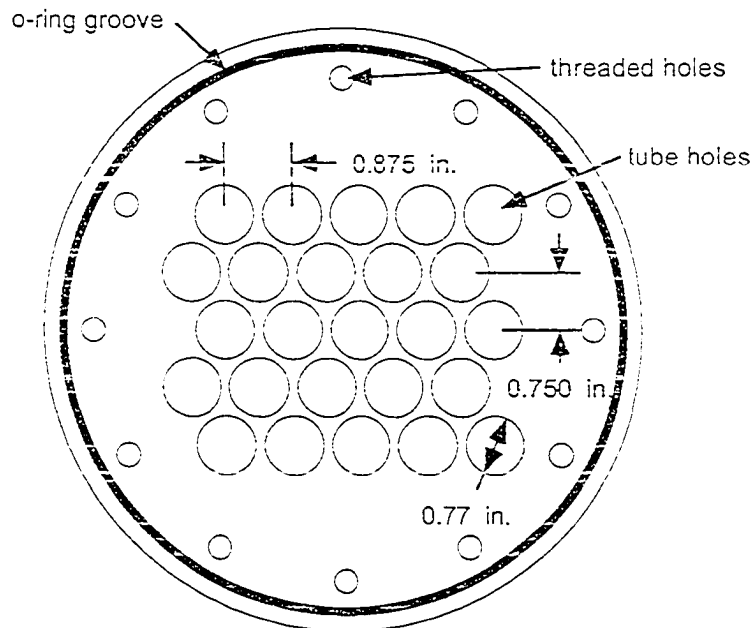


Figure 3.3: Schematic of tube-sheet

Table 3.2: Water-side heat transfer enhancement specifications for the different tube geometries

tube	ridge count	ridge height	spiral angle
26-fpi	10	0.381 mm (0.015 in)	40°
40-fpi	10	0.381 mm (0.015 in)	50°
Tu-Cii	38	0.508 mm (0.020 in)	40°
G-SC	25	0.540 mm (0.021 in)	20°

Fastening the tubes into the tube-sheets required that a number of technical difficulties be addressed. The joint between the tube and tube-sheet must be leak-free for the maximum water-side-shell-side pressure difference of interest, which in this case is 1030 kPa (150 psia). Initially the tube sheets were constructed from brass, and the tubes were fastened to the tube sheets by soldering. Because of the high temperature required for soldering, the tubes expanded during the soldering process and the bundle warped to a point that it could not be properly installed in the test section. The second approach used steel tube-sheets and a soft solder that had a low melting temperature. Although the use of the low-temperature solder prevented warping of the bundle, leak-proof joints could not be obtained.

The next approach was to use mechanical rolling to fasten the tubes into the tube-sheets. During the rolling process, the tube is placed into the tube-sheet and radially expanded by using a rolling tool. During the expansion, a leak-tight friction fit should develop between the tube and tube-sheet. The tube material should be softer than the tube-sheet material, and care must be taken not to over-roll the tube in order to prevent material failure. The amount to which the tube should be rolled is a matter of trial and error. A discussion on the art of tube rolling can be found in Fisher and Brown (1954).

The tubes were supplied with soft, plain ends suitable for rolling. The first choice of tube-sheet material was 6065-T651 aluminum alloy. This alloy is quite hard, yet relatively inexpensive and easy to machine. Aluminum is also resistant to corrosion, which is important because one side of the tube-sheet is exposed to water. The thickness of the tube-sheets was chosen to be 25.4 mm (1 in). This choice was based on the discussion in Fisher and Brown (1954), consultation with several industry personnel, and an investigation of several other heat exchangers in the laboratory. The use of aluminum tube-sheets was not successful, as small pinhole leaks that could not be fixed were present in the rolled joints. Because of the bundle pitch, the ligatures between the holes are quite thin, and even though the aluminum alloy used was quite hard, the ligatures were not able to withstand the stresses of the rolling process. Thus, the holes in the tube-sheets deformed just enough to prevent a leak-tight joint.

The final choice of tube-sheet material was 316 stainless steel, which is significantly stronger than aluminum and corrosion resistant as well, but also substantially more expensive and more difficult to machine. No problems were encountered in producing leak-tight joints using the stainless steel tube-sheets.

Impingement plates were installed on the top of the tube bundle to disperse the incoming refrigerant vapor. Diversion plates were installed on the sides of the bundle to ensure that all vapor entering the test section flowed through the bundle. The diversion plates consist of a steel frame covered with glass, which allows viewing of the condensation phenomenon from the test section sight windows. The space between the diversion plates and the sides of the tube bundle is the same as the space between adjacent tubes in the bundle. In an actual refrigerant condenser, the entire shell is filled with tubes and the refrigerant is forced to flow through the bundle. Without the diversion plates installed in the test section, the refrigerant vapor follows the path of least resistance and flows around, instead of through, the bundle. When the refrigerant in the test section flows around the bundle, the amount of condensation that

occurs on the perimeter tubes is higher than the amount of condensation that would normally occur on the perimeter tubes of an actual condenser.

A single-pass water flow arrangement is used. In order to insure that the water flow rate through all tubes was uniform, the tubes on the water outlet end of the bundle were fitted with rubber stoppers containing a 25.4 mm (1 in) long piece of 4.763 mm (0.1875 in) i.d. copper tube. The stoppers induced a large pressure drop, causing losses in the inlet water header to be negligible, thus creating a uniform water distribution.

Refrigerant Loop

The refrigerant loop is used to set the refrigerant inlet condition to the test section. Refrigerant is pumped into the boiler, which is a 7.315 m (24 ft) long section of 19.1 mm (0.75 in) o.d. stainless steel tube. The refrigerant is boiled by passing electrical current through the walls of the boiler tube. The current is supplied by a 40 kVA SCR controlled rectifier.

After leaving the boiler, the refrigerant passes into the primary superheater, which is a 1.83 m (6 ft) section of 38.1 mm (1.5 in) i.d. copper pipe wrapped with electric heat tapes. Downstream of the primary superheater is the secondary superheater, which is a 610 mm (2 ft) section of 38.1 mm (1.5 in) i.d. copper pipe wrapped with electric heat tapes.

Initially, the superheaters were constructed from 19.1 mm (0.75 in) o.d. copper tube. However, a large pressure drop occurred across the superheaters, causing the boiler pressure to be relatively high. Since the pressure in the boiler was elevated, the refrigerant boiling temperature was also elevated, and the boiler tube would have been operated at excessively high temperatures in order to boil the refrigerant unless changes were made to the superheaters. Increasing the diameter of the superheater pipe eliminated the large pressure drop and allowed the boiler to operate at a safe temperature.

After leaving the superheaters, the refrigerant flows into the test section and condenses

on the tube bundle. The condensed refrigerant leaving the test section flows through a shell-and-tube condenser and then into a chilled storage tank which is located at the inlet of the pump. The condenser is necessary to subcool the refrigerant liquid so that it can be pumped. The storage vessel insures that the pump will never be starved for liquid.

A diaphragm-type positive displacement pump is used to circulate the refrigerant. The diaphragm pump is well suited to the present study for several reasons. First, the diaphragm pump prevents any oil from entering the refrigerant, as would be the case if a compressor was used to circulate the refrigerant. Secondly, the diaphragm pump is not plagued by the shaft seal leakage problems which affect conventional centrifugal and gear pumps. Thirdly, the diaphragm pump does not require the working fluid to provide lubrication for its internal moving parts, as gear pumps do. Finally, the diaphragm pump can withstand pressures up to 6890 kPa (1000 psia) and is significantly cheaper than magnetically coupled centrifugal pumps of the same pressure capabilities.

The original rig construction contained a coaxial condenser instead of the shell-and-tube-storage vessel combination described above. The design of the coaxial unit was such that significant liquid holdup occurred in the unit, causing the pump to cavitate. This cavitation eventually led to failure of the diaphragms within the pump. The coaxial condenser was also oversized, making control of the refrigerant subcooling nearly impossible. The usual condition was for the refrigerant leaving the coaxial condenser to be subcooled far beyond the level necessary for pumping. The elevated subcooling level decreased the capacity of the boiler, as a significant portion of the boiler energy was required to remove the subcooling.

The refrigerant loop also contains a degassing tower, which is a 1.52 m (5 ft) high length of 102 mm (4 in) i.d. copper pipe mounted vertically. During a degassing cycle, refrigerant is boiled and fed into the middle of the tower. The heavier vapor refrigerant condenses on a small coil installed in the top of the tower and falls to the bottom of the tower, while the

lighter non-condensable gases collect in the top of the tower and are periodically purged.

Water Loop

Water is pumped through the tube bundle to cool the tube surfaces during condensation, and hence remove the energy released from the refrigerant during the condensation process. The water leaving the tube bundle is split off into two streams for purposes of controlling the test section inlet temperature. One stream passes through a set of liquid-to-liquid heat exchangers, where the energy added as the water passes through the tube bundles is removed. The other stream passes through an SCR-controlled electric heater. The electric heater is used to precisely control the water temperature at the test section inlet. The two streams then merge and flow into the test section. Two centrifugal pumps are used to circulate the water.

The water loop also contains an in-line filtration system to clean the water. The filtration system consists of eight cartridge-type household water filters connected in a parallel arrangement. Before the filtration system was installed, the water became quite rusty after only one day of use, which required the water to be drained on a daily basis. Also, the water boxes had to be removed daily so that mineral deposits could be cleaned from the the inner tube surfaces. Since energy calculations are performed on the water loop, accurate water specific heat values are necessary. Therefore, corrosion inhibitors could not be added to the water because their effect on specific heat was not known. The filtration system as presently installed removes all of the rust and mineral particles from the water on a continuous basis.

Glycol Chiller

The cold source for the liquid-to-liquid heat exchangers, the refrigerant subcoolers, and the condenser in the degassing tower is a nominal 141 kW (480 000 Btu/hr) packaged chiller unit capable of supplying 35 kW (120 000 Btu/hr) at an evaporator temperature of -17.7°C

(0°F). The chiller unit has a 4 cylinder compressor equipped with unloading and a 1140 l (300 gal) water/glycol storage tank.

Data Acquisition System

The data acquisition system consists of two switch/control units and a high resolution digital multimeter controlled by an 80386 SX computer. The computer program that obtains the transducer measurements from the instruments is also capable of making water and refrigerant energy transfer rate calculations.

The temperatures necessary for the calculation of the shell-side heat transfer coefficient (except for the refrigerant saturation temperature) were measured with thermistors calibrated to an accuracy of $\pm 0.025^{\circ}\text{C}$ (0.045°F); other temperatures were measured with Type-T thermocouples.

Pressures were measured with strain gage pressure transducers having accuracies of $\pm 0.25\% \times (\text{full scale})$. Since the saturation pressure is a critical parameter, a redundant measurement was taken by a capacitance-type pressure transducer. The pressure measurements obtained from the strain gage transducer were used in the heat transfer coefficient calculations, because the strain-gage transducer has a higher accuracy than the capacitance-type transducer; the redundant measurement was used only as a check. Because HFC-134a and CFC-12 have higher vapor pressures than HCFC-123 and CFC-11, transducers with different ranges were used to minimize the experimental uncertainty. Strain-gage transducers with a range of 0-1034 kPa (0-150 psia) were used during the HFC-134a and CFC-12 tests, and strain-gage transducers with a range of 0-345 kPa (0-50 psia) were used during the HCFC-123 and CFC-11 tests.

The refrigerant and water flow rates were measured by coriolis-effect mass flow meters having an accuracy of $\pm (0.2\% \times (\text{flow rate}) + (\text{meter zero stability}))$. A summary of the

Table 3.3: Uncertainties in the measured parameters

measurement	transducer	uncertainty
refrigerant inlet temperature	thermistor	$\pm 0.025^{\circ}\text{C}$ (0.045°F)
refrigerant outlet temperature	thermistor	$\pm 0.025^{\circ}\text{C}$ (0.045°F)
bulk water inlet temperature	thermistor	$\pm 0.025^{\circ}\text{C}$ (0.045°F)
bulk water outlet temperature	thermistor	$\pm 0.025^{\circ}\text{C}$ (0.045°F)
tube water outlet temperatures	thermistor	$\pm 0.025^{\circ}\text{C}$ (0.045°F)
refrigerant pressure	strain gage	± 2.59 kPa (0.375 psia) HFC-134a and CFC-12 ± 0.862 kPa (0.125 psia) HCFC-123 and CFC-11
refrigerant mass flow rate	coriolis effect	$\pm(0.002\dot{m}_{ref} + 0.002$ kg/min) $\pm(0.002\dot{m}_{ref} + 0.004$ lbm/min)
water mass flow rate	coriolis effect	$\pm(0.002\dot{m}_w + 0.150$ kg/min) $\pm(0.002\dot{m}_w + 0.331$ lbm/min)

measurement uncertainties is given in Table 3.3. Since the test facility has nearly 50 different transducers, about 1 minute is required to scan through all the transducers.

The saturation temperature of the refrigerant in the test section was computed from the test section pressure measurement. Under the conditions of the present study, direct measurement of the saturation temperature was not possible. Because the refrigerant entered the test section as superheated vapor and exited as slightly subcooled liquid, the refrigerant normally underwent a temperature change of 4°C (7.2°F) as it passed through the test section. In order for the saturation temperature to be accurately measured, the exact location of the saturation temperature within the test section must be known. Determination of this location so that the saturation temperature could be measured within $\pm 0.2^{\circ}\text{C}$ (0.36°F) is nearly impossible, and most likely depends on the amount of superheat, type refrigerant, and tube geometry.

The saturation temperature can also be obtained from the saturation pressure, via the refrigerant saturation temperature-pressure relationship. The pressure remained constant throughout the test section, and since a phase change was taking place in the test section,

the test section pressure was the saturation pressure. Even though highly accurate pressure transducers were used, the sensitivity of the saturation pressure to the saturation temperature for the refrigerants used in this study caused the uncertainty in the derived saturation temperature to be rather high relative to the other measured temperatures. For instance, $\partial T_{sat}/\partial P_{sat}$ at 35°C (95°F) for HFC-134a is 0.041°C/kPa (0.51°F/psia) and 0.22°C/kPa (2.7°F/psia) for HCFC-123. The uncertainty in the derived saturation temperature was approximately $\pm 0.11^\circ\text{C}$ (0.2°F) for HFC-134a and CFC-12, and approximately $\pm 0.2^\circ\text{C}$ (0.36°F) for HCFC-123 and CFC-11. The derivation of the saturation temperature uncertainty can be found in Appendix A.

The uncertainty in the calculated shell-side heat transfer coefficient (w_{h_o}) is quite sensitive to the uncertainty in the saturation temperature. At low heat fluxes, nearly 75% of w_{h_o} is due to the uncertainty in the saturation temperature. At high heat fluxes, approximately 60% of w_{h_o} is due to the uncertainty in the saturation temperature.

CHAPTER 4. EXPERIMENTAL PROCEDURE

This chapter describes the procedures used to operate the shell-side heat transfer coefficient test facility, as well as the techniques used to calculate shell-side heat transfer coefficients using the data obtained from the facility. Before any shell-side heat transfer coefficients can be calculated, the water-side heat transfer coefficient must be known. The first section of this chapter describes the methods used to determine the water-side heat transfer coefficients for the tubes used in this study.

Determination of the Water-side Heat Transfer Coefficient

In order to calculate the shell-side heat transfer coefficient using the log-mean temperature difference (LMTD) approach, the heat transfer coefficient must be known for the water flow. If tubes with smooth inner surfaces are used, an appropriate correlation (such as the Gnielinski (1976) correlation) can be used to predict the water-side heat transfer coefficient.

During the first part of this study, finned tubes with a smooth inner surface were used. Unfortunately, the high water-side resistance of the smooth inner surface caused large imbalances between the shell-side and water-side heat transfer resistances, and this imbalance prevented accurate calculation of the shell-side heat transfer coefficient. Thus, finned tubes with water-side heat transfer enhancements were necessary. The Tu-Cii and G-SC are normally manufactured with water-side enhancements. Although the manufacturer had water-side heat transfer data available for the 26-fpi, 40-fpi, and Tu-Cii, new correlations were developed

for these tubes. Because the tube length in this experiment is significantly shorter than the tubes used in the manufacturer's tests, entrance effects might have caused the manufacturer's water-side values to be incorrect for the present experiment. No water-side heat transfer coefficient data were available for the G-SC.

The method used to determine the water-side heat transfer coefficient required the shell-side boiling of HFC-134a (Thors, 1992). Two tubes were installed into the test section using a specially designed endcap. The water connection was made so that the water followed a series path through the two tubes. The test section was filled with HFC-134a until the tubes were submerged. Warm water was circulated through the tubes, which caused the HFC-134a to boil off the tube surface. The heat flux and saturation temperature of the HFC-134a were held constant while the water flow rate was varied.

The heat flux was controlled by adding a fixed amount of energy to the water with the electric heater, while the saturation temperature was maintained by controlling the temperature of the water/glycol circulating through the downstream condenser. The water temperature was allowed to vary, while the saturation temperature was set at 14°C (57.2°F) with a deviation of no more than ±0.2°C (0.36°F). This saturation temperature resulted in water temperatures similar to those found in the actual condenser bundle. The heat flux was 27 500 W/m² (8700 Btu/(hr-ft²)) and was allowed to vary by no more than 5%. The water flow rates corresponded to those necessary for a 2°C (3.6°F) water temperature change across the condenser bundle for the tube loading range of interest in this study.

The mathematical equations governing the water-side heat transfer are:

$$q = \dot{m}_w C_p (T_{w,in} - T_{w,out}) = U_o A_o \times \text{LMTD} \quad (4.1)$$

where

$$\text{LMTD} = \frac{T_{w,in} - T_{w,out}}{\ln \frac{T_{w,out} - T_{sat}}{T_{w,in} - T_{sat}}} \quad (4.2)$$

$$\frac{1}{U_o} = \frac{A_o}{A_i} \frac{1}{h_i} + \frac{1}{h_o} + A_o R_{tw} \quad (4.3)$$

$$h_i = \text{STC} \frac{k_w}{D_i} \text{Re}_w^8 \text{Pr}_w^{.33} \left(\frac{\mu_w}{\mu_{tw}} \right)^{.14} \quad (4.4)$$

Equation 4.4 is a form of the familiar Sieder-Tate equation for flow in circular passages, where STC is the Sieder-Tate coefficient for the particular geometry. For this equation, the properties of water are evaluated at the average bulk temperature $(T_{w,in} + T_{w,out})/2$. The parameter μ_{tw} should be evaluated at the tube wall temperature. Since the tube wall temperature could not be calculated in this case, μ_{tw} was evaluated at $(T_{sat} + T_{w,bulk})/2$. Substituting Equation 4.4 into Equation 4.3 yields:

$$\underbrace{\frac{1}{U_o} - A_o R_{tw}}_Y = \underbrace{\frac{1}{h_o}}_a + \frac{1}{\underbrace{\text{STC}}_b} \underbrace{\frac{A_o/A_i}{\frac{k_w}{D_i} \text{Re}_w^8 \text{Pr}_w^{.33} \left(\frac{\mu_w}{\mu_{tw}} \right)^{.14}}}_X \quad (4.5)$$

The tube wall thermal resistance in Equation 4.5 is given by

$$R_{tw} = \frac{\ln(D_r/D_i)}{2\pi k_{tw} L} \quad (4.6)$$

Equation 4.5 is of the form

$$Y = a + bX \quad (4.7)$$

An X - Y pair was computed for each data point taken in the experiment described above. The unknowns are the intercept a , which is the inverse of the shell-side heat transfer coefficient, and b , which is the inverse of the STC. The hope is that the slope (and thus the STC) would remain constant over the entire range of the X parameter. a and b were determined by fitting a line through the X - Y pairs. Since the intercept must be constant for this method to be successful, the shell-side heat transfer coefficient must be held constant. Since the pool boiling heat transfer coefficient is a function of heat flux and fluid properties, great care was taken to maintain constant heat flux and saturation temperature during the tests.

Figure 4.1 shows the 26-fpi and 40-fpi water-side heat transfer coefficient test results while Figure 4.2 shows the Tu-Cii and G-SC water-side heat transfer coefficient test results for the flow rate range of interest in this study. The experimentally determined STCs are: 0.058 for the 26-fpi, 0.055 for the 40-fpi, 0.065 for the Tu-Cii, and 0.054 for the G-SC. The Reynolds number range of the fit data was $7500 < Re < 26\ 000$ for the 40-fpi, $8100 < Re < 34\ 000$ for the 26-fpi, $7100 < Re < 26\ 000$ for the Tu-Cii, and $8000 < Re < 34\ 000$ for the G-SC. The water-side heat transfer enhancement of the four tubes is similar, as the STCs are within 20 % of each other. For the fin tubes, the values of h_i predicted with these STCs differ from the manufacturer's values by less than 5%. For all tubes, the STC appears to remain constant over the flow rate range of interest.

The determination of the STC for the Tu-Cii posed a difficult challenge. The spiral heat transfer enhancement of the Tu-Cii is designed to provide an STC of 0.068 for $Re_D > 20\ 000$. However, for the water-side flow range of interest in this study ($9000 < Re_D < 18\ 000$), the STC of the Tu-Cii is not constant, and drops to roughly 0.04 at the lower flow rates. Such a high water-side resistance makes accurate calculation of the shell-side heat transfer coefficient nearly impossible.

The first attempt to solve this problem involved the insertion of a solid core insert to form an annulus for the water to flow through. Theoretical studies show that for turbulent flow ($Re_H > 10\ 000$), such inserts cause a significant increase in the water-side heat transfer coefficient. Unfortunately, for a given mass flow rate, Re_H decreases as the insert diameter increases. Thus, the installation of inserts in the present study caused Re to drop well below 10 000, which characterizes flow in the laminar-turbulent transition region. Since turbulent flow heat transfer resistance is significantly smaller than laminar flow heat transfer resistance, shifting the flow towards the laminar regime is not desirable, and the inserts actually caused an increase in the water-side resistance.

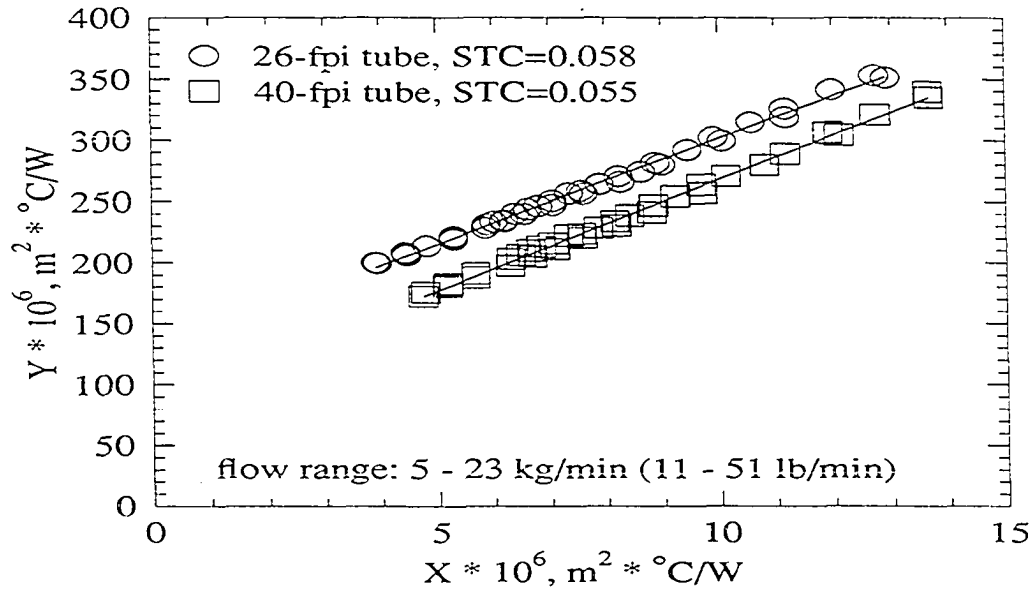


Figure 4.1: Water-side STC data for the 26-fpi and 40-fpi geometries

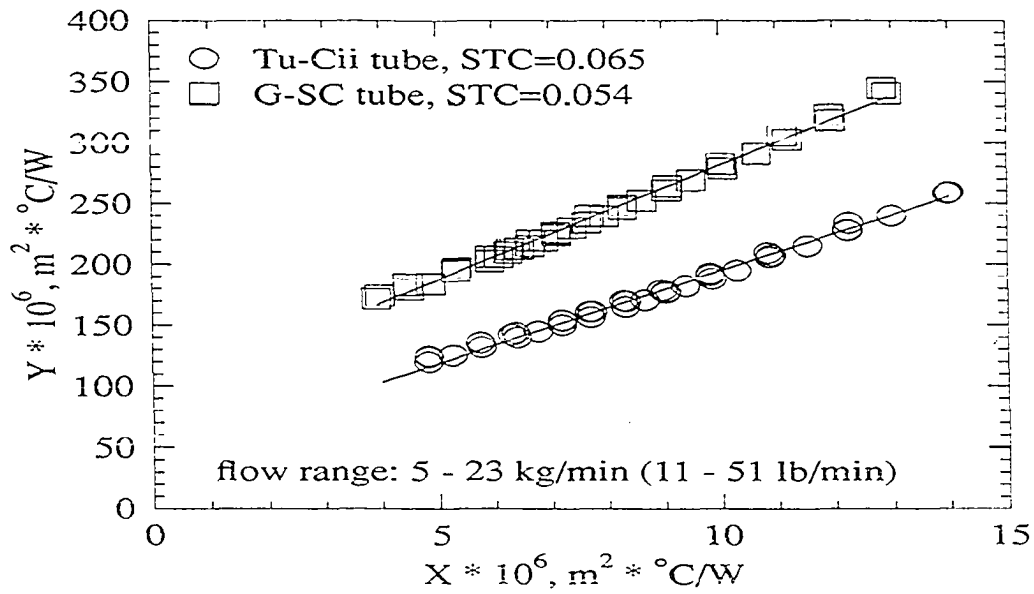


Figure 4.2: Water-side STC data for the Tu-Cii and G-SC geometries

The water-side resistance problem was finally alleviated by installing a spring-type turbulator used by a refrigeration equipment manufacturer (Glamm, 1993). The device consists of a spring that is constructed from a small diameter wire. The spring is simultaneously stretched and inserted into the tube. The original diameter of the spring is such that a friction fit develops between the stretched spring and the tube wall, thus holding the spring in place. The effect of the spring is to continually promote turbulence along the length of the tube. The pressure drop caused by the spring turbulator is very small. Although the STC produced by the spring turbulator is 5% smaller than the normal value, the STC is constant over the flow range of interest.

Rig Operation

Before the test facility was charged with refrigerant, the system was evacuated with a high-vacuum pump for at least 8 hours. After evacuation, the facility was allowed to set for several hours in order to check for leaks. The test facility was then charged, and the refrigerant degassed for 8 hours. After degassing, the refrigerant was stored in the test section and the saturation temperature computed from the saturation pressure was compared to the temperature registered by the thermistors in the test section. If the agreement was not within the uncertainty of the transducers, the degassing cycle was repeated.

Data readings were recorded in order of increasing nominal bundle load, starting at 16 kW (54 000 Btu/hr) and proceeding to 36 kW (123 000 Btu/hr) in increments of 2 kW (6800 Btu/hr). A short study was performed in which data readings were taken in order of decreasing bundle load to determine if any hysteresis was present. The calculated heat transfer coefficients appeared to be independent of whether the data points were taken in order of increasing or decreasing bundle load. Since the rig was easier to operate by increasing the bundle load, the data were taken in order of increasing bundle load.

During condensations tests, the following conditions were maintained:

1. the saturation temperature of the refrigerant in the test section was maintained at $35^{\circ}\text{C} \pm 0.1^{\circ}\text{C}$ ($95^{\circ}\text{F} \pm 0.18^{\circ}\text{F}$),
2. the refrigerant entering the test section was superheated by $3\text{--}5^{\circ}\text{C}$ ($5.4\text{--}9^{\circ}\text{F}$),
3. the temperature change of the water flowing through the bundle was kept at $2^{\circ}\text{C} \pm 0.1^{\circ}\text{C}$ ($3.6^{\circ}\text{F} \pm 0.18^{\circ}\text{F}$).

In order to calculate the shell-side condensing coefficients, the following parameters were measured:

1. the temperature of the refrigerant vapor entering the test section,
2. the temperature of the refrigerant condensate leaving the test section,
3. the temperature of the water entering the test section,
4. the bulk temperature of the water leaving the test section,
5. the temperature of the water leaving the middle tube of each bundle row,
6. the refrigerant pressure in the test section,
7. the refrigerant and water mass flow rates.

For a particular bundle load, the refrigerant and water flow rates were set to appropriate values. Next, the boiler and superheater power levels were adjusted until the appropriate inlet superheat was obtained, while the water temperature at the inlet of the test section was adjusted until the test section saturation temperature was correct. The condensate leaving the test section was visually inspected for vapor bubbles. If any uncondensed vapor was found

in the condensate, a throttling valve downstream of the test section was closed until all of the incoming vapor was condensed on the bundle. If necessary, the water temperature was adjusted to compensate for changes in the test section saturation temperature caused by the adjustment of the throttling valve. Finally, after all control adjustments were made, the rig was operated for several minutes so that steady state was attained. When the rig had come to steady state, 10 data scans were made by the computer and the measured data saved to disk. This scanning process took approximately 10 minutes. After the data run was completed, the rig was shut down, and a short repeatability run was taken the next day.

Data Reduction

The data from the 10 scans were loaded into a spreadsheet and then inspected for any anomalies. The spreadsheet then averaged the 10 scans and wrote the averaged data values to a file. Finally, a FORTRAN program used the averaged data to compute the shell-side heat transfer coefficients, using the equations listed below.

The shell-side heat transfer coefficient was calculated using the LMTD method. In this approach,

$$q = U_o A_o \times \text{LMTD} \quad (4.8)$$

where the log-mean temperature difference (LMTD) is defined as

$$\text{LMTD} = \frac{T_{w,out} - T_{w,in}}{\ln \frac{T_{sat} - T_{w,in}}{T_{sat} - T_{w,out}}} \quad (4.9)$$

and

$$\frac{1}{U_o} = \frac{A_o}{A_i} \frac{1}{h_i} + \frac{1}{h_o} + A_o R_{tw} \quad (4.10)$$

where

$$h_i = \text{STC} \frac{k_w}{D_i} \text{Re}_w^{0.8} \text{Pr}_w^{0.33} \left(\frac{\mu_w}{\mu_{tw}} \right)^{0.14} \quad (4.11)$$

For this equation, the properties of water are evaluated at the average bulk temperature $(T_{w,in} + T_{w,out})/2$. The parameter μ_{tw} is evaluated at $(T_{sat} + T_{w,bulk})/2$.

The energy transfer rate can be calculated from either the refrigerant energy transfer rate

$$q = \dot{m}_{ref}(i_{ref,out} - i_{ref,in}) \quad (4.12)$$

or the water energy transfer rate

$$q = \dot{m}_w C_p (T_{w,out} - T_{w,in}) \quad (4.13)$$

For the bundle heat transfer coefficient calculations, the refrigerant energy transfer rate and the bulk water-side energy transfer rate typically differed by less than 5%, and the two values were averaged to determine the energy transfer rate for the bundle. For the row heat transfer coefficient calculations, the energy transfer rate could only be determined from the water-side flow. In the case of the row coefficients, the tube flow rate was assumed to be 1/25th of the bulk flow rate. Experimental measurement of the water flow rates from the middle tube of each row indicated that the actual flow rate differed from the assumed tube flow rate by less than 1%.

After q was calculated, U_o was calculated from Equation 4.8. The shell-side heat transfer coefficient, h_o , can then be calculated by rearrangement of Equation 4.10:

$$h_o = \frac{1}{\frac{1}{U_o} - \frac{A_o}{A_i} \frac{1}{h_i} - A_o R_{tw}} \quad (4.14)$$

The temperature of the outer tube surface, which was used to find the driving temperature difference $T_{sat} - T_{s,o}$, can be calculated from

$$T_{s,o} = T_{w,bulk} + q \left(\frac{1}{\pi D_i L h_i} + \frac{\ln(D_r/D_i)}{2\pi k_{tw} L} \right) \quad (4.15)$$

This method was used to calculate the average shell-side bundle heat transfer coefficients as well as the average shell-side heat transfer coefficients for the middle tube of each row. The

tube length used in the calculation of the outer surface area was 603 mm (23.75 in), which was the length of enhanced surface exposed to the refrigerant. The nominal outer diameter of the tube was used to calculate the surface area. In other words, the tube outer surface area was equal to the surface area of a smooth tube of the same diameter as the enhanced tube nominal diameter. The nominal outer surface area was used so that comparisons could be made between all the geometries tested, as the actual outer surface area of the Tu-Cii is not known. Using the nominal surface area also allows performance comparison on a unit length basis. The tube dimensions used in the heat transfer coefficient calculations are given in Table 3.1.

As a check on the tube energy transfer rates, the FORTRAN program computed an estimate of bundle heat flux based on the middle tube heat fluxes by multiplying each tube heat flux by five, adding the weighted tube heat fluxes together, and dividing the sum by 25. The actual bundle heat flux and estimated heat flux generally differed by less than 5%.

Uncertainty of the Shell-side Heat Transfer Coefficients

Experimental uncertainty

The transducers used to obtain parameter measurements from the experimental test facility are real devices, and therefore the measurements returned by the transducers are subject to some uncertainty. Since the calculated shell-side heat transfer coefficients are based on transducer measurements, the calculated coefficients are also subject to experimental uncertainty.

The method used to determine the experimental uncertainty in the calculated heat transfer coefficients is the propagation of errors approach described in Holman (1984). This method uses the squares of the uncertainties in the independent parameters to compute the uncertainty in the calculated coefficients. A full derivation of the equations used to calculate the

experimental uncertainty in the shell-side heat transfer coefficients is given in Appendix A. The calculated uncertainties are given in Appendices B, C, D and E, which list the measured parameters and calculated data in tabular form for each data run. The uncertainties will be discussed in further detail in subsequent chapters.

Statistical uncertainty

There may also be statistical uncertainties in the calculated heat transfer coefficients due to random variations in the measured parameters. In order to determine the statistical uncertainty, a particular data point must be re-taken several times over a long period of time. With this information, confidence intervals can be placed on the calculated coefficients.

Due to time constraints, obtaining enough repeatability data in order to determine the statistical uncertainty was not possible. As a compromise, a short repeatability run was taken for each refrigerant-tube combination. The repeatability run was compared to the original data set. The variation between the data sets was found to be well within the experimental uncertainty. Thus, there appears to be no significant random variation in the shell side heat transfer coefficients.

Adaptation of Theoretical Models to the Current Study

The next two chapters will discuss the shell-side heat transfer coefficients obtained during the present study. During this discussion, heat transfer coefficients as predicted by the Pearson-Withers (P-W) and Webb-Murawski (W-M) models discussed in Chapter 2 are also shown for comparison purposes. Several important aspects of adapting the models to the current study are discussed below.

The Pearson-Withers (P-W) correlation

The P-W correlation requires that the outer tube surface temperature, $T_{s,o}$, be known. As discussed in Chapter 4, this temperature is calculated, not directly measured. The equivalent diameter D_{eq} is also required for each tube geometry. For the 26-fpi and 40-fpi tubes, D_{eq} is provided by the manufacturer. For the G-SC, D_{eq} was computed from tube dimensions supplied by the manufacturer. Insufficient information was available to calculate D_{eq} for the Tu-Cii, so no P-W predictions are given for the Tu-Cii.

Since the P-W correlation was derived from data for 26-fpi and 19-fpi tubes, using the model for the 40-fpi and G-SC tubes is somewhat of an extrapolation. The 40-fpi uses the same type of fins but has a higher fin density than the tubes used in the development of the P-W correlation. The G-SC has the same fin density but has a different fin shape than the tubes used in the development of the P-W correlation. Also, HCFC-22 was the only working fluid used during the development of the P-W correlation.

The heat transfer coefficients given by the P-W correlation are based on the actual outer surface area of the tube, while the heat transfer coefficients determined in this study are based on the nominal outer surface area. Since the predicted and experimental heat transfer coefficients must have the same area basis before they can be compared, the heat transfer coefficients predicted by the P-W correlation have been converted to a nominal outer surface area basis.

The Webb-Murawski (W-M) correlation

The W-M correlation requires that the condensate flow rate from each tube row be known. The flow rate of the condensate draining from the tube rows is difficult to determine for the tube bundles in this study. A real-time measurement of the condensate flow rate from each tube row is impossible because of the confined space. Therefore, the condensate flow rate

must be estimated, which is also difficult because the bundles use a staggered arrangement with a very tight pitch. The horizontal pitch is 22.2 mm (0.875 in), which leaves only a 3.18 mm (0.125 in) gap between the tubes in any given row. The vertical pitch is 19.1 mm (0.75 in), which leaves no gap between the rows (thus, the staggering of the rows).

For the staggered arrangement used in this study, the tubes in rows 1, 3, and 5 are directly in line, while the tubes in rows 2 and 4 are directly in line. Most of the condensate from the tubes in row 1 falls directly downwards to the tubes in row 3. However, because of the tight pitch, side drainage due to vapor velocity effects, and splashing, some of the condensate from row 1 inevitably falls on row 2. The same phenomena affect the condensate draining from rows 2, 3, and 4. The condensate flow rates will be estimated as follows: all condensate draining from row 1 is assumed to fall on row 3, all condensate draining from row 3 is assumed to fall on row 5, and all condensate falling from row 2 is assumed to fall on row 4.

For the outside columns (which can be viewed from the sight windows), visual observation of the condensation phenomenon indicated that the condensate generally drains straight down, but that splashing is noticeable at high bundle loads. Thus, the above assumption should provide a reasonable estimation of the actual tube condensate flow rates.

Webb and Murawski did not test a 40-fpi tube, and thus no W-M correlation constants are available for the 40-fpi tube. The 26-fpi W-M constants will be used to estimate the 40-fpi heat transfer coefficients. It should be mentioned that CFC-11 was the only working fluid used in the development of the W-M correlation.

CHAPTER 5. HFC-134a SHELL-SIDE CONDENSATION RESULTS

Shell-side condensation heat transfer coefficients for HFC-134a are presented in this chapter. Bundles constructed from four different tube geometries were tested over a nominal heat flux range of $16\,000\text{ W/m}^2$ ($5100\text{ Btu}/(\text{hr}\cdot\text{ft}^2)$) to $41\,000\text{ W/m}^2$ ($13\,000\text{ Btu}/(\text{hr}\cdot\text{ft}^2)$). For each tube geometry, average bundle heat transfer coefficients as well as the average heat transfer coefficient for the middle tube of each row are presented in graphical format. The HFC-134a row and bundle average heat transfer coefficients are compared to those for the condensation of CFC-12. A complete tabular listing of the entire set of HFC-134a data taken during this study can be found in Appendix B, while a tabular listing of the CFC-12 data can be found in Appendix C. In the following discussion, row 1 refers to the top row of the bundle, with the row number increasing towards the bottom of the bundle. For example, row 5 is the bottom row in the bundle.

As discussed in Chapter 4, the nominal outer surface area of the tube was used in the calculation of the shell-side heat transfer coefficient. The nominal outer surface area is based on the nominal outer diameter of the tube so that the tube outer surface area was equal to the surface area of a smooth tube of the same diameter as the enhanced tube nominal diameter. Thus, the heat transfer coefficients presented in this chapter are based on the nominal tube outer surface area, not the actual tube outer surface area.

Results for the 26-fpi Geometry

Average bundle heat transfer coefficient results

Figure 5.1 shows that the average shell-side bundle heat transfer coefficient ($h_{o,B}$) for the 26-fpi geometry decreases with increasing heat flux. An increasing bundle heat flux corresponds to an increasing refrigerant mass flow rate. As the mass flow rate (and hence, heat flux) increases, the liquid layer on the tubes becomes larger. The measured value of $h_{o,B}$ drops from 14 840 W/(m²·K) (2610 Btu/(hr·ft²·F)) to 12 610 W/(m²·K) (2220 Btu/(hr·ft²·F)), which is 15%, over the heat flux range tested (16 000 W/m² (5100 Btu/(hr·ft²)) - 41 000 W/m² (13 000 Btu/(hr·ft²))). The data for the repeatability run are also plotted on Figure 5.1. The repeatability of the experiment can be seen by comparing the data points for run 1 and run 2. This figure indicates that the data for $h_{o,B}$ can be repeated over the entire range of bundle loads tested, as the difference between the two runs is generally less than 2% over the entire heat flux range tested.

Figure 5.2 shows the variation of $h_{o,B}$ with the LMTD, while Figure 5.3 shows the variation of $h_{o,B}$ with the condensation temperature difference, $T_{sat} - T_{s,o}$. As previously discussed, the wall temperature is calculated, not directly measured. As the LMTD and $T_{sat} - T_{s,o}$ increase, more refrigerant is condensed. Thus, an increasing LMTD and $T_{sat} - T_{s,o}$ correspond to an increasing heat flux. The LMTD is a measure of the overall water-refrigerant temperature difference that drives the condensation, while $T_{sat} - T_{s,o}$ is the portion of the overall temperature difference that occurs between the tube outer surface and the refrigerant. Since the same trend in $h_{o,B}$ is present in both figures, the trend in $h_{o,B}$ is due to a shell-side phenomenon.

Uncertainty bars are also plotted on Figure 5.2, and show that the experimental uncertainty in $h_{o,B}$ ranges from $\pm 9\%$ to $\pm 15\%$. This figure indicates that $h_{o,B}$ decreases as the LMTD, and hence heat flux, increases. As the LMTD increases, $T_{sat} - T_{w,out}$ and

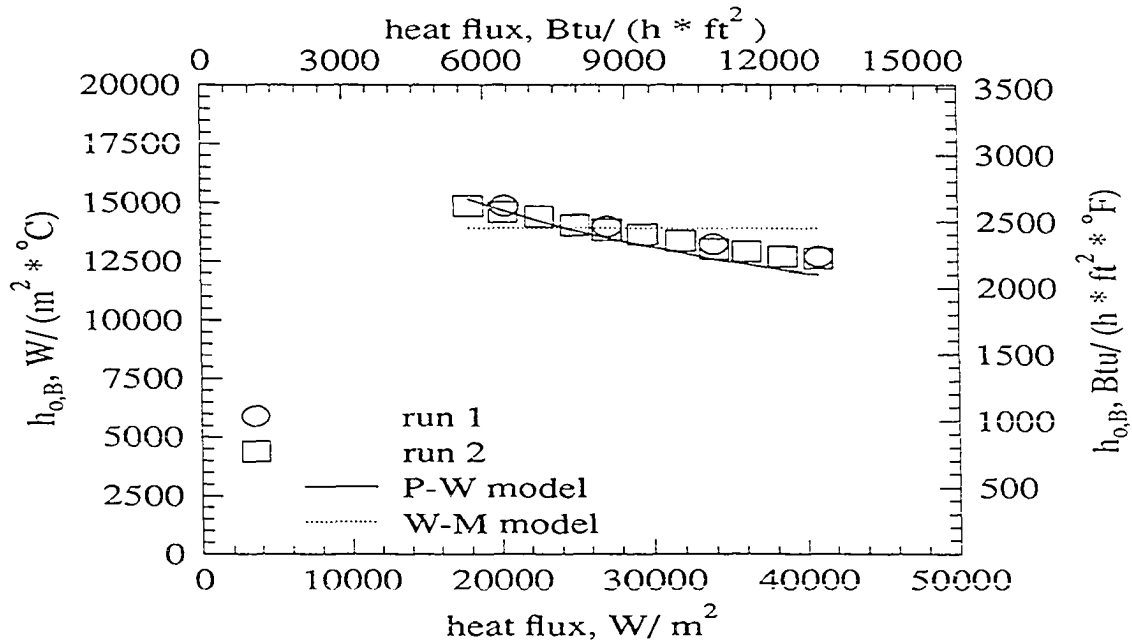


Figure 5.1: Average shell-side bundle heat transfer coefficient vs. heat flux for the condensation of HFC-134a on the 26-fpi geometry

$T_{sat} - T_{w,in}$ increase, but the uncertainty in these temperature differences remains the same. Therefore, the uncertainty in these temperature differences becomes less significant as the temperature differences increase. The calculation of $h_{o,B}$ is quite sensitive to these temperature differences, thus $w_{h_{o,B}}$ decreases as the uncertainty in these temperature differences becomes less significant. The data for the repeatability run are also plotted on Figures 5.2 and 5.3.

Average row heat transfer coefficient results

Figure 5.4 shows the behavior of the average heat transfer coefficients for the middle tube of each row ($h_{o,R}$) at different bundle loads for the 26-fpi. This figure indicates that $h_{o,R}$ for rows 1 and 2 generally decreases with increasing bundle load, but $h_{o,R}$ for rows 3, 4, and 5 is independent of bundle load. The value of $h_{o,R}$ for rows 1 and 2 drops about 20% over the

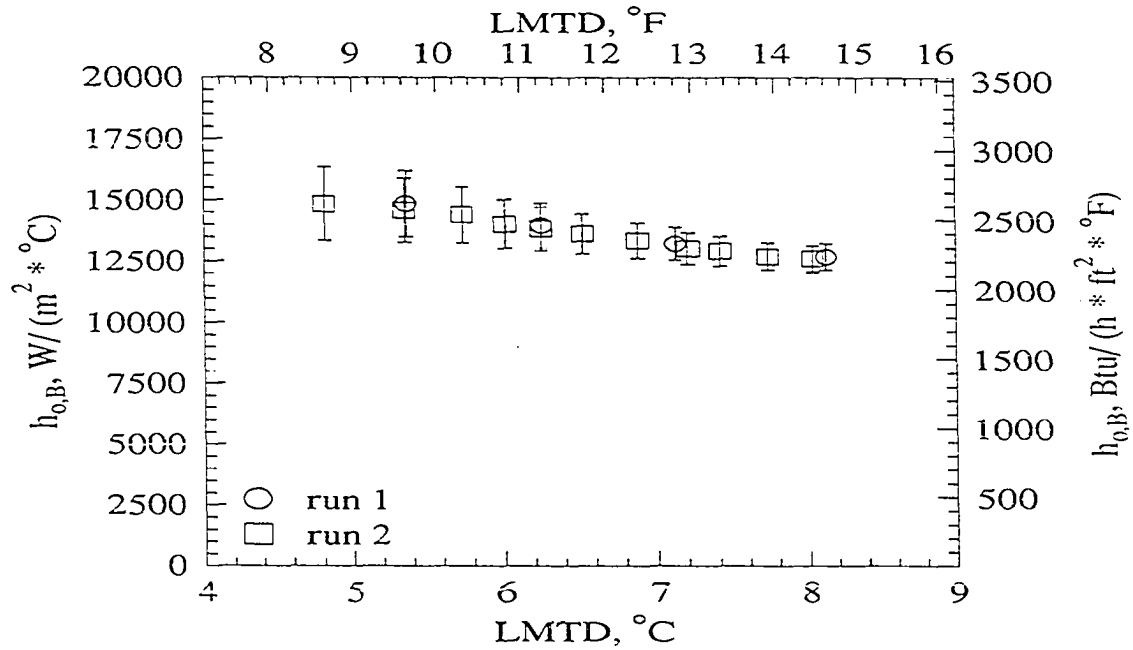


Figure 5.2: Average shell-side bundle heat transfer coefficient vs. LMTD for the condensation of HFC-134a on the 26-fpi geometry

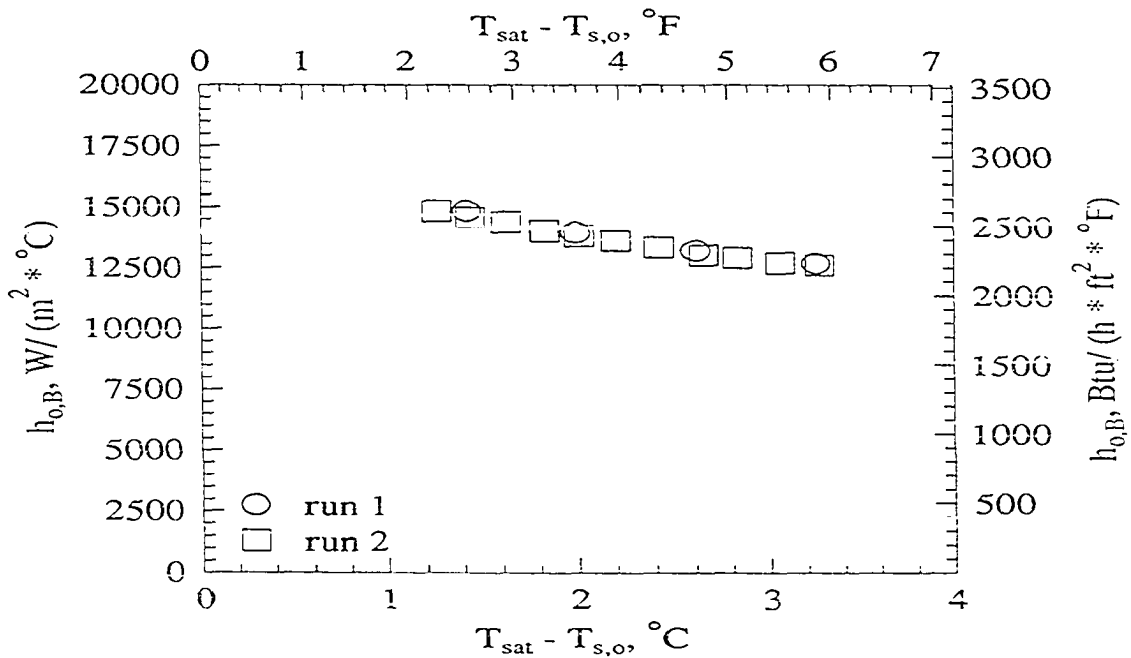


Figure 5.3: Average shell-side bundle heat transfer coefficient vs. condensation temperature difference for the condensation of HFC-134a on the 26-fpi geometry

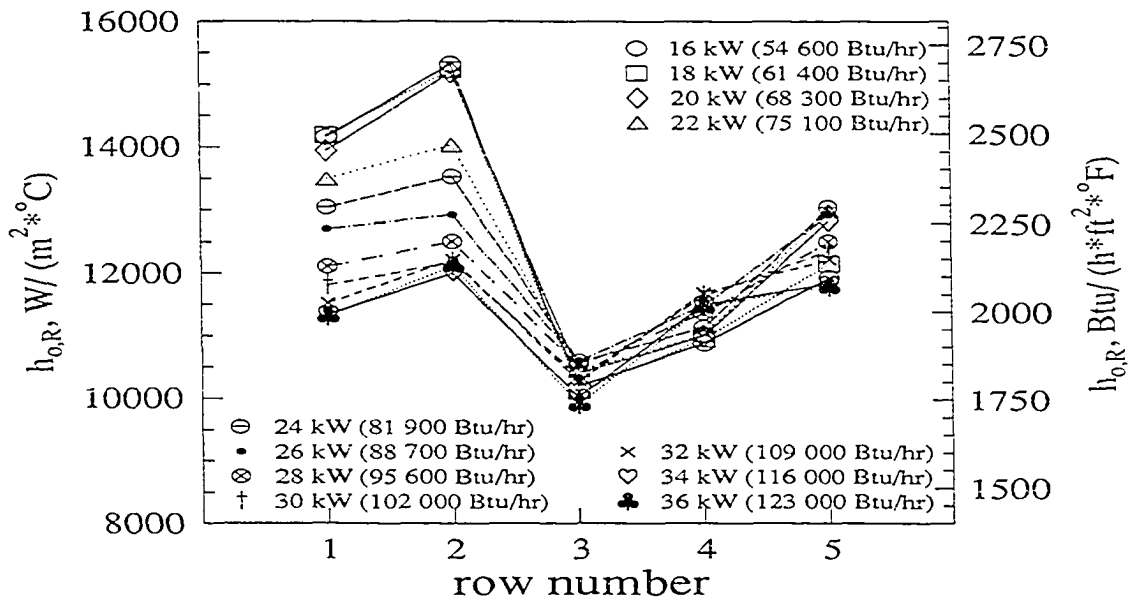


Figure 5.4: Average shell-side row heat transfer coefficient vs. row number for the condensation of HFC-134a on the 26-fpi geometry

bundle load range tested (16–36 kW, or 54 600–123 000 Btu/hr). As bundle load increases, the amount of condensate draining on rows 3, 4, and 5 increases. Thus, the data indicate that the 26-fpi is not affected by liquid inundation from higher rows.

The decrease of $h_{o,R}$ for rows 1 and 2 with increasing bundle load is consistent with the single-tube theory, which predicts that $h_{o,R}$ will drop as $T_{sat} - T_{s,o}$ increases. In the present data, $T_{sat} - T_{s,o}$ increases with heat flux. Since row 1 is not subject to condensate drainage and row 2 is subject to very little condensate drainage, these rows can be expected to behave as the single tube does, and $h_{o,R}$ for rows 1 and 2 drops with increasing heat flux. Since increasing heat flux is directly proportional to increasing bundle load, the data also imply that the drop in $h_{o,B}$ with increasing heat flux is due to the phenomena occurring in rows 1 and 2 only.

In general, Figure 5.4 shows that $h_{o,R}$ increases from row 1 to 2, decreases from row

2 to 3, then increases through row 5. The magnitude of the increase of $h_{o,R}$ from row 1 to 2 is not dependent on bundle load, and ranges from 3% at 26 kW (88 700 Btu/hr) to 9% at 20 kW (68 300 Btu/hr). The magnitude of the decrease in $h_{o,R}$ from row 2 to 3 is largest at low bundle loads, and ranges from 18% at a bundle load of 36 kW (123 000 Btu/hr) to 33% at a bundle load 16 kW (54 600 Btu/hr). The magnitude of the increase in $h_{o,R}$ from rows 3 to 5 is approximately 18% for all bundle loads.

The increase in $h_{o,R}$ from row 1 to 2 was also observed by Honda et al. (1992), who suggest that the increase may be due to a vapor velocity effect. The vapor velocity approaching row 1 is quite small because of the large surface area at the top of the bundle. However, the vapor velocity approaching row 2 will be significantly larger, because the vapor must flow through the narrow gaps between the tubes of row 1 in order to reach row 2. The reduction in flow area will result in an increase in the vapor velocity at the top of row 2. The vapor velocity tends to rip the condensate layer from the tube surface, thus increasing the heat transfer. Therefore, the 26-fpi bundle appears to be subject to vapor velocity effects.

Row 3 has the lowest values of $h_{o,R}$. Since the instrumented tube in row 3 is in the middle tube of the bundle, this tube is one of three tubes in the bundle which does not have any surface exposed to the vapor spaces in the test section. Thus, this tube may be starved of vapor. Also, row 3 is the first row to be fully inundated by condensate draining from a tube directly above it.

The value of $h_{o,R}$ increases over rows 4 and 5. Row 5 has its entire bottom surface exposed to refrigerant vapor. Thus, any vapor which passes around the sides of the bundle can condense on row 5. Some of this vapor can also condense on row 4, since a small portion of each tube in row 4 is also exposed to the vapor at the bottom of the condenser. Honda et al. (1991) predicts a jump in $h_{o,R}$ as the dripping mode changes from column mode to sheet mode. Since the instrumented tubes are internal to the bundle, it was not possible to see if a

transition from column to sheet mode was occurring.

As of this writing, no archival data were available for the condensation of HFC-134a on tube bundles. The data of Honda et al. (1992) for the condensation of CFC-113 on a 1024-fpm (26-fpi) staggered bundle do show the increase in $h_{o,R}$ from row 1 to 2. The data of Honda et al. (1991) also shows the same trend for the condensation of CFC-113 on an in-line smooth-tube bundle with a vapor velocity of 18.9 m/s (62 ft/s). The trend is also shown for a 1024-fpm (26-fpi) in-line bundle with a vapor velocity of 3.4 m/s (11.2 ft/s), although to a lesser extent than with the smooth bundle. The vapor velocity in the gap between the tubes of the first row is less than 1 m/s (3.28 ft/s).

Figure 5.5 shows the repeatability of $h_{o,R}$ for two different bundle loads. The repeatability of the experiment can be seen by comparing the data points for run 1 and run 2. This figure indicates that the data for $h_{o,R}$ can be repeated over the entire range of bundle loads tested, as the difference in the row coefficients for the two runs is less than 2%. Uncertainty bars are also presented for the 18 kW (61 400 Btu/hr) run to demonstrate the level of uncertainty in the row-by-row analysis. Figure 5.5 also demonstrates the large drop in $h_{o,R}$ with increasing bundle load for rows 1 and 2, and the independence of $h_{o,R}$ with bundle load for rows 3, 4, and 5.

Comparison to the P-W and W-M correlations

Values of $h_{o,R}$ as predicted by the P-W (Pearson and Withers (1969)) and the W-M (Webb and Murawski (1990)) correlations are plotted on Figure 5.1. The application of these two correlations to the present study was discussed in Chapter 4. The P-W correlation predicts a 21% drop in $h_{o,B}$ as the heat flux increases from 16 000 W/m² (5100 Btu/(hr-ft²)) to 41 000 W/m² (13 000 Btu/(hr-ft²)). The measured values of $h_{o,B}$ show a 15% drop over the same heat flux range, and are in excellent agreement with the P-W correlation. The W-M

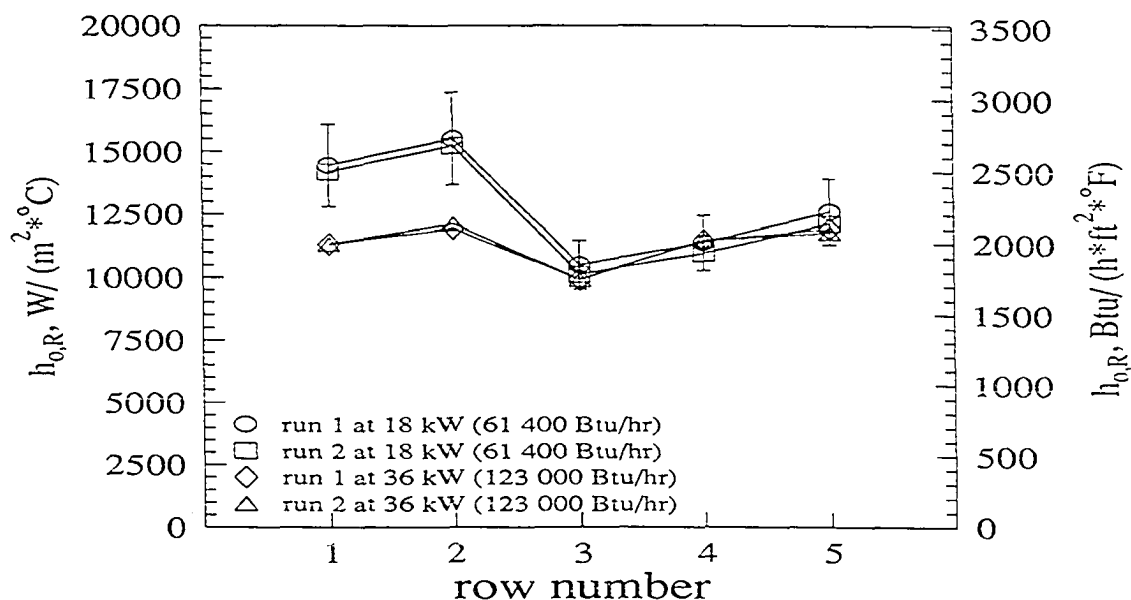


Figure 5.5: Average shell-side row heat transfer coefficient vs. row number for the condensation of HFC-134a on the 26-fpi geometry

correlation predicts that $h_{o,B}$ is not affected by the amount of condensate draining from the tube, and is thus independent of heat flux.

As previously mentioned, rows 3, 4, and 5 show no condensate inundation effects, which is in agreement with the W-M correlation. Webb and Murawski (1990) report that the fins of 26-fpi prevent the draining condensate from spreading axially and further covering the condensing surface. The decrease in $h_{o,R}$ for rows 1 and 2 with increasing bundle load is consistent with the P-W model. The P-W correlation is based on single-tube theory, which predicts that h_o will drop as $T_{sat} - T_{s,o}$ increases. As bundle load increases, $T_{sat} - T_{s,o}$ increases because of the thickening liquid layer on the tube, and hence $h_{o,R}$ drops with increasing bundle load.

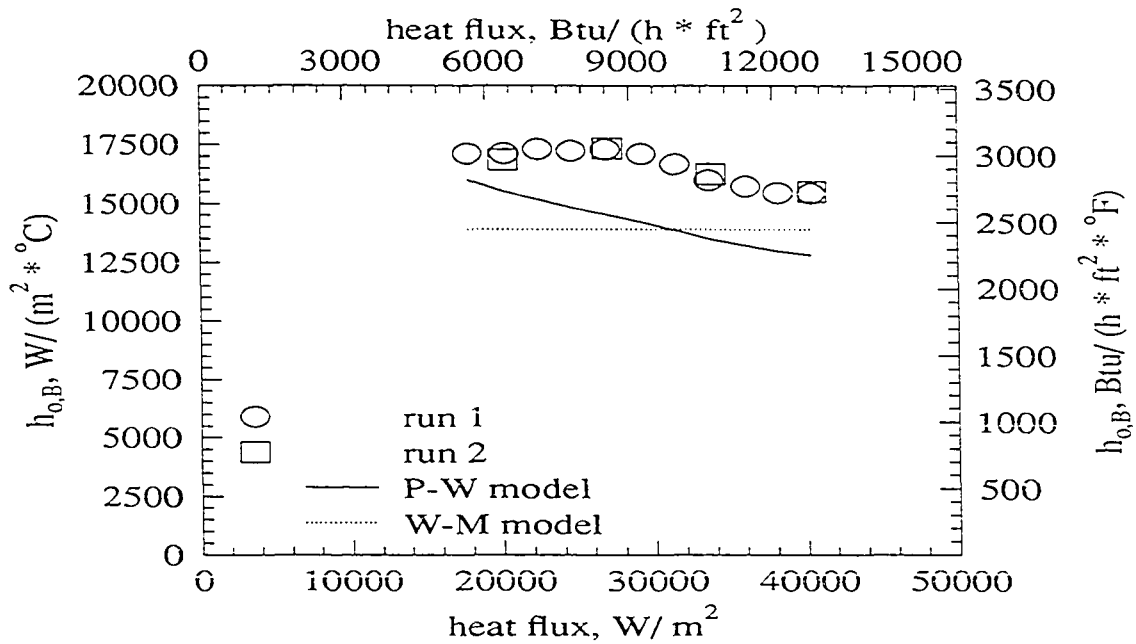


Figure 5.6: Average shell-side bundle heat transfer coefficient vs. heat flux for the condensation of HFC-134a on the 40-fpi geometry

Results for the 40-fpi Geometry

Average bundle heat transfer coefficient results

Figure 5.6 shows that the average shell-side bundle heat transfer coefficient ($h_{o,B}$) for the 40-fpi geometry is fairly constant at approximately 17 200 $W/(m^2 \cdot K)$ (3030 $Btu/(hr \cdot ft^2 \cdot F)$) as heat flux increases through 30 000 W/m^2 (8900 $Btu/(hr \cdot ft^2)$), then decreases by 10% to 15 500 $W/(m^2 \cdot K)$ (2700 $Btu/(hr \cdot ft^2 \cdot F)$) as the heat flux increases to 41 000 W/m^2 (13 000 $Btu/(hr \cdot ft^2)$). An increasing bundle heat flux corresponds to an increasing refrigerant mass flow rate. As the mass flow rate (and hence, heat flux) increases, the liquid layer on the tubes becomes larger, and the heat transfer resistance increases. The data suggest that up through a heat flux of 30 000 W/m^2 (8900 $Btu/(hr \cdot ft^2)$), the 40-fpi is able to sufficiently drain the condensate so that no effect of liquid layer thickness is seen.

The data for the repeatability run are also plotted on Figure 5.6. The repeatability of the experiment can be seen by comparing the data points for run 1 and run 2. This figure indicates that the data for $h_{o,B}$ can be repeated over the entire range of bundle loads tested, as the difference between the two runs is less than 2%.

Figure 5.7 shows the variation of $h_{o,B}$ with the LMTD. Figure 5.8 shows the variation of $h_{o,B}$ with the condensation temperature difference, $T_{sat} - T_{s,o}$. The wall temperature is calculated, not directly measured. Since the same trends in $h_{o,B}$ are present in both figures, the trend in $h_{o,B}$ is due to a shell-side phenomenon.

Uncertainty bars are also plotted on Figure 5.7, and show that the experimental uncertainty in $h_{o,B}$ ranges from $\pm 6\%$ to $\pm 13\%$. This figure indicates that $w_{h_{o,B}}$ decreases as the heat flux increases. As the heat flux increases, $T_{sat} - T_{w,out}$ and $T_{sat} - T_{w,in}$ increase, but the uncertainty in these temperature differences remains the same. Therefore, the uncertainty in these temperature differences becomes less significant as the temperature differences increase. The calculation of $h_{o,B}$ is quite sensitive to these temperature differences, thus $w_{h_{o,B}}$ decreases as the uncertainty in these temperature differences becomes less significant. The data for the repeatability run are also plotted on Figures 5.7 and 5.8.

Average row heat transfer coefficient results

Figure 5.9 shows the row behavior of the 40-fpi for different bundle loads. This figure indicates that $h_{o,R}$ for rows 2 through 5 generally decreases with increasing bundle load, with the decrease in $h_{o,R}$ being more significant for rows 4 and 5. For example, $h_{o,R}$ for row 3 decreases from 17 340 W/(m²·K) (3050 Btu/(hr·ft²·F)) at a bundle load of 16 kW (54 600 Btu/hr) to 16 180 W/(m²·K) (2850 Btu/(hr·ft²·F)) at a bundle load of 36 kW (123 000 Btu/hr), which is a 7% drop, while over the same bundle load interval, $h_{o,R}$ for row 5 decreases from 14 840 W/(m²·K) (2600 Btu/(hr·ft²·F)) to 11 130 W/(m²·K) (1960 Btu/(hr·ft²·F)), which is

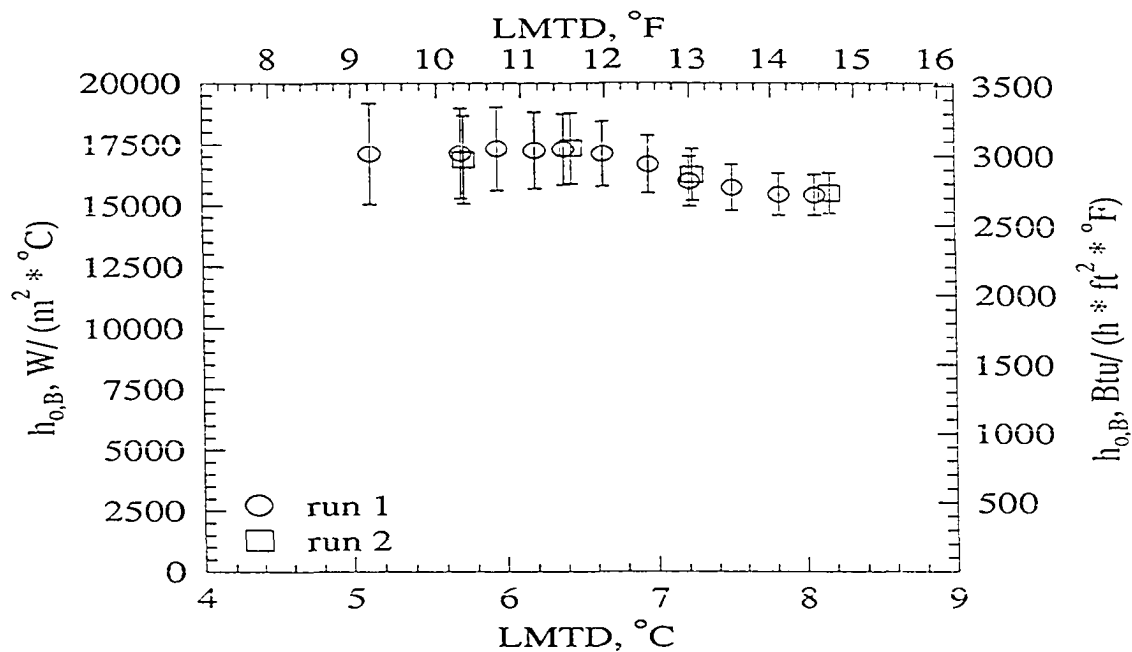


Figure 5.7: Average shell-side bundle heat transfer coefficient vs. LMTD for the condensation of HFC-134a on the 40-fpi geometry

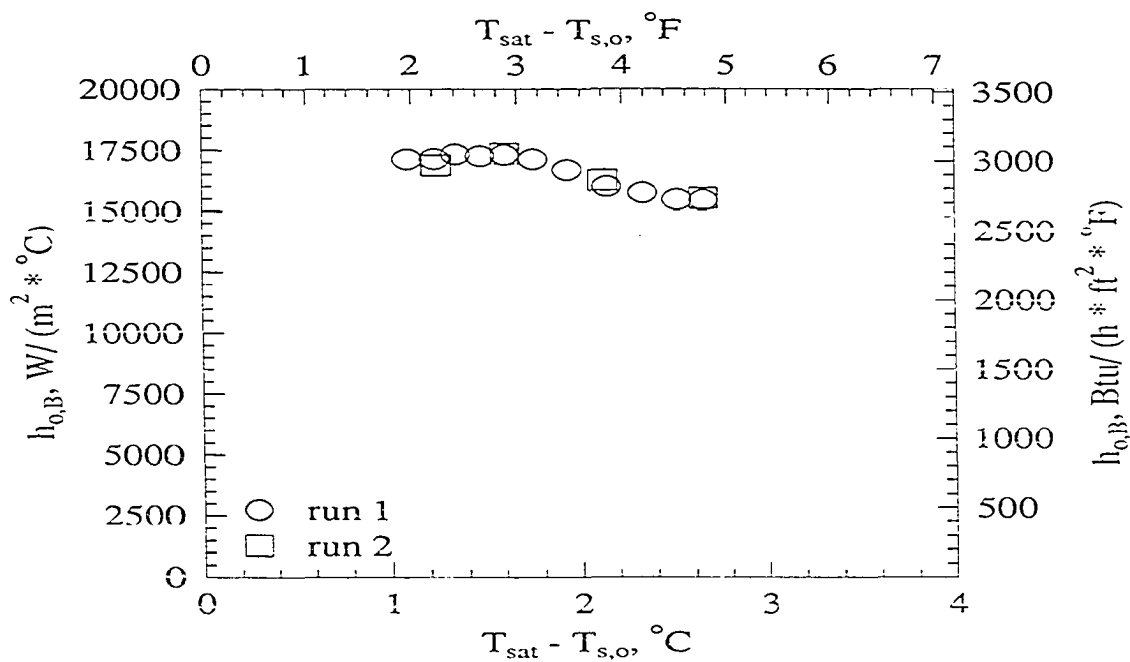


Figure 5.8: Average shell-side bundle heat transfer coefficient vs. condensation temperature difference for the condensation of HFC-134a on the 40-fpi geometry

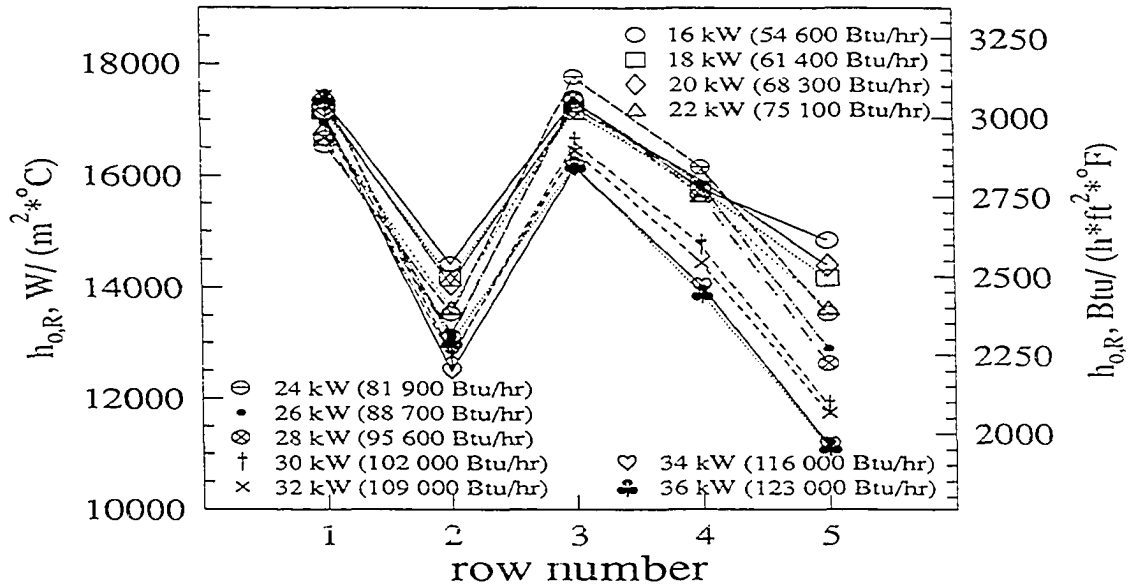


Figure 5.9: Average shell-side row heat transfer coefficient vs. row number for the condensation of HFC-134a on the 40-fpi geometry

a 25% drop.

The decrease in $h_{o,R}$ may be partly due to the increase in liquid layer on the tube as bundle load increases. Also, the 40-fpi may be susceptible to condensate inundation effects. The decrease in $h_{o,R}$ is more noticeable in rows 4 and 5, which are the rows that would be most inundated with drainage from the higher rows. The 40-fpi has shorter fins than the 26-fpi, and may not prevent axial spreading of the condensate as well as the 26-fpi.

The variation of $h_{o,R}$ for row 1 appears to be independent of bundle load. The minimum value of $h_{o,R}$ for row 1 is $16\,530\text{ W}/(\text{m}^2\cdot\text{K})$ ($2910\text{ Btu}/(\text{hr}\cdot\text{ft}^2\cdot\text{F})$) and occurs at a bundle load of 24 kW ($81\,900\text{ Btu/hr}$), while the maximum value of $17\,430\text{ W}/(\text{m}^2\cdot\text{K})$ ($3070\text{ Btu}/(\text{hr}\cdot\text{ft}^2\cdot\text{F})$) occurs at 32 kW ($109\,000\text{ Btu/hr}$).

In general, Figure 5.9 shows that $h_{o,R}$ decreases from row 1 to 2, increases from row 2 to 3, then decreases through row 5. The magnitude of the decrease in $h_{o,R}$ from row 1 to 2 is

dependent on bundle load and ranges from 17% at a bundle load of 16 kW (54 600 Btu/hr) to approximately 25% for the 4 highest bundle loads tested. The magnitude of the increase in $h_{o,R}$ from row 2 to 3 appears to be independent of bundle load, and ranges from 20% at a bundle load of 16 kW (54 600 Btu/hr) to 33% at a bundle load of 28 kW (95 600 Btu/hr). The magnitude of the decrease in $h_{o,R}$ from row 3 to 5 is dependent on bundle load and ranges from 16% at a bundle load of 16 kW (54 600 Btu/hr) to 36% at bundle load of 36 kW (123 000 Btu/hr).

The row-to-row behavior of this bundle is quite peculiar. The decreases in $h_{o,R}$ from row 1 to 2 and from row 3 to 5 can be explained by a thickening liquid layer, but the reason for the increase in $h_{o,R}$ from row 2 to 3 is unknown. Michael et al. (1992) noticed a “saw-tooth” row effect (ie. alternating increasing and decreasing condensing coefficients) during steam condensation in staggered bundles. The variation was attributed to the odd numbered rows having 4 active tubes, while the even numbered rows had three active tubes. The rows with three active tubes performed better. Although the bundles in these tests all have the same number of active tubes in each row, the row staggering may have an effect similar to that experienced by Michael et al. The data of Honda et al. (1992) for staggered bundles and the data of Honda et al. (1991) for in-line bundles show a similar saw-tooth row variation. No explanation is given, other than that the variation may be due to experimental uncertainty. CFC-113 was used in both Honda et al. (1992) and Honda et al. (1991).

Figure 5.10 shows the repeatability of $h_{o,R}$ for two different bundle loads. The repeatability of the experiment can be seen by comparing the data points for run 1 and run 2. This figure indicates that the data for $h_{o,R}$ can be repeated over the entire range of bundle loads tested, as the difference between the two runs is less than 2%. Uncertainty bars are also presented for one of the 18 kW (61 400 Btu/hr) runs to demonstrate the level of uncertainty in the row-by-row analysis. This figure also demonstrates the drop in $h_{o,R}$ with bundle load for

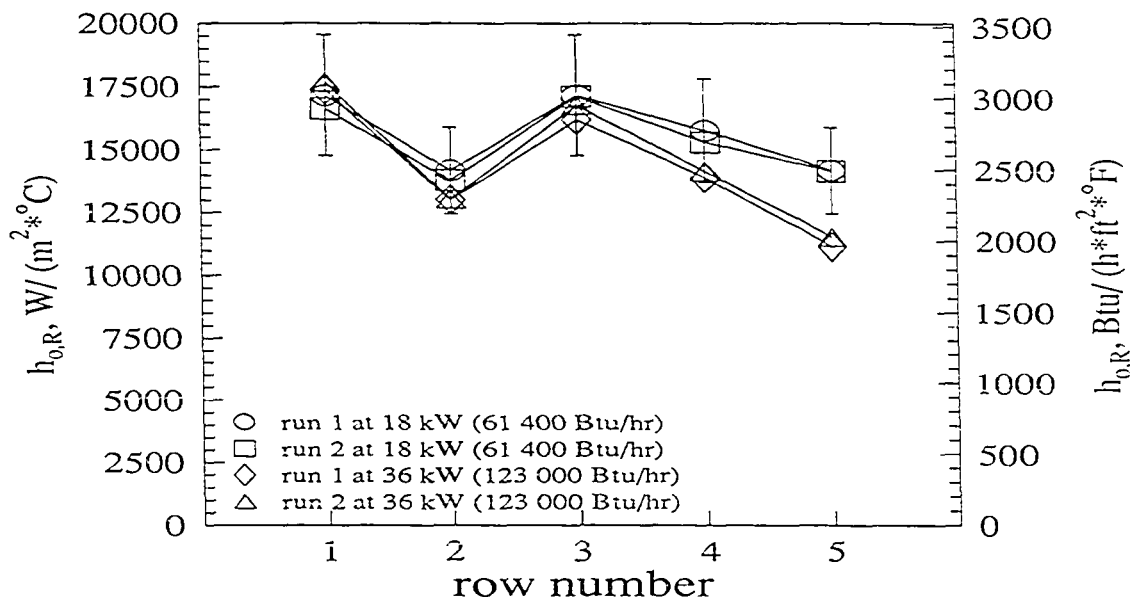


Figure 5.10: Average shell-side row heat transfer coefficient vs. row number for the condensation of HFC-134a on the 40-fpi geometry

rows 4 and 5. Since the uncertainty bands for the first three rows overlap for the the bundle load range tested, the variation in the first three rows with bundle load may also be due to experimental uncertainty.

Comparison to P-W and W-M correlations

Values of $h_{o,R}$ as predicted by the P-W and W-M correlations are plotted on Figure 5.6. The P-W correlation predicts a 20% drop in $h_{o,B}$ as the heat flux increases from $16\,000\,W/m^2$ ($5100\,Btu/(hr \cdot ft^2)$) to $41\,000\,W/m^2$ ($13\,000\,Btu/(hr \cdot ft^2)$). The measured values of $h_{o,B}$, which drop 10% over the same heat flux range, initially follow the W-M correlation for low heat fluxes, and the P-W correlation for high heat fluxes. As previously discussed, both correlations are extrapolated for the 40-fpi geometry. The W-M correlation predicts that $h_{o,B}$ is not affected by the amount of condensate draining from the tube, and is thus independent

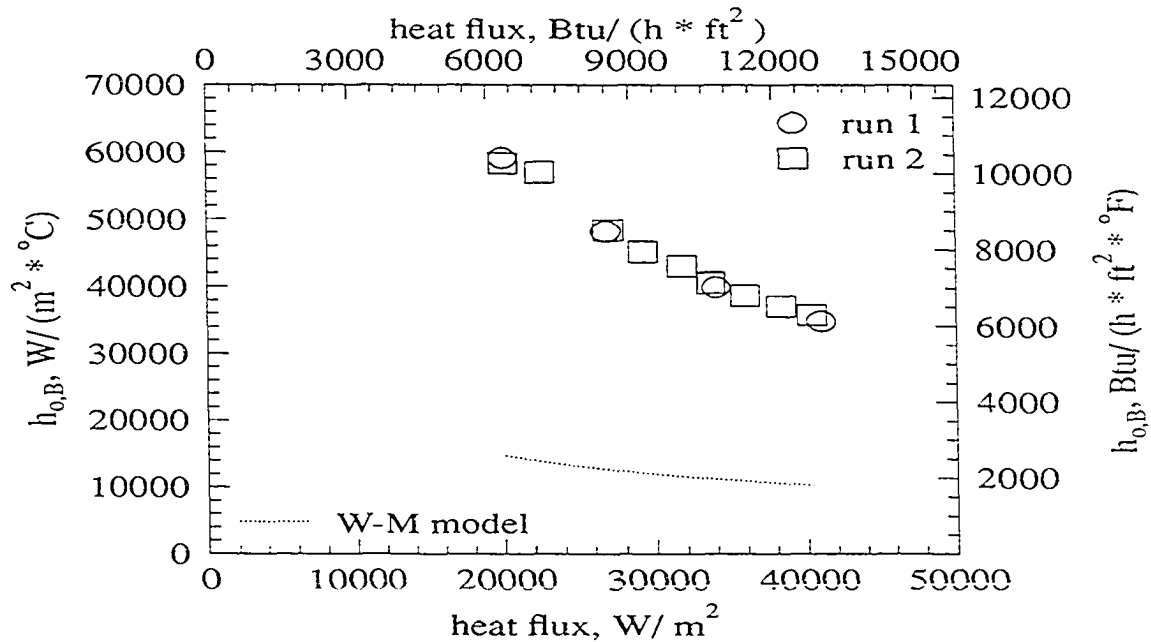


Figure 5.11: Average shell-side bundle heat transfer coefficient vs. heat flux for the condensation of HFC-134a on the Tu-Cii geometry

of heat flux.

Results for the Tu-Cii Geometry

Average bundle heat transfer coefficient results

Figure 5.11 shows that the average shell-side bundle heat transfer coefficient $h_{o,B}$ for the Tu-Cii geometry drops significantly with increasing heat flux. An increasing bundle heat flux corresponds to an increasing refrigerant mass flow rate. As the mass flow rate (and hence, heat flux) increases, the liquid layer on the tubes becomes larger, and the heat transfer resistance increases. The measured values of $h_{o,B}$ drop from 58 340 W/(m²·K) (10 270 Btu/(hr·ft²·F)) at 20 000 W/m² (6350 Btu/(hr·ft²)) to 35 760 W/(m²·K) (6300 Btu/(hr·ft²·F)) at 41 000 W/m² (13 000 Btu/(hr·ft²)), which is a 39% decrease.

Visual observation of the Tu-Cii indicated that the condensate did not always drain vertically downward, but often ran axially along the tube. Thus, the positions of the draining condensate columns was not fixed. This axial movement of the condensate floods the tube area that would normally be available for condensation. This phenomenon was unique to the Tu-Cii. Even though the Tu-Cii performance drops significantly with heat flux, the Tu-Cii still has a higher $h_{o,B}$ over the entire heat flux range than the other geometries tested.

Figure 5.12 shows the variation of $h_{o,B}$ with the LMTD. Figure 5.13 shows the variation of $h_{o,B}$ with the condensation temperature difference, $T_{sat} - T_{s,o}$. The wall temperature is calculated, not directly measured. Since the same trends in $h_{o,B}$ are present in both figures, the trend in $h_{o,B}$ is due to a shell-side phenomenon.

Uncertainty bars are also plotted on Figure 5.12, and show that the experimental uncertainty in $h_{o,B}$ ranges from $\pm 11\%$ to $\pm 36\%$. This figure indicates that $w_{h_{o,B}}$ decreases as the LMTD increases. As the LMTD increases, $T_{sat} - T_{w,out}$ and $T_{sat} - T_{w,in}$ increase, but the uncertainty in these temperature differences remains the same. Thus, the uncertainty in the temperature differences becomes less significant as the temperature differences increase. The calculation of $h_{o,B}$ is quite sensitive to these temperature differences (and hence, the LMTD), thus $w_{h_{o,B}}$ decreases as the uncertainty in these temperature differences becomes less significant.

The uncertainty is also sensitive to the imbalance between the water-side and shell-side resistances. At low heat fluxes, the water flow rate through the tube bundle is quite low, causing a large water-side heat transfer resistance. Also at low heat fluxes, the Tu-Cii performs very well because of the small amount of condensate draining from the tubes, and the shell-side heat transfer resistance is relatively small.

Equation 4.14 is extremely sensitive to the imbalance between the water-side and shell-side resistances, and when the imbalance is large, the experimental uncertainty increases.

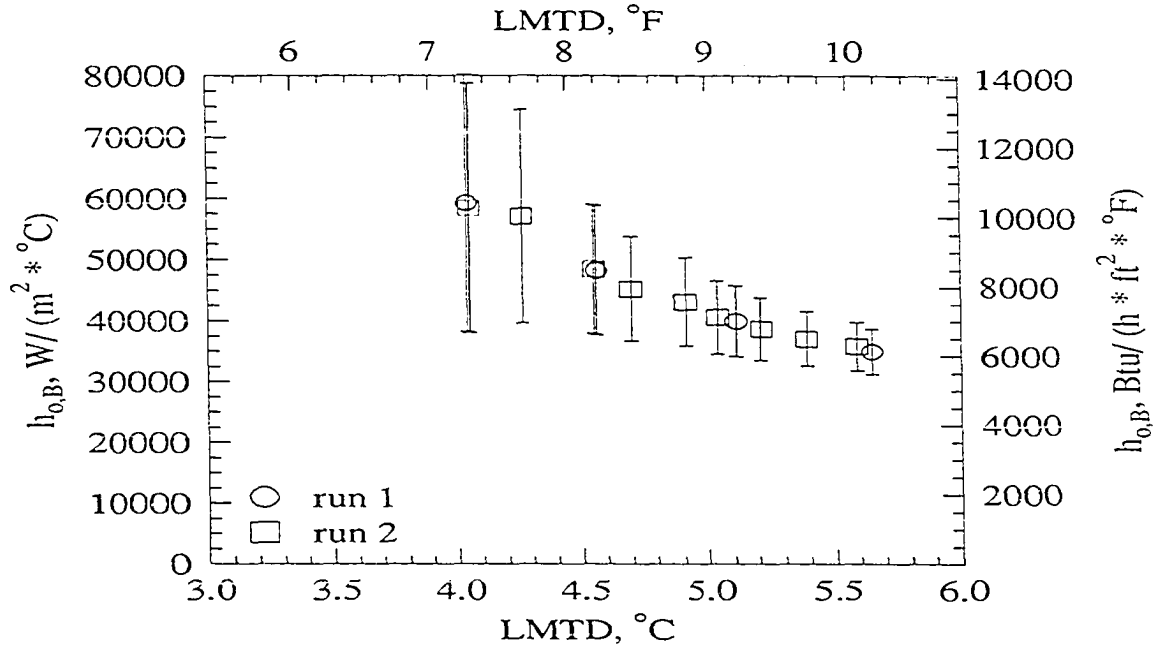


Figure 5.12: Average shell-side bundle heat transfer coefficient vs. LMTD for the condensation of HFC-134a on the Tu-Cii geometry

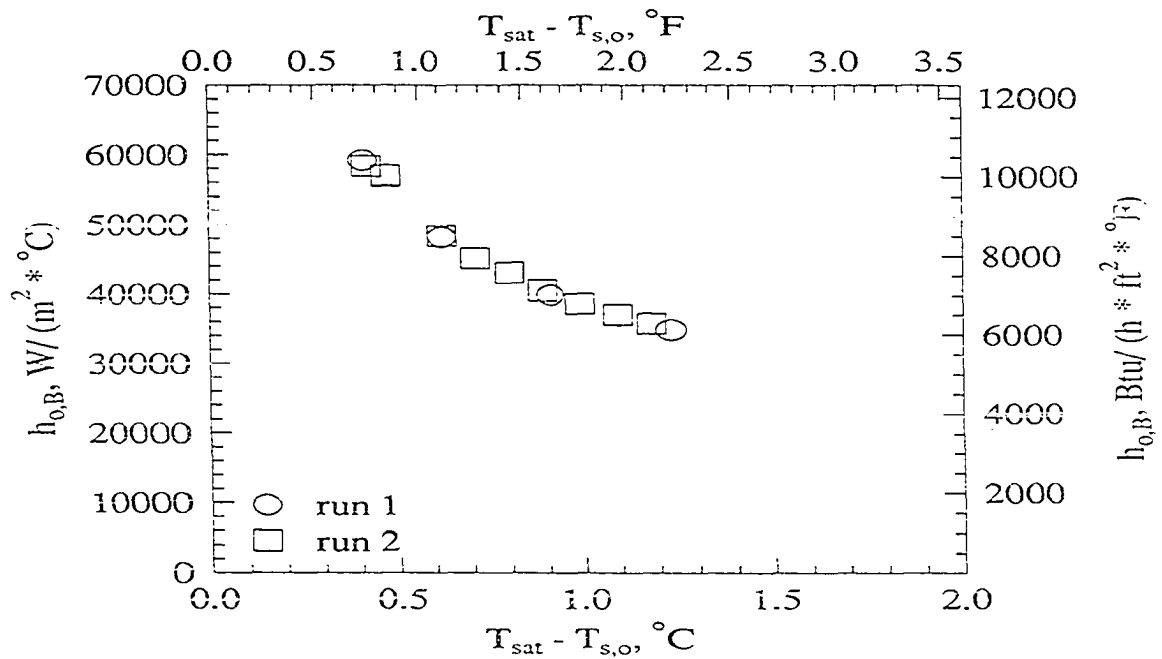


Figure 5.13: Average shell-side bundle heat transfer coefficient vs. condensation temperature difference for the condensation of HFC-134a on the Tu-Cii geometry

During condensation on the Tu-Cii at heat flux of $20\,000\text{ W/m}^2$ ($6340\text{ Btu}/(\text{hr}\cdot\text{ft}^2)$), the water-side resistance is approximately nine times larger than the calculated shell-side resistance. Since the Tu-Cii has both a large resistance imbalance and a small LMTD at low heat fluxes, the uncertainty is quite high. Since the LMTD increases as heat flux increases and the water-side resistance decreases as heat flux increases, the uncertainty drops off rapidly with increasing heat flux.

The data for the repeatability run are plotted on Figures 5.11– 5.13. The repeatability of the experiment can be seen by comparing the data points for run 1 and run 2. These figures indicate that the data for $h_{o,B}$ can be repeated over the entire range of bundle loads tested, as the difference between the two runs is less than 2%.

Average row heat transfer coefficient results

Figure 5.14 shows the row behavior of the Tu-Cii for different bundle loads. This figure indicates that $h_{o,R}$ for all rows decreases with increasing bundle load, with the decrease being more pronounced for rows 1 and 2. The decrease in $h_{o,R}$ with bundle load ranges from 24% for row 5 to 49% for row 1. As heat flux increases, the amount of condensate draining from the tubes increases. The decrease in $h_{o,R}$ with increasing bundle load (and hence heat flux) demonstrates that Tu-Cii is quite sensitive to the amount of condensate draining from the tube. Since rows 3, 4 and 5 are always inundated with condensate draining from higher rows, the effect on $h_{o,R}$ of additional condensation due to increasing heat flux is not as dramatic on these rows as it is on rows 1 and 2.

Figure 5.14 also shows the row-to-row behavior of the Tu-Cii geometry. The behavior of $h_{o,R}$ between row 1 and 2 is rather peculiar. At a bundle load of 18 kW ($61\,400\text{ Btu/hr}$), $h_{o,R}$ decreases by 9% from row 1 to 2. For bundle loads of 20 , 24 , and 26 kW ($68\,300$, $81\,900$, and $88\,700\text{ Btu/hr}$), $h_{o,R}$ does not change from row 1 to 2. For a bundle load of

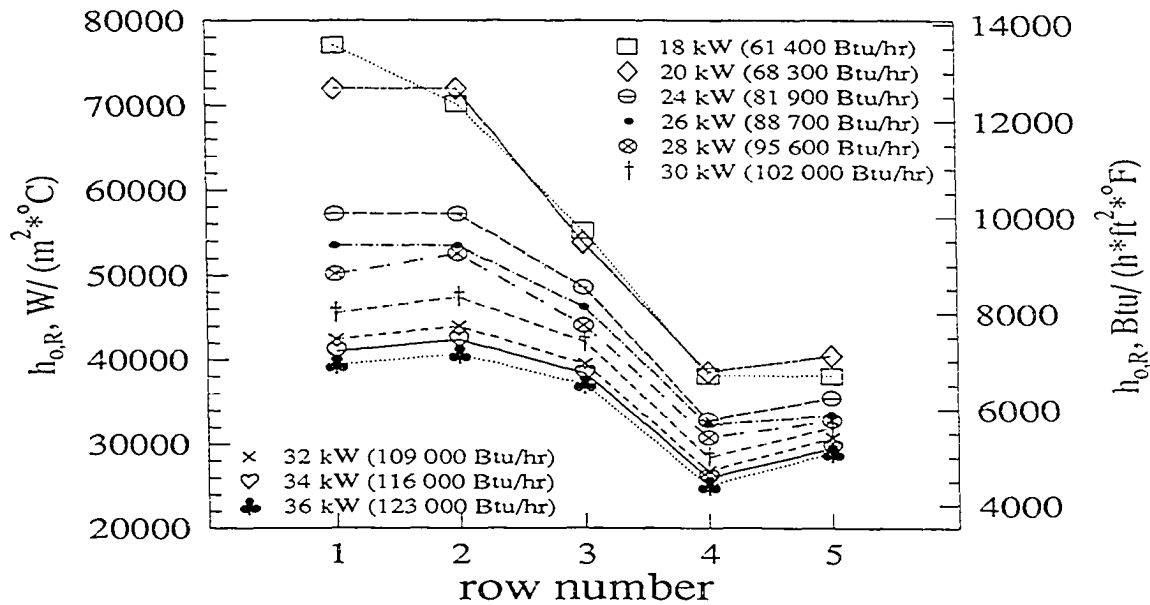


Figure 5.14: Average shell-side row heat transfer coefficient vs. row number for the condensation of HFC-134a on the Tu-Cii geometry

28 kW (95 600 Btu/hr), $h_{o,R}$ increases by 5% from row 1 to 2. At 36 kW (123 000 Btu/hr), $h_{o,R}$ increases by 3% from row 1 to 2. This behavior may be due to the vapor velocity effect discussed earlier. The vapor velocity at the top of row 2 is larger than the vapor velocity for row 1 because of the flow area constriction above row 2. As the bundle load increases, the vapor velocity at the top of row 2 increases and may become large enough to cause the increase in $h_{o,R}$ from row 1 to 2. The decrease in $h_{o,R}$ from row 2 to 4 is due to the effects of drainage from higher rows. The decrease in $h_{o,R}$ from row 2 to 4 ranges from 38% at 36 kW (123 000 Btu/hr) to 46% at 18 kW (61 400 Btu/hr).

The increase in $h_{o,R}$ from row 4 to 5 may be due to the fact that the entire bottom surface of row 5 is exposed to the vapor space at the bottom of the test section. The increase in $h_{o,R}$ from row 4 to 5 ranges from a negligible change at 18 kW (61 400 Btu/hr) to 16% at 36 kW (123 000 Btu/hr). As bundle load increases, more vapor may pass through the first four

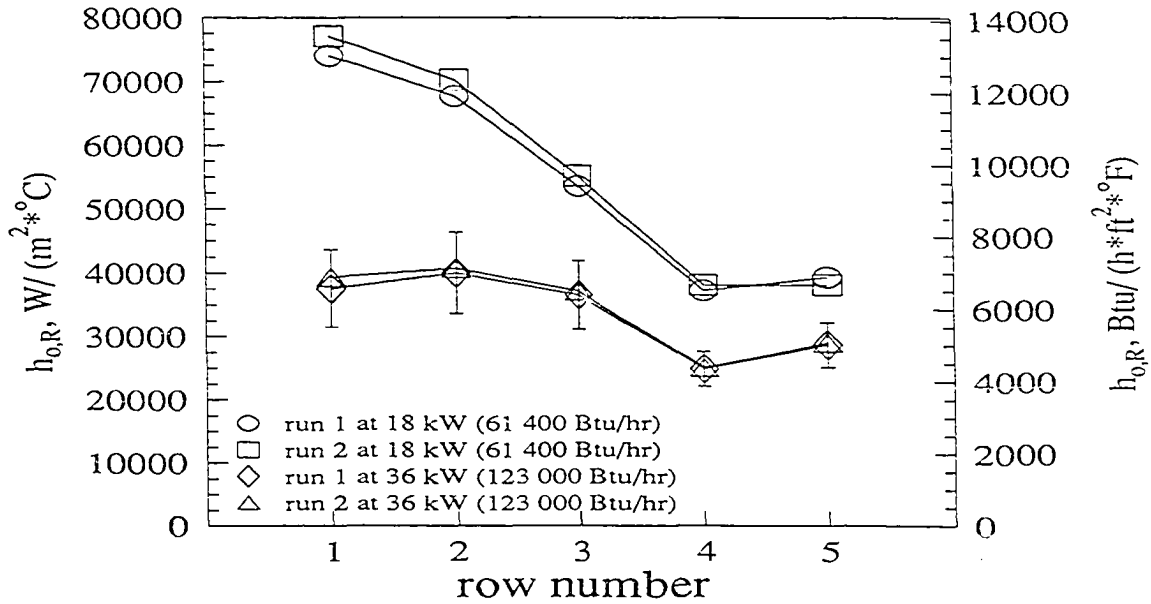


Figure 5.15: Average shell-side row heat transfer coefficient vs. row number for the condensation of HFC-134a on the Tu-Cii geometry

rows of the bundle without condensing. The uncondensed vapor condenses on row 5, which explains why the magnitude of the increase in $h_{o,R}$ from row 4 to 5 increases with increasing bundle load. The row-to-row trend of the Tu-Cii is very similar to the 26-fpi, except that the minimum $h_{o,R}$ occurs in row 3 for the 26-fpi and in row 4 for the Tu-Cii.

Figure 5.15 shows the repeatability of $h_{o,R}$ for two different bundle loads. The repeatability of the experiment can be seen by comparing the data points for run 1 and run 2. This figure indicates that the data for $h_{o,R}$ can be repeated over the entire range of bundle loads tested, as the difference between the two runs is less than 4%. Uncertainty bars are also presented for the 36 kW (123 000 Btu/hr) run to demonstrate the level of uncertainty in the row-by-row analysis. This figure also demonstrates the significant drop in $h_{o,R}$ with bundle load for rows 1 and 2.

The 16 kW (54 600 Btu/hr) point for the Tu-Cii is not presented because of its high

experimental uncertainty. The 22 kW (75 100 Btu/hr) point for the Tu-Cii is not presented because a transducer malfunction occurred while the point was being taken.

Comparison to P-W and W-M correlations

Values of $h_{o,R}$ as predicted by the W-M correlation are plotted on Figure 5.11. The W-M correlation predicts that $h_{o,B}$ decreases by 30% as heat flux increases from 16 000 W/m² (5100 Btu/(hr·ft²)) to 41 000 W/m² (13 000 Btu/(hr·ft²)). The measured values of $h_{o,B}$ drop 39% over the same heat flux range. Webb and Murawski (1991) state that the Tu-Cii geometry allows the condensate to spread axially along the tube, instead of draining the condensate. Webb and Murawski also report that the Tu-Cii was more affected by the amount of condensate draining from the tube than the 26-fpi and G-SC. The observations of Webb and Murawski (1991) are in good agreement with the present study.

The magnitude of $h_{o,B}$ predicted by the W-M correlation for the Tu-Cii is three to four times lower than the measured values. The W-M correlation was developed using only one refrigerant, CFC-11, which has the poorest heat transfer performance of the four refrigerants tested in this study. Also, it appears that the Tu-Cii is particularly well suited to HFC-134a condensation. Therefore, it is not surprising that the W-M correlations does not properly predict the magnitude of $h_{o,B}$ for this tube. As mentioned previously, no D_{eq} was available for the Tu-Cii, so the P-W correlation is not plotted.

Results for G-SC Geometry

Average bundle heat transfer coefficient results

Figure 5.16 shows that the average shell-side bundle heat transfer coefficient $h_{o,B}$ for the G-SC geometry remains constant at 16 200 W/(m²·K) (2850 Btu/(hr·ft²·F)) up to a heat flux of 27 000 W/m² (8570 Btu/(hr·ft²)) and then decreases with increasing heat flux to

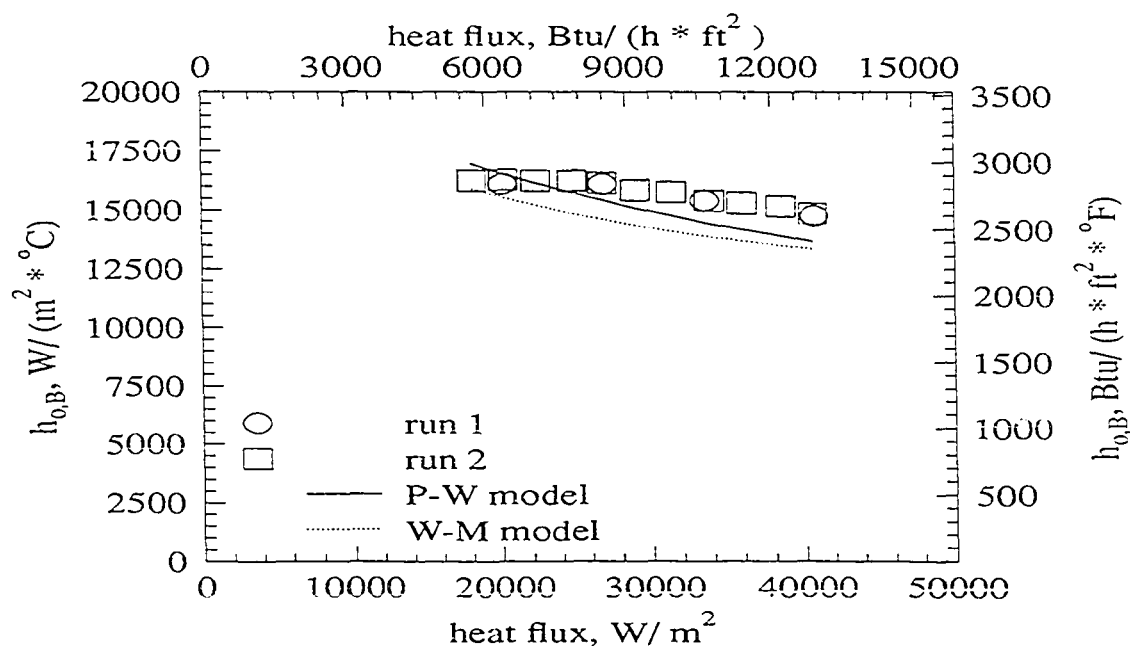


Figure 5.16: Average shell-side bundle heat transfer coefficient vs. heat flux for the condensation of HFC-134a on the G-SC geometry

14 830 $W/(m^2 \cdot K)$ (2610 $Btu/(hr \cdot ft^2 \cdot F)$) at a heat flux of 41 000 W/m^2 (13 000 $Btu/(hr \cdot ft^2)$). An increasing bundle heat flux corresponds to an increasing refrigerant mass flow rate. As the mass flow (and hence, heat flux) increases, the liquid layer on the tubes becomes larger. The data indicate that the G-SC is not affected by the amount of condensate draining from the tube at low heat fluxes, and only mildly affected at high heat fluxes, as $h_{o,B}$ drops only 9% over the higher heat fluxes.

The G-SC only performs better than the 26-fpi tube. Visual observation of the condensation phenomenon indicated that there was significant liquid holdup in the Y-shaped fins of the G-SC. The flooding angle ϕ_f was observed to be nearly 90° at high bundle loads. The condensate, instead of draining, floods the condensation area, thus reducing the performance of the tube.

The data for the repeatability run is also plotted on Figure 5.16. The repeatability of

the experiment can be seen by comparing the data points for run 1 and run 2. These figures indicate that the data for $h_{o,B}$ can be repeated over the entire range of bundle loads tested, as the difference between the two runs is less than 1%.

Figure 5.17 shows the variation of $h_{o,B}$ with LMTD, while Figure 5.18 shows the variation of $h_{o,B}$ with the condensation temperature difference, $T_{sat} - T_{s,o}$. As previously discussed, the wall temperature is calculated, not directly measured. As the LMTD and $T_{sat} - T_{s,o}$ increase, more refrigerant is condensed. Thus, an increasing LMTD and $T_{sat} - T_{s,o}$ correspond to an increasing heat flux. Since the same trend in $h_{o,B}$ is present in both figures, the trend in $h_{o,B}$ is due to a shell-side phenomenon.

Uncertainty bars are also plotted on Figure 5.17. This figure indicates that $w_{h_{o,B}}$ decreases as the LMTD, and hence heat flux, increases. As the LMTD increases, $T_{sat} - T_{w,out}$ and $T_{sat} - T_{w,in}$ increase, but the uncertainty in these temperature differences remains the same. Therefore, the uncertainty in these temperature differences becomes less significant as the temperature differences increase. The calculation of $h_{o,B}$ is quite sensitive to these temperature differences, thus $w_{h_{o,B}}$ decreases as the uncertainty in these temperature differences becomes less significant. Since the smallest LMTD corresponds to the lowest heat flux tested, the experimental uncertainty in $h_{o,B}$ ranges from $\pm 5\%$ at a heat flux of $16\,000\text{ W/m}^2$ ($5100\text{ Btu}/(\text{hr}\cdot\text{ft}^2)$) to $\pm 12\%$ at $41\,000\text{ W/m}^2$ ($13\,000\text{ Btu}/(\text{hr}\cdot\text{ft}^2)$). The data for the repeatability run are also plotted on Figures 5.17 and 5.18.

Average row heat transfer coefficients results

Figure 5.19 shows the row behavior of the G-SC for different bundle loads. This figure indicates that $h_{o,R}$ for all rows generally decreases with increasing bundle load. The condensate draining from the tubes increases with bundle load, thus increasing the shell-side resistance, and decreasing $h_{o,R}$. The largest drop in $h_{o,R}$ occurs in rows 1 and 4, where

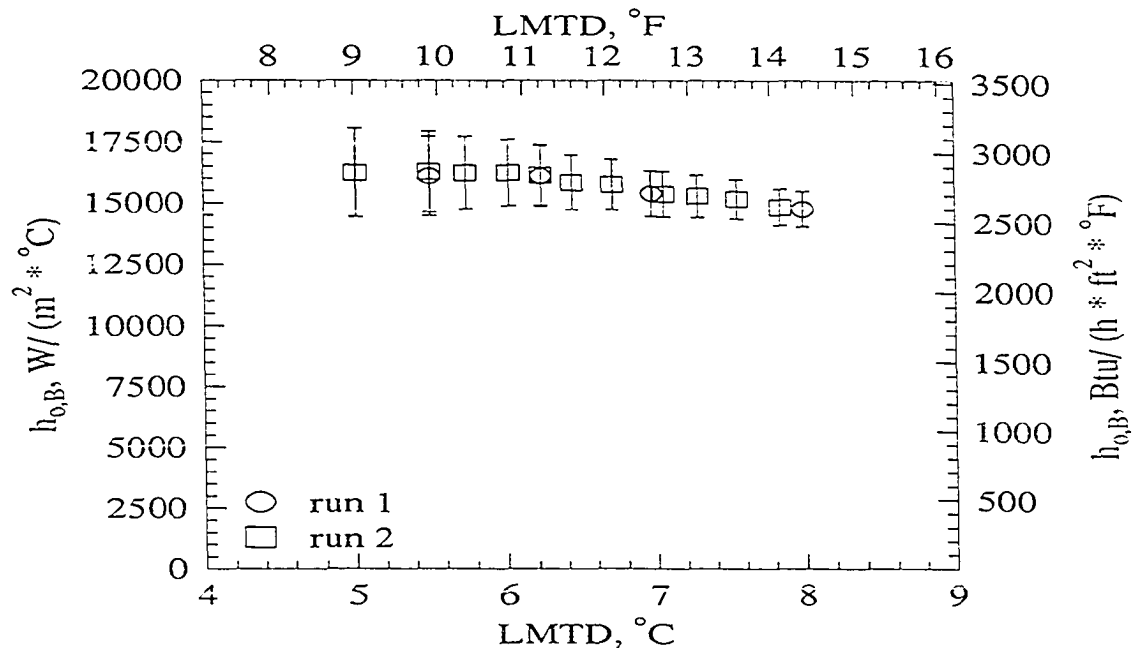


Figure 5.17: Average shell-side bundle heat transfer coefficient vs. LMTD for the condensation of HFC-134a on the G-SC geometry

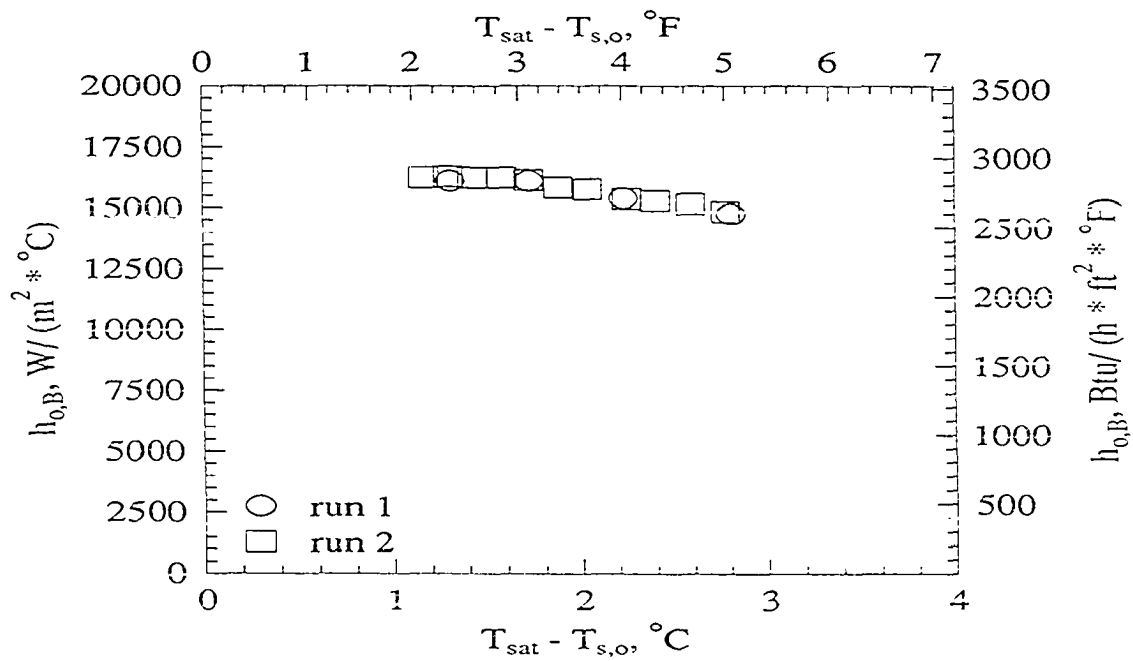


Figure 5.18: Average shell-side bundle heat transfer coefficient vs. condensation temperature difference for the condensation of HFC-134a on the G-SC geometry

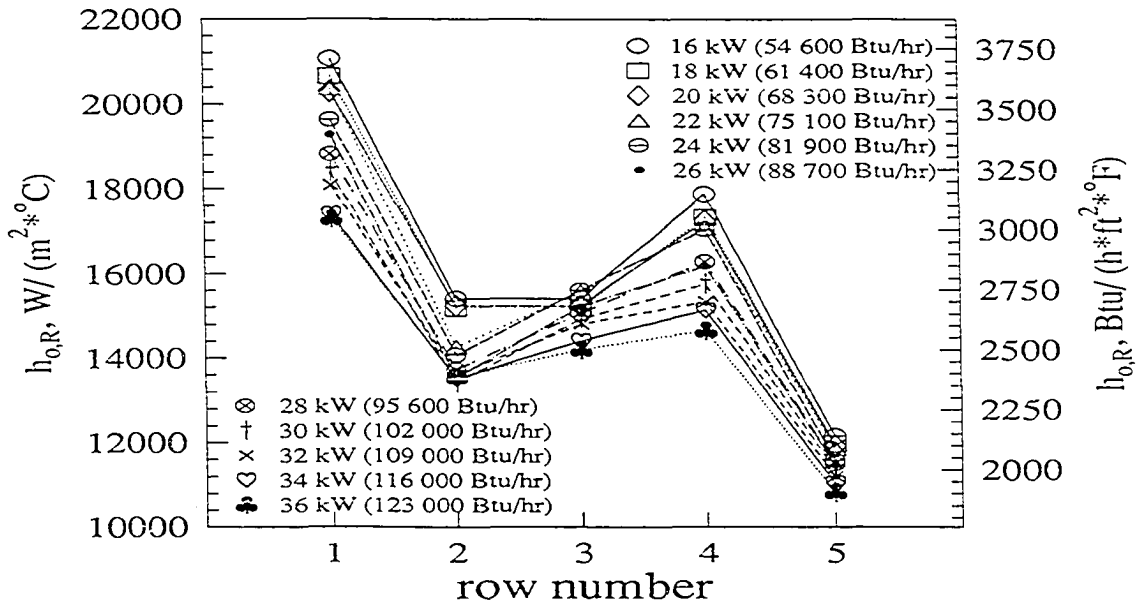


Figure 5.19: Average shell-side row heat transfer coefficient vs. row number for the condensation of HFC-134a on the G-SC geometry

$h_{o,R}$ decreases by 18% over the bundle range tested. The smallest drop in $h_{o,R}$ occurs in row 3, where $h_{o,R}$ drops only 8% over the bundle range tested.

In general, Figure 5.19 shows that $h_{o,R}$ decreases from row 1 to 2, increases from row 2 to 4, then decreases sharply through row 5. The magnitude of the decrease in $h_{o,R}$ from row 1 to 2 is not dependent on bundle load, and ranges from 22% at bundle loads of 34 and 36 kW (116 000 and 123 000 Btu/hr) to 30% at bundle loads of 22 and 26 kW (75 100 and 88 700 Btu/hr). The magnitude of the increase in $h_{o,R}$ from row 2 to 4 is not dependent on bundle load, and ranges from 8% at a bundle load of 36 kW (123 000 Btu/hr) to 20% at bundle loads of 22 and 26 kW (75 100 and 88 700 Btu/hr). The magnitude of the decrease in $h_{o,R}$ from row 4 to 5 depends on bundle load, and ranges from 26% at a bundle load of 36 kW (123 000 Btu/hr) to 32% at a bundle load of 16 kW (54 600 Btu/hr).

This behavior is somewhat similar to the behavior of the 40-fpi, except that the second

peak in $h_{o,R}$ occurs in row 4 for the G-SC, instead of row 3. The sharp drop in $h_{o,R}$ from row 4 to 5 may be due to the fact that row 5 is being inundated by condensation from rows 1 and 3. Since the G-SC retains much of the condensate in its Y shaped fins, much of the condensate draining from rows 1 and 3 may be retained in the fins of row 5, thus reducing the performance of this row. The reason for the peak of $h_{o,R}$ in row 4 is unknown.

Figure 5.20 shows the repeatability of the $h_{o,R}$ data for two different bundle loads. The repeatability of the experiment can be seen by comparing the data points for run 1 and run 2. This figure indicates that the data for $h_{o,R}$ can be repeated over the entire range of bundle loads tested. The difference between the two runs is less than 2%, except for row 1 at 18 kW (61 400 Btu/hr), where the difference between the two runs is 6%. Uncertainty bars are also presented for one of the 18 kW (61 400 Btu/hr) runs to demonstrate the level of uncertainty in the row by row analysis. This figure also demonstrates the drop in $h_{o,R}$ with increasing bundle load.

Comparison to P-W and W-M correlations

Values of $h_{o,R}$ as predicted by the P-W and W-M correlations are plotted on Figure 5.16. The measured values of $h_{o,B}$, which drop roughly 9% as the heat flux increases from 16 000 W/m² (5100 Btu/(hr·ft²)) to 41 000 W/m² (13 000 Btu/(hr·ft²)), agree well with the P-W correlation, which predicts a 20% drop for the same heat flux range. The magnitude of $h_{o,B}$ predicted by the W-M correlation is about 10% less than the data. Once again, this may be due to the fact the the W-M correlation was developed using only CFC-11. The W-M correlation predicts a 16% drop in $h_{o,B}$ as heat flux increases over the range tested.

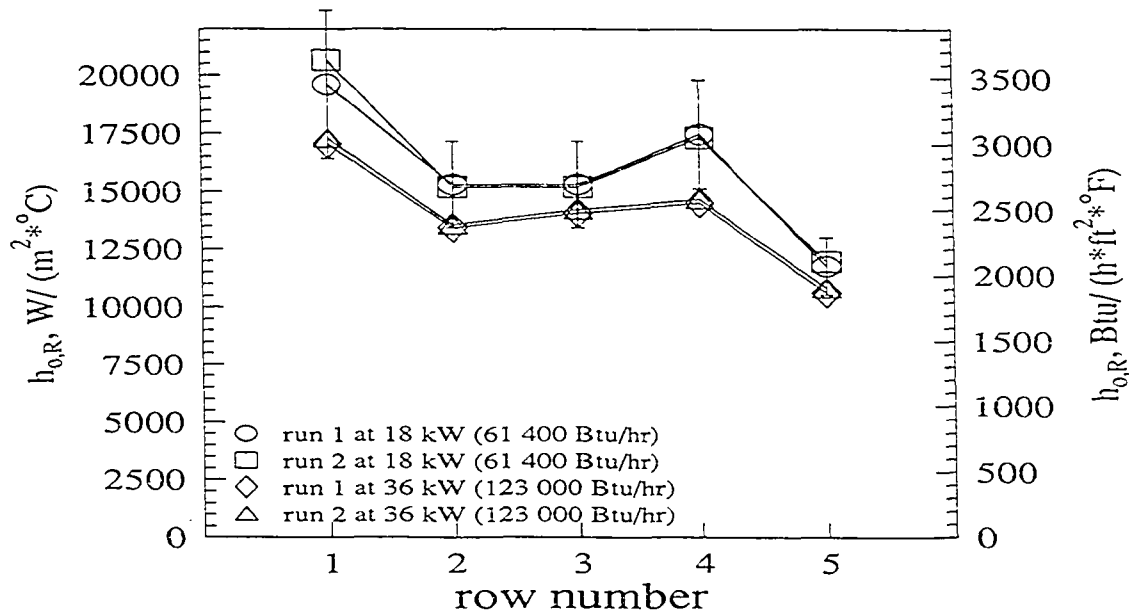


Figure 5.20: Average shell-side row heat transfer coefficient vs. row number for the condensation of HFC-134a on the G-SC geometry

Comparison of HFC-134a and CFC-12 Heat Transfer Coefficients

Comparison of average bundle heat transfer coefficients

Figures 5.21–5.24 compare the values of $h_{o,B}$ for HFC-134a and CFC-12 for the 26-fpi, 40-fpi, Tu-Cii, and G-SC bundles respectively. In all cases, for a given heat flux, the HFC-134a heat transfer coefficients are higher than those for CFC-12. For the 26-fpi, 40-fpi, and G-SC, the HFC-134a $h_{o,B}$ values are approximately 20% larger than the CFC-12 $h_{o,B}$ values over the heat flux range tested. For the Tu-Cii, the difference in $h_{o,B}$ for the two refrigerants varies with heat flux. At $16\,000\ W/m^2$ ($5100\ Btu/(hr \cdot ft^2)$), $h_{o,B}$ for HFC-134a is 100% larger than that for CFC-12, while at $41\,000\ W/m^2$ ($13\,000\ Btu/(hr \cdot ft^2)$), $h_{o,B}$ for HFC-134a is 33% larger than that for CFC-12.

The improved performance of HFC-134a over CFC-12 is due to the fact that the thermo-

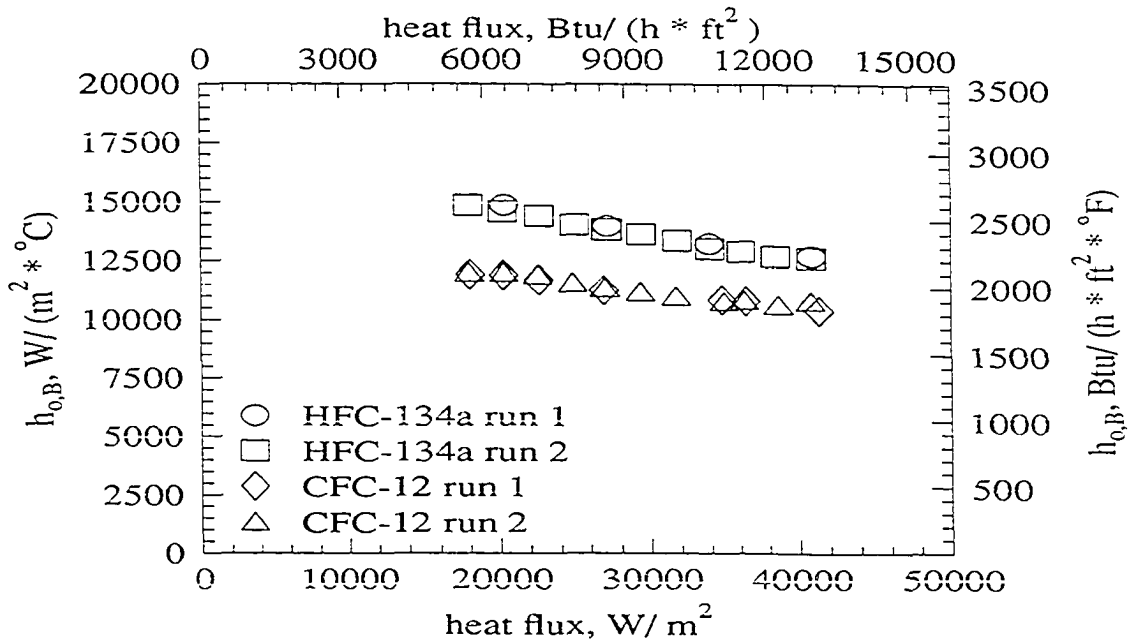


Figure 5.21: Comparison of the HFC-134a and CFC-12 average shell-side bundle heat transfer coefficients for the 26-fpi geometry

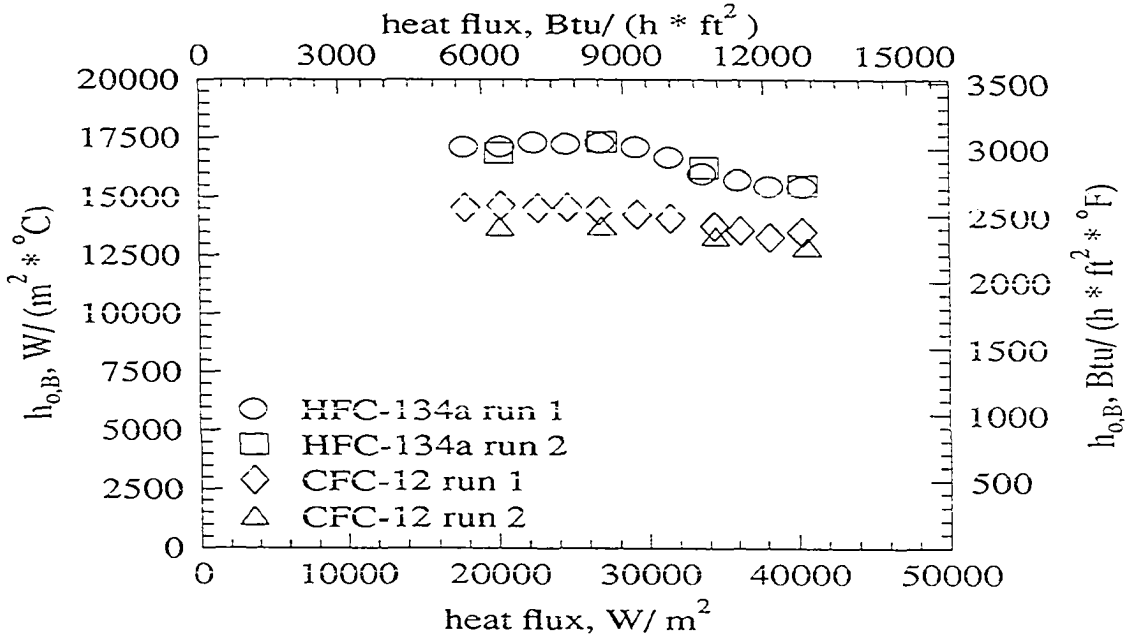


Figure 5.22: Comparison of the HFC-134a and CFC-12 average shell-side bundle heat transfer coefficients for the 40-fpi geometry

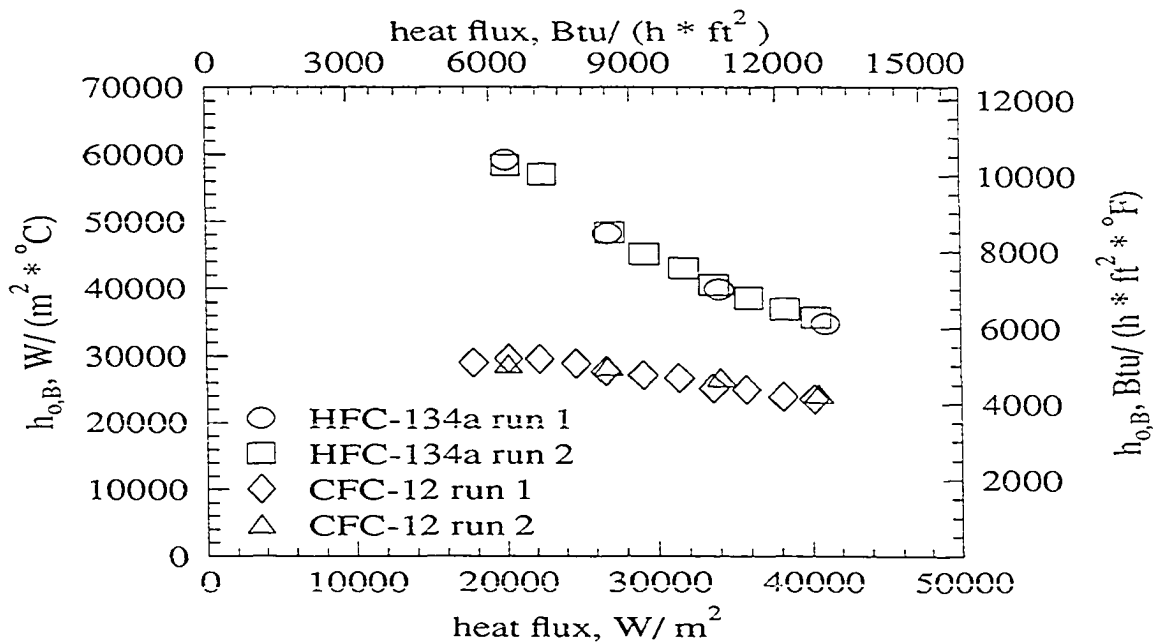


Figure 5.23: Comparison of the HFC-134a and CFC-12 average shell-side bundle heat transfer coefficients for the Tu-Cii geometry

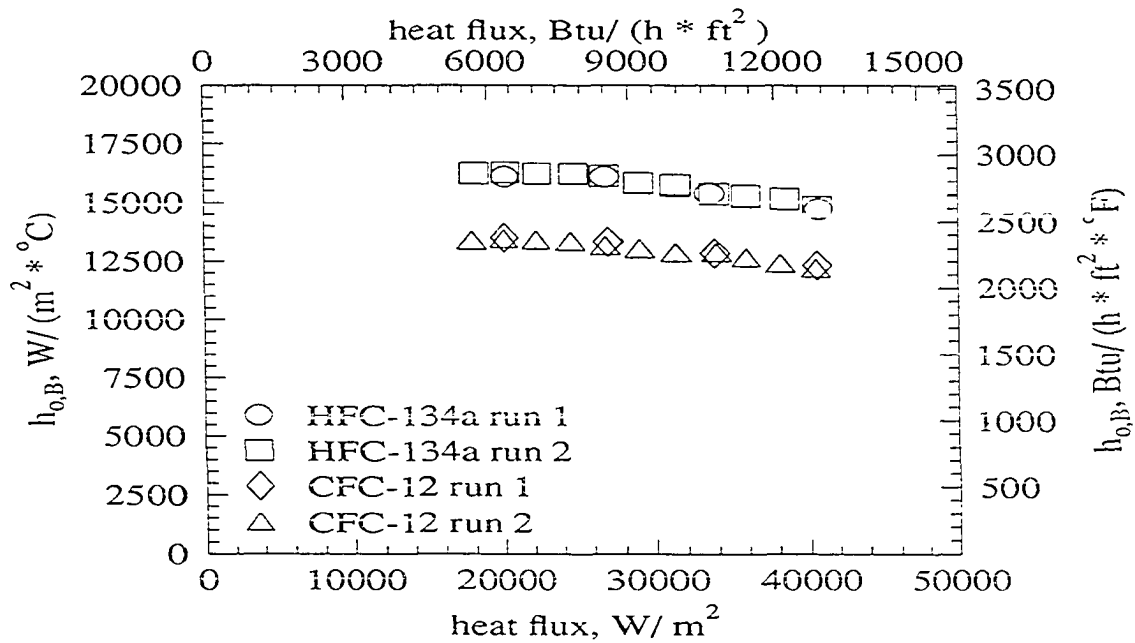


Figure 5.24: Comparison of the HFC-134a and CFC-12 average shell-side bundle heat transfer coefficients for the G-SC geometry

physical properties of HFC-134a are generally more favorable for condensation heat transfer than those of CFC-12. First, the enthalpy of vaporization for HFC-134a is roughly 23% larger than that of CFC-12. Thus, at a given heat flux, the CFC-12 mass flux is 23% larger than the HFC-134a mass flux. The larger mass flux results in a larger liquid layer on the tubes, which decreases the condensation heat transfer coefficient. Secondly, the liquid thermal conductivity of HFC-134a is 17% larger than that of CFC-12, resulting in better heat transfer through the condensate layer on the tube surface. Thirdly, the surface tension of CFC-12 is 36% larger than that of HFC-134a. Surface tension forces are responsible for liquid retention in the draining channels of the tube, and hence flooding of the tube surface. The liquid viscosity of HFC-134a is 3% larger than that of CFC-12. A higher liquid viscosity would increase the drag between the wall and the downward flowing condensate, thus decreasing the heat transfer coefficient.

In comparison to CFC-12, the surface tension, enthalpy of vaporization, and liquid thermal conductivity of HFC-134a are better suited to condensation heat transfer, and outweigh the negative effect of HFC-134a's larger liquid viscosity. Thermophysical properties for HFC-134a and CFC-12 are given in Table 5.1. Properties for CFC-113, which was used to obtain the Honda et al. (1991 and 1992) data discussed in this chapter, are also given in this table. The properties of HFC-134a are also more favorable for condensation heat transfer than those of CFC-113.

Figures 5.21–5.24 also indicate that $h_{o,B}$ generally decreases with increasing heat flux for all tube geometries, although the change is much more dramatic for the Tu-Cii. Figure 5.23 indicates that at low heat fluxes, the Tu-Cii $h_{o,B}$ for HFC-134a is 100% higher than Tu-Cii $h_{o,B}$ for CFC-12. However, the experimental uncertainty at low heat fluxes is approximately $\pm 35\%$. Thus, the improvement of the HFC-134a Tu-Cii $h_{o,B}$ over the CFC-12 value at low heat fluxes may not be as dramatic as shown in Figure 5.23.

Table 5.1: Property comparison for HFC-134a, CFC-12, and CFC-113 at 35°C

property	HFC-134a	CFC-12	CFC-113
P_{sat} , kPa	886.900	838.000	64.990
v_f , m ³ /kg	8.5670E-04	7.8470E-04	6.4900E-04
v_g , m ³ /kg	2.3060E-02	2.0510E-02	2.0240E-01
ρ_f , kg/m ³	1167.00	1274.00	1541.00
ρ_g , kg/m ³	43.36	48.75	4.94
i_{fg} , kJ/kg	168.40	129.70	144.40
$C_{p,f}$, kJ/(kg·K)	1.472	1.040	0.893
$C_{p,g}$, kJ/(kg·K)	1.080	0.779	0.653
μ_f , μPa·s	188.40	182.00	579.80
μ_g , μPa·s	12.78	13.24	10.51
k_f , mW/(m·K)	76.11	63.06	68.43
k_g , mW/(m·K)	15.05	10.88	9.04
σ , mN/m	6.78	10.74	15.14

The data for the CFC-12 repeatability run is also plotted on Figure 5.21 – Figure 5.24. The repeatability of the experiment can be seen by comparing the data points for run 1 and run 2. These figures indicate that the data for $h_{o,B}$ can be repeated over the entire range of bundle loads tested. The difference between the two CFC-12 runs is less than 2% for the 26-fpi, Tu-Cii and G-SC bundles. The difference between the two CFC-12 runs for the 40-fpi bundle is less than 6%. Generally, the uncertainty in $h_{o,B}$ for CFC-12 ranges from $\pm 4\%$ to $\pm 12\%$ for the 26-fpi, 40-fpi, and G-SC, and from $\pm 9\%$ to $\pm 22\%$ for the Tu-Cii. In all cases, the uncertainty decreases with increasing heat flux.

Comparison of average row heat transfer coefficients

Figures 5.25–5.28 compare the HFC-134a and CFC-12 $h_{o,R}$ behavior for the 26-fpi, 40-fpi, Tu-Cii, and G-SC bundles, respectively. These figures indicate that for a given tube geometry, the row-to-row behavior is essentially the same for both refrigerants, although the row-to-row behavior differs significantly between the four tube geometries. The Tu-Cii row heat transfer coefficients are also subject to higher uncertainties at low heat fluxes, as discussed in the previous section.

The data for the CFC-12 repeatability run are also plotted on Figures 5.25–5.28. The repeatability of the experiment can be seen by comparing the data points for run 1 and run 2. These figures indicate that the CFC-12 data for the row heat transfer coefficients can be repeated over the entire range of bundle loads tested. The uncertainty in the CFC-12 average row heat transfer coefficients ranges from $\pm 5\%$ to $\pm 16\%$ for all geometries except the Tu-Cii, which has uncertainties ranging from $\pm 9\%$ to $\pm 34\%$. In all cases, the uncertainty decreases with increasing heat flux.

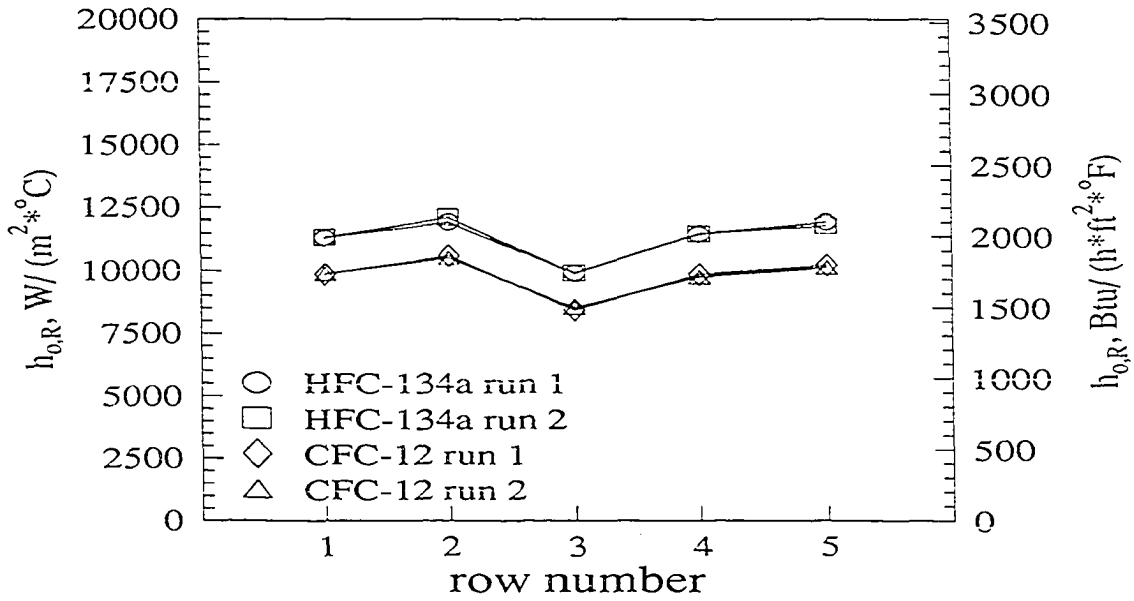


Figure 5.25: Comparison of the HFC-134a and CFC-12 average shell-side row heat transfer coefficients for the 26-fpi geometry at a bundle load of 36 kW (123 000 Btu/hr)

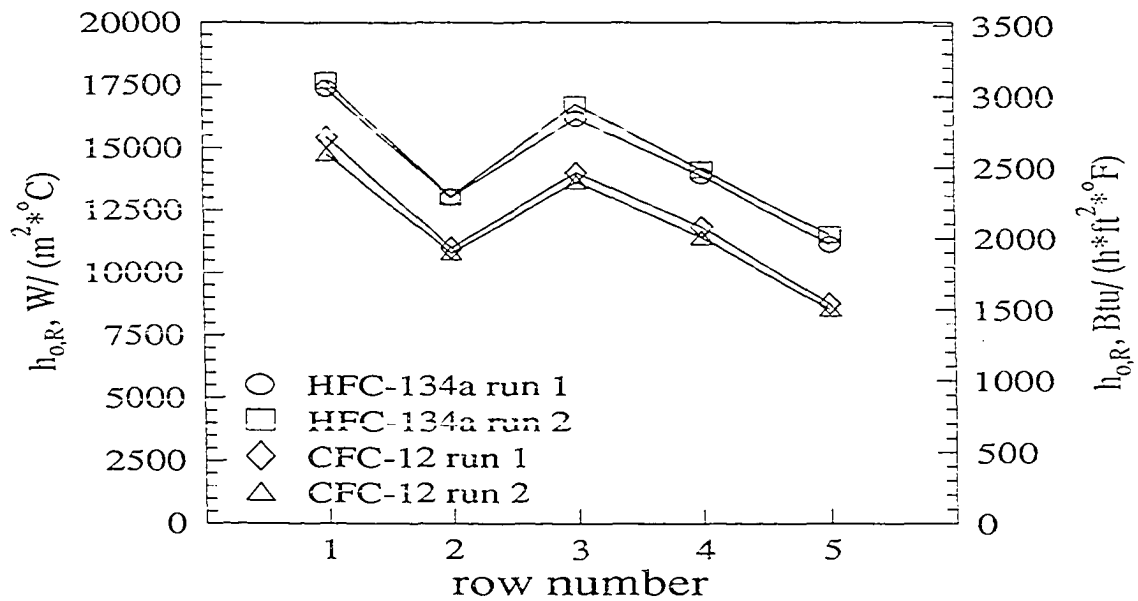


Figure 5.26: Comparison of the HFC-134a and CFC-12 average shell-side row heat transfer coefficients for the 40-fpi geometry at a bundle load of 36 kW (123 000 Btu/hr)

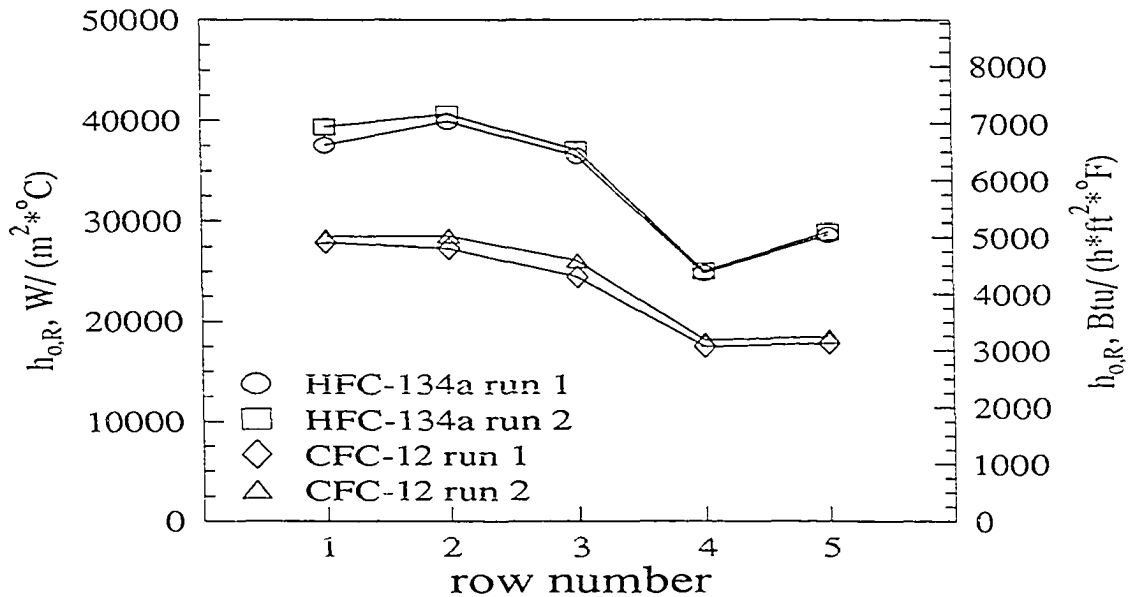


Figure 5.27: Comparison of the HFC-134a and CFC-12 average shell-side row heat transfer coefficients for the Tu-Cii geometry at a bundle load of 36 kW (123 000 Btu/hr)

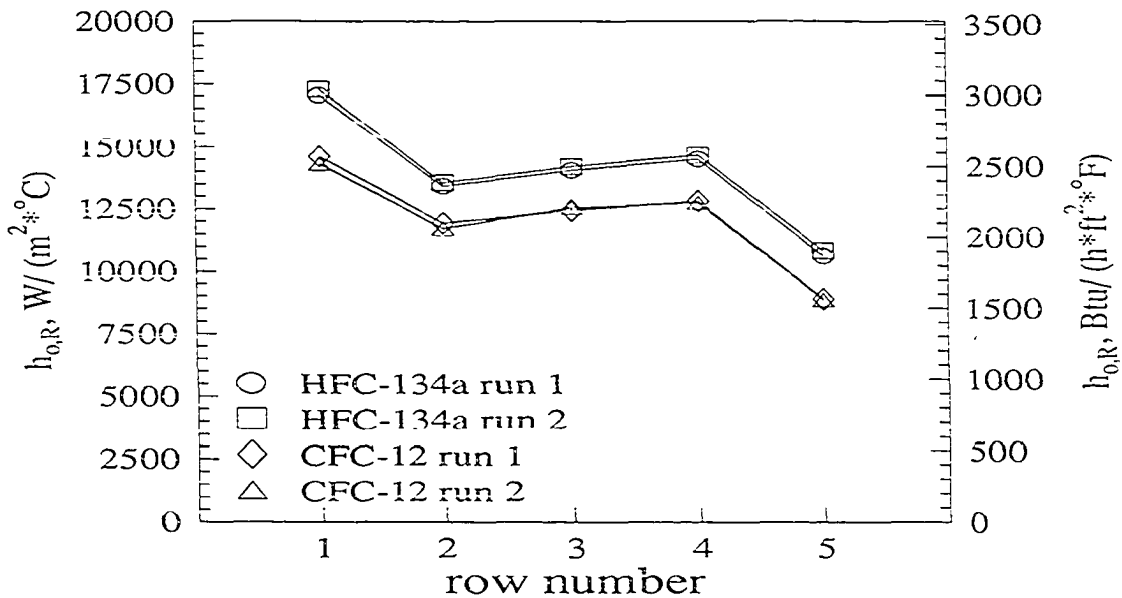


Figure 5.28: Comparison of the HFC-134a and CFC-12 average shell-side row heat transfer coefficients for the G-SC geometry at a bundle load of 36 kW (123 000 Btu/hr)

Comparison of Bundle Geometries

Figure 5.29 compares the average shell-side bundle heat transfer coefficients of HFC-134a for the different tube geometries. At $16\,000\text{ W/m}^2$ ($5100\text{ Btu}/(\text{hr}\cdot\text{ft}^2)$) the values of $h_{o,B}$ for the Tu-Cii are three times higher than the values of $h_{o,B}$ for the other tube geometries while at $41\,000\text{ W/m}^2$ ($13\,000\text{ Btu}/(\text{hr}\cdot\text{ft}^2)$), the values of $h_{o,B}$ for the Tu-Cii are two times larger than the values of $h_{o,B}$ for the other geometries. Figure 5.30 compares the CFC-12 $h_{o,B}$ for the different tube geometries, and shows that the values of $h_{o,B}$ for the Tu-Cii are generally two times larger than the values of $h_{o,B}$ for the other geometries across the entire heat flux range.

For HFC-134a, the low fin 40-fpi performs better than the longer finned G-SC, as the values of $h_{o,B}$ for the 40-fpi are 5% higher than the values of $h_{o,B}$ for the G-SC over the entire heat flux range. The 26-fpi is the worst performer, as its values of $h_{o,B}$ are 8% lower than those of the G-SC at $16\,000\text{ W/m}^2$ ($5100\text{ Btu}/(\text{hr}\cdot\text{ft}^2)$), and 16% lower at $41\,000\text{ W/m}^2$ ($13\,000\text{ Btu}/(\text{hr}\cdot\text{ft}^2)$). For CFC-12, the low fin 40-fpi also performs better than the longer finned G-SC, as the values of $h_{o,B}$ for the 40-fpi are approximately 10% higher than the values for the G-SC across the entire heat flux range tested. The 26-fpi is again the worst performer, as its values of $h_{o,B}$ are 10% lower than those of the G-SC at $16\,000\text{ W/m}^2$ ($5100\text{ Btu}/(\text{hr}\cdot\text{ft}^2)$), and 15% lower at $41\,000\text{ W/m}^2$ ($13\,000\text{ Btu}/(\text{hr}\cdot\text{ft}^2)$).

The Tu-Cii has been optimized for the condensation of organic fluids, so the fact that it is the best performer is not surprising. Even though the low-fin 40-fpi has 7% less surface area per unit length than the 26-fpi, the 40-fpi still out-performs the 26-fpi. The fin spacing of the 40-fpi is 0.457 mm (0.018 in), while the fin spacing of the 26-fpi is 0.672 mm (0.0265 in). The optimum fin spacing for CFC-12 as predicted by Honda et al. (1989) is 0.3 mm (0.0118 in). Since the 40-fpi is closer to the optimum fin spacing than the 26-fpi, the 40-fpi should perform better. Since the G-SC is essentially a 26-fpi with modified fins and has only a 3.5%

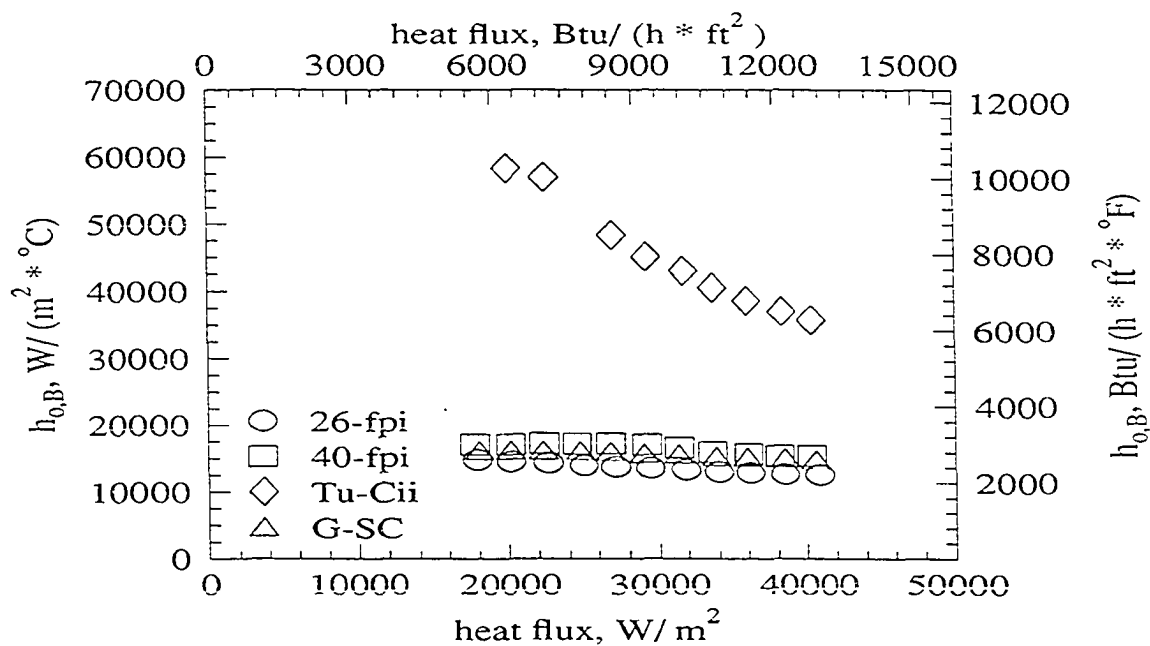


Figure 5.29: Comparison of the HFC-134a average shell-side bundle heat transfer coefficients for the four tube geometries

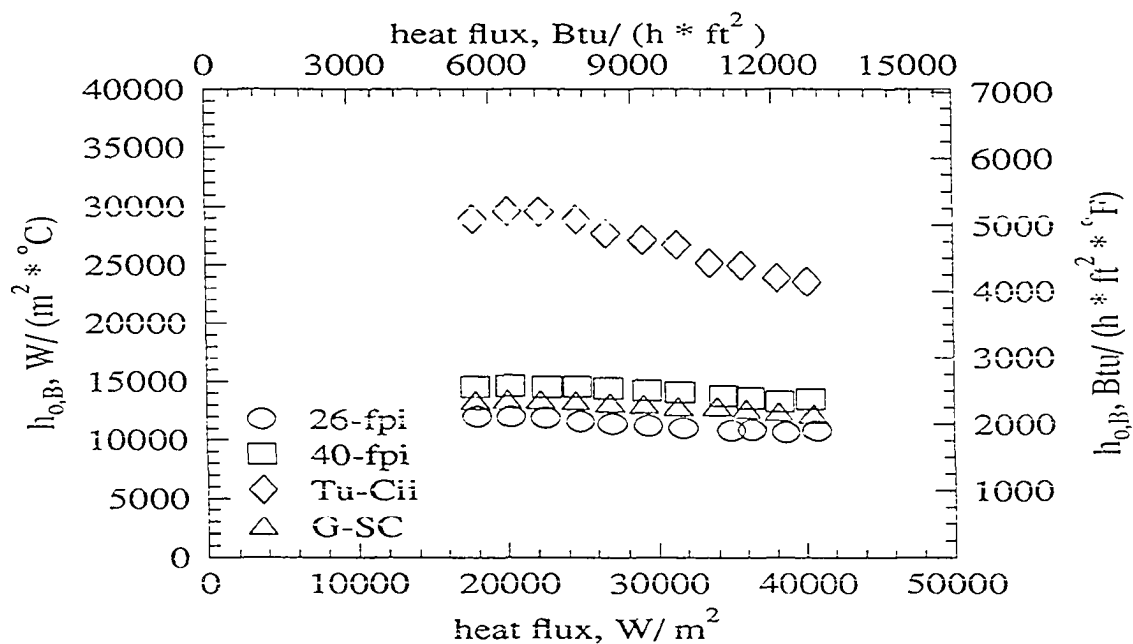


Figure 5.30: Comparison of the CFC-12 average shell-side bundle heat transfer coefficients for the four tube geometries

increase in surface area per unit length over the 26-fpi, The G-SC performance should be similar to the 26-fpi.

Summary

1. Increasing the heat flux causes the average shell-side bundle heat transfer coefficient to drop for all four geometries.
2. The Tu-Cii is the best performing geometry, followed by the 40-fpi, G-SC, and finally the 26-fpi geometry. These trends hold true for both HFC-134a and CFC-12.
3. Of the four tube geometries tested, the average shell-side heat transfer coefficient of Tu-Cii is most affected by the amount of condensate draining from the tube.
4. The row-to-row average shell-side heat transfer coefficient behavior differs significantly between the four geometries.
5. For a given tube geometry, the row-to-row average shell-side heat transfer coefficient behavior is the same for both HFC-134a and CFC-12.
6. For all four tube geometries, the HFC-134a average shell-side heat transfer coefficients are higher than those for CFC-12.

CHAPTER 6. HCFC-123 SHELL-SIDE CONDENSATION RESULTS

Shell-side condensation heat transfer coefficients for HCFC-123 are presented in this chapter. Bundles constructed from four different tube geometries were tested over a nominal heat flux range of $16\,000\text{ W/m}^2$ ($5100\text{ Btu}/(\text{hr}\cdot\text{ft}^2)$) to $41\,000\text{ W/m}^2$ ($13\,000\text{ Btu}/(\text{hr}\cdot\text{ft}^2)$). For each tube geometry, average bundle heat transfer coefficients as well as the average heat transfer coefficient for the middle tube of each row are presented in graphical format. The HCFC-123 row and bundle average heat transfer coefficients are compared to those for the condensation of CFC-11. A complete tabular listing of the entire set of HCFC-123 data taken during this study can be found in Appendix D, while a tabular listing of the CFC-11 data can be found in Appendix E. In the following discussion, row 1 refers to the top row of the bundle, with the row number increasing towards the bottom of the bundle. For example, row 5 is the bottom row in the bundle.

As discussed in Chapter 4, the nominal outer surface area of the tube was used in the calculation of the shell-side heat transfer coefficient. The nominal outer surface area is based on the nominal outer diameter of the tube so that the tube outer surface area was equal to the surface area of a smooth tube of the same diameter as the enhanced tube nominal diameter. Thus, the heat transfer coefficients presented in this chapter are based on the nominal tube outer surface area, not the actual tube outer surface area.

Results for the 26-fpi Geometry

Average bundle heat transfer coefficient results

Figure 6.1 shows that the average shell-side bundle heat transfer coefficient ($h_{o,B}$) for the 26-fpi geometry decreases with increasing heat flux. An increasing bundle heat flux corresponds to an increasing refrigerant mass flow rate. As the mass flow rate (and hence, heat flux) increases, the liquid layer on the tubes becomes larger. The measured value of $h_{o,B}$ drops from $14\,090\text{ W}/(\text{m}^2\cdot\text{K})$ ($2480\text{ Btu}/(\text{hr}\cdot\text{ft}^2\cdot\text{F})$) to $11\,860\text{ W}/(\text{m}^2\cdot\text{K})$ ($2090\text{ Btu}/(\text{hr}\cdot\text{ft}^2\cdot\text{F})$), which is 16%, over the heat flux range tested ($16\,000\text{ W}/\text{m}^2$ ($5100\text{ Btu}/(\text{hr}\cdot\text{ft}^2)$) - $41\,000\text{ W}/\text{m}^2$ ($13\,000\text{ Btu}/(\text{hr}\cdot\text{ft}^2)$)). The data for the repeatability run are also plotted on Figure 6.1. The repeatability of the experiment can be seen by comparing the data points for run 1 and run 2. This figure indicates that the data for $h_{o,B}$ can be repeated over the entire range of bundle loads tested, as the difference between the two runs is less than 3% over the entire heat flux range.

Figure 6.2 shows the variation of $h_{o,B}$ with the LMTD, while Figure 6.3 shows the variation of $h_{o,B}$ with the condensation temperature difference, $T_{sat} - T_{s,o}$. The wall temperature is calculated, not directly measured. As the LMTD and $T_{sat} - T_{s,o}$ increase, more refrigerant is condensed. Thus, an increasing LMTD and $T_{sat} - T_{s,o}$ correspond to an increasing heat flux. The LMTD is a measure of the overall water-refrigerant temperature difference that drives the condensation, while $T_{sat} - T_{s,o}$ is the portion of the overall temperature difference that occurs between the tube outer surface and the refrigerant. Since the same trend in $h_{o,B}$ is present in both figures, the trend in $h_{o,B}$ is due to a shell-side phenomenon.

Uncertainty bars are also plotted on Figure 6.2, and show that the experimental uncertainty in $h_{o,B}$ ranges from $\pm 7\%$ to $\pm 16\%$. This figure indicates that $w_{h_{o,B}}$ decreases as the LMTD, and hence heat flux, increases. As the LMTD increases, $T_{sat} - T_{w,out}$ and

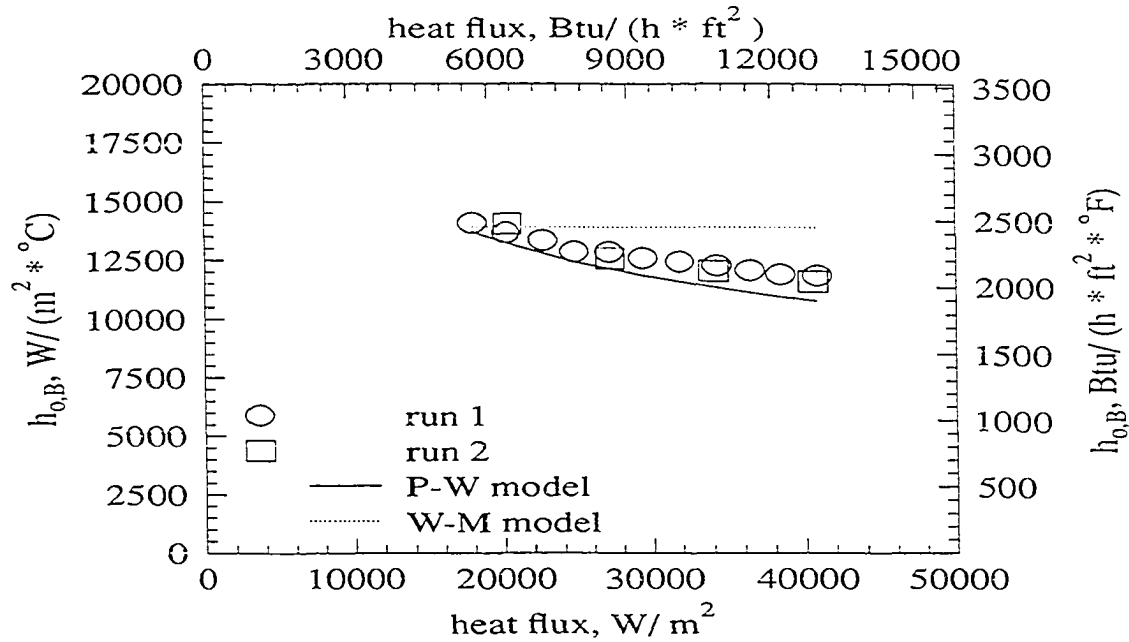


Figure 6.1: Average shell-side bundle heat transfer coefficient vs. heat flux for the condensation of HCFC-123 on the 26-fpi geometry

$T_{sat} - T_{w,in}$ increase, but the uncertainty in these temperature differences remains the same. Therefore, the uncertainty in these temperature differences becomes less significant as the temperature differences increase. The calculation of $h_{o,B}$ is quite sensitive to these temperature differences, thus $w_{h_{o,B}}$ decreases as the uncertainty in these temperature differences becomes less significant. The data for the repeatability run are also plotted in Figures 6.2 and 6.3.

The only archival data available for the condensation of HCFC-123 on bundles are that of Murata et al. (1990), who tested in-line bundles that were two columns wide by eight rows deep. The bundles were constructed from 1024-fpm (26-fpi) and 1181-fpm (30-fpi) stainless steel tubes. The condensation temperature difference range of the Murata et al. data is nearly identical to the range in the present study.

The magnitude of Murata et al. data is approximately 50% lower than the present data.

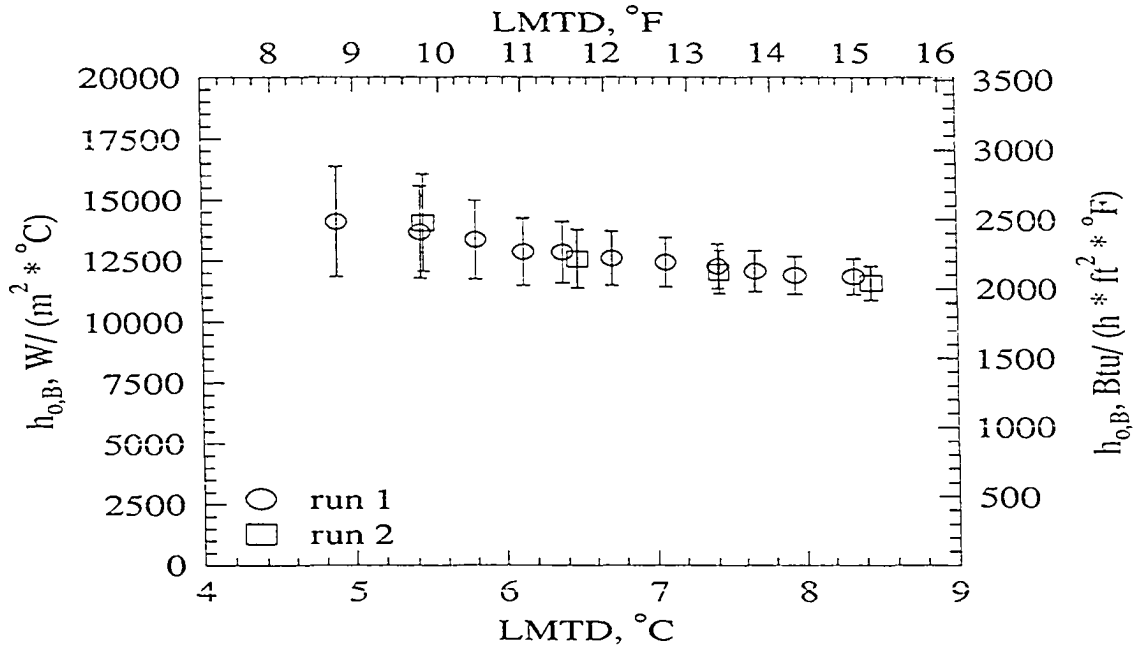


Figure 6.2: Average shell-side bundle heat transfer coefficient vs. LMTD for the condensation of HCFC-123 on the 26-fpi geometry

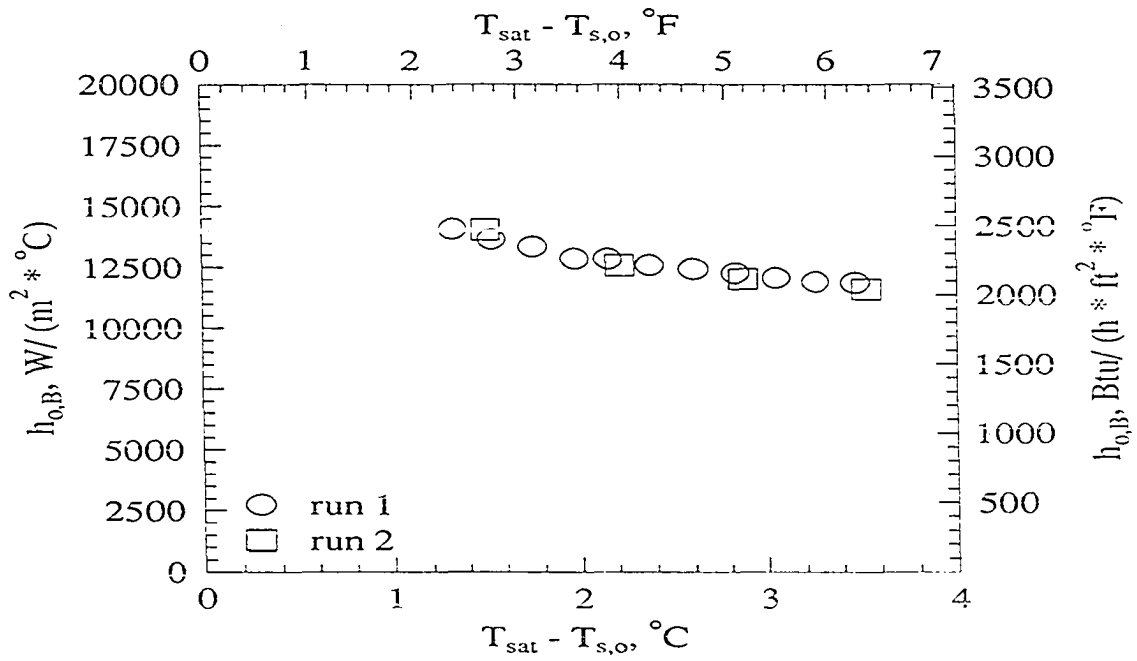


Figure 6.3: Average shell-side bundle heat transfer coefficient vs. condensation temperature difference for the condensation of HCFC-123 on the 26-fpi geometry

This difference is most likely due to the use of stainless steel tubes in the Murata study. The thermal conductivity of stainless steel is an order of magnitude lower than that of copper, and therefore the stainless steel tubes have a lower fin efficiency than copper tubes. The Murata data show a 14% decrease in $h_{o,B}$ over the the condensation temperature difference range tested, which is in good agreement with the 16% drop found in this study.

Average row heat transfer coefficient results

Figure 6.4 shows the behavior of the average shell-side heat transfer coefficient for the middle tube of each row ($h_{o,R}$) at different bundle loads for the 26-fpi. This figure indicates that $h_{o,R}$ for rows 1 and 2 generally decreases with increasing bundle load, but that $h_{o,R}$ for rows 3, 4, and 5 is independent of bundle load. The values of $h_{o,R}$ for rows 1 and 2 drop 22% and 16% respectively over the bundle load range tested (16–36 kW, or 54 600–123 000 Btu/hr). The change in $h_{o,R}$ for rows 3, 4, and 5 is less than 4%. As bundle load increases, the amount of condensate draining on rows 3, 4, and 5 increases. Thus, the data indicate that the 26-fpi is not affected by liquid inundation from higher rows. This same trend was noticed in the HFC-134a data. The Murata et al. (1990) data only report $h_{o,R}$ for rows 1, 4, and 8. Their data do indicate that $h_{o,R}$ drops with increasing bundle load.

The decrease of $h_{o,R}$ for rows 1 and 2 with increasing bundle load is consistent with the single-tube theory, which predicts that $h_{o,R}$ will drop as $T_{sat} - T_{s,o}$ increases. In the present data, $T_{sat} - T_{s,o}$ increases with heat flux. Since row 1 is not subject to condensate drainage and row 2 is subject to very little condensate drainage, these rows may be expected to behave as the single tube does, and $h_{o,R}$ for rows 1 and 2 should drop with increasing heat flux. Since increasing heat flux is directly proportional to increasing bundle load, the data also imply that the drop in $h_{o,B}$ with increasing heat flux is due to the phenomena occurring in rows 1 and 2 only.

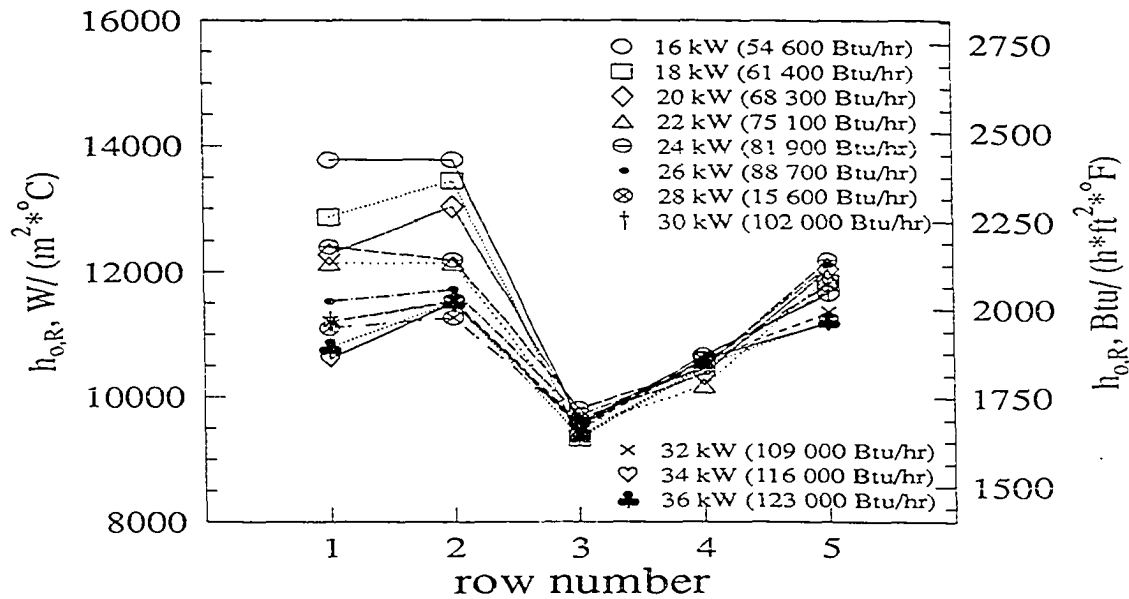


Figure 6.4: Average shell-side row heat transfer coefficient vs. row number for the condensation of HCFC-123 on the 26-fpi geometry

In general, Figure 6.4 shows that $h_{o,R}$ increases from row 1 to 2, decreases from row 2 to 3, then increases through row 5. The magnitude of the increase in $h_{o,R}$ from row 1 to 2 is not dependent on bundle load, and ranges from 2% at bundle loads of 26 and 28 kW (88 700 and 95 600 Btu/hr) to 8% at 34 kW (116 000 Btu/hr). At bundle loads of 16 and 22 kW (54 600 and 75 100 Btu/hr), $h_{o,R}$ remains constant from row 1 to 2, while at a bundle load of 24 kW (81 900 Btu/hr), $h_{o,R}$ actually increases by 2%. The magnitude of the decrease in $h_{o,R}$ from row 2 to 3 is largest at low bundle loads, and ranges from 19% at a bundle load of 36 kW (123 000 Btu/hr) to 30% at a bundle load of 16 kW (54 600 Btu/hr). In general, the magnitude of the increase in $h_{o,R}$ from rows 3 to 5 is decreases with increasing bundle load and ranges from 17% to 26% over the bundle load range tested. Similar trends were also found the the HFC-134a data.

The increase in $h_{o,R}$ from row 1 to row 2 was also observed by Honda et al. (1992),

who suggest that the increase may be due to a vapor velocity effect. The vapor velocity approaching row 1 is quite small because of the large surface area at the top of the bundle. However, the vapor velocity approaching row 2 will be significantly larger, because the vapor must flow through the narrow gaps between the tubes of row 1 in order to reach row 2. The reduction in flow area will result in an increase in the vapor velocity at the top of row 2. The HCFC-123 data collaborate the suggestion made in the previous chapter that the 26-fpi bundle is subject to vapor velocity effects.

Row 3 has the lowest values of $h_{o,R}$. Since the instrumented tube in row 3 is the middle tube of the bundle, this tube is one of three tubes in the bundle which does not have any of its surface exposed to the vapor spaces in the test section. Thus, this tube may be starved of vapor. Also, row 3 is the first row to be fully inundated by condensate draining from a tube directly above it.

The value of $h_{o,R}$ increases over rows 4 and 5. Row 5 has its entire bottom surface exposed to refrigerant vapor. Thus, any vapor which passes around the sides of the bundle can condense on row 5. Some of this vapor can also condense on row 4, since a small portion of each tube in row 4 is also exposed to the vapor at the bottom of the condenser. Honda et al. (1991) do predict a jump in $h_{o,R}$ as the dripping mode changes from column mode to sheet mode. Since the instrumented tubes are internal, it was not possible to see if a transition from column to sheet mode was occurring. Murata et al. (1990) report that $h_{o,R}$ for row 4 was lower than that of row 1, but that $h_{o,R}$ for row 8 was similar to $h_{o,R}$ for row 1. This observation is in good agreement with the present data. Murata et al. did not observe a transition from column to sheet mode.

Figure 6.5 shows the repeatability of $h_{o,R}$ for two different bundle loads. The repeatability of the experiment can be seen by comparing the data points for run 1 and run 2. This figure indicates that the data for $h_{o,R}$ can be repeated over the entire range of bundle loads tested,

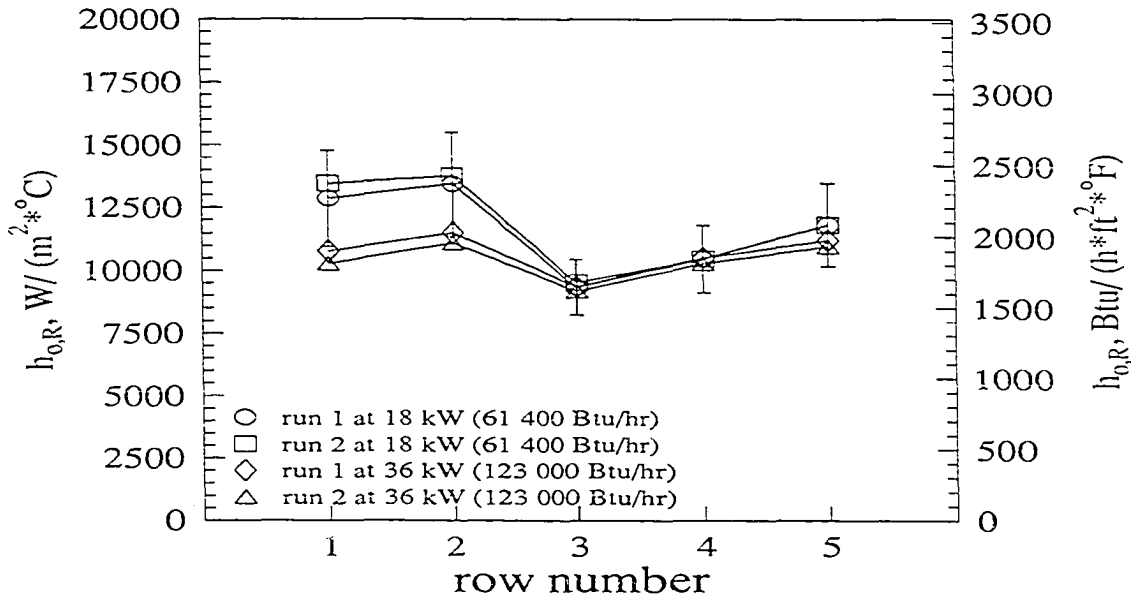


Figure 6.5: Average shell-side row heat transfer coefficient vs. row number for the condensation of HCFC-123 on the 26-fpi geometry

as the difference in the row coefficients for the two runs is less than 5%. Uncertainty bars are also presented for the 18 kW (61 400 Btu/hr) run to demonstrate the level of uncertainty in the row-by-row analysis. This figure also demonstrates the drop in $h_{o,R}$ with bundle load for rows 1 and 2, and the independence of $h_{o,R}$ with bundle load for rows 3, 4, and 5.

Comparison to the P-W and W-M correlations

Values of $h_{o,R}$ as predicted by the P-W (Pearson and Withers (1969)) and W-M (Webb and Murawski (1990)) correlations are plotted on Figure 6.1. The application of these two correlations to the present study is discussed in Chapter 4. The P-W correlation predicts a 21% drop in $h_{o,B}$ as the heat flux increases from 16 000 W/m² (5100 Btu/(hr·ft²)) to 41 000 W/m² (13 000 Btu/(hr·ft²)). The measured values of $h_{o,B}$ show a 16% drop over the same heat flux range and are in excellent agreement with the P-W correlation. The W-M correlation predicts

that $h_{o,B}$ is not affected by the amount of condensate draining from the tube, and is thus independent of heat flux.

As previously mentioned, rows 3, 4, and 5 show no condensate inundation effects, which is in agreement with the W-M correlation. Webb and Murawski (1990) report that the fins of 26-fpi prevent the draining condensate from spreading axially and further covering the condensing surface. The decrease in $h_{o,R}$ with increasing bundle load for rows 1 and 2 is consistent with the P-W model. The P-W correlation is based on single-tube theory, which predicts that h_o will drop as $T_{sat} - T_{s,o}$ increases. As bundle load increases, $T_{sat} - T_{s,o}$ increases because of the thickening liquid layer on the tube, and hence $h_{o,R}$ drops with increasing bundle load.

Results for the 40-fpi Geometry

Average bundle heat transfer coefficient results

Figure 6.6 shows that the average shell-side bundle heat transfer coefficient $h_{o,B}$ for the 40-fpi geometry is fairly constant at approximately 17 000 W/(m²·K) (3000 Btu/(hr·ft²·F)) as heat flux increases through 22 000 W/m² (7000 Btu/(hr·ft²)), then decreases by 17% to 14 110 W/(m²·K) (2480 Btu/(hr·ft²·F)) as the heat flux increases to 41 000 W/m² (13 000 Btu/(hr·ft²)). An increasing bundle heat flux corresponds to an increasing refrigerant mass flow rate. As the mass flow rate (and hence, heat flux) increases, the liquid layer on the tubes becomes larger, and the heat transfer resistance increases. The data suggest that up through a heat flux of 22 000 W/m² (7000 Btu/(hr·ft²)), the 40-fpi is able to sufficiently drain the condensate so that no effect of liquid layer thickness is seen.

A similar trend is found in the HFC-134a 40-fpi data discussed in the previous chapter. For HFC-134a, the liquid layer effect begins at a heat flux of 30 000 W/m² (9500 Btu/(hr·ft²)). The surface tension and liquid viscosity of HCFC-123 are twice as large as those for HFC-

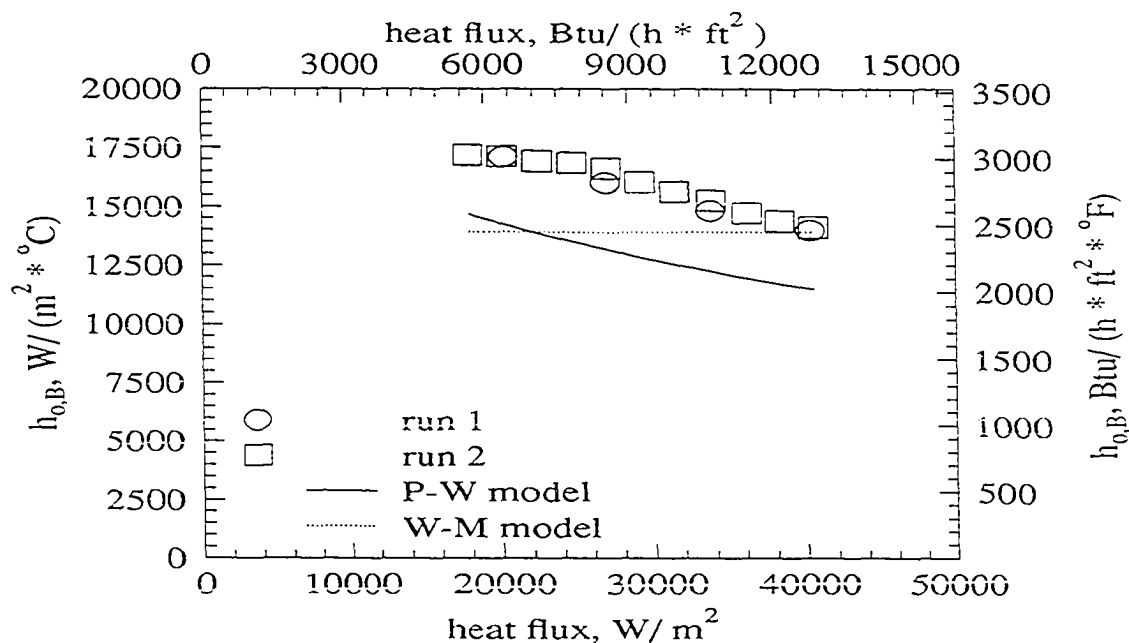


Figure 6.6: Average shell-side bundle heat transfer coefficient vs. heat flux for the condensation of HCFC-123 on the 40-fpi geometry

134a. Since an increase in these properties would cause increased condensate holdup on the tube, $h_{o,B}$ for HCFC-123 begins to decrease at a lower heat flux.

The data for the repeatability run are also plotted on Figure 6.6. The repeatability of the experiment can be seen by comparing the data points for run 1 and run 2. This figure indicates that the data for $h_{o,B}$ can be repeated over the entire range of bundle loads tested, as the difference between the two runs is less than 4%.

Figure 6.7 shows the variation of $h_{o,B}$ with the LMTD, while Figure 6.8 shows the variation of $h_{o,B}$ with the condensation temperature difference, $T_{sat} - T_{s,o}$. The wall temperature is calculated, not directly measured. Since the same trends in $h_{o,B}$ are present in both figures, the trend in $h_{o,B}$ is due to a shell-side phenomenon.

Uncertainty bars are also plotted on Figure 6.7, and show that the experimental uncertainty in $h_{o,B}$ ranges from $\pm 8\%$ to $\pm 20\%$. This figure indicates that $w_{h_{o,B}}$ decreases as the heat

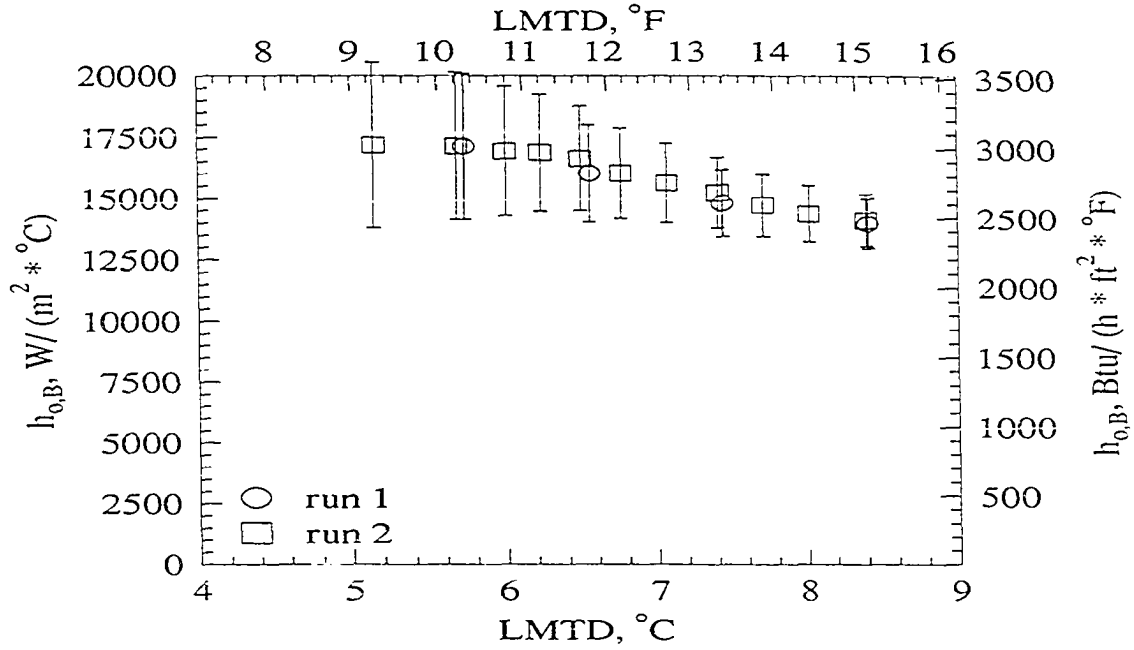


Figure 6.7: Average shell-side bundle heat transfer coefficient vs. LMTD for the condensation of HCFC-123 on the 40-fpi geometry

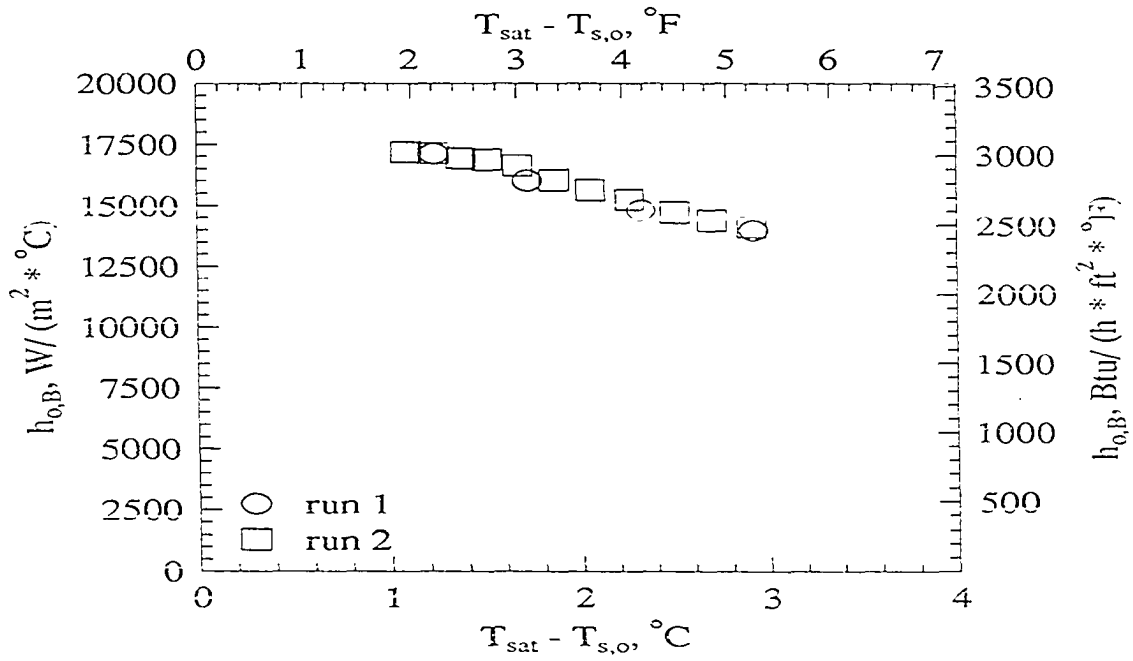


Figure 6.8: Average shell-side bundle heat transfer coefficient vs. condensation temperature difference for the condensation of HCFC-123 on the 40-fpi geometry

flux increases. As the heat flux increases, $T_{sat} - T_{w,out}$ and $T_{sat} - T_{w,in}$ increase, but the uncertainty in these temperature differences remains the same. Therefore, the uncertainty in these temperature differences becomes less significant as the temperature differences increase. The calculation of $h_{o,B}$ is quite sensitive to these temperature differences, thus $w_{h_{o,B}}$ decreases as the uncertainty in these temperature differences becomes less significant. The data for the repeatability run are also plotted on Figures 6.7 and 6.8.

Average row heat transfer coefficient results

Figure 6.9 shows the row behavior of the 40-fpi for different bundle loads. This figure indicates that $h_{o,R}$ for rows 1–5 generally decreases with increasing bundle load, with the decrease being more significant for row 5 and least significant for row 1. For row 1, $h_{o,R}$ drops by 4% while $h_{o,R}$ for row 5 drops by 21% over the bundle load range tested. The decrease in $h_{o,R}$ for rows 2, 3, and 4 is 14%, 9%, and 11% respectively. These trends are quite similar to those found in the 40-fpi data for HFC-134a discussed in the previous chapter, except that $h_{o,R}$ for row 1 increases slightly with increasing bundle load for HFC-134a.

The decrease in $h_{o,R}$ may be partly due to the increase in liquid layer on the tube as bundle load increases. Also, the 40-fpi may be susceptible to condensate inundation effects. The decrease in $h_{o,R}$ is more noticeable in row 5, which is the row that would be most inundated with drainage from the higher rows. The 40-fpi has shorter fins than the 26-fpi, and may not prevent axial spreading of the condensate as well as the 26-fpi.

In general, Figure 6.9 shows that $h_{o,R}$ decreases from row 1 to 2, increases from row 2 to 3, then decreases through row 5. The magnitude of the decrease in $h_{o,R}$ from row 1 to 2 is dependent on bundle load and ranges from 19% at a bundle load of 16 kW (54 600 Btu/hr) to approximately 27% for the 3 highest bundle loads tested. The magnitude of the increase in $h_{o,R}$ from row 2 to 3 appears to be independent of bundle load, and ranges from 16%

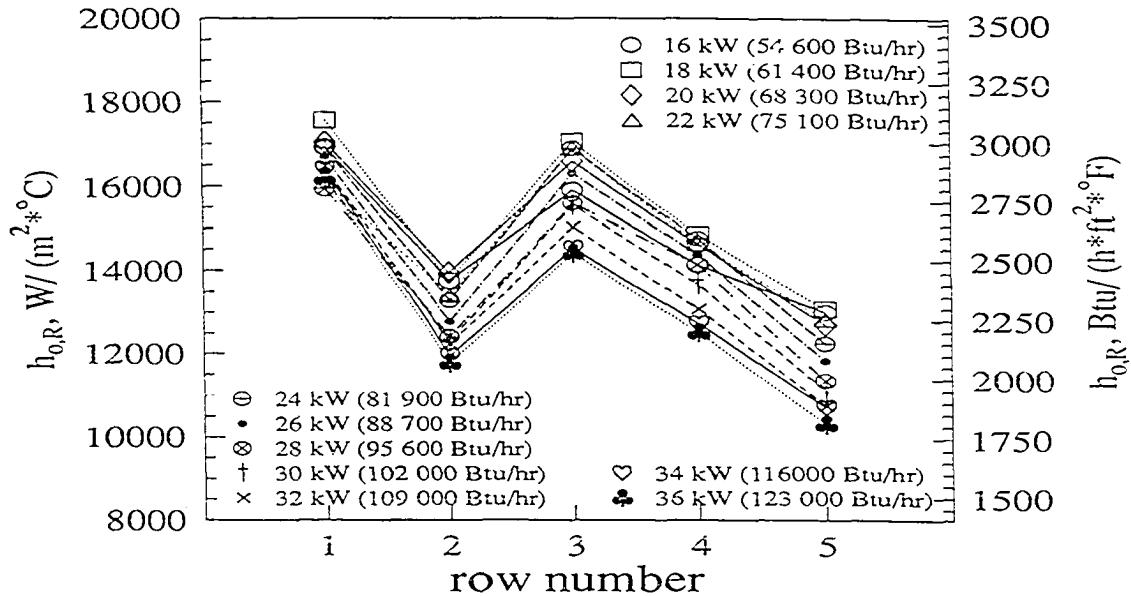


Figure 6.9: Average shell-side row heat transfer coefficient vs. row number for the condensation of HCFC-123 on the 40-fpi geometry

at a bundle load of 16 kW (54 600 Btu/hr) to 28% at a bundle load of 26 kW (88 700 Btu/hr). The magnitude of the decrease in $h_{o,R}$ from row 3 to 5 is dependent on bundle load and ranges from 18% at a bundle load of 16 kW (54 600 Btu/hr) to 28% for bundle loads of 24 kW (81 900 Btu/hr) and higher.

The row-to-row behavior of this bundle is quite peculiar and quite similar to the row-to-row behavior found in the 40-fpi data for HFC-134a. The decreases in $h_{o,R}$ from row 1 to 2 and from row 3 to 5 can be explained by a thickening liquid layer, but the reason for the increase in $h_{o,R}$ from row 2 to 3 is unknown. The “saw-tooth” effect observed by Michael et al. (1992), which was discussed in the previous chapter, may be occurring on this bundle. The data of Honda et al. (1992) for staggered bundles and the data of Honda et al. (1991) for in-line bundles show a similar saw-tooth row variation. No explanation is given, other than that the variation may be due to experimental uncertainty. CFC-113 was used in both Honda

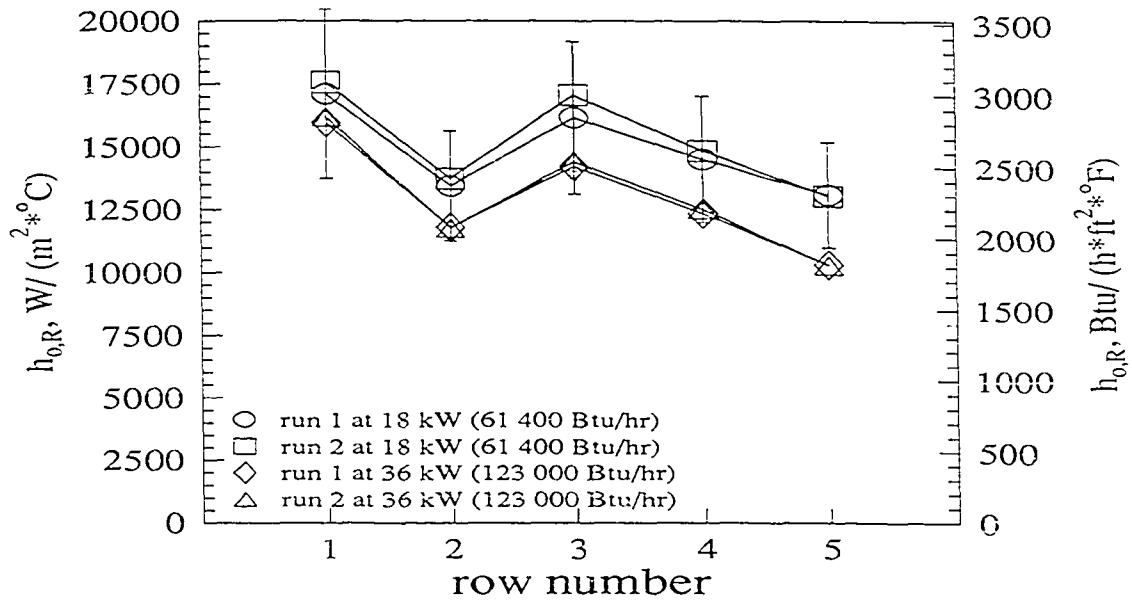


Figure 6.10: Average shell-side row heat transfer coefficient vs. row number for the condensation of HCFC-123 on the 40-fpi geometry

et al. (1992) and Honda et al. (1991).

Figure 6.10 shows the repeatability of $h_{o,R}$ for two different bundle loads. The repeatability of the experiment can be seen by comparing the data points for run 1 and run 2. This figure indicates that the data for $h_{o,R}$ can be repeated over the entire range of bundle loads tested, as the difference between the two runs is less than 6%. Uncertainty bars are also presented for one of the 18 kW (61 400 Btu/hr) runs to demonstrate the level of uncertainty in the row by row analysis. This figure also demonstrates the drop in $h_{o,R}$ with bundle load for rows 4 and 5.

Comparison to P-W and W-M correlations

Values of $h_{o,R}$ as predicted by the P-W and W-M correlations are plotted on Figure 6.6. The P-W correlation predicts a 22% drop in $h_{o,B}$ as the heat flux increases from 16 000 W/m²

(5100 Btu/(hr·ft²)) to 41 000 W/m² (13 000 Btu/(hr·ft²)). The measured values of $h_{o,B}$, which drop 17% over the same heat flux range, initially follow the W-M correlation for low heat fluxes, and the P-W correlation for high heat fluxes. As previously discussed, both correlations are extrapolated for the 40-fpi geometry. The W-M correlation predicts that $h_{o,B}$ is not affected by the amount of condensate draining from the tube, and is thus independent of heat flux.

Results for Tu-Cii Geometry

Average bundle heat transfer coefficient results

Figure 6.11 shows that the Tu-Cii average shell-side bundle heat transfer coefficient $h_{o,B}$ drops considerably with increasing heat flux. An increasing bundle heat flux corresponds to an increasing refrigerant mass flow rate. As the mass flow rate (and hence, heat flux) increases, the liquid layer on the tubes becomes larger, and the heat transfer resistance increases. The measured values of $h_{o,B}$ drop from 29 000 W/(m²·K) (5110 Btu/(hr·ft²·F)) at 16 000 W/m² (5100 Btu/(hr·ft²)) to 20 230 W/(m²·K) (3560 Btu/(hr·ft²·F)) at 41 000 W/m² (13 000 Btu/(hr·ft²)), which is a 30% decrease.

Visual observation of the Tu-Cii indicated that the condensate did not always drain vertically downward, but often ran axially along the tube. Thus, the positions of the draining condensate columns were not fixed. This axial movement of the condensate floods the tube area that would normally be available for condensation. This phenomenon was unique to the Tu-Cii. Even though the Tu-Cii performance drops significantly with heat flux, the Tu-Cii still has a higher $h_{o,B}$ over the entire heat flux range than the other geometries tested.

Figure 6.12 shows the variation of $h_{o,B}$ with the LMTD. Figure 6.13 shows the variation of $h_{o,B}$ with the condensation temperature difference, $T_{sat} - T_{s,o}$. The wall temperature is calculated, not directly measured. Since the same trends in $h_{o,B}$ are present in both figures,

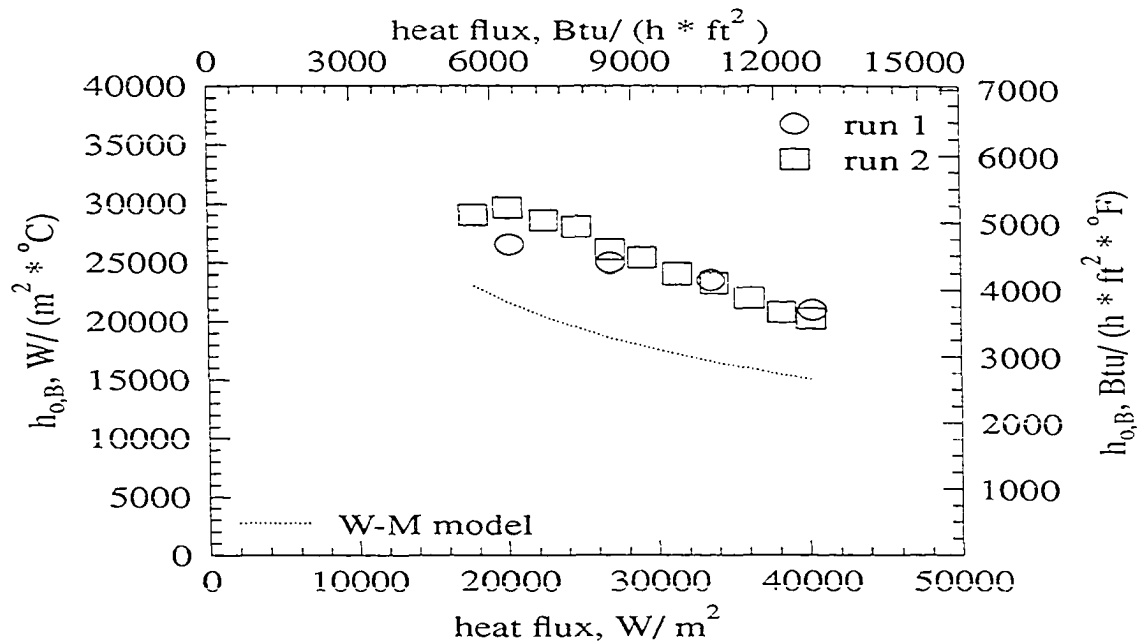


Figure 6.11: Average shell-side bundle heat transfer coefficient vs. heat flux for the condensation of HCFC-123 on the Tu-Cii geometry

the trend in $h_{o,B}$ is due to a shell-side phenomenon.

Uncertainty bars are also plotted on Figure 6.12, and show that the experimental uncertainty in $h_{o,B}$ ranges from $\pm 11\%$ to $\pm 34\%$. This figure indicates that $w_{h_{o,B}}$ decreases as the LMTD increases. As the LMTD increases, $T_{sat} - T_{w,out}$ and $T_{sat} - T_{w,in}$ increase, but the uncertainty in these temperature differences remains the same. Thus, the uncertainty in the temperature differences becomes less significant as the temperature differences increase. The calculation of $h_{o,B}$ is quite sensitive to these temperature differences (and hence, the LMTD), thus $w_{h_{o,B}}$ decreases as the uncertainty in these temperature differences becomes less significant.

The uncertainty is also sensitive to the imbalance between the water-side and shell-side resistances. At low heat fluxes, the water flow rate through the tube bundle is quite low, causing a large water-side heat transfer resistance. Also at low heat fluxes, the Tu-Cii performs very

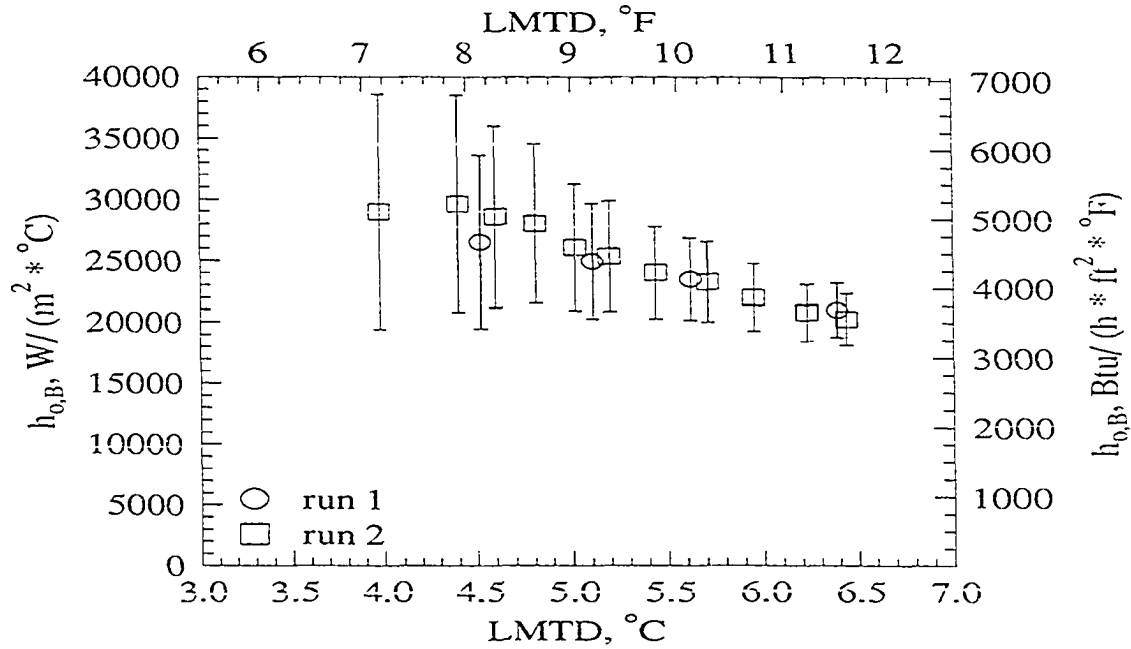


Figure 6.12: Average shell-side bundle heat transfer coefficient vs. LMTD for the condensation of HCFC-123 on the Tu-Cii geometry

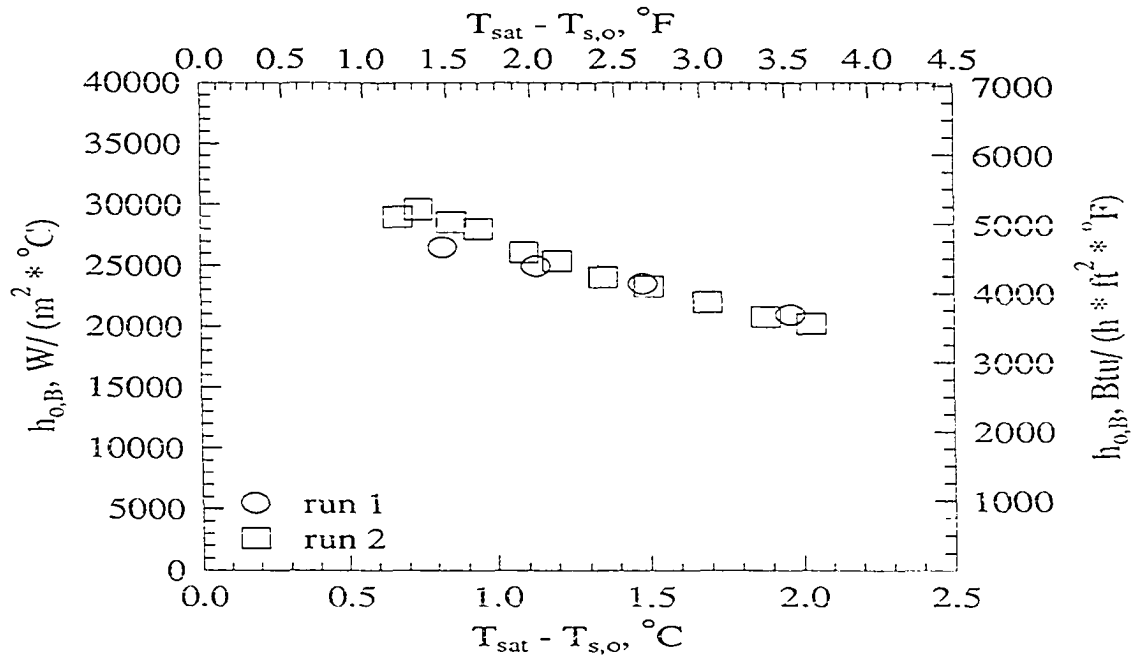


Figure 6.13: Average shell-side bundle heat transfer coefficient vs. condensation temperature difference for the condensation of HCFC-123 on the Tu-Cii geometry

well because of the small amount of condensate draining from the tubes, and the shell-side heat transfer resistance is relatively small.

Equation 4.14 is extremely sensitive to the imbalance between the water-side and shell-side resistances, and when the imbalance is large, the experimental uncertainty increases. During condensation on the Tu-Cii at a heat flux of $16\,000\text{ W/m}^2$ ($5100\text{ Btu/(hr}\cdot\text{ft}^2)$), the water-side resistance is approximately five times larger than the calculated shell-side resistance. Since the Tu-Cii has both a large resistance imbalance and a small LMTD at low heat fluxes, the uncertainty is quite high. Because the LMTD increases as heat flux increases and the water-side resistance decreases as heat flux increases, the uncertainty drops off rapidly with increasing heat flux. Although the imbalance between the shell-side and water-side resistances is not as severe as it is for HFC-134a condensation, the resistance imbalance is large enough to cause the HCFC-123 Tu-Cii uncertainties to be higher than those for the other three geometries.

The data for the repeatability run are plotted on Figures 6.11–6.13. The repeatability of the experiment can be seen by comparing the data points for run 1 and run 2. These figures indicate that the data for $h_{o,B}$ can be repeated over the entire range of bundle loads tested. The difference between the two runs is less than 4%, except for the $20\,000\text{ W/m}^2$ ($6350\text{ Btu/(hr}\cdot\text{ft}^2)$) point, where the difference between the two runs is 11%. The larger difference between run 1 and run 2 at this heat flux may be due to experimental uncertainty, which is 30% at this point.

Average row heat transfer coefficient results

Figure 6.14 shows the row behavior of the Tu-Cii for different bundle loads. This figure indicates that $h_{o,R}$ for all rows decreases with increasing bundle load, with the decrease being more pronounced for row 2. The decrease in $h_{o,R}$ with bundle load ranges from 13% for row 3 to 33% for row 2. The decrease in $h_{o,R}$ with bundle load for rows 1, 4, and 5 is 17%, 20%,

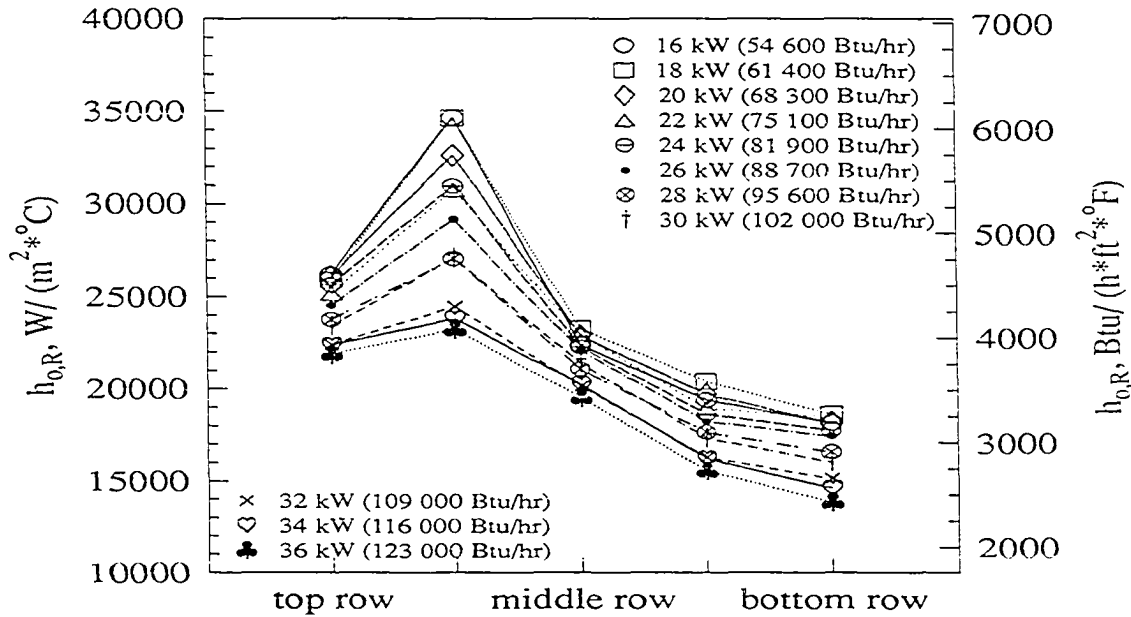


Figure 6.14: Average shell-side row heat transfer coefficient vs. row number for the condensation of HCFC-123 on the Tu-Cii geometry

and 24% respectively. As heat flux increases, the amount of condensate draining from the tubes increases. Thus, the decrease in $h_{o,R}$ with increasing bundle load (and hence heat flux) demonstrates that the Tu-Cii is significantly affected by the amount of condensate draining from the tube.

Figure 6.14 also shows the row-to-row behavior for the Tu-Cii geometry and indicates that $h_{o,R}$ increases from row 1 to 2, and then decreases from row 2 to 5. The magnitude of the increase in $h_{o,R}$ from row 1 to 2 is quite dependent on heat flux, and ranges from 6% at a bundle load of 36 kW (123 000 Btu/hr) to 32% at a bundle load of 16 kW (54 600 Btu/hr). The increase in $h_{o,R}$ from row 1 to 2 is most likely due to a vapor velocity effect. The vapor velocity at the top of row 2 is higher than the vapor velocity at the top of row 1 because of the restriction in flow area above row 2. At low bundle loads, the favorable heat transfer effect of vapor velocity combined with the favorable heat transfer effect of a small liquid layer cause

the significant jump in $h_{o,R}$. As bundle load increases, the effect of increasing liquid layer thickness begins to counteract the vapor velocity effect, and the magnitude of the increase in $h_{o,R}$ from row 1 to 2 decreases. Since HCFC-123 has a relatively high surface tension and liquid viscosity, both of which tend to prevent the condensate from draining, the unfavorable effect on heat transfer of an increasing liquid layer is compounded by the unfavorable effect on heat transfer of poor drainage.

The decrease in $h_{o,R}$ from row 2 to 5 is due to the effects of drainage from higher rows. The magnitude of the decrease in $h_{o,R}$ from row 2 to 5 is independent of bundle load and ranges from 38% at 32 kW (109 000 Btu/hr) to 48% at 16 kW (54 600 Btu/hr).

Figure 6.15 shows the repeatability of $h_{o,R}$ for two different bundle loads. The repeatability of the experiment can be seen by comparing the data points for run 1 and run 2. The difference between two runs is less than 1% at a bundle load of 36 kW (123 000 Btu/hr), but rises to 20% at a bundle load of 18 kW (61 400 Btu/hr). The disagreement between the two runs at 18 kW (61 400 Btu/hr) may be due to experimental error, as this is the only point where such a large disagreement exists. Uncertainty bars are also presented for the 18 kW (61 000 Btu/hr) run to demonstrate the level of uncertainty in the row by row at low heat fluxes.

Comparison of HCFC-123 and HFC-134a for the Tu-Cii geometry

Both the HFC-134a and HCFC-123 data for the Tu-Cii tube show a large drop in $h_{o,B}$ with increasing heat flux over the heat flux range tested. The drop in $h_{o,B}$ over the bundle heat flux range tested is 39% for HFC-134a, while the drop for HCFC-123 is 43%. Thus, both data sets indicate that the Tu-Cii is significantly affected by the amount of condensate draining from the tubes. The magnitude of the HFC-134a $h_{o,B}$ values are twice the HCFC-123 values. This is due to the surface tension and liquid viscosity of HCFC-123, which, as previously discussed, are less favorable to heat transfer than those for HFC-134a.

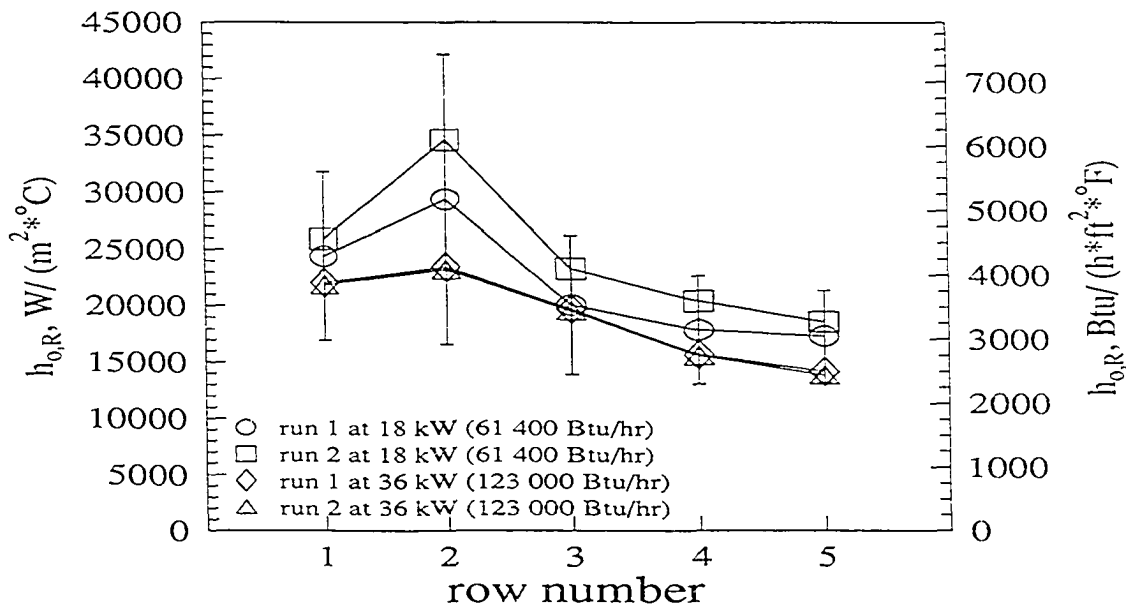


Figure 6.15: Average shell-side row heat transfer coefficient vs. row number for the condensation of HCFC-123 on the Tu-Cii geometry

The row-to-row trends found in the Tu-Cii HCFC-123 condensation data are somewhat different than those found in the HFC-134a condensation data. The HFC-134a data do not show the large increase in $h_{o,R}$ from row 1 to 2 at low heat fluxes that the HCFC-123 data do. The large increase in $h_{o,R}$ from row 1 to 2 for HCFC-123 was attributed to a vapor velocity effect. The vapor density of HFC-134a is five times larger than that of HCFC-123, therefore the vapor velocity of HCFC-123 is five times larger than that of HFC-134a. Because the vapor velocity is higher, vapor velocity effects may be more significant for HCFC-123.

The HFC-134a data show an increase in $h_{o,R}$ from row 4 to 5, while the HCFC-123 data show a drop in $h_{o,R}$ from row 4 to 5. The increase in $h_{o,R}$ found in the HFC-134a data was attributed to the fact that row 5 has its entire bottom surface exposed to the vapor in the bottom of the test section. The higher surface tension and liquid viscosity of HCFC-123 will cause more condensate retention on the tubes relative to HFC-134a. Thus, row 5 will have a

larger liquid layer during HCFC-123 condensation, and the larger liquid layer will reduce the amount of vapor that can condense on that row. For HCFC-123, the large liquid layer effect is stronger than the effect of additional exposed surface area, and $h_{o,R}$ does not increase from row 4 to 5.

The HFC-134a data show a 49% drop in $h_{o,R}$ for row 1 over the bundle load range tested, which is larger than the 17% drop shown for HCFC-123. As reported in the previous chapter, the Tu-Cii drains the HFC-134a extremely well at low bundle loads, but the performance drops rapidly as bundle load increases. Because of surface tension and liquid viscosity effects, the Tu-Cii does not drain HCFC-123 as well HFC-134a at low heat fluxes. Since the HCFC-123 $h_{o,R}$ for row 1 is low (relative to HFC-134a) to begin with, the decrease in $h_{o,R}$ for row 1 as bundle load increases is not as severe as that for HFC-134a.

Comparison to P-W and W-M correlations

Values of $h_{o,R}$ as predicted by the W-M correlation are plotted on Figure 6.11. The W-M correlation predicts that $h_{o,B}$ drops by 35% as the heat flux increases from 16 000 W/m² (5100 Btu/(hr·ft²)) to 41 000 W/m² (13 000 Btu/(hr·ft²)). The measured values of $h_{o,B}$ drop 43% over the same heat flux range, which agrees well with the drop in $h_{o,R}$ predicted by the correlation. Webb and Murawski (1991) state that the Tu-Cii geometry allows the condensate to spread axially along the tube, instead of draining the condensate. Webb and Murawski also report that the Tu-Cii was more affected by the amount of condensate draining from the tube than the 26-fpi and G-SC. The observations of Webb and Murawski (1991) are in good agreement with the present study.

The magnitude of the $h_{o,B}$ predicted by the W-M correlation for the Tu-Cii is approximately 20% lower than the measured values. The W-M correlation was developed using only one refrigerant, CFC-11, which has the poorest heat transfer performance of the 4 refrigerants

tested in this study. Therefore, it is not surprising that the W-M model does not properly predict the magnitude of $h_{o,B}$ for this tube.

As mentioned previously, no $D_{\epsilon q}$ was available for the Tu-Cii, so the P-W correlation is not plotted.

Results for G-SC Geometry

Average bundle heat transfer coefficient results

Figure 6.16 shows that the average shell-side bundle heat transfer coefficient ($h_{o,B}$) for the G-SC geometry drops from approximately 14 000 W/(m²·K) (2460 Btu/(hr·ft²·F)) to 12 520 W/(m²·K) (2200 Btu/(hr·ft²·F)) as the heat flux increases from 16 000 W/m² (5100 Btu/(hr·ft²)) to 41 000 W/m² (13 000 Btu/(hr·ft²)). An increasing bundle heat flux corresponds to an increasing refrigerant mass flow rate. As the mass flow (and hence, heat flux) increases, the liquid layer on the tubes becomes larger. The data indicate that the G-SC is only mildly affected by the amount of condensate draining from the tubes, as the measured $h_{o,B}$ drops only 11% over the heat flux range tested.

The G-SC only performs better than the 26-fpi tube. Visual observation of the condensation phenomenon indicated that there was significant liquid holdup in the Y-shaped fins of the G-SC. The flooding angle ϕ_f was observed to be nearly 90° at high bundle loads. The condensate, instead of draining, floods the condensation area, thus reducing the performance of the tube.

The data for the repeatability run are also plotted on Figure 6.16. The repeatability of the experiment can be seen by comparing the data points for run 1 and run 2. These figures indicate that the data for $h_{o,B}$ can be repeated over the entire range of bundle loads tested, as the difference between the two runs is less than 4%.

Figure 6.17 shows the variation of $h_{o,B}$ with LMTD, while Figure 6.18 shows the

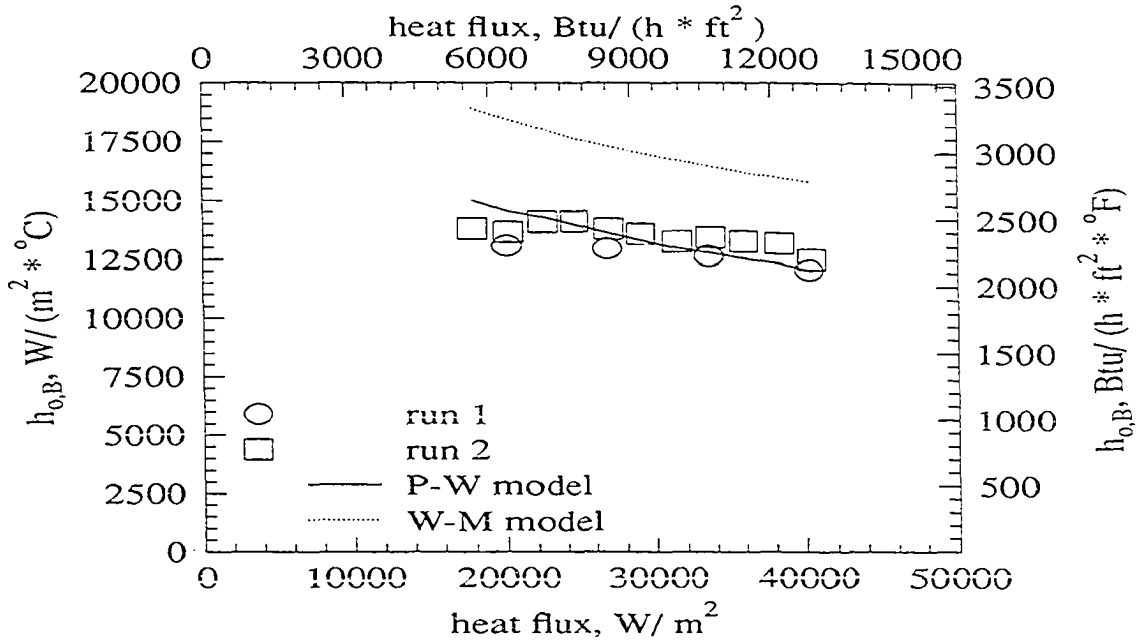


Figure 6.16: Average shell-side bundle heat transfer coefficient vs. heat flux for the condensation of HCFC-123 on the G-SC geometry

variation of $h_{o,B}$ with the condensation temperature difference, $T_{sat} - T_{s,o}$. The wall temperature is calculated, not directly measured. As the LMTD and $T_{sat} - T_{s,o}$ increase, more refrigerant is condensed. Thus, an increasing LMTD and $T_{sat} - T_{s,o}$ correspond to an increasing heat flux. Since the same trend in $h_{o,B}$ is present in both figures, the trend in $h_{o,B}$ is due to a shell-side phenomenon.

Uncertainty bars are also plotted on Figure 6.17. This figure indicates that $w_{h_{o,B}}$ decreases as the LMTD, and hence heat flux, increases. As the LMTD increases, $T_{sat} - T_{w,out}$ and $T_{sat} - T_{w,in}$ increase, but the uncertainty in these temperature differences remains the same. Therefore, the uncertainty in these temperature differences becomes less significant as the temperature differences increase. The calculation of $h_{o,B}$ is quite sensitive to these temperature differences, thus $w_{h_{o,B}}$ decreases as the uncertainty in these temperature differences becomes less significant. Since the smallest LMTD corresponds to the lowest

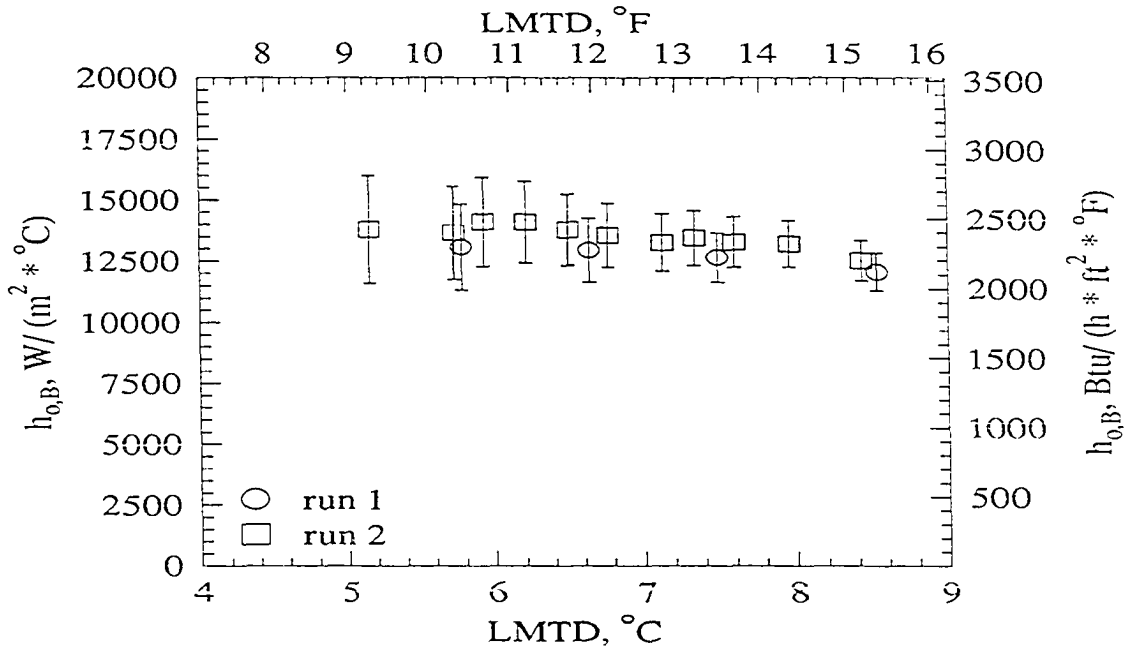


Figure 6.17: Average shell-side bundle heat transfer coefficient vs. LMTD for the condensation of HCFC-123 on the G-SC geometry

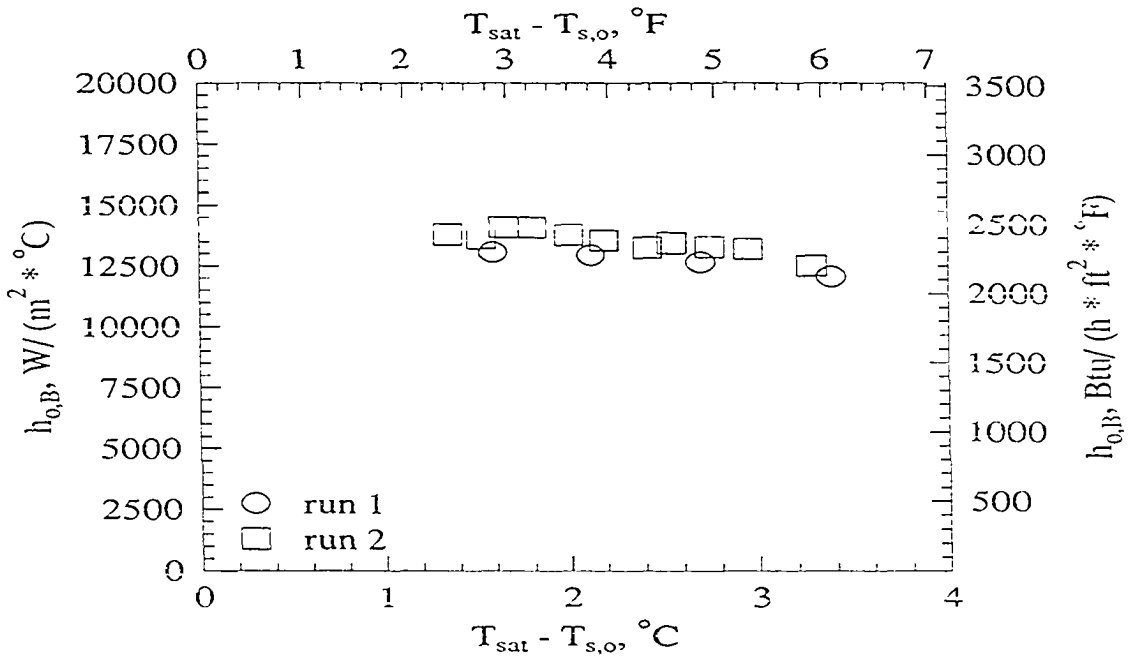


Figure 6.18: Average shell-side bundle heat transfer coefficient vs. condensation temperature difference for the condensation of HCFC-123 on the G-SC geometry

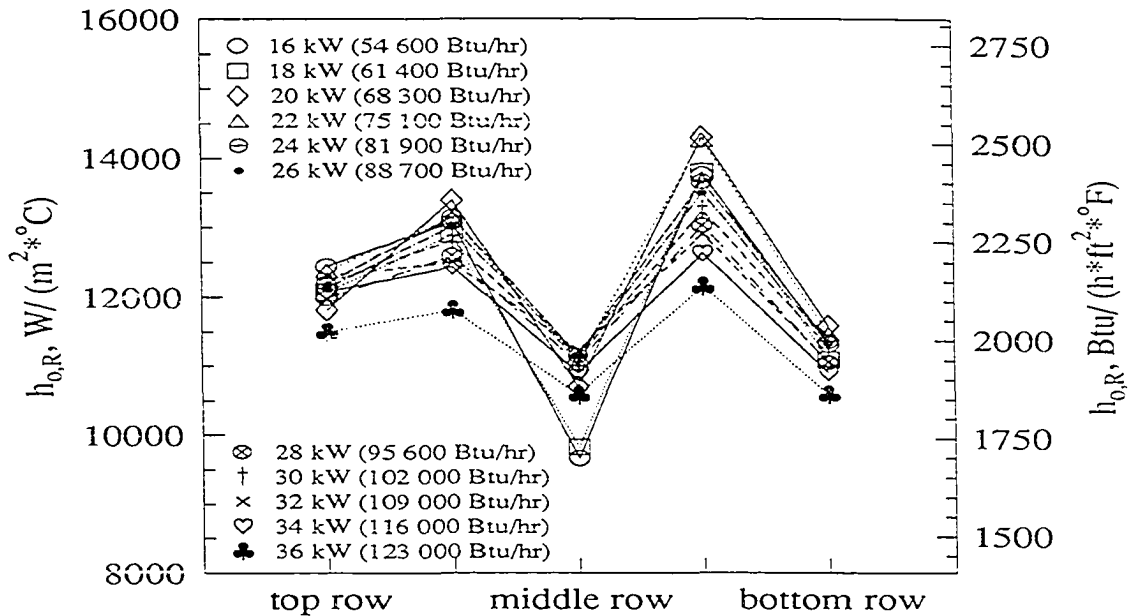


Figure 6.19: Average shell-side row heat transfer coefficient vs. row number for the condensation of HCFC-123 on the G-SC geometry

heat flux tested, the experimental uncertainty in $h_{o,B}$ ranges from $\pm 7\%$ at a heat flux of $16\,000\,W/m^2$ ($5100\,Btu/(hr \cdot ft^2)$) to $\pm 16\%$ at $41\,000\,W/m^2$ ($13\,000\,Btu/(hr \cdot ft^2)$). The data for the repeatability run are also plotted on Figures 6.17 and 6.18.

Average row heat transfer coefficients results

Figure 6.19 shows the row behavior of the G-SC geometry at different bundle loads. This figure indicates that $h_{o,R}$ for rows 1, 2, 4, and 5 generally decreases by about 10% as the bundle load increases from 16 kW ($54\,600\,Btu/hr$) to 36 kW ($123\,000\,Btu/hr$). For row 3, $h_{o,R}$ increases by about 10% over the same bundle load range. These trends indicate that the G-SC is not greatly affected by the amount of condensate draining from the tubes. Theoretically, $h_{o,R}$ should decrease as bundle load increases, because of the thickening condensate layer. The reason for the increase in $h_{o,R}$ with bundle load for row 3 is not known.

In general, Figure 6.19 shows that $h_{o,R}$ increases from row 1 to 2, decreases from row 2 to 3, increases from row 3 to 4, then decreases from row 4 to 5. The magnitude of the increase in $h_{o,R}$ from row 1 to 2 is approximately 5% for all bundle loads, except at a bundle load of 20 kW (68 300 Btu/hr), where the magnitude of the increase in $h_{o,R}$ from row 1 to 2 is 13%. The increase in $h_{o,R}$ from row 1 to 2 may be due to a vapor velocity effect. The vapor velocity at the top of row 2 is greater than the vapor velocity at the top of row 1 because of the flow area constriction above row 2. An increased vapor velocity tends to rip the condensate from the tube and expose more tube surface for condensation.

The magnitude of the decrease in $h_{o,R}$ from row 2 to 3 is dependent on bundle load, and ranges from 10% at a bundle load of 36 kW (123 000 Btu/hr) to 26% at a bundle load of 16 kW (54 600 Btu/hr). Row 3 is in the middle of the bundle and may be starved for vapor, thus causing the decrease in $h_{o,R}$ from row 2 to 3. The magnitude of the increase in $h_{o,R}$ from row 3 to 4 depends on bundle load, and ranges from 15% at a bundle load of 36 kW (123 000 Btu/hr) to 42% at a bundle load of 16 kW (54 600 Btu/hr). The behavior of $h_{o,R}$ for this row is quite peculiar, and the reason for the peak in $h_{o,R}$ at row 4 is unknown. The magnitude of the decrease in $h_{o,R}$ from row 4 to 5 depends on bundle load, and ranges from 13% at a bundle load of 36 kW (123 000 Btu/hr) to 18% at a bundle load of 16 kW (54 600 Btu/hr). A drop in $h_{o,R}$ from row 4 to 5 is expected, since row 5 is the most inundated row in the bundle.

Figure 6.20 shows the repeatability of the $h_{o,R}$ data for two different bundle loads. The repeatability of the experiment can be seen by comparing the data points for run 1 and run 2. This figure indicates that the data for $h_{o,R}$ can be repeated over the entire range of bundle loads tested, as the difference between the two runs is less than 5%. Uncertainty bars are also presented for one of the 18 kW (61 400 Btu/hr) runs to demonstrate the level of uncertainty on the row by row analysis.

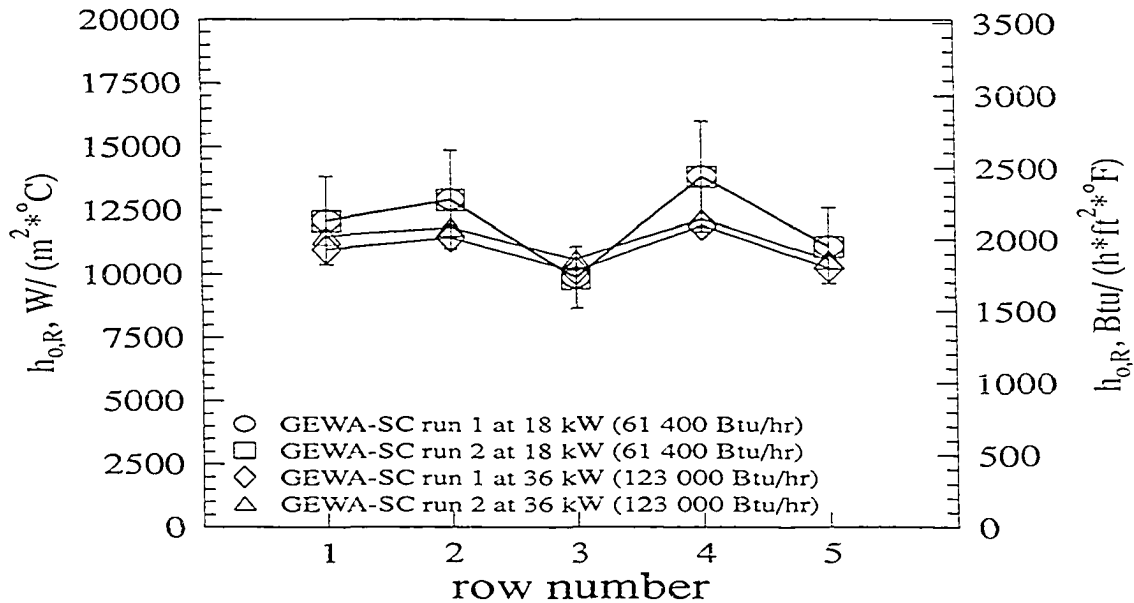


Figure 6.20: Average shell-side row heat transfer coefficient vs. row number for the condensation of HCFC-123 on the G-SC geometry

Comparison of HCFC-123 and HFC-134a for the G-SC geometry

Both the HFC-134a and HCFC-123 G-SC data show a small decrease in $h_{o,B}$ with increasing heat flux. The drop in $h_{o,B}$ over the bundle heat flux range tested is 9% for HFC-134a, while the drop for HCFC-123 is 11%. Thus, both data sets indicate that the G-SC is not greatly affected by the amount of condensate draining from the tubes. The HFC-134a $h_{o,B}$ values are 15% higher than the HCFC-123 values. This difference is due to the surface tension and liquid viscosity of HCFC-123, which, as previously discussed, are less favorable to heat transfer than those for HFC-134a.

The row-to-row trends found in the G-SC condensation data for HCFC-123 are somewhat different than those found in the HFC-134a condensation data. The HFC-134a data show a significant decrease in $h_{o,R}$ from row 1 to 2, while the HCFC-123 data show an increase in $h_{o,R}$ from row 1 to 2. The increase in $h_{o,R}$ from row 1 to 2 for HCFC-123 is attributed

to a vapor velocity effect. The vapor density of HFC-134a is five times larger than that of HCFC-123, therefore the vapor velocity of HCFC-123 is five times larger than that of HFC-134a. Because the vapor velocity is higher, vapor velocity effects may be more significant for HCFC-123. Since the vapor velocity of HFC-134a is relatively small, the liquid condensate is not ripped away, and $h_{o,R}$ drops from row 1 to 2 because of an increasing liquid layer. Both refrigerants show an increase from row 3 to 4 and a decrease from row 4 to 5.

Comparison to P-W and W-M correlations

Values of $h_{o,R}$ as predicted by the P-W and W-M correlations are plotted on Figure 6.16. The measured values of $h_{o,B}$, which drop approximately 11% as the heat flux increases from 16 000 W/m² (5100 Btu/(hr·ft²)) to 41 000 W/m² (13 000 Btu/(hr·ft²)), agree well with the P-W correlation, which predicts a 19% drop for the same heat flux range. The magnitude of $h_{o,B}$ predicted by the W-M correlation is about 30% higher than the data, which may be due to the fact the W-M correlation was developed using only CFC-11. The W-M correlation predicts a 17% drop in $h_{o,B}$ over the same heat flux range.

Comparison of HCFC-123 and CFC-11 Heat Transfer Coefficients

Comparison of average bundle heat transfer coefficients

Figures 6.21–6.24 compare the values of $h_{o,B}$ for HCFC-123 and CFC-11 for the 26-fpi, 40-fpi, Tu-Cii, and G-SC bundles respectively. For CFC-11 condensation on the 26-fpi, 40-fpi, and G-SC bundles, $h_{o,B}$ increases with increasing heat flux, which is a unique behavior. For the Tu-Cii bundle, $h_{o,B}$ increases with increasing heat flux up to 25 000 W/m² (7900 Btu/(hr·ft²)), then $h_{o,B}$ decreases with increasing heat flux through 41 000 W/m² (13 000 Btu/(hr·ft²)). As heat flux increases, so does the vapor velocity. The CFC-11 data suggest that the effect of vapor velocity, which is to rip away the condensate and increase

Table 6.1: Property comparison for HCFC-123, CFC-11, and CFC-113 at 35°C

property	HCFC-123	CFC-11	CFC-113
P_{sat} , kPa	130.600	147.700	64.990
v_f , m ³ /kg	6.9540E-04	6.8580E-04	6.4900E-04
v_g , m ³ /kg	1.2170E-01	1.1910E-01	2.0240E-01
ρ_f , kg/m ³	1438.00	1458.00	1541.00
ρ_g , kg/m ³	8.22	8.40	4.94
i_{fg} , kJ/kg	167.50	173.40	144.40
$C_{p,f}$, kJ/(kg·K)	1.032	0.903	0.893
$C_{p,g}$, kJ/(kg·K)	0.710	0.615	0.653
μ_f , $\mu\text{Pa}\cdot\text{s}$	386.30	367.60	579.80
μ_g , $\mu\text{Pa}\cdot\text{s}$	10.91	11.22	10.51
k_f , mW/(m·K)	75.81	84.03	68.43
k_g , mW/(m·K)	10.06	8.85	9.04
σ , mN/m	14.10	16.37	15.14

the heat transfer, is dominant for CFC-11. The thermophysical properties for HCFC-123 and CFC-11, which are shown in Table 6.1 are quite similar, except that the surface tension of CFC-11 is 14% higher than that of HCFC-123.

At 16 000 W/m² (5100 Btu/(hr·ft²)), the HCFC-123 $h_{o,B}$ values are approximately 30% larger than the CFC-11 values. However, at 41 000 W/m² (13 000 Btu/(hr·ft²)), the HCFC-123 $h_{o,B}$ values are approximately 10% larger than the CFC-11 values.

The data for the CFC-11 repeatability run are also plotted on Figures 6.21– 6.24. The repeatability of the experiment can be seen by comparing the data points for run 1 and run

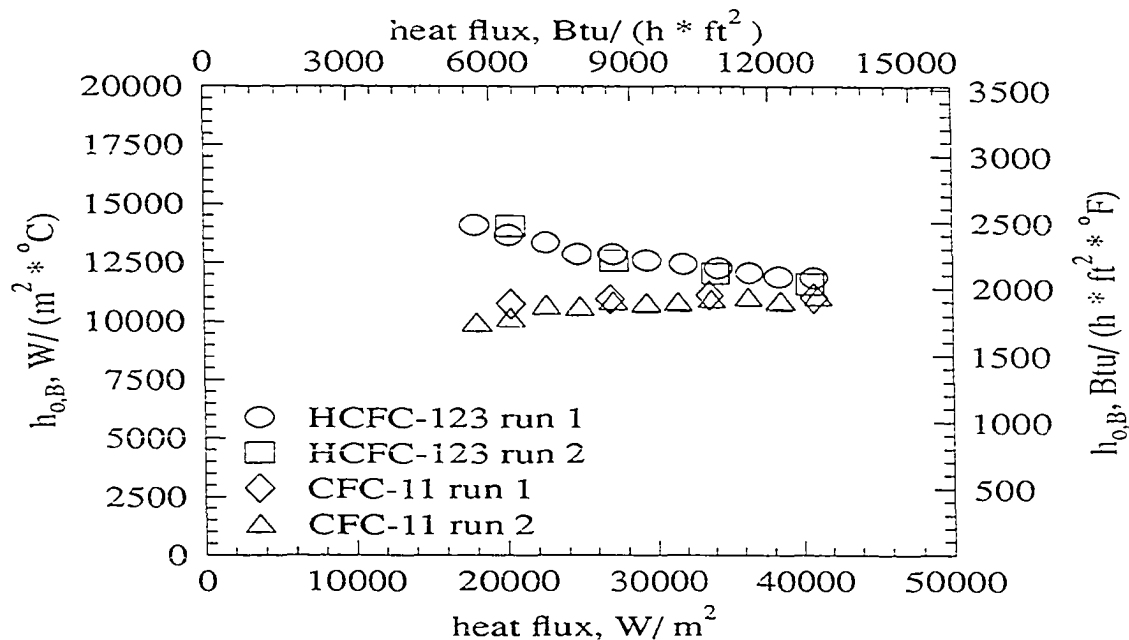


Figure 6.21: Comparison of the HCFC-123 and CFC-11 average shell-side bundle heat transfer coefficients for the 26-fpi geometry

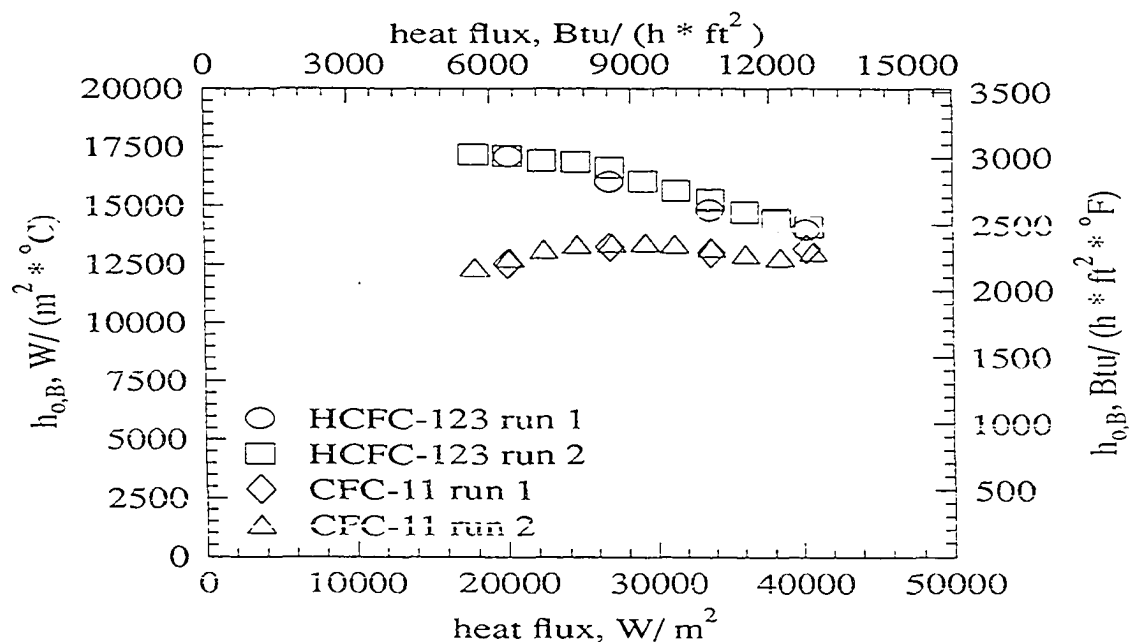


Figure 6.22: Comparison of the HCFC-123 and CFC-11 average shell-side bundle heat transfer coefficients for the 40-fpi geometry

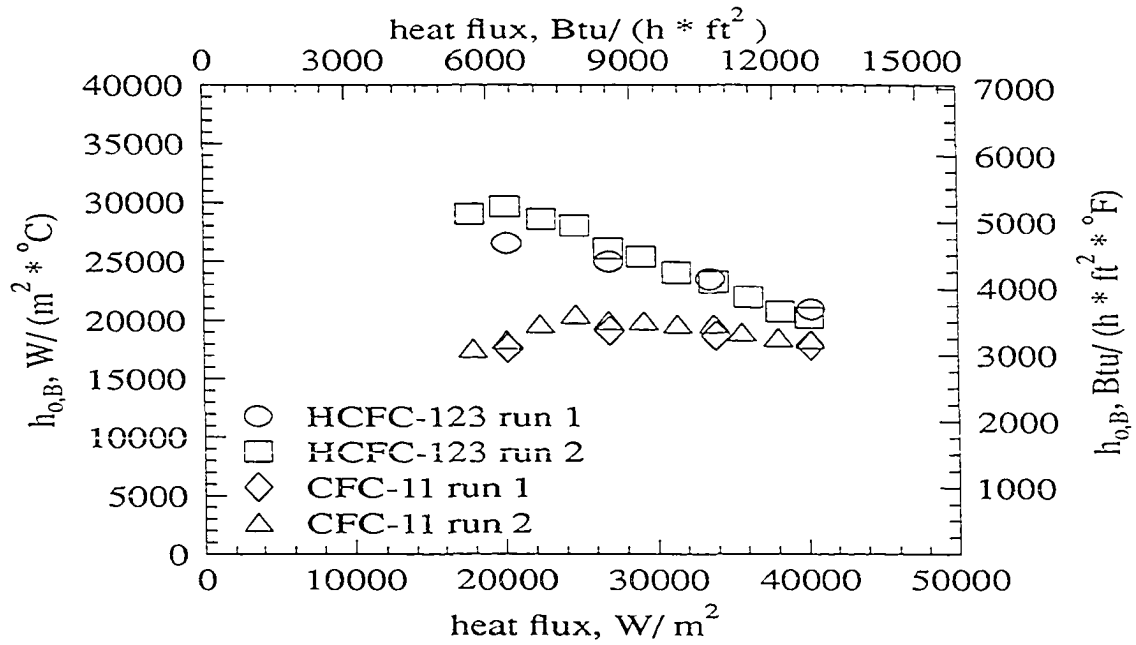


Figure 6.23: Comparison of the HCFC-123 and CFC-11 average shell-side bundle heat transfer coefficients for the Tu-Cii geometry

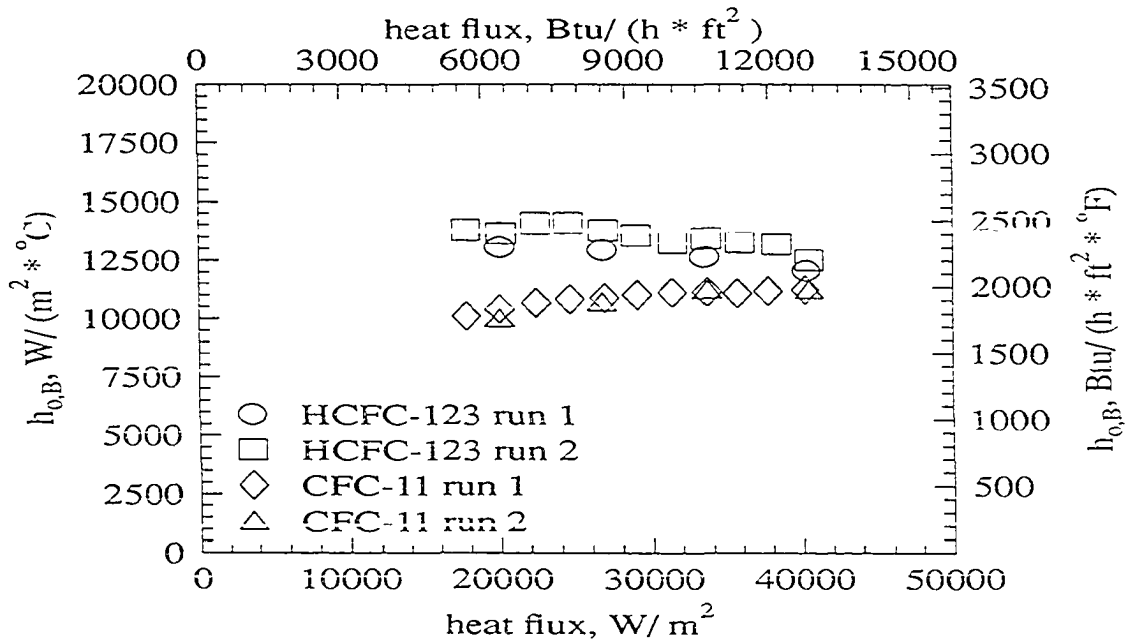


Figure 6.24: Comparison of the HCFC-123 and CFC-11 average shell-side bundle heat transfer coefficients for the G-SC geometry

2. These figures indicate that the data for the average bundle heat transfer coefficients can be repeated over the entire range of bundle loads tested. The difference between the two CFC-11 runs for all geometries is generally less than 5%. Generally, the uncertainty in the CFC-11 average bundle heat transfer coefficients ranges from $\pm 6\%$ to $\pm 20\%$ for all geometries.

Comparison of average row heat transfer coefficients

Figures 6.25–6.28 compare the HCFC-123 and CFC-11 $h_{o,R}$ behavior for the 26-fpi, 40-fpi, Tu-Cii, and G-SC bundles, respectively. These figures indicate that for a given tube geometry, the row-to-row behavior is essentially the same for both refrigerants, although the row-to-row behavior differs significantly between the four tube geometries.

The data for the CFC-11 repeatability run are also plotted on Figures 6.25–6.28. The repeatability of the experiment can be seen by comparing the data points for run 1 and run 2. These figures indicate that the CFC-11 data for the row heat transfer coefficients can be repeated over the entire range of bundle loads tested. The uncertainty in the CFC-11 average row heat transfer coefficients ranges from $\pm 7\%$ to $\pm 22\%$ for all geometries.

Comparison of Bundle Geometries

Figure 6.29 compares the HCFC-123 $h_{o,B}$ for the different tube geometries. At $16\,000\text{ W/m}^2$ ($5100\text{ Btu}/(\text{hr}\cdot\text{ft}^2)$) the values of $h_{o,B}$ for the Tu-Cii are 70% higher than the values of $h_{o,B}$ for the 40-fpi. At $41\,000\text{ W/m}^2$ ($13\,000\text{ Btu}/(\text{hr}\cdot\text{ft}^2)$) the values of $h_{o,B}$ for the Tu-Cii are 43% larger than the values of $h_{o,B}$ for the 40-fpi. The low fin 40-fpi performs better than the longer finned G-SC, as the values of $h_{o,B}$ for the 40-fpi are 25% higher than the values of $h_{o,B}$ for the G-SC at $16\,000\text{ W/m}^2$ ($5100\text{ Btu}/(\text{hr}\cdot\text{ft}^2)$), and 13% higher at $41\,000\text{ W/m}^2$ ($13\,000\text{ Btu}/(\text{hr}\cdot\text{ft}^2)$). The 26-fpi is the worst performer, as its values of $h_{o,B}$ are approximately 5% lower than those of the G-SC across the heat flux range tested.

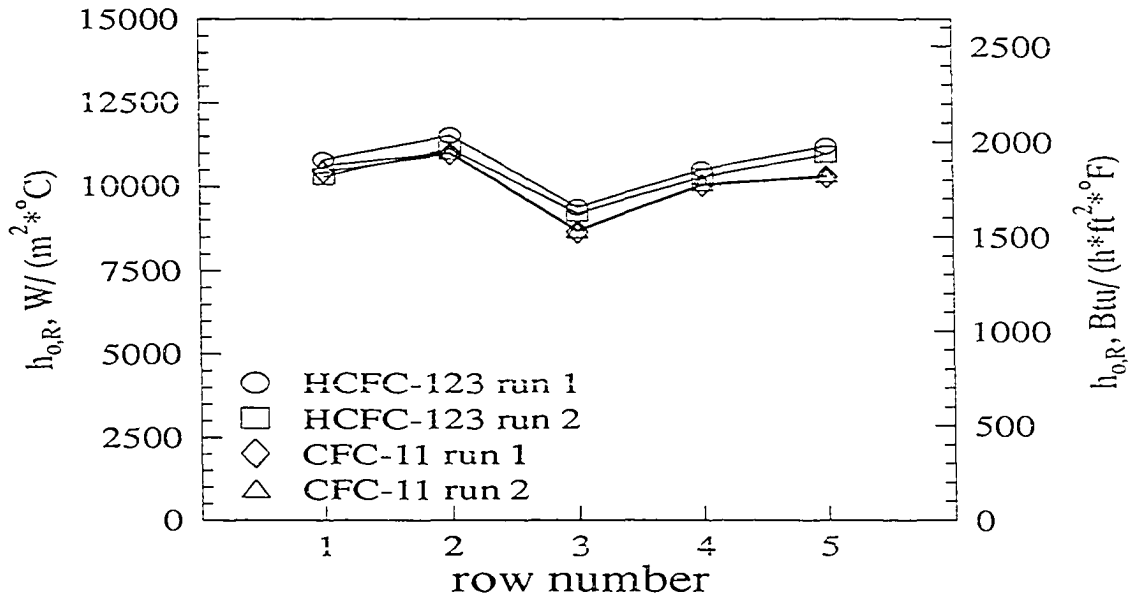


Figure 6.25: Comparison of the HCFC-123 and CFC-11 average shell-side row heat transfer coefficients for the 26-fpi geometry at a bundle load of 36 kW (123 000 Btu/hr)

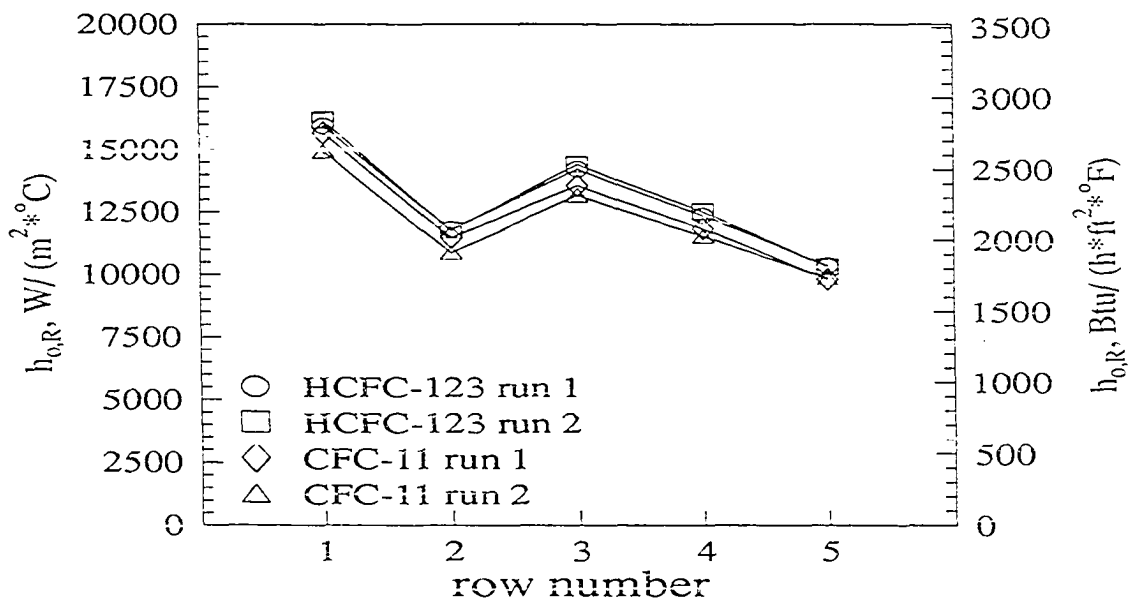


Figure 6.26: Comparison of the HCFC-123 and CFC-11 average shell-side row heat transfer coefficients for the 40-fpi geometry at a bundle load of 36 kW (123 000 Btu/hr)

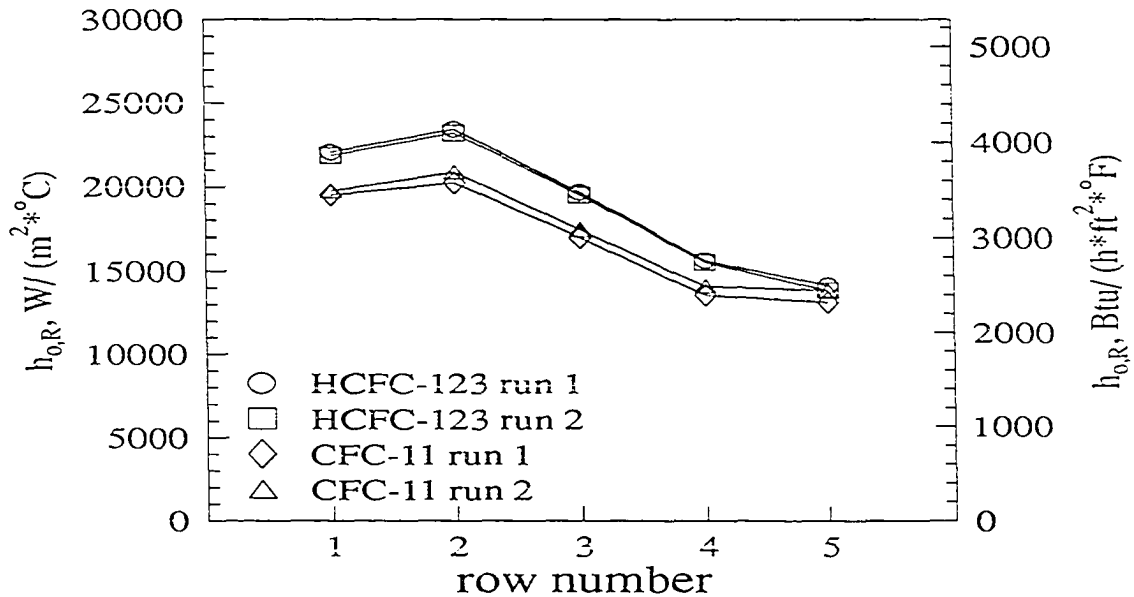


Figure 6.27: Comparison of the HCFC-123 and CFC-11 average shell-side row heat transfer coefficients for the Tu-Cii geometry at a bundle load of 36 kW (123 000 Btu/hr)

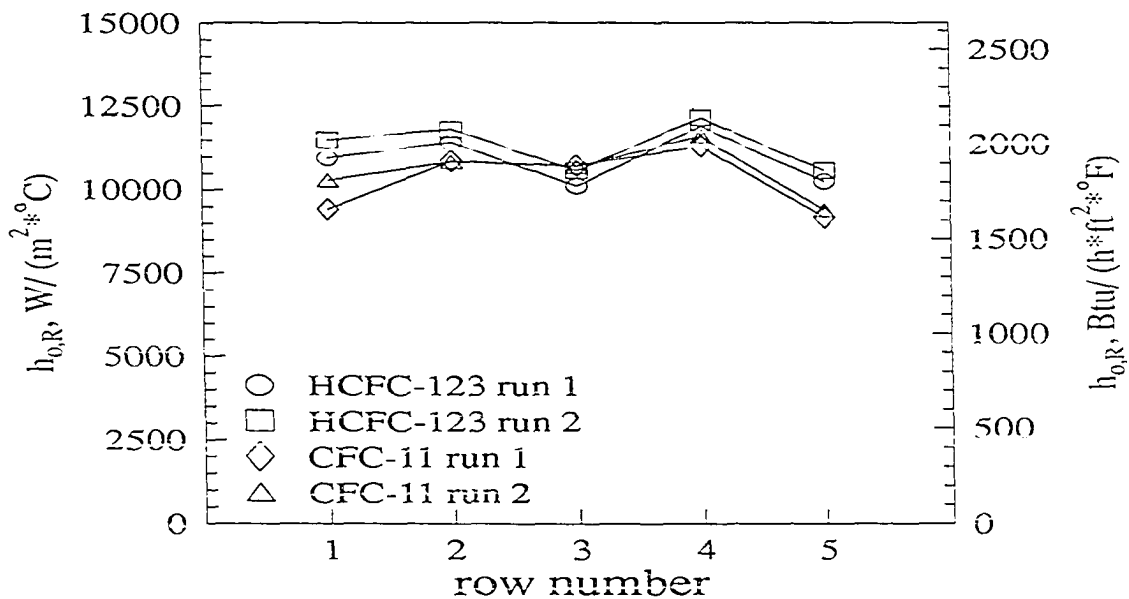


Figure 6.28: Comparison of the HCFC-123 and CFC-11 average shell-side row heat transfer coefficients for the G-SC geometry at a bundle load of 36 kW (123 000 Btu/hr)

The Murata et al. (1990) single tube data show that the 1181-fpm (30-fpi) $h_{o,B}$ values are approximately 14% higher than those for the 1024-fpm (26-fpi). However, the Murata data indicate that the 1181-fpm (30-fpi) is more affected by condensate inundation than is the 1024-fpm (26-fpi). Both the present data and the Murata data indicate that $h_{o,B}$ increases with increasing fin pitch.

Figure 6.30 compares the CFC-11 $h_{o,B}$ for the different tube geometries, and shows that the values of $h_{o,B}$ for the Tu-Cii are approximately 45% larger than the values of $h_{o,B}$ for the 40-fpi across the entire heat flux range. For CFC-11, the low fin 40-fpi also performs better than the longer finned G-SC, as the values of $h_{o,B}$ for the 40-fpi are 22% higher than the G-SC values at 16 000 W/m² (5100 Btu/(hr·ft²)), and 15% higher at 41 000 W/m² (13 000 Btu/(hr·ft²)). The values of $h_{o,B}$ for the 26-fpi are nearly identical to the values of the G-SC.

The Tu-Cii has been optimized for the condensation of organic fluids, so the fact that it is the best performer is not surprising. Even though the short-fin 40-fpi has 7% less surface area per unit length than the 26-fpi, the 40-fpi still out-performs the 26-fpi. The fin spacing of the 40-fpi is 0.457 mm (0.018 in), while the fin spacing of the 26-fpi is 0.672 mm (0.0265 in). The optimum fin spacing for CFC-12 as predicted by Honda et al. (1989) is 0.3 mm (0.0118 in). Since the 40-fpi is closer to the optimum fin spacing than the 26-fpi, the 40-fpi should perform better. Since the G-SC is essentially a 26-fpi with modified fins and has only a 3.5% increase in surface area per unit length over the 26-fpi, the G-SC performance should be similar to the 26-fpi.

Summary

1. For HCFC-123, increasing the heat flux causes the average bundle shell-side heat transfer coefficient to drop for all four tube geometries.

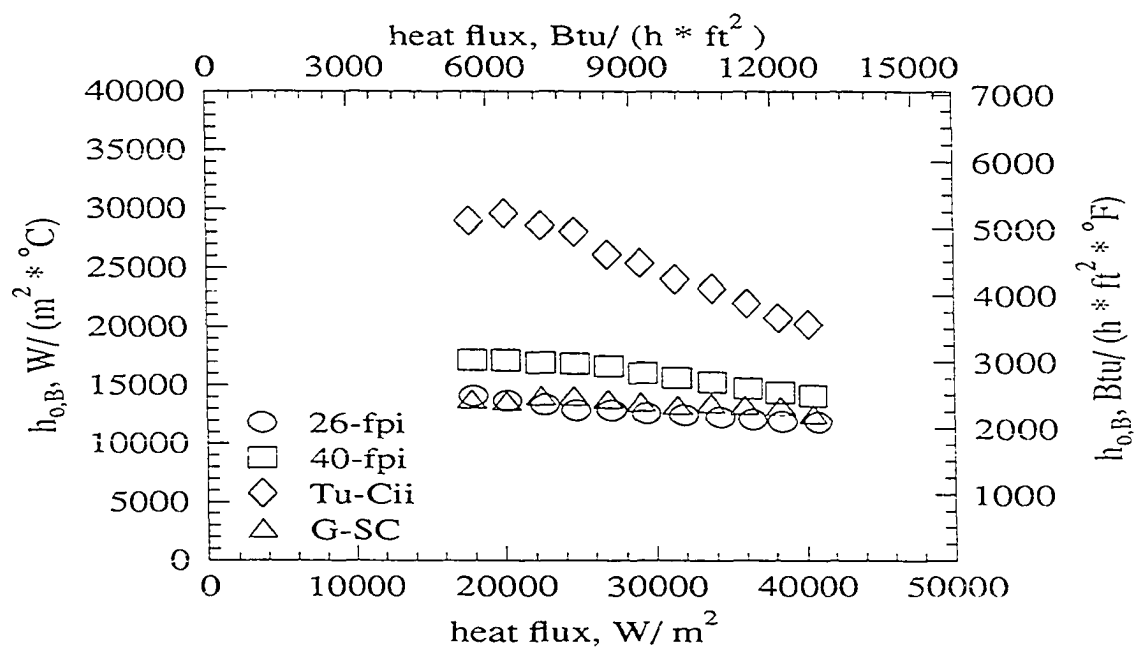


Figure 6.29: Comparison of the HCFC-123 average shell-side bundle heat transfer coefficients for the four tube geometries

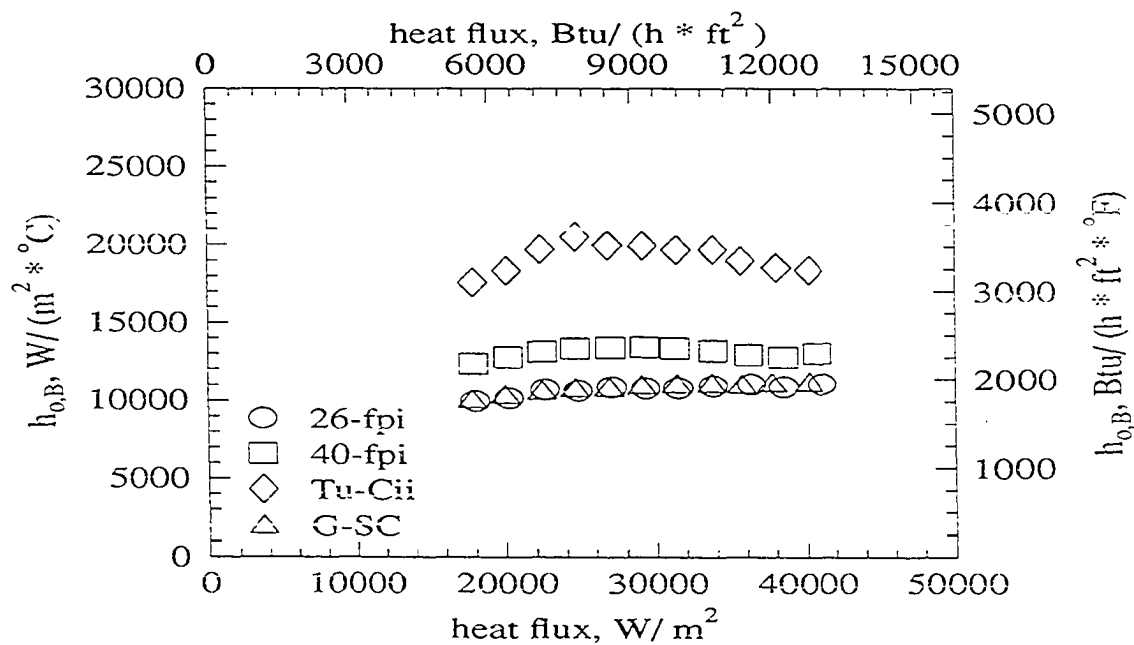


Figure 6.30: Comparison of the CFC-11 average shell-side bundle heat transfer coefficients for the four tube geometries

2. For CFC-11, increasing the heat flux causes the average shell-side bundle heat transfer coefficient to increase for all four geometries.
3. For HCFC-123, the Tu-Cii is the best performing geometry, followed by the 40-fpi, G-SC, and finally the 26-fpi geometry.
4. For CFC-11, the Tu-Cii is the best performing geometry, followed by the 40-fpi, and finally the G-SC and 26-fpi. The G-SC and 26-fpi perform similarly for CFC-11 condensation.
5. Of the four tube geometries tested, the average shell-side heat transfer coefficient of Tu-Cii is most affected by the amount of condensate draining from the tube.
6. The row-to-row average shell-side heat transfer coefficient behavior differs significantly between the four geometries.
7. For a given tube geometry, the row-to-row average shell-side heat transfer coefficient behavior is the same for both HCFC-123 and CFC-11.
8. For all four tube geometries, the HCFC-123 average shell-side heat transfer coefficients are higher than those for CFC-11.

CHAPTER 7. DESIGN CORRELATIONS FOR HFC-134a AND HCFC-123

Although the shell-side heat transfer coefficient data presented in the previous chapters can be used in the graphical and tabular formats, the data can be more conveniently used by designers if the data are correlated with an appropriate equation. Several shell-side condensation correlations have been previously discussed in Chapter 2. In this chapter, a semi-empirical correlation is presented for the HFC-134a and HCFC-123 average shell-side bundle heat transfer coefficients presented in the previous two chapters. The correlation is also applicable to CFC-12. The next section will discuss the form of the correlation used to fit the experimental data.

Form of the Correlation Used to Fit the Experimental Data

The Beatty and Katz (1948), Pearson and Withers (1969), and Webb and Murawski (1990) correlations discussed in Chapter 2 are examples of *semi-empirical* correlations. Because of the complexities of the condensation phenomenon, the governing equations cannot be completely solved. One method of obtaining a correlation is to incorporate the relevant physical parameters and several adjustable constants into an equation, and use experimental data to determine the value of the adjustable constants. A correlation developed in this manner is known as a semi-empirical correlation.

For laminar condensation on a tube with negligible vapor velocities, the relevant physical parameters are:

1. tube load or heat flux, which indicates the thickness of the liquid layer on the tube;
2. thermal conductivity of the condensate, which determines how well energy is transferred through the condensate;
3. surface tension of the condensate, which is responsible for thinning of the liquid layer as well as liquid retention in the tubes;
4. viscosity of the condensate, which is responsible for shear stresses that retard the downward flow of the condensate;
5. liquid and vapor density of the refrigerant, which determine the body force on the condensate due to gravity.

As discussed in Chapter 2, Webb and Murawski (1990) were successful in correlating the row condensation heat transfer coefficient as a function of the condensate Reynolds number only. The condensate Reynolds number is the ratio of the condensate mass flow rate to the condensate viscosity, and thus includes the effects of condensate thickness and the shear stress in the condensate layer. This simple correlation worked well for Webb and Murawski because they used only one refrigerant (CFC-11) at one saturation temperature. Since thermal conductivity, surface tension, viscosity, and density all vary with temperature and refrigerant, the Webb-Murawski data cannot show the dependence of heat transfer on these parameters. Because the present study involves several refrigerants (and hence, variable fluid properties), the Webb-Murawski correlation is not sophisticated enough to fit the present data.

The Webb-Murawski correlation does present a good starting point, however. The condensate Reynolds number includes the condensate mass flow rate, which is an indicator of the heat flux, as well as the viscosity of the liquid condensate. Surface tension and density can be expressed dimensionlessly by using the Bond number (Bo), which is the ratio of buoyancy forces to surface tension forces. The conductivity of the condensate layer can be expressed

dimensionlessly by using the Prandtl number (Pr), which is the ratio of momentum diffusion to thermal diffusion in the condensate layer. Finally, the problem can be completely non-dimensionalized by introducing the Nusselt number, which is the dimensionless expression of the shell-side heat transfer coefficient.

The Nusselt number is assumed to take the following form:

$$\underbrace{\frac{h_{o,B} D_o}{k_f}}_{\text{Nu}} = a \underbrace{\left[\frac{4\dot{m}_r}{\mu_f L N_c} \right]^b}_{\text{Re}} \underbrace{\left[\frac{g(\rho_f - \rho_g)L^2}{\sigma} \right]^c}_{\text{Bo}} \underbrace{\left[\frac{C_{p,f} \mu_f}{k_f} \right]^d}_{\text{Pr}} \quad (7.1)$$

Taking logarithms of both side yields:

$$\ln \text{Nu} = \ln a + b \ln \text{Re} + c \ln \text{Bo} + d \ln \text{Pr} \quad (7.2)$$

The constants a , b , c , and d in Equation 7.2 can be determined by fitting the experimental data using conventional multiple linear regression techniques.

For the Reynolds number used in the above equations, \dot{m}_r is the mass flow rate of the refrigerant entering the condenser, L is the length of the tube bundle, and N_c is the number of columns in the bundle. Thus, the flow rate used in this correlation represents the mass flow rate draining from one column of tubes. Since the average shell-side bundle heat transfer coefficients presented in the previous two chapters are based on the nominal outer surface area of the tube, the heat transfer coefficients predicted by Equation 7.1 will be based on the nominal tube outer surface area as well.

Comparison of Correlation to Experimental Data

Since the geometry for each of the four tube types tested is different, it is reasonable to expect that the physical parameters described above may interact differently for each geometry. Therefore, a set of constants was calculated for each of the four tube geometries. These constants are listed in Table 7.1. Only the HFC-134a, HCFC-123, and CFC-12 data

Table 7.1: Constants for Equation 7.1

geometry	a	b	c	d
26-fpi	6.369×10^3	-0.200	0.100	-0.445
40-fpi	1.387×10^4	-0.179	0.043	-0.417
Tu-Cii	4.530×10^{-1}	-0.472	1.114	-1.081
G-SC	1.914×10^3	-0.116	0.159	-0.460

were used in determining the correlation constants. As discussed in the previous chapter, CFC-11 condensation is significantly affected by vapor shear. Since the correlation proposed above does not account for vapor shear effects, the CFC-11 data were not used during the calculation of the correlation constants.

The constants a , b , c , and d are unique for a given tube geometry. Thus, a set of constants a , b , c , and d are applicable to only one tube geometry, and a unique set of constants must be determined for each tube geometry that the correlation is to be used with. Once a set of constants has been determined for a particular tube geometry, the correlation can be used for a variety of different refrigerants.

Figures 7.1– 7.4 show the actual and predicted values of the average shell-side bundle heat transfer coefficient ($h_{o,B}$) for the four tube geometries tested in this study. These figures indicate that the correlation generally does quite well at predicting the trend in the average shell-side bundle heat transfer coefficients.

Figures 7.5– 7.8 show the difference between the actual and predicted values of $h_{o,B}$. For the 26-fpi geometry, the predicted values of $h_{o,B}$ are within 2% of the actual values across the entire heat flux range tested. For the 40-fpi geometry, the predicted values of $h_{o,B}$ are within 6% of the actual values across the heat flux range tested. For the Tu-Cii geometry, the predicted values of $h_{o,B}$ are within 10% of the actual values, except at 16 000 W/m² (5100 Btu/(hr·ft²)), where the difference is 20%. For the G-SC, the predicted values of $h_{o,B}$ are within 5% of the actual values across the entire heat flux range.

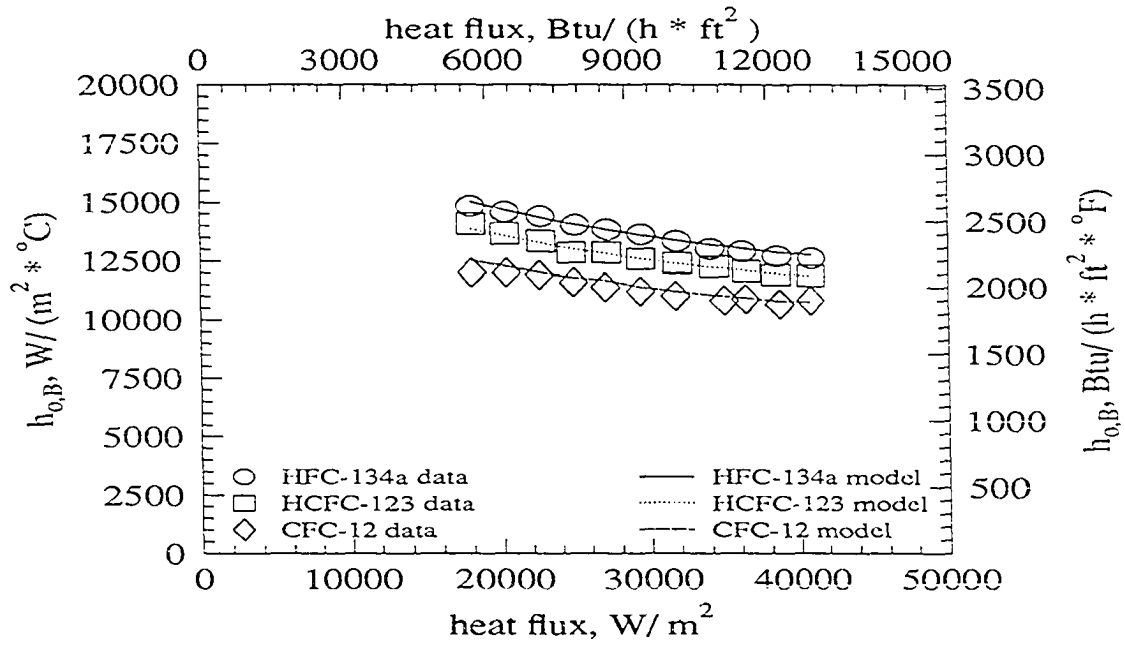


Figure 7.1: Actual and predicted average shell-side bundle heat transfer coefficients for the 26-fpi geometry

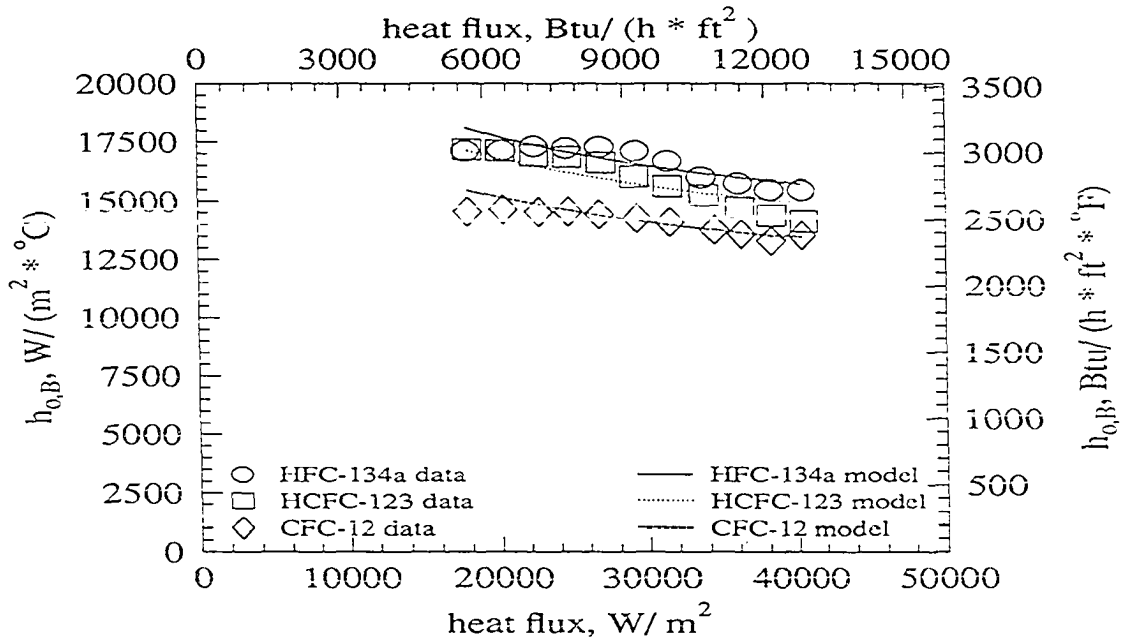


Figure 7.2: Actual and predicted average shell-side bundle heat transfer coefficients for the 40-fpi geometry

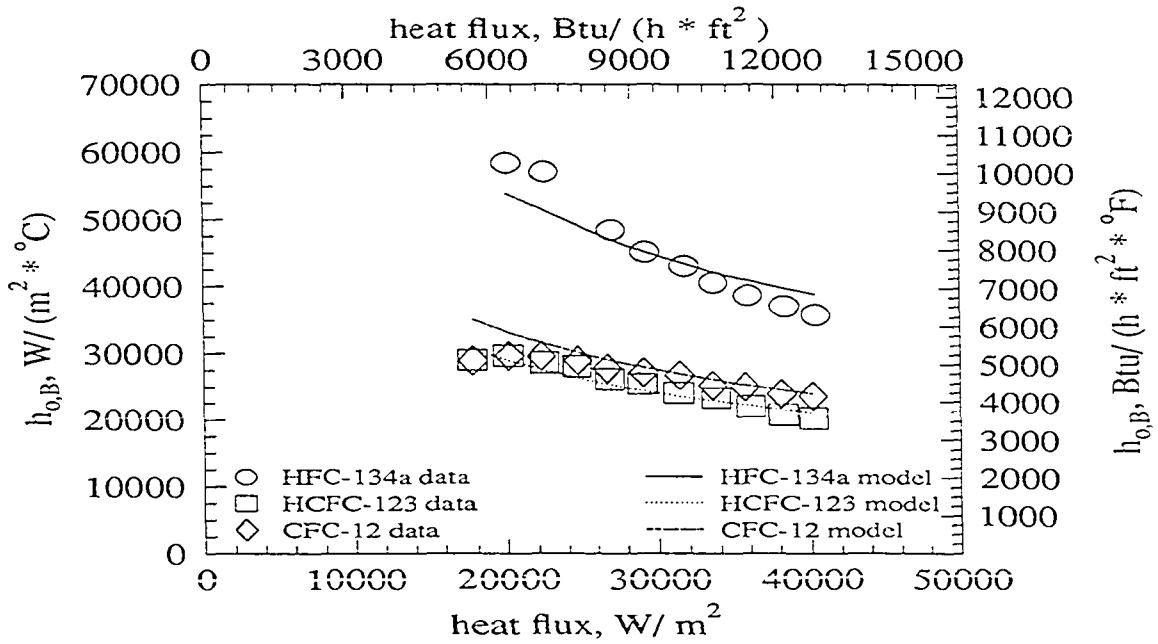


Figure 7.3: Actual and predicted average shell-side bundle heat transfer coefficients for the Tu-Cii geometry

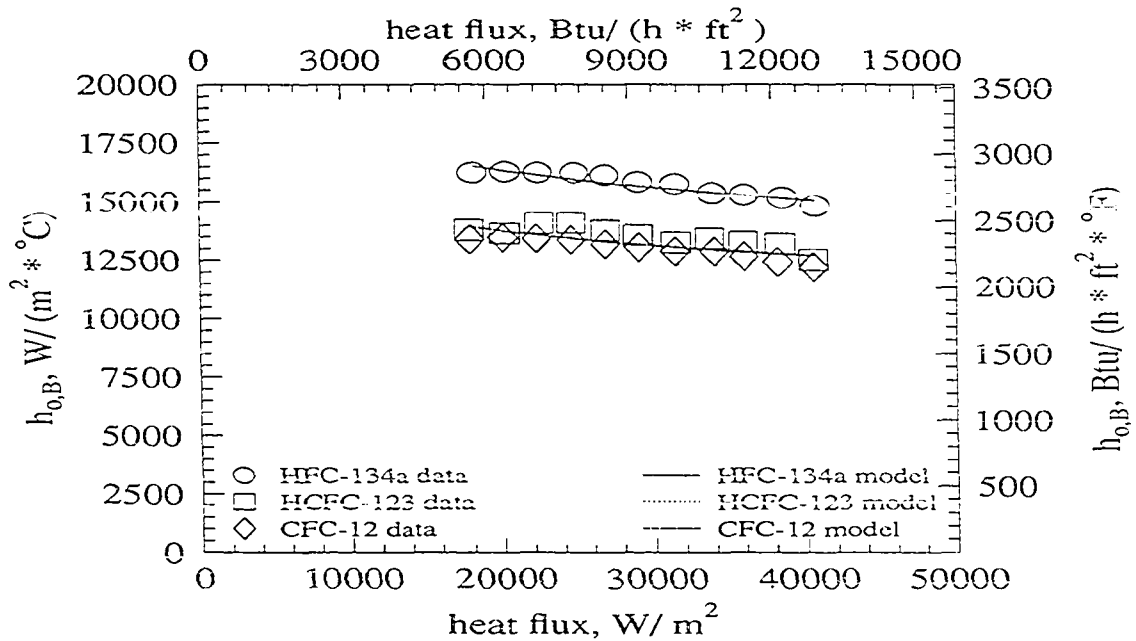


Figure 7.4: Actual and predicted average shell-side bundle heat transfer coefficients for the G-SC geometry

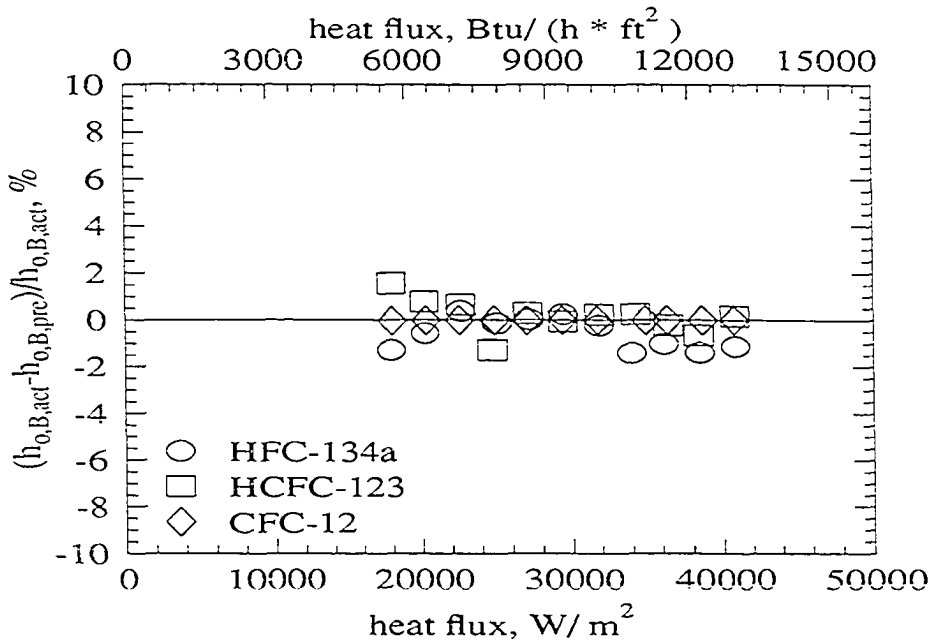


Figure 7.5: Difference between the actual and predicted average shell-side bundle heat transfer coefficients for the 26-fpi geometry

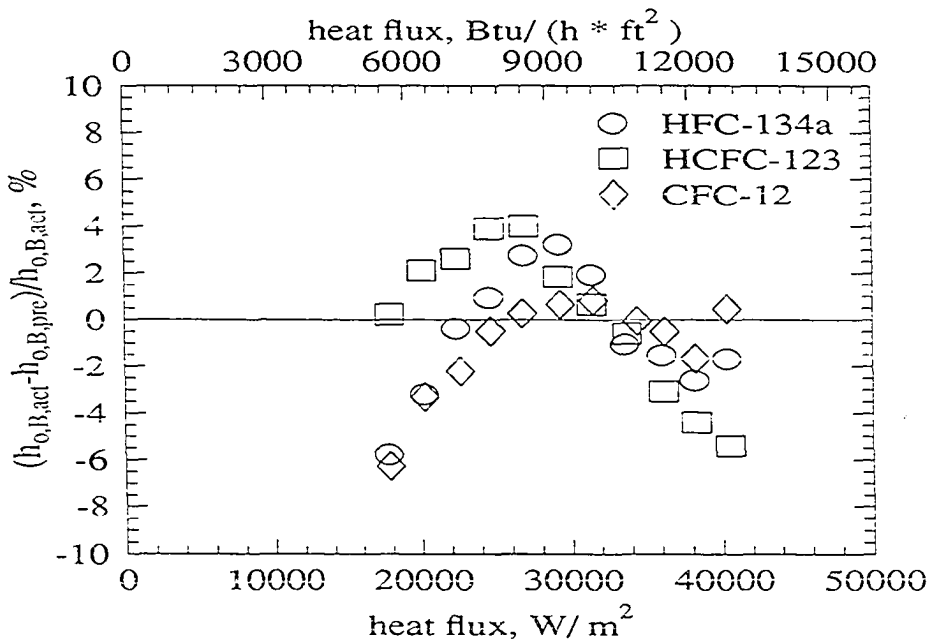


Figure 7.6: Difference between the actual and predicted average shell-side bundle heat transfer coefficients for the 40-fpi geometry

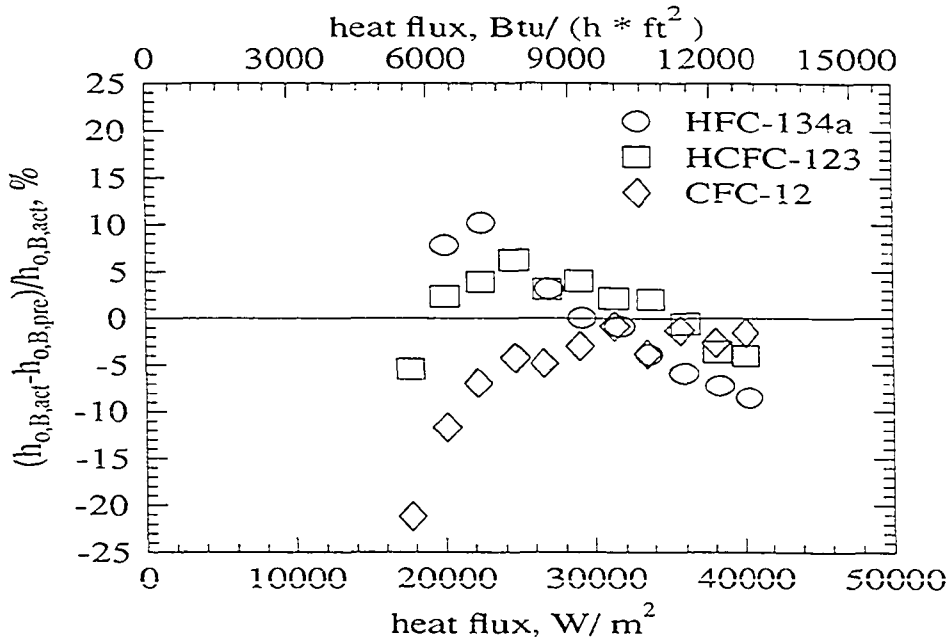


Figure 7.7: Difference between the actual and predicted average shell-side bundle heat transfer coefficients for the Tu-Cii geometry

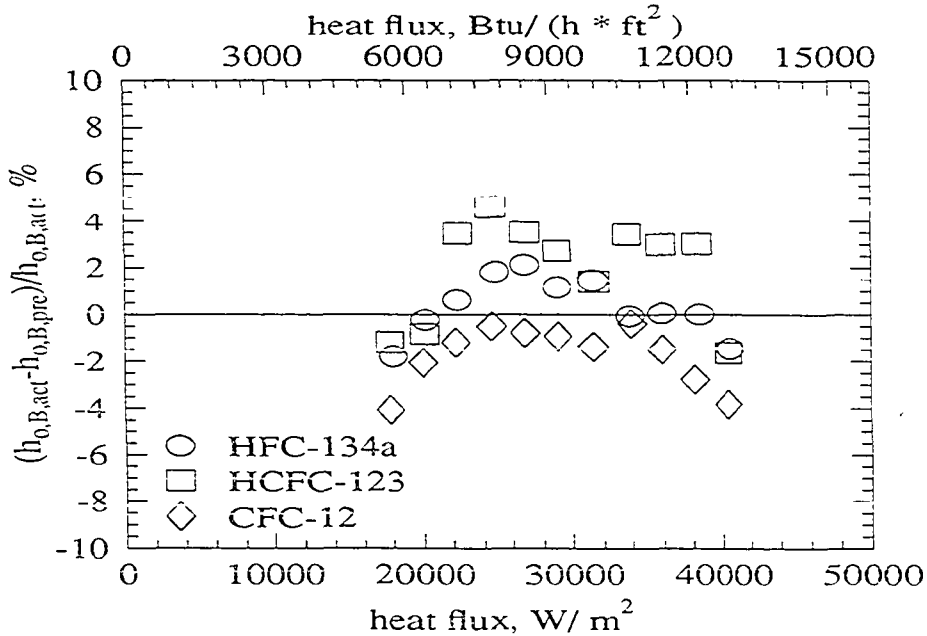


Figure 7.8: Difference between the actual and predicted average shell-side bundle heat transfer coefficients for the G-SC geometry

Limitations on the Present Correlation

Since the correlation constants listed in Table 7.1 were determined with a limited data set, the correlation is technically only valid for the conditions under which the data used to develop the correlation were obtained. Therefore, care must be taken when applying the correlation to conditions that do not coincide with those used to obtain the current data set. The test conditions under which the present data were obtained along with the effect of these conditions on the validity of the correlation are discussed below.

1. The present data were obtained using only copper tubes. Because copper has a relatively high thermal conductivity, the fin efficiency was assumed to be 100% for the development of the present correlation. The thermal conductivity of other tube materials, such as stainless steel, may be as much as an order of magnitude lower than that of copper, and therefore these tubes will have fin efficiencies well below 100%. For enhanced tubes that have well defined geometries (such as finned tubes), Equation 7.1 should be used in conjunction with the fin efficiency in order to calculate the effective shell-side bundle heat transfer coefficient. For enhanced tubes that do not have geometries for which a fin efficiency can be easily determined (such as the Tu-Cii), a new set of constants should be determined for Equation 7.1 when using tubes constructed from materials other than copper.
2. Only 19.1 mm (0.75in) nominal o.d. tubes and a bundle length of 610 mm (24 in) were used to obtain the current data set. The correlation does account for tube diameter and length. However, the correlation has not yet been tested with other tube diameters and bundle lengths, so whether the correlation adequately accounts for variations in tube dimensions is not known.

3. Only 5-row by 5-column bundles with one pitch arrangement were used to obtain the data set used in the development of the correlation. The correlation should be experimentally verified for other bundle sizes and pitch arrangements.
4. The present data were obtained over a heat flux range of $16\,000\text{ W/m}^2$ ($5100\text{ Btu}/(\text{hr}\cdot\text{ft}^2)$) to $41\,000\text{ W/m}^2$ ($13\,000\text{ Btu}/(\text{hr}\cdot\text{ft}^2)$). As the discussion in the previous chapters indicates, $h_{o,B}$ is dependent on heat flux. Therefore, the correlation should be experimentally verified for heat fluxes beyond the range of the present data.
5. HFC-134a, HCFC-123, and CFC-12 data were used to develop the correlation constants. The shell-side heat transfer coefficient is dependent on thermophysical properties. Although the three refrigerants used in the development of the correlation have a wide variation in thermophysical properties, they do not cover the entire range of thermophysical properties that may be encountered. For example, CFC-113 has a larger liquid density, larger liquid viscosity, and smaller liquid specific heat than the three refrigerants used to develop the correlation. The correlation should be experimentally verified for refrigerants other than HFC-134a, HCFC-123, and CFC-12.
6. Thermophysical properties are also dependent on saturation temperature, so the correlation should be used with caution for saturation temperatures that are different from 35°C (95°F). For example, the liquid viscosity of HFC-134a at 50°C (122°F) does not fall within the viscosity range of the data used to develop the correlation, and is nearly 15% lower than the lowest viscosity used in the development of the correlation constants.
7. The correlation does not account for vapor shear, and it should be used with caution when vapor shear effects are significant.

Even with the above listed limitations, the correlation proposed in this chapter should prove useful for many design conditions. The heat flux range and saturation temperature chosen for the present study are quite representative of the conditions found in actual refrigerant condensers. Copper is the most common tube material used throughout the refrigeration industry, and the 19.1 mm (0.75in) nominal o.d. tube size is also one of the most popular sizes.

CHAPTER 8. CONCLUSIONS

The purpose of the current study was to measure shell-side heat transfer coefficients for the condensation of HFC-134a and HCFC-123 on tube bundles using a staggered tube arrangement. For comparison purposes, shell-side heat transfer coefficients were also measured for CFC-12 and CFC-11. The average shell-side bundle heat transfer coefficient and the shell-side heat transfer coefficient for the middle tube of each row were computed. The tube bundles were constructed from 4 different tube geometries of the type commonly used in the refrigeration industry. The data were obtained at a saturation temperature of 35°C (95°F) and over a heat flux range of 16 000 W/m² (5100 Btu/(hr-ft²)) to 41 000 W/m² (13 000 Btu/(hr-ft²)). The conditions are typical of those found in refrigerant condensers.

Summary of HFC-134a Data

For HFC-134a condensation, the Turbo C-II was the best performing tube, followed by the 40-fpi, the GEWA SC, and the 26-fpi, in that order. The shell-side heat transfer coefficients for the Turbo C-II are 130% higher than those for the 40-fpi (the second best performing tube) at the highest heat flux tested, and 240% higher at the lowest heat flux tested. The 40-fpi shell-side heat transfer coefficients are 5% greater than those of the GEWA SC, while the GEWA SC shell-side heat transfer coefficients are 9%–18% higher than those of the 26-fpi.

For all tube geometries, the average shell-side heat transfer coefficients decrease with increasing heat flux, with the decrease ranging from 9% for the GEWA SC to 39% for the

Turbo C-II over the heat flux range tested. The row-to-row shell-side heat transfer coefficient behavior is different for each tube geometry.

The shell-side heat transfer coefficients of HFC-134 for the 26-fpi, 40-fpi, and GEWA SC are 20% higher than those for CFC-12. For the Turbo C-II, the HFC-134a shell-side heat transfer coefficients range from 50% higher at the highest heat flux tested to 100% higher at the lowest heat flux tested. These differences are due to the thermophysical properties of HFC-134a being more favorable to condensation heat transfer than those of CFC-12. For a given tube geometry, the row-to-row shell-side heat transfer coefficient behavior for HFC-134a and CFC-12 is quite similar.

Summary of HCFC-123 Data

For HCFC-123 condensation, the Turbo C-II was the best performing tube, followed by the 40-fpi, the GEWA SC and the 26-fpi, in that order. The shell-side heat transfer coefficients for the Turbo C-II are 70% higher than those for the 40-fpi (the second best performing tube) at the lowest heat flux tested, and 40% higher at the highest heat flux tested. The 40-fpi shell-side heat transfer coefficients are 13%–25% higher than those of the GEWA SC, while the GEWA SC shell-side heat transfer coefficients are 10% higher than those of the 26-fpi.

For HCFC-123 condensation on all tube geometries, the average shell-side heat transfer coefficients decrease with increasing heat flux, with the decrease ranging from 9% for the GEWA SC to 30% for the Turbo C-II over the heat flux range tested. For CFC-11, the average shell-side heat transfer coefficients increased by approximately 10% with increasing heat flux over the heat flux range tested. The increasing shell-side heat transfer coefficient with heat flux suggests that CFC-11 is greatly affected by vapor velocity. The row-to-row shell-side heat transfer coefficient behavior of each tube geometry is different.

The shell-side heat transfer coefficients of HCFC-123 are as much as 60% higher than

those for CFC-11 at the lowest heat flux tested, but only 10% higher at highest heat flux tested. The improvement is due to the lower surface tension of HCFC-123 relative to CFC-11. For a given tube geometry, the row-to-row heat transfer coefficient profiles for HCFC-123 and CFC-11 are quite similar.

BIBLIOGRAPHY

- Beatty, Kenneth O. Jr., and Donald L. Katz. "Condensation of Vapors on Outside of Finned Tubes." *Chemical Engineering Progress* 44, no. 1 (1948): 55–70.
- Butterworth, D. "Developments in the Design of Shell and Tube Condensers." *ASME Winter Annual Meeting, Atlanta*, ASME Reprint 77-WA/HT-24 (1977).
- Chen, Michael Ming. "An Analytical Study of Laminar Film Condensation: Part 2—Single and Multiple Horizontal Tubes." *Transactions of the ASME, Journal of Heat Transfer* 83, (1961): 55–60.
- Collier, John, G. *Convective Boiling and Condensation*. 2nd ed. New York: McGraw-Hill, 1981.
- Fisher, F. F., and G. J. Brown. "Tube Expanding and Related Subjects." *Transactions of the ASME* 76, (1954): 563–575.
- Gaddis, E. S. "Solution of the Two Phase Boundary-Layer Equations for Laminar Film Condensation of Vapor Flowing Perpendicular to a Horizontal Cylinder." *International Journal of Heat and Mass Transfer* 22 (1979): 371–382.
- Glamm, Paul. The Trane Company. Personal communication. 1993.
- Gnielinski, V. "New Equations for Heat and Mass Transfer in Turbulent Pipe and Channel Flow." *International Chemical Engineering* 16, no. 2, (1976): 359–368.
- Gogonin, I. I., and A. R. Dorokhov. "Enhancement of Heat Transfer in Horizontal Shell-and-tube Condensers." *HEAT TRANSFER—Soviet Research* 13, no. 3 (1981): 119–125.
- Gregorig, Von Romano. "Hautkondensation an feingewellten Oberflächen bei Berücksichtigung der Oberflächenspannungen." *Zeitschrift für angewandte Mathematik und Physik* 5, (1954): 36–49.
- Honda, H., and T. Fujii. "Condensation of Flowing Vapor on a Horizontal Tube—Numerical

- Analysis as a Conjugate Heat Transfer Problem.” *Transactions of the ASME, Journal of Heat Transfer* 106, (1984): 841–848.
- Honda, H., and S. Nozu. “A Prediction Method for Heat Transfer During Film Condensation on Horizontal Low Integral-Fin Tubes.” *Transactions of the ASME, Journal of Heat Transfer* 109, (1987): 218–225.
- Honda, H., S. Nozu, and Y. Takeda. “A Theoretical Model of Film Condensation in a Bundle of Horizontal Low Finned Tubes.” *Transactions of the ASME, Journal of Heat Transfer* 111, (1989): 525–532.
- Honda, H., S. Nozu, and B. Uchima. “A Generalized Prediction Method for Heat Transfer During Film Condensation on a Horizontal Low Finned Tube.” In *Proceedings of the 2nd ASME-JSME thermal engineering joint conference*, edited by P. Marto and I. Tanasawa. JSME 4, (1987): 385–392.
- Honda, H., B. Uchima, S. Nozu, H. Nakata, and E. Torigoe. “Film Condensation of R-113 on In-Line Bundles of Horizontal Finned Tubes.” *Transactions of the ASME, Journal of Heat Transfer* 113, (1991): 479–486.
- Honda, H., B. Uchima, S. Nozu, E. Torigoe, and S. Imai. “Film Condensation of R-113 on Staggered Bundles of Horizontal Finned Tubes.” *Transactions of the ASME, Journal of Heat Transfer* 114, (1992): 442–449.
- Incropera, Frank P., and David P. DeWitt. *Fundamentals of Heat and Mass Transfer*. 3rd ed. New York: John Wiley & Sons, 1990.
- Ishihara, K. I., and J. W. Palen. “Condensation of Pure Fluids on Horizontal Finned Tube Bundles.” In *Proceedings of the Symposium on Condensers: Theory and Practice*, Institution of Chemical Engineers Symposium Series No. 75, (1983): 429–446.
- Karkhu, V. A., and V. P. Borovkov. “Film Condensation of Vapor at Finely-Finned Horizontal Tubes.” *HEAT TRANSFER–Soviet Research* 3, no. 2 (1971): 183–191.
- Katz, D. L., and J. M. Geist. “Condensation on Six Finned Tubes in a Vertical Row.” *Transactions of the American Society of Mechanical Engineers* 70, (1948): 907–914.
- Kern, Donald Q. “Mathematical Development of Tube Loading in Horizontal Condensers.” *A.I.Ch.E. Journal* 4, no. 2 (1958): 157–160.
- Kreith, Frank, and William Z. Black. *Basic Heat Transfer*. New York: Harper & Row, 1980.
- Marto, P. J. “Heat Transfer in Condensation.” In *Boilers, Evaporators, and Condensers* ed. S. Kakac, 525–570. New York: John Wiley & Sons, Inc., 1991.

- Marto, P. J. "An Evaluation of Film Condensation on Horizontal Integral-Fin Tubes." *Transactions of the ASME, Journal of Heat Transfer* 110, (1988a): 1287-1305.
- Marto, P. J. "Fundamentals of Condensation." In *Two-Phase Flow Heat Exchangers* ed. S. Kakac et al., 221-290. Dordrecht: Kluwer Academic Publishers, 1988b.
- Marto, P. J. "Heat Transfer and Two-Phase flow During Shell-side Condensation." *Heat Transfer Engineering* 5, (1984): 31-61.
- Murata, Keiji, Norimitsu Abe, and Kenichi Hashizume. "Condensation Heat Transfer in a Bundle of Horizontal Integral-fin Tubes." In *Proceedings – 9th International Heat Transfer Conference* 4, (1990): 259–264.
- Nusselt, Wilhelm. "The Condensation of Steam on Cooled Surfaces". *Chemical Engineering Fundamentals* 1, no. 2 (1982): 6–19. Translated by D. Fullarton.
- Pearson, John F., and James G. Withers. "New Finned Tube Configuration Improves Refrigerant Condensing." *ASHRAE Journal* 11, no. 6 (1969): 77–82.
- Rohsenow, W. M., J.M. Weber, and A.T. Ling. "Effect of Vapor Velocity on Laminar and Turbulent Film Condensation." *Transactions of the ASME* 78, (1956): 1637-1774.
- Rose, J. W. "Effect of Pressure Gradient in Forced Convection Film Condensation on a Horizontal Tube." *International Journal of Heat and Mass Transfer* 27, no. 1 (1984): 39–47.
- Rose, J. W. "Fundamentals of Condensation Heat Transfer: Laminar Film Condensation." *JSME International Journal Series II*, 31, no. 3 (1988): 357–375.
- Rohsenow, W. M., J.M. Weber, and A.T. Ling. "Effect of Vapor Velocity on Laminar and Turbulent Film Condensation." *Transactions of the ASME* 78, (1956): 1637-1774.
- Shekrladze, I. G. and V. I. Gomelauri. "Theoretical Study of Laminar Film Condensation of Flowing Vapour." *International Journal of Heat and Mass Transfer* 9 (1966): 581–591.
- Short, B. E., and H. E. Brown. "Condensation of Vapors on Vertical Banks of Horizontal Tubes." *Institution of Mechanical Engineers. Proceedings of the General Discussion of Heat Transfer*, (1951): 27-31.
- Smirnov, G. F., and I. I. Lukanov. "Study of Heat Transfer from Freon-11 Condensing on a Bundle of Finned Tubes." *HEAT TRANSFER–Soviet Research* 4, no. 3 (1972): 51–55.
- Sparrow, E. M., and J. L. Gregg. "Laminar Condensation Heat Transfer on a Horizontal Cylinder." *Transactions of the ASME, Journal of Heat Transfer* 81, (1959): 291-296.

Thors, Petur. Wolverine Tube, Inc. Personal Communication. 1992.

Webb, R. L. "The Effects of Vapor Velocity and Tube Bundle Geometry on Condensation in Shell-side Refrigeration Condensers." *ASHRAE Transactions* 90 part 1, (1984a): 5–25.

Webb, R. L. "Shell-side Condensation in Refrigerant Condensers." *ASHRAE Transactions* 90 part 1, (1984b): 39–59.

Webb, Ralph L., and Dennis L. Gee. "Analytical Predictions for a New Concept Spine-Fin Surface Geometry." *ASHRAE Transactions* 84, (1979): 274–283.

Webb, R. L., and C. G. Murawski. "Row Effect for R-11 Condensation on Enhanced Tubes." *Transactions of the ASME, Journal of Heat Transfer* 112, (1990): 768–776.

Webb, R. L., T. M. Rudy, and M. A. Kedzierski. "Prediction of the Condensation on Horizontal Integral-Fin Tubes." *Transactions of the ASME, Journal of Heat Transfer* 107, (1985): 369–376.

APPENDIX A. DERIVATION OF UNCERTAINTY ANALYSIS EQUATIONS

The method used to determine the experimental uncertainty in the calculated heat transfer coefficients is the propagation of errors approach described in Holman (1984). This method uses the squares of the uncertainties in the independent parameters to compute the uncertainty in the calculated quantity. For any calculated quantity y , the uncertainty in the calculated value of y , w_y is calculated from

$$w_y = \left[\left(\frac{\partial y}{\partial x_1} w_{x_1} \right)^2 + \left(\frac{\partial y}{\partial x_2} w_{x_2} \right)^2 + \cdots + \left(\frac{\partial y}{\partial x_n} w_{x_n} \right)^2 \right]^{1/2} \quad (\text{A.1})$$

where $x_1 \cdots x_n$ are the independent parameters which are used to calculate y , and $w_{x_1} \cdots w_{x_n}$ are the uncertainties in the independent parameters.

The shell-side heat transfer coefficient is calculated from Equation 4.14. Substitution of Equation 4.8 into Equation 4.14 yields

$$h_o = \frac{q h_i}{\frac{h_i A_o (T_{w,out} - T_{w,in})}{\ln \frac{T_{sat} - T_{w,in}}{T_{sat} - T_{w,out}}} - q (A_o / A_i) - q A_o R_{tw}} \quad (\text{A.2})$$

In order to find the uncertainty in h_o , Equation A.2 must be differentiated with respect to the independent variables q , h_i , T_{sat} , $T_{w,in}$, $T_{w,out}$, A_o , A_i , and R_{tw} . The partial derivatives are then used to calculate w_{h_o} by the method of Equation A.1. The partial derivatives with respect to A_o , A_i , and R_{tw} are neglected since these parameters are based on arbitrary nominal diameters and a nominal tube length. After neglecting the aforementioned

partial derivatives, the governing uncertainty equation becomes

$$w_{h_o} = \left[\left(\frac{\partial h_o}{\partial q} w_q \right)^2 + \left(\frac{\partial h_o}{\partial h_i} w_{h_i} \right)^2 + \left(\frac{\partial h_o}{\partial T_{sat}} w_{T_{sat}} \right)^2 + \left(\frac{\partial h_o}{\partial T_{w,in}} w_{T_{w,in}} \right)^2 + \left(\frac{\partial h_o}{\partial T_{w,out}} w_{T_{w,out}} \right)^2 \right]^{1/2} \quad (\text{A.3})$$

Each of the terms in the right side of the above equation will be discussed in detail in the following sections.

Uncertainty Due To Heat Transfer Rate

The partial derivative of Equation A.2 with respect to q is given by

$$\frac{\partial h_o}{\partial q} = \frac{h_i}{\frac{h_i A_o (T_{w,out} - T_{w,in})}{\ln \frac{T_{sat} - T_{w,in}}{T_{sat} - T_{w,out}}} - q(A_o/A_i) - q A_o R_{tw} h_i} \frac{q h_i (-A_o/A_i - A_o R_{tw} h_i)}{\left[\frac{h_i A_o (T_{w,out} - T_{w,in})}{\ln \frac{T_{sat} - T_{w,in}}{T_{sat} - T_{w,out}}} - q(A_o/A_i) - q A_o R_{tw} h_i \right]^2} \quad (\text{A.4})$$

As discussed in Chapter 4, the energy transfer rate can be calculated from either the refrigerant energy transfer rate

$$q_{ref} = \dot{m}_{ref} (i_{ref,out} - i_{ref,in}) \quad (\text{A.5})$$

or the water energy transfer rate

$$q_w = \dot{m}_w C_p (T_{w,out} - T_{w,in}) \quad (\text{A.6})$$

By using a repeated application of Equation A.1, w_q can be calculated using the following equations.

For the calculation of $h_{o,B}$, which is based on both q_w and q_{ref}

$$q = (q_{ref} + q_w)/2 \quad (A.7)$$

$$w_q = \frac{1}{2} [w_{q_{ref}}^2 + w_{q_w}^2]^{1/2} \quad (A.8)$$

For the calculation of $h_{o,R}$, which is based on q_w only,

$$q = q_w \quad (A.9)$$

$$w_q = w_{q_w} \quad (A.10)$$

Applying the method of Equation A.1 to Equations A.5 and A.6, $w_{q_{ref}}$ and w_{q_w} can be calculated as follows:

$$w_{q_{ref}} = [((i_{ref,out} - i_{ref,in})w_{\dot{m}_{ref}})^2 + (\dot{m}_{ref}w_{i_{ref,out}})^2 + (\dot{m}_{ref}w_{i_{ref,in}})^2]^{1/2} \quad (A.11)$$

$$w_{q_w} = [(C_p(T_{w,out} - T_{w,in})w_{\dot{m}_w})^2 + (\dot{m}_w C_p w_{T_{w,out}})^2 + (\dot{m}_w C_p w_{T_{w,in}})^2]^{1/2} \quad (A.12)$$

where

$$\begin{aligned} w_{T_{w,out}} &= \pm 0.025^\circ\text{C} \\ w_{T_{w,in}} &= \pm 0.025^\circ\text{C} \\ w_{\dot{m}_{ref}} &= \pm (0.002\dot{m}_{ref} + 0.002\text{kg/min}) \\ w_{\dot{m}_w} &= \pm (0.002\dot{m}_w + 0.150\text{kg/min}); \text{ bulk flow rate} \\ w_{\dot{m}_w} &= \pm 0.01\dot{m}_w; \text{ tube flow rate} \end{aligned} \quad (A.13)$$

The uncertainty in C_p is neglected.

The enthalpy i is a function of temperature and pressure. Therefore, by Equation A.1

$$w_{i_{ref,in}} = \left[\left(\frac{\partial i_{ref,in}}{\partial p_{sat}} w_{p_{sat}} \right)^2 + \left(\frac{\partial i_{ref,in}}{\partial T_{ref,in}} w_{T_{ref,in}} \right)^2 \right]^{1/2} \quad (A.14)$$

$$w_{i_{ref,out}} = \left[\left(\frac{\partial i_{ref,out}}{\partial p_{sat}} w_{p_{sat}} \right)^2 + \left(\frac{\partial i_{ref,out}}{\partial T_{ref,out}} w_{T_{ref,out}} \right)^2 \right]^{1/2} \quad (A.15)$$

where

$$\begin{aligned} w_{T_{ref,in}} &= \pm 0.025^\circ\text{C} \\ w_{T_{ref,out}} &= \pm 0.025^\circ\text{C} \\ w_{p_{sat}} &= \pm 2.585\text{kPa, HFC-134a and CFC-12} \\ w_{p_{sat}} &= \pm 0.8618\text{kPa, HCFC-123 and CFC-11} \end{aligned} \quad (A.16)$$

The enthalpy partial derivatives are computed by using the computerized property equations and applying a finite difference method centered around p_{sat} , $T_{ref,in}$, and $T_{ref,out}$. For p_{sat} , a grid size of 40 kPa is used. For $T_{ref,in}$ and $T_{ref,out}$, a grid size of 10°C is used.

Uncertainty Due To the Water-side Heat Transfer Coefficient

The partial derivative of Equation A.2 with respect to h_i is given by

$$\frac{\partial h_o}{\partial h_i} = \frac{q}{\frac{h_i A_o (T_{w,out} - T_{w,in})}{\ln \frac{T_{sat} - T_{w,in}}{T_{sat} - T_{w,out}}} - q(A_o/A_i) - q A_o R_{tw} h_i} \quad (A.17)$$

$$\frac{q h_i \left[\frac{A_o (T_{w,out} - T_{w,in})}{\ln \frac{T_{sat} - T_{w,in}}{T_{sat} - T_{w,out}}} - q(A_o/A_i) \right]}{\left[\frac{h_i A_o (T_{w,out} - T_{w,in})}{\ln \frac{T_{sat} - T_{w,in}}{T_{sat} - T_{w,out}}} - q(A_o/A_i) - q A_o R_{tw} h_i \right]^2}$$

The uncertainty in the water-side heat transfer coefficient, w_{h_i} , is taken to be $0.005 h_i$.

Uncertainty Due to the Saturation Temperature

The partial derivative of Equation A.2 with respect to T_{sat} is given by

$$\frac{\partial h_o}{\partial T_{sat}} = \frac{qh_i^2 A_o (T_{w,out} - T_{w,in}) \left[\frac{1}{T_{sat} - T_{w,out}} - \frac{T_{sat} - T_{w,in}}{(T_{sat} - T_{w,out})^2} \right]}{\left[\frac{h_i A_o (T_{w,out} - T_{w,in})}{\ln \frac{T_{sat} - T_{w,in}}{T_{sat} - T_{w,out}}} - q(A_o/A_i) - qA_o R_{tw} h_i \right]^2} \times \frac{T_{sat} - T_{w,out}}{\ln \left[\frac{T_{sat} - T_{w,in}}{T_{sat} - T_{w,out}} \right]^2 (T_{sat} - T_{w,out})} \quad (A.18)$$

The saturation temperature is calculated from the saturation pressure. Therefore, by Equation A.1

$$w_{T_{sat}} = \frac{\partial T_{sat}}{\partial p_{sat}} w_{p_{sat}} \quad (A.19)$$

This partial derivative is computed by the computerized refrigerant property routines. $w_{p_{sat}}$ is given above.

Uncertainty Due To the Inlet Water Temperature

The partial derivative of Equation A.2 with respect to $T_{w,in}$ is given by

$$\frac{\partial h_o}{\partial T_{w,in}} = \frac{qh_i \left[\frac{-h_i A_o}{\ln \frac{T_{sat} - T_{w,in}}{T_{sat} - T_{w,out}}} + \frac{h_i A_o (T_{w,out} - T_{w,in})}{\ln \left[\frac{T_{sat} - T_{w,in}}{T_{sat} - T_{w,out}} \right]^2 (T_{sat} - T_{w,in})} \right]}{\left[\frac{h_i A_o (T_{w,out} - T_{w,in})}{\ln \frac{T_{sat} - T_{w,in}}{T_{sat} - T_{w,out}}} - q(A_o/A_i) - qA_o R_{tw} h_i \right]^2} \quad (A.20)$$

The uncertainty in $T_{w,in}$ is given above.

Uncertainty Due to the Outlet Water Temperature

The partial derivative of Equation A.2 with respect to $T_{w,out}$ is given by

$$\frac{\partial h_o}{\partial T_{w,in}} = \frac{qh_i \left[\frac{h_i A_o}{\ln \frac{T_{sat} - T_{w,in}}{T_{sat} - T_{w,out}}} - \frac{h_i A_o (T_{w,out} - T_{w,in})}{\ln \left[\frac{T_{sat} - T_{w,in}}{T_{sat} - T_{w,out}} \right]^2 (T_{sat} - T_{w,out})} \right]}{\left[\frac{h_i A_o (T_{w,out} - T_{w,in})}{\ln \frac{T_{sat} - T_{w,in}}{T_{sat} - T_{w,out}}} - q(A_o/A_i) - q A_o R_{tw} h_i \right]^2} \quad (A.21)$$

The uncertainty in $T_{w,out}$ is given above.

APPENDIX B. TABULATED HFC-134a CONDENSATION DATA

Table B.1: Refrigerant-side data for the 26-fpi geometry

run	q W	T_{sat} °C	inlet outlet		middle tube $T_{s,o}$					\dot{m} kg/min
			sh °C	sc °C	row 1 °C	row 2 °C	row 3 °C	row 4 °C	row 5 °C	
af18	18110	35.05	3.44	.14	33.60	33.68	33.23	33.33	33.45	6.35
af24	24190	35.03	4.64	.19	32.95	33.00	32.66	32.74	32.95	8.41
af30	30130	35.02	3.33	.17	32.19	32.27	31.97	32.19	32.30	10.56
af36	36130	34.97	4.99	.29	31.47	31.58	31.18	31.50	31.58	12.51
af16	16010	35.04	5.61	.13	33.74	33.81	33.39	33.47	33.56	5.53
af18	18020	34.98	4.10	.17	33.52	33.59	33.12	33.22	33.34	6.28
af20	20180	34.97	4.71	.21	33.31	33.41	32.93	33.00	33.21	7.01
af22	22280	35.01	4.11	.21	33.13	33.18	32.77	32.84	33.08	7.77
af24	24140	35.01	4.12	.20	32.92	32.97	32.60	32.68	32.92	8.42
af26	26150	35.06	3.91	.19	32.76	32.78	32.46	32.60	32.78	9.13
af28	28240	34.95	3.58	.23	32.36	32.41	32.12	32.25	32.41	9.87
af30	30170	35.02	3.31	.26	32.20	32.25	31.95	32.17	32.28	10.57
af32	32040	35.00	3.19	.23	31.96	32.07	31.73	31.98	32.07	11.24
af34	34070	34.94	2.46	.28	31.65	31.76	31.40	31.68	31.74	12.00
af36	36160	35.01	3.84	.24	31.51	31.65	31.22	31.53	31.59	12.61

Table B.2: Water-side data for the 26-fpi geometry

run	q W	$T_{bulk,in}$ °C	$T_{bulk,out}$ °C	LMTD °C	\dot{m}_{bulk} kg/min	\dot{m}_{tube} kg/min	Re	$\frac{h_i}{W}$ $\frac{m^2}{K}$
af18	18020	28.63	30.63	5.40	129.55	5.18	9560	6690
af24	24150	27.72	29.73	6.27	172.39	6.90	12470	8330
af30	30270	26.85	28.86	7.14	215.41	8.62	15290	9870
af36	36570	25.76	27.84	8.15	251.63	10.07	17440	11050
af16	15860	29.26	31.08	4.86	125.09	5.00	9340	6540
af18	17930	28.58	30.56	5.39	130.00	5.20	9580	6700
af20	20110	28.17	30.20	5.77	142.33	5.69	10400	7180
af22	22220	27.93	29.95	6.04	158.22	6.33	11500	7800
af24	24140	27.71	29.71	6.26	173.16	6.93	12520	8360
af26	26190	27.49	29.49	6.54	187.84	7.51	13520	8900
af28	28340	27.01	29.03	6.90	201.04	8.04	14320	9350
af30	30340	26.76	28.79	7.23	213.83	8.55	15150	9800
af32	32240	26.54	28.55	7.44	230.01	9.20	16210	10360
af34	34390	26.15	28.17	7.76	244.48	9.78	17080	10840
af36	36520	25.92	27.95	8.06	258.62	10.34	17980	11310

Table B.3: Row data for the 26-fpi geometry

run	row 1		row 2		row 3		row 4		row 5	
	$T_{w,out}$ °C	q'' W/m ²								
af18	30.62	20170	30.65	20480	30.47	18650	30.51	19060	30.56	19560
af24	29.70	26710	29.72	26980	29.59	25220	29.62	25630	29.70	26710
af30	28.78	32530	28.81	33040	28.70	31180	28.78	32530	28.82	33210
af36	27.75	39180	27.79	39970	27.65	37220	27.76	39380	27.79	39970
af16	31.07	17720	31.10	18010	30.93	16340	30.96	16640	31.00	17030
af18	30.56	20040	30.59	20340	30.40	18410	30.44	18820	30.49	19330
af20	30.18	22500	30.22	22940	30.03	20830	30.06	21160	30.14	22050
af22	29.93	24760	29.95	25010	29.79	23030	29.82	23400	29.91	24510
af24	29.68	26690	29.70	26960	29.56	25070	29.59	25470	29.68	26690
af26	29.45	28810	29.46	28950	29.34	27190	29.39	27930	29.46	28950
af28	28.97	30830	28.99	31150	28.88	29420	28.93	30200	28.99	31150
af30	28.72	32960	28.74	33300	28.63	31460	28.71	32800	28.75	33460
af32	28.47	34740	28.51	35460	28.39	33300	28.48	34920	28.51	35460
af34	28.09	36920	28.13	37690	28.00	35200	28.10	37110	28.12	37500
af36	27.86	39260	27.91	40270	27.76	37240	27.87	39460	27.89	39870

Table B.4: Shell-side heat transfer coefficients and uncertainties for the 26-fpi geometry

run	bundle				row 1		row 2		row 3		row 4		row 5	
	q'' W/m ²	q' W/m	h_o $\frac{W}{m^2 K}$	w ± %										
af18	20290	1200	14840	10.	14440	11.	15510	12.	10490	9.	11370	10.	12630	10.
af24	27160	1600	13960	7.	13140	8.	13630	9.	10840	8.	11410	8.	13140	8.
af30	33930	2000	13220	6.	11630	7.	12170	7.	10320	6.	11630	7.	12360	7.
af36	40840	2410	12690	5.	11310	6.	11930	6.	9910	6.	11460	6.	11930	6.
af16	17910	1060	14840	11.	14160	12.	15320	13.	10190	10.	10890	10.	11930	11.
af18	20190	1190	14570	9.	14190	11.	15230	12.	10120	9.	10960	9.	12150	10.
af20	22640	1340	14390	8.	13940	10.	15190	11.	10400	8.	11000	9.	12840	10.
af22	25000	1480	14020	8.	13490	9.	14030	9.	10450	8.	11010	8.	12990	9.
af24	27130	1600	13820	7.	13040	8.	13530	9.	10590	7.	11130	8.	13040	8.
af26	29400	1740	13630	6.	12700	8.	12920	8.	10600	7.	11490	7.	12920	8.
af28	31790	1880	13360	6.	12110	7.	12500	7.	10530	7.	11370	7.	12500	7.
af30	33990	2010	13020	6.	11810	7.	12170	7.	10340	6.	11630	7.	12360	7.
af32	36110	2130	12910	5.	11520	6.	12220	7.	10270	6.	11690	6.	12220	7.
af34	38460	2270	12700	5.	11340	6.	12000	6.	10020	6.	11500	6.	11830	6.
af36	40830	2410	12610	5.	11320	6.	12110	6.	9910	6.	11470	6.	11790	6.

Table B.5: Refrigerant-side data for the 40-fpi geometry

run	q W	T_{sat} °C	inlet outlet		middle tube $T_{s,o}$					\dot{m} kg/min
			sh °C	sc °C	row 1 °C	row 2 °C	row 3 °C	row 4 °C	row 5 °C	
ag16	16000	34.99	4.32	.11	33.92	33.75	33.92	33.84	33.78	5.57
ag18	18160	35.04	3.40	.16	33.81	33.62	33.81	33.73	33.62	6.36
ag20	20110	35.04	4.63	.17	33.69	33.46	33.69	33.60	33.49	6.99
ag22	22060	35.05	4.02	.15	33.55	33.30	33.58	33.47	33.30	7.70
ag24	24090	35.04	4.45	.15	33.39	33.12	33.47	33.36	33.12	8.39
ag26	26160	34.97	3.33	.33	33.20	32.85	33.23	33.12	32.82	9.16
ag28	28100	35.03	3.54	.26	33.10	32.74	33.16	33.01	32.68	9.83
ag30	30070	35.04	3.81	.19	32.98	32.53	32.95	32.77	32.40	10.51
ag32	32180	35.02	4.30	.24	32.86	32.33	32.76	32.55	32.18	11.21
ag34	34000	34.99	3.21	.25	32.65	32.09	32.56	32.31	31.87	11.65
ag36	35980	34.99	6.40	.25	32.55	32.01	32.42	32.14	31.70	12.35
ag18	18040	34.96	2.80	.17	33.70	33.51	33.73	33.62	33.54	6.34
ag24	24180	35.02	3.92	.19	33.37	33.11	33.43	33.31	33.11	8.44
ag30	30150	35.01	3.78	.26	32.95	32.49	32.95	32.80	32.43	10.53
ag36	35960	35.04	4.76	.29	32.62	32.06	32.53	32.22	31.81	12.48

Table B.6: Water-side data for the 40-fpi geometry

run	q W	$T_{bulk,in}$ °C	$T_{bulk,out}$ °C	LMTD °C	\dot{m}_{bulk} kg/min	\dot{m}_{tube} kg/min	Re	h_i $\frac{W}{m^2 \cdot K}$
ag16	15760	28.92	30.72	5.14	125.35	5.01	8470	5240
ag18	17950	28.29	30.27	5.74	130.17	5.21	8690	5370
ag20	19920	28.04	30.03	5.99	143.65	5.75	9540	5800
ag22	21870	27.80	29.80	6.25	156.87	6.27	10360	6200
ag24	23890	27.61	29.59	6.44	173.07	6.92	11380	6700
ag26	26040	27.27	29.26	6.72	187.87	7.51	12260	7130
ag28	28040	27.02	29.03	7.02	200.20	8.01	13000	7480
ag30	30050	26.78	28.77	7.30	216.72	8.67	13990	7950
ag32	32310	26.47	28.47	7.60	231.97	9.28	14870	8370
ag34	34260	26.10	28.13	7.94	241.97	9.68	15390	8620
ag36	36200	25.86	27.90	8.18	255.04	10.20	16140	8970
ag18	17910	28.18	30.17	5.76	129.31	5.17	8610	5340
ag24	24070	27.53	29.54	6.49	172.41	6.90	11320	6670
ag30	30260	26.72	28.73	7.32	215.84	8.63	13920	7920
ag36	36370	25.77	27.87	8.28	249.20	9.97	15750	8800

Table B.7: Row data for the 40-fpi geometry

run	row 1		row 2		row 3		row 4		row 5	
	$T_{w,out}$ °C	q'' W/m ²								
ag16	30.74	17750	30.68	17170	30.74	17750	30.71	17460	30.69	17260
ag18	30.28	20160	30.21	19450	30.28	20160	30.25	19850	30.21	19450
ag20	30.03	22350	29.95	21460	30.03	22350	30.00	22020	29.96	21570
ag22	29.80	24410	29.71	23310	29.81	24530	29.77	24050	29.71	23310
ag24	29.58	26530	29.49	25320	29.61	26930	29.57	26390	29.49	25320
ag26	29.26	29090	29.14	27340	29.27	29240	29.23	28650	29.13	27190
ag28	29.04	31310	28.92	29440	29.06	31620	29.01	30840	28.90	29130
ag30	28.80	34060	28.65	31540	28.79	33900	28.73	32880	28.61	30860
ag32	28.52	37000	28.35	33940	28.49	36460	28.42	35200	28.30	33030
ag34	28.18	39160	28.00	35780	28.15	38600	28.07	37090	27.93	34460
ag36	27.96	41680	27.79	38300	27.92	40880	27.83	39100	27.69	36320
ag18	30.17	20020	30.10	19320	30.18	20120	30.14	19720	30.11	19420
ag24	29.53	26700	29.44	25490	29.55	26960	29.51	26430	29.44	25490
ag30	28.75	34090	28.60	31570	28.75	34090	28.70	33250	28.58	31240
ag36	27.93	41890	27.75	38400	27.90	41300	27.80	39360	27.67	36840

Table B.8: Shell-side heat transfer coefficients and uncertainties for the 40-fpi geometry

run	bundle				row 1		row 2		row 3		row 4		row 5	
	q'' W/m ²	q' W/m	h_o $\frac{W}{m^2 K}$	w ± %										
ag16	17740	1050	17110	13.	17340	16.	14410	14.	17340	16.	15770	15.	14840	14.
ag18	20170	1200	17130	11.	17150	14.	14170	12.	17150	14.	15760	13.	14170	12.
ag20	22360	1330	17320	10.	17230	13.	14060	11.	17230	13.	15920	12.	14400	11.
ag22	24540	1460	17240	10.	16850	12.	13630	10.	17280	12.	15650	11.	13630	10.
ag24	26810	1590	17300	9.	16530	11.	13530	10.	17770	11.	16150	11.	13530	10.
ag26	29170	1730	17120	8.	16940	10.	13160	9.	17330	11.	15850	10.	12900	9.
ag28	31360	1860	16670	8.	16660	10.	13120	8.	17390	10.	15650	9.	12640	8.
ag30	33590	1990	15990	7.	16930	9.	12740	8.	16590	9.	14760	9.	11870	8.
ag32	36030	2140	15730	6.	17430	9.	12780	7.	16440	9.	14450	8.	11740	7.
ag34	38130	2260	15460	6.	17060	8.	12480	7.	16150	8.	14030	8.	11160	7.
ag36	40330	2390	15440	6.	17380	8.	13020	7.	16180	8.	13890	7.	11130	7.
ag18	20080	1190	16860	11.	16630	14.	13790	12.	17110	14.	15300	13.	14140	12.
ag24	26960	1600	17340	9.	16660	11.	13640	10.	17470	11.	15900	11.	13640	10.
ag30	33750	2000	16250	7.	16940	9.	12750	8.	16940	9.	15340	9.	12310	8.
ag36	40410	2400	15510	6.	17670	8.	13040	7.	16750	8.	14140	7.	11520	7.

Table B.9: Refrigerant-side data for the Tu-Cii geometry

run	q W	T_{sat} °C	inlet outlet		middle tube $T_{s,o}$					\dot{m} kg/min
			sh °C	sc °C	row 1 °C	row 2 °C	row 3 °C	row 4 °C	row 5 °C	
ac18	17990	34.92	3.44	.11	34.57	34.55	34.48	34.34	34.36	6.30
ac24	24060	35.00	2.47	.17	34.44	34.46	34.37	34.17	34.22	8.48
ac30	30460	34.99	3.93	.33	34.15	34.17	34.09	33.78	33.89	10.62
ac36	36490	35.05	3.56	.25	33.89	33.95	33.87	33.47	33.63	12.77
ac18	18010	34.99	3.10	.12	34.65	34.63	34.56	34.42	34.42	6.33
ac20	20210	34.99	4.73	.14	34.60	34.60	34.50	34.36	34.38	7.02
ac24	24210	35.02	3.51	.18	34.47	34.47	34.40	34.18	34.23	8.48
ac26	26180	35.02	3.08	.21	34.40	34.40	34.32	34.10	34.12	9.19
ac28	28370	34.98	2.81	.24	34.27	34.30	34.19	33.94	33.99	9.97
ac30	30140	34.97	2.15	.23	34.16	34.19	34.11	33.80	33.91	10.64
ac32	32170	34.95	2.53	.26	34.03	34.06	33.98	33.64	33.77	11.32
ac34	34300	35.07	3.27	.24	34.07	34.09	34.01	33.64	33.78	12.03
ac36	36100	35.00	3.42	.24	33.91	33.93	33.85	33.45	33.61	12.64

Table B.10: Water-side data for the Tu-Cii geometry

run	q W	$T_{bulk,in}$ °C	$T_{bulk,out}$ °C	LMTD °C	\dot{m}_{bulk} kg/min	\dot{m}_{tube} kg/min	Re	h_i $\frac{W}{m^2 K}$
ac18	17820	29.82	31.79	4.08	129.69	5.19	9120	6650
ac24	23960	29.36	31.37	4.59	171.16	6.85	11920	8270
ac30	30360	28.79	30.83	5.16	214.70	8.59	14780	9860
ac36	36810	28.32	30.37	5.69	257.60	10.30	17550	11350
ac18	17860	29.87	31.85	4.09	129.44	5.18	9110	6640
ac20	20090	29.64	31.66	4.30	142.80	5.71	10010	7170
ac24	24090	29.40	31.40	4.58	173.14	6.93	12070	8350
ac26	26090	29.26	31.25	4.74	188.03	7.52	13070	8900
ac28	28390	28.99	31.01	4.96	201.62	8.06	13930	9390
ac30	30090	28.87	30.87	5.08	215.35	8.61	14840	9880
ac32	32180	28.67	30.68	5.26	229.82	9.19	15770	10390
ac34	34310	28.62	30.63	5.44	244.27	9.77	16750	10910
ac36	36140	28.32	30.37	5.64	253.31	10.13	17260	11200

Table B.11: Row data for the Tu-Cii geometry

run	row 1		row 2		row 3		row 4		row 5	
	$T_{w,out}$ °C	q'' W/m ²								
ac18	31.82	20280	31.81	20180	31.78	19880	31.72	19270	31.73	19370
ac24	31.40	27170	31.41	27300	31.37	26770	31.29	25700	31.31	25970
ac30	30.85	34410	30.86	34580	30.83	34080	30.71	32070	30.75	32740
ac36	30.39	41490	30.41	41890	30.38	41290	30.23	38280	30.29	39490
ac18	31.89	20340	31.88	20240	31.85	19940	31.79	19340	31.79	19340
ac20	31.69	22890	31.69	22890	31.65	22440	31.59	21780	31.60	21890
ac24	31.44	27350	31.44	27350	31.41	26940	31.32	25730	31.34	26000
ac26	31.29	29700	31.29	29700	31.26	29260	31.17	27940	31.18	28090
ac28	31.04	32320	31.05	32470	31.01	31850	30.91	30280	30.93	30590
ac30	30.90	34180	30.91	34350	30.88	33850	30.76	31840	30.80	32510
ac32	30.70	36480	30.71	36660	30.68	36120	30.55	33800	30.60	34690
ac34	30.66	38960	30.67	39150	30.64	38580	30.50	35920	30.55	36870
ac36	30.40	41000	30.41	41190	30.38	40600	30.23	37650	30.29	38830

Table B.12: Shell-side heat transfer coefficients and uncertainties for the Tu-Cii geometry

run	bundle				row 1		row 2		row 3		row 4		row 5	
	q'' W/m ²	q' W/m	h_o $\frac{W}{m^2 K}$	w ± %										
ac18	20010	1190	59150	36.	74050	51.	67650	47.	53500	38.	37220	28.	39260	29.
ac24	26820	1590	48180	22.	55570	30.	58920	32.	47350	26.	33420	19.	36160	21.
ac30	33980	2020	39880	15.	43730	20.	45480	20.	40580	18.	27710	14.	31140	15.
ac36	40950	2430	34860	11.	37560	15.	39900	15.	36480	14.	24830	11.	28660	12.
ac18	20040	1190	58340	35.	77070	53.	70200	49.	55150	39.	38080	28.	38080	28.
ac20	22520	1340	57010	31.	71950	45.	71950	45.	53790	34.	38490	26.	40460	27.
ac24	26990	1600	48360	22.	57170	31.	57170	31.	48550	26.	32800	19.	35440	20.
ac26	29200	1730	45120	19.	53460	27.	53460	27.	46210	24.	32270	17.	33440	18.
ac28	31710	1880	43040	17.	50150	23.	52530	24.	44050	21.	30740	16.	32810	16.
ac30	33650	2000	40540	15.	45520	20.	47420	21.	42110	19.	28390	14.	32010	15.
ac32	35950	2130	38620	14.	42380	18.	43950	19.	39500	17.	26770	13.	30740	14.
ac34	38330	2270	37030	13.	40950	17.	42360	17.	38370	16.	25950	12.	29520	13.
ac36	40350	2390	35760	12.	39380	15.	40640	16.	37060	15.	25030	11.	28960	12.

Table B.13: Refrigerant-side data for the G-SC geometry

run	q W	T_{sat} °C	inlet outlet		middle tube $T_{s,o}$					\dot{m} kg/min
			sh °C	sc °C	row 1 °C	row 2 °C	row 3 °C	row 4 °C	row 5 °C	
ad18	18080	34.99	2.72	.13	33.86	33.62	33.62	33.75	33.34	6.37
ad24	24080	35.05	3.11	.17	33.56	33.18	33.26	33.40	32.88	8.45
ad30	30030	35.02	3.02	.25	33.04	32.61	32.67	32.84	32.30	10.54
ad36	36270	35.06	2.51	.33	32.51	32.07	32.16	32.22	31.59	12.77
ad16	16260	34.99	3.39	.15	34.03	33.77	33.77	33.90	33.54	5.70
ad18	18130	34.98	3.25	.14	33.89	33.61	33.61	33.74	33.35	6.36
ad20	20040	34.97	3.18	.18	33.76	33.47	33.47	33.60	33.17	7.03
ad22	22260	35.05	3.62	.17	33.72	33.31	33.42	33.53	33.07	7.79
ad24	24020	35.03	3.10	.20	33.54	33.13	33.27	33.38	32.85	8.43
ad26	25990	35.02	2.64	.22	33.39	32.91	33.08	33.16	32.66	9.15
ad28	28080	35.05	3.91	.23	33.25	32.80	32.94	33.05	32.52	9.81
ad30	30270	35.03	3.05	.26	33.05	32.56	32.74	32.82	32.27	10.62
ad32	32160	34.97	3.29	.25	32.83	32.37	32.51	32.57	32.02	11.27
ad34	34400	35.02	3.55	.23	32.67	32.23	32.34	32.43	31.84	12.04
ad36	36260	35.01	2.34	.30	32.50	32.05	32.14	32.20	31.60	12.78

Table B.14: Water-side data for the G-SC geometry

run	q W	$T_{bulk,in}$ °C	$T_{bulk,out}$ °C	LMTD °C	\dot{m}_{bulk} kg/min	\dot{m}_{tube} kg/min	Re	h_i $\frac{W}{m^2 K}$
ad18	17970	28.43	30.43	5.57	129.42	5.18	9660	6390
ad24	24050	27.76	29.77	6.33	171.70	6.87	12640	7960
ad30	30150	27.01	29.01	7.07	216.86	8.67	15690	9520
ad36	36740	25.96	28.07	8.11	250.72	10.03	17740	10580
ad16	16120	28.99	30.84	5.07	125.01	5.00	9430	6250
ad18	18030	28.42	30.42	5.58	129.52	5.18	9670	6400
ad20	19980	28.17	30.17	5.81	143.19	5.73	10630	6910
ad22	22190	27.97	29.99	6.10	158.18	6.33	11700	7470
ad24	24070	27.73	29.75	6.33	171.43	6.86	12610	7950
ad26	26020	27.53	29.52	6.54	187.75	7.51	13740	8530
ad28	28170	27.28	29.29	6.81	201.77	8.07	14690	9010
ad30	30450	26.93	28.95	7.14	216.29	8.65	15630	9500
ad32	32330	26.63	28.66	7.38	229.66	9.19	16490	9930
ad34	34650	26.41	28.43	7.66	245.36	9.81	17520	10450
ad36	36610	26.11	28.15	7.96	258.24	10.33	18320	10850

Table B.15: Row data for the G-SC geometry

run	row 1		row 2		row 3		row 4		row 5	
	$T_{w,out}$ °C	q'' W/m ²								
ad18	30.50	20790	30.41	19890	30.41	19890	30.46	20390	30.30	18780
ad24	29.85	27990	29.71	26120	29.74	26520	29.79	27190	29.60	24650
ad30	29.09	35010	28.94	32490	28.96	32820	29.02	33830	28.83	30630
ad36	28.15	42420	28.00	39510	28.03	40090	28.05	40480	27.84	36390
ad16	30.93	18820	30.83	17850	30.83	17850	30.88	18340	30.74	16980
ad18	30.50	21010	30.39	19900	30.39	19900	30.44	20410	30.29	18900
ad20	30.26	23230	30.15	22000	30.15	22000	30.20	22560	30.04	20780
ad22	30.08	25900	29.93	24060	29.97	24550	30.01	25050	29.84	22960
ad24	29.83	27940	29.68	25950	29.73	26610	29.77	27140	29.58	24620
ad26	29.61	30310	29.44	27830	29.50	28710	29.53	29150	29.35	26520
ad28	29.37	32730	29.21	30220	29.26	31010	29.30	31630	29.11	28660
ad30	29.04	35420	28.87	32570	28.93	33570	28.96	34080	28.77	30890
ad32	28.74	37610	28.58	34760	28.63	35650	28.65	36010	28.46	32620
ad34	28.51	39990	28.36	37140	28.40	37900	28.43	38470	28.23	34660
ad36	28.23	42490	28.08	39490	28.11	40090	28.13	40490	27.93	36480

Table B.16: Shell-side heat transfer coefficients and uncertainties for the G-SC geometry

run	bundle				row 1		row 2		row 3		row 4		row 5	
	q'' W/m ²	q' W/m	h_o $\frac{W}{m^2 K}$	w ± %										
ad18	20090	1190	16100	11.	19610	15.	15290	12.	15290	12.	17470	14.	11780	10.
ad24	26820	1600	16090	8.	19580	12.	14340	10.	15260	10.	17020	11.	11570	8.
ad30	33530	1990	15390	7.	18180	9.	13730	8.	14230	8.	15870	9.	11400	7.
ad36	40680	2420	14740	5.	17050	8.	13430	7.	14060	7.	14500	7.	10620	6.
ad16	18040	1070	16240	12.	21070	17.	15410	14.	15410	14.	17870	15.	12160	12.
ad18	20150	1200	16280	11.	20660	16.	15180	12.	15180	12.	17330	14.	11980	10.
ad20	22300	1330	16230	10.	20290	14.	15240	11.	15240	11.	17250	12.	11930	10.
ad22	24770	1470	16230	9.	20360	13.	14260	10.	15570	11.	17080	11.	11860	9.
ad24	26800	1590	16130	8.	19630	12.	14070	9.	15620	10.	17050	11.	11590	8.
ad26	28980	1720	15830	8.	19280	11.	13530	9.	15220	9.	16190	10.	11460	8.
ad28	31350	1860	15750	7.	18820	10.	13730	8.	15070	9.	16290	9.	11510	8.
ad30	33830	2010	15370	7.	18380	9.	13430	8.	14920	8.	15760	8.	11360	7.
ad32	35940	2140	15280	6.	18080	9.	13600	7.	14810	8.	15340	8.	11210	7.
ad34	38480	2290	15160	6.	17390	8.	13500	7.	14410	7.	15150	8.	11040	6.
ad36	40600	2420	14830	5.	17290	8.	13550	7.	14200	7.	14660	7.	10830	6.

APPENDIX C. TABULATED CFC-12 CONDENSATION DATA

Table C.1: Refrigerant-side data for the 26-fpi geometry

run	q W	T_{sat} °C	inlet outlet		middle tube $T_{s,o}$					\dot{m} kg/min
			sh °C	sc °C	row 1 °C	row 2 °C	row 3 °C	row 4 °C	row 5 °C	
cf16	16150	35.00	2.50	.18	33.42	33.47	33.00	33.13	33.20	7.23
cf18	18110	35.02	3.76	.18	33.26	33.31	32.81	32.94	33.01	8.05
cf20	20160	34.98	3.26	.20	32.98	33.05	32.57	32.67	32.82	8.99
cf24	24020	35.04	3.94	.26	32.56	32.62	32.19	32.35	32.48	10.67
cf30	30850	34.98	3.18	.30	31.59	31.73	31.29	31.56	31.67	13.75
cf32	32370	34.95	4.26	.29	31.36	31.50	31.08	31.36	31.48	14.34
cf36	36320	34.96	.93	.36	30.81	30.99	30.44	30.81	30.90	16.06
cf16	16020	34.97	2.46	.23	33.41	33.43	32.99	33.11	33.21	7.17
cf18	18050	35.02	3.77	.22	33.27	33.30	32.78	32.90	33.02	8.02
cf20	20020	35.00	3.97	.22	33.03	33.08	32.59	32.70	32.82	8.89
cf22	22100	35.01	3.81	.29	32.77	32.84	32.33	32.46	32.61	9.81
cf24	23960	35.09	4.05	.39	32.59	32.65	32.20	32.38	32.49	10.63
cf26	26030	35.01	3.03	.28	32.23	32.31	31.91	32.09	32.23	11.61
cf28	28090	35.01	2.99	.38	31.95	32.03	31.62	31.87	31.98	12.53
cf30	30950	35.05	2.51	.41	31.62	31.74	31.32	31.60	31.71	13.84
cf32	32160	34.97	3.50	.26	31.44	31.53	31.11	31.41	31.47	14.31
cf34	34170	34.99	2.49	.38	31.17	31.29	30.83	31.14	31.23	15.28
cf36	36280	34.96	2.53	.43	30.95	31.09	30.61	30.92	31.01	15.67

Table C.2: Water-side data for the 26-fpi geometry

run	q W	$T_{bulk,in}$ °C	$T_{bulk,out}$ °C	LMTD °C	\dot{m}_{bulk} kg/min	\dot{m}_{tube} kg/min	Re	$\frac{h_i}{W}$ m ² K
cf16	15980	28.88	30.70	5.20	125.56	5.02	9300	6540
cf18	17950	28.25	30.24	5.76	129.45	5.18	9470	6660
cf20	20070	27.88	29.88	6.09	144.48	5.78	10490	7240
cf24	23950	27.29	29.29	6.72	171.77	6.87	12310	8270
cf30	31080	25.99	28.06	7.92	215.79	8.63	15030	9790
cf32	32520	25.84	27.86	8.08	230.57	9.22	16000	10310
cf36	37230	25.01	27.08	8.89	258.81	10.35	17630	11210
cf16	15980	28.93	30.74	5.13	126.99	5.08	9410	6600
cf18	18040	28.24	30.25	5.77	128.76	5.15	9420	6630
cf20	20090	27.90	29.92	6.09	142.79	5.71	10370	7180
cf22	22170	27.58	29.59	6.42	158.12	6.32	11400	7760
cf24	24090	27.35	29.36	6.72	171.64	6.87	12320	8270
cf26	26220	26.94	28.95	7.04	187.11	7.48	13310	8820
cf28	28360	26.57	28.60	7.41	201.07	8.04	14180	9310
cf30	31230	26.12	28.16	7.89	220.39	8.82	15390	9970
cf32	32550	25.91	27.93	8.04	230.81	9.23	16040	10320
cf34	34630	25.54	27.58	8.42	243.99	9.76	16820	10750
cf36	36280	25.26	27.30	8.67	255.05	10.20	17470	11110

Table C.3: Row data for the 26-fpi geometry

run	row 1		row 2		row 3		row 4		row 5	
	$T_{w,out}$ °C	q'' W/m ²								
cf16	30.71	17980	30.73	18180	30.54	16310	30.59	16800	30.62	17090
cf18	30.25	20260	30.27	20460	30.07	18440	30.12	18940	30.15	19250
cf20	29.87	22500	29.90	22840	29.71	20690	29.75	21140	29.81	21820
cf24	29.28	26750	29.30	27020	29.14	24870	29.20	25670	29.25	26340
cf30	28.00	33940	28.05	34790	27.89	32080	27.99	33770	28.03	34450
cf32	27.79	35360	27.84	36270	27.69	33560	27.79	35360	27.83	36090
cf36	27.01	40510	27.07	41720	26.88	37870	27.01	40510	27.04	41110
cf16	30.73	17890	30.74	17980	30.56	16200	30.61	16690	30.65	17090
cf18	30.25	20250	30.26	20350	30.05	18240	30.10	18740	30.15	19240
cf20	29.90	22460	29.92	22680	29.73	20560	29.77	21000	29.82	21560
cf22	29.57	24620	29.60	24990	29.40	22520	29.45	23140	29.51	23880
cf24	29.33	26590	29.35	26860	29.18	24580	29.25	25520	29.29	26060
cf26	28.90	28700	28.93	29140	28.78	26940	28.85	27960	28.90	28700
cf28	28.54	30840	28.57	31310	28.42	28950	28.51	30370	28.55	31000
cf30	28.09	33970	28.13	34660	27.98	32080	28.08	33800	28.12	34490
cf32	27.87	35400	27.90	35940	27.75	33230	27.86	35220	27.88	35580
cf34	27.51	37610	27.55	38380	27.39	35320	27.50	37420	27.53	38000
cf36	27.23	39320	27.28	40320	27.11	36920	27.22	39120	27.25	39720

Table C.4: Shell-side heat transfer coefficients and uncertainties for the 26-fpi geometry

run	bundle				row 1		row 2		row 3		row 4		row 5	
	q'' W/m ²	q' W/m	h_o W/m ² K	w ± %										
cf16	18050	1070	11910	10.	11790	11.	12330	11.	8350	9.	9190	10.	9760	10.
cf18	20260	1200	11870	9.	11900	10.	12390	10.	8530	8.	9320	9.	9840	9.
cf20	22600	1330	11670	8.	11470	9.	12130	9.	8710	8.	9300	8.	10310	9.
cf24	26950	1590	11250	6.	10990	8.	11350	8.	8860	7.	9700	7.	10480	8.
cf30	34790	2050	10860	5.	10130	6.	10830	6.	8770	6.	10000	6.	10550	6.
cf32	36460	2150	10810	5.	9950	6.	10630	6.	8750	6.	9950	6.	10490	6.
cf36	41320	2440	10380	4.	9850	5.	10590	6.	8430	5.	9850	5.	10210	5.
cf16	17980	1060	12010	10.	11760	11.	12030	11.	8310	9.	9150	10.	9920	10.
cf18	20280	1200	12000	9.	11950	10.	12190	10.	8280	8.	9030	9.	9870	9.
cf20	22540	1330	11900	8.	11680	9.	12120	9.	8700	8.	9290	8.	10120	8.
cf22	24870	1470	11590	7.	11200	8.	11790	9.	8510	7.	9200	7.	10130	8.
cf24	27000	1590	11380	6.	10840	8.	11190	8.	8610	7.	9570	7.	10170	7.
cf26	29350	1730	11210	6.	10460	7.	10940	7.	8770	7.	9710	7.	10460	7.
cf28	31720	1870	11020	6.	10180	7.	10620	7.	8610	6.	9760	6.	10320	7.
cf30	34930	2060	10810	5.	10010	6.	10560	6.	8660	6.	9880	6.	10420	6.
cf32	36350	2150	10870	5.	10120	6.	10530	6.	8660	6.	9990	6.	10260	6.
cf34	38650	2280	10650	5.	9920	6.	10440	6.	8540	5.	9800	6.	10170	6.
cf36	40770	2410	10300	4.	9870	6.	10500	6.	8530	5.	9750	6.	10120	6.

Table C.5: Refrigerant-side data for the 40-fpi geometry

run	q W	T_{sat} °C	inlet outlet		middle tube $T_{s,o}$					\dot{m} kg/min
			sh °C	sc °C	row 1 °C	row 2 °C	row 3 °C	row 4 °C	row 5 °C	
cg16	15990	35.05	2.54	.23	33.75	33.56	33.75	33.70	33.53	7.16
cg18	18100	34.98	2.70	.21	33.54	33.34	33.51	33.45	33.26	8.09
cg20	20240	34.95	4.75	.26	33.31	33.14	33.37	33.25	33.00	8.94
cg22	22040	35.01	4.36	.27	33.26	33.03	33.29	33.18	32.89	9.76
cg24	23890	34.98	3.04	.26	33.12	32.83	33.12	32.98	32.63	10.66
cg26	26130	35.03	3.24	.31	32.97	32.58	32.97	32.82	32.38	11.64
cg28	28030	35.00	2.30	.29	32.81	32.42	32.81	32.60	32.12	12.56
cg30	30640	35.05	3.15	.32	32.66	32.14	32.60	32.35	31.77	13.66
cg32	32230	35.01	3.26	.34	32.52	31.90	32.40	32.12	31.53	14.35
cg34	34020	34.97	2.96	.41	32.31	31.71	32.18	31.84	31.24	15.17
cg36	36120	34.99	3.26	.43	32.23	31.53	32.04	31.69	31.03	15.55
cg18	18030	34.98	3.47	.23	33.50	33.26	33.42	33.34	33.17	8.02
cg24	24040	35.00	3.25	.33	32.99	32.70	32.99	32.88	32.53	10.71
cg30	30740	35.02	2.73	.36	32.58	31.99	32.45	32.21	31.66	13.73
cg36	36110	35.02	2.62	.35	32.11	31.44	31.95	31.57	30.90	16.14

Table C.6: Water-side data for the 40-fpi geometry

run	q W	$T_{bulk,in}$ °C	$T_{bulk,out}$ °C	LMTD °C	\dot{m}_{bulk} kg/min	\dot{m}_{tube} kg/min	Re	h_i $\frac{W}{m^2 K}$
cg16	15980	28.73	30.56	5.41	125.03	5.00	8410	5220
cg18	18120	28.02	30.01	5.97	131.35	5.25	8720	5390
cg20	20320	27.65	29.65	6.32	145.33	5.81	9570	5830
cg22	22130	27.43	29.46	6.59	157.03	6.28	10290	6190
cg24	24010	27.24	29.23	6.79	173.14	6.93	11290	6670
cg26	26290	26.93	28.94	7.15	187.49	7.50	12150	7090
cg28	28350	26.61	28.64	7.44	201.40	8.06	12960	7480
cg30	31010	26.29	28.31	7.84	220.31	8.81	14070	8010
cg32	32640	25.99	28.02	8.10	231.04	9.24	14660	8300
cg34	34440	25.69	27.71	8.37	245.00	9.80	15440	8670
cg36	36120	25.43	27.48	8.66	253.40	10.14	15880	8880
cg18	18040	27.91	29.91	6.08	129.77	5.19	8590	5340
cg24	24190	27.07	29.09	6.95	172.03	6.88	11180	6630
cg30	31040	26.14	28.17	7.96	219.91	8.80	14000	7990
cg36	36720	25.22	27.30	8.88	253.63	10.15	15820	8870

Table C.7: Row data for the 40-fpi geometry

run	row 1		row 2		row 3		row 4		row 5	
	$T_{w,out}$ °C	q'' W/m ²								
cg16	30.55	17800	30.48	17120	30.55	17800	30.53	17610	30.47	17030
cg18	30.00	20240	29.93	19520	29.99	20130	29.97	19930	29.90	19210
cg20	29.64	22500	29.58	21830	29.66	22730	29.62	22280	29.53	21260
cg22	29.45	24680	29.37	23700	29.46	24800	29.42	24310	29.32	23090
cg24	29.24	26940	29.14	25600	29.24	26940	29.19	26270	29.07	24650
cg26	28.95	29470	28.82	27570	28.95	29470	28.90	28740	28.75	26550
cg28	28.66	31970	28.53	29930	28.66	31970	28.59	30870	28.43	28370
cg30	28.35	35320	28.18	32400	28.33	34970	28.25	33600	28.06	30340
cg32	28.08	37570	27.88	33980	28.04	36860	27.95	35240	27.76	31820
cg34	27.78	39850	27.59	36220	27.74	39080	27.63	36990	27.44	33360
cg36	27.56	42000	27.34	37660	27.50	40820	27.39	38650	27.18	34510
cg18	29.92	20300	29.83	19390	29.89	19990	29.86	19690	29.80	19080
cg24	29.09	26900	28.99	25570	29.09	26900	29.05	26370	28.93	24760
cg30	28.22	35590	28.03	32340	28.18	34910	28.10	33540	27.92	30460
cg36	27.38	42430	27.17	38290	27.33	41450	27.21	39080	27.00	34930

Table C.8: Shell-side heat transfer coefficients and uncertainties for the 40-fpi geometry

run	bundle				row 1		row 2		row 3		row 4		row 5	
	q'' W/m ²	q' W/m	h_o $\frac{W}{m^2 K}$	w ± %										
cg16	17860	1060	14540	12.	14230	14.	11840	12.	14230	14.	13470	13.	11550	12.
cg18	20230	1200	14630	11.	14580	13.	12310	11.	14220	13.	13540	12.	11510	11.
cg20	22660	1340	14530	10.	14090	11.	12340	10.	14770	12.	13470	11.	11110	10.
cg22	24670	1460	14540	9.	14510	11.	12260	10.	14840	11.	13600	10.	11100	9.
cg24	26760	1590	14430	8.	14840	10.	12120	9.	14840	10.	13370	10.	10630	8.
cg26	29290	1740	14260	8.	14610	10.	11440	8.	14610	10.	13250	9.	10130	8.
cg28	31500	1870	14090	7.	14900	9.	11770	8.	14900	9.	13090	8.	9960	7.
cg30	34440	2040	13760	6.	15030	9.	11250	7.	14500	8.	12630	8.	9330	7.
cg32	36240	2150	13570	6.	15380	8.	11060	7.	14350	8.	12360	7.	9230	6.
cg34	38240	2270	13290	6.	15220	8.	11240	7.	14240	8.	11950	7.	9020	6.
cg36	40350	2390	13510	6.	15440	8.	11000	7.	14010	7.	11840	7.	8760	6.
cg18	20150	1200	13730	10.	14210	12.	11530	11.	13210	12.	12330	11.	10800	10.
cg24	26940	1600	13770	8.	13730	10.	11330	9.	13730	10.	12690	9.	10170	8.
cg30	34520	2050	13320	6.	14820	8.	10800	7.	13820	8.	12080	8.	9130	7.
cg36	40690	2410	12880	5.	14750	7.	10780	6.	13650	7.	11420	6.	8530	6.

Table C.9: Refrigerant-side data for the Tu-Cii geometry

run	q W	T_{sat} °C	inlet outlet		middle tube $T_{s,o}$					\dot{m} kg/min
			sh °C	sc °C	row 1 °C	row 2 °C	row 3 °C	row 4 °C	row 5 °C	
cc16	16050	34.98	3.36	.18	34.47	34.37	34.23	34.12	34.16	7.15
cc18	18130	34.99	2.82	.21	34.38	34.31	34.17	34.03	34.05	8.10
cc20	20030	35.01	3.53	.22	34.35	34.25	34.13	33.96	34.01	8.91
cc22	22220	35.02	4.04	.26	34.28	34.18	34.06	33.86	33.91	9.86
cc24	24040	34.94	3.85	.31	34.12	34.04	33.89	33.67	33.72	10.67
cc26	26210	34.95	4.51	.31	34.04	33.99	33.82	33.56	33.64	11.59
cc28	28230	34.94	4.08	.34	33.89	33.87	33.69	33.41	33.51	12.51
cc30	30150	34.92	3.85	.40	33.70	33.67	33.54	33.21	33.31	13.37
cc32	32140	35.01	3.17	.36	33.69	33.69	33.56	33.19	33.29	14.32
cc34	34120	35.00	2.38	.40	33.56	33.53	33.40	33.00	33.08	15.26
cc36	35860	35.03	2.05	.43	33.48	33.46	33.32	32.87	32.89	16.07
cc18	18110	34.92	2.27	.24	34.34	34.27	34.15	34.01	34.03	8.12
cc24	24140	34.95	3.45	.30	34.14	34.10	33.97	33.75	33.77	10.74
cc30	30570	34.96	3.66	.32	33.80	33.75	33.67	33.31	33.42	13.59
cc36	36180	35.03	2.16	.36	33.51	33.51	33.41	32.92	32.95	16.21

Table C.10: Water-side data for the Tu-Cii geometry

run	q W	$T_{bulk,in}$ °C	$T_{bulk,out}$ °C	LMTD °C	\dot{m}_{bulk} kg/min	\dot{m}_{tube} kg/min	Re	$\frac{h_i}{W}$ $\frac{m^2}{K}$
cc16	15780	30.02	31.83	4.02	125.30	5.01	8830	6480
cc18	17910	29.49	31.48	4.47	129.06	5.16	9010	6600
cc20	19780	29.39	31.37	4.60	143.93	5.76	10030	7200
cc22	21990	29.16	31.16	4.83	157.94	6.32	10950	7740
cc24	23690	28.94	30.92	4.98	172.10	6.88	11880	8270
cc26	25810	28.76	30.74	5.17	187.32	7.49	12880	8830
cc28	27940	28.56	30.55	5.36	201.52	8.06	13790	9340
cc30	29930	28.31	30.31	5.60	215.47	8.62	14670	9830
cc32	31780	28.27	30.25	5.74	230.14	9.21	15650	10360
cc34	34130	27.99	30.00	6.01	244.83	9.79	16560	10860
cc36	36030	27.86	29.87	6.19	257.91	10.32	17390	11300
cc18	17870	29.43	31.41	4.46	129.62	5.18	9040	6620
cc24	23860	28.94	30.93	5.00	171.70	6.87	11850	8250
cc30	30410	28.33	30.36	5.61	215.68	8.63	14700	9840
cc36	36220	27.85	29.88	6.20	256.69	10.27	17310	11260

Table C.11: Row data for the Tu-Cii geometry

run	row 1		row 2		row 3		row 4		row 5	
	$T_{w,out}$ °C	q'' W/m ²								
cc16	31.91	18430	31.87	18040	31.81	17450	31.76	16960	31.78	17160
cc18	31.55	20690	31.52	20380	31.46	19780	31.40	19180	31.41	19280
cc20	31.44	22960	31.40	22510	31.35	21950	31.28	21170	31.30	21390
cc22	31.24	25560	31.20	25070	31.15	24460	31.07	23470	31.09	23720
cc24	31.01	27720	30.98	27320	30.92	26510	30.83	25310	30.85	25580
cc26	30.84	30320	30.82	30020	30.75	29000	30.65	27550	30.68	27980
cc28	30.63	32460	30.62	32300	30.55	31200	30.44	29480	30.48	30110
cc30	30.38	34540	30.37	34370	30.32	33530	30.19	31350	30.23	32020
cc32	30.32	36710	30.32	36710	30.27	35810	30.13	33310	30.17	34020
cc34	30.07	39620	30.06	39430	30.01	38480	29.86	35620	29.89	36200
cc36	29.94	41740	29.93	41540	29.88	40540	29.71	37130	29.72	37330
cc18	31.49	20880	31.46	20570	31.41	20070	31.35	19460	31.36	19560
cc24	31.01	27920	30.99	27650	30.94	26990	30.85	25780	30.86	25920
cc30	30.42	35240	30.40	34910	30.37	34400	30.23	32050	30.27	32720
cc36	29.94	41940	29.94	41940	29.90	41140	29.72	37550	29.73	37750

Table C.12: Shell-side heat transfer coefficients and uncertainties for the Tu-Cii geometry

run	bundle				row 1		row 2		row 3		row 4		row 5	
	q'' W/m ²	q' W/m	h_o $\frac{W}{m^2 K}$	w $\pm \%$										
cc16	17780	1060	28930	22.	41280	34.	33200	28.	25350	23.	20960	19.	22550	20.
cc18	20130	1190	29590	20.	38490	29.	33380	26.	26140	21.	21250	18.	21950	18.
cc20	22240	1320	29540	18.	38880	27.	32640	23.	26980	20.	21450	16.	22820	17.
cc22	24700	1470	28890	16.	37980	24.	32400	21.	27190	18.	21330	15.	22580	15.
cc24	26670	1580	27700	15.	36660	21.	32800	19.	26890	17.	20820	14.	21960	14.
cc26	29070	1720	27110	13.	35990	19.	33580	18.	26970	15.	20650	13.	22270	13.
cc28	31380	1860	26710	12.	32830	17.	31820	16.	26030	14.	19830	12.	21790	12.
cc30	33560	1990	25150	11.	29520	14.	28730	14.	25230	13.	18730	10.	20430	11.
cc32	35710	2120	24930	10.	28780	13.	28780	13.	25410	12.	18660	10.	20280	11.
cc34	38130	2260	23880	9.	28540	13.	27860	12.	24810	11.	18200	9.	19290	10.
cc36	40160	2380	23540	9.	27920	12.	27290	12.	24430	11.	17480	9.	17800	9.
cc18	20100	1190	28800	20.	40690	30.	35090	27.	28340	22.	22780	19.	23570	19.
cc24	26810	1590	28440	15.	37660	22.	34900	20.	29330	18.	22430	14.	23060	15.
cc30	34070	2020	26780	11.	32140	15.	30360	15.	27990	14.	20030	11.	21900	12.
cc36	40450	2400	24340	9.	28550	12.	28550	12.	26060	11.	18130	9.	18470	9.

Table C.13: Refrigerant-side data for the G-SC geometry

run	q W	T_{sat} °C	inlet outlet		middle tube $T_{s,o}$					\dot{m} kg/min
			sh °C	sc °C	row 1 °C	row 2 °C	row 3 °C	row 4 °C	row 5 °C	
cd18	18030	34.96	3.38	.19	33.63	33.34	33.37	33.52	33.05	8.03
cd24	24200	34.95	2.95	.26	33.13	32.79	32.91	32.99	32.41	10.80
cd30	30300	34.96	3.08	.26	32.56	32.16	32.27	32.36	31.66	13.42
cd36	36150	35.03	3.40	.38	32.04	31.62	31.71	31.77	30.96	16.08
cd16	16090	35.00	4.74	.20	33.87	33.61	33.64	33.74	33.36	7.12
cd18	18020	35.04	3.50	.17	33.75	33.47	33.49	33.62	33.18	8.03
cd20	19980	34.99	3.30	.21	33.53	33.22	33.30	33.40	32.90	8.90
cd22	22080	35.00	4.59	.26	33.33	33.03	33.11	33.22	32.68	9.77
cd24	24120	35.01	2.93	.28	33.20	32.87	32.98	33.06	32.48	10.77
cd26	26060	34.94	3.10	.26	32.97	32.60	32.69	32.80	32.15	11.62
cd28	28180	34.98	3.57	.27	32.79	32.45	32.56	32.65	31.96	12.54
cd30	30400	35.00	2.26	.28	32.61	32.27	32.35	32.44	31.72	13.62
cd32	32080	35.00	2.96	.25	32.40	32.05	32.16	32.19	31.49	14.32
cd34	34080	35.02	2.78	.30	32.19	31.81	31.93	31.99	31.18	15.22
cd36	36140	35.02	3.19	.39	31.98	31.57	31.72	31.75	30.94	16.10

Table C.14: Water-side data for the G-SC geometry

run	q W	$T_{bulk,in}$ °C	$T_{bulk,out}$ °C	LMTD °C	\dot{m}_{bulk} kg/min	\dot{m}_{tube} kg/min	Re	$\frac{h_i}{W}$ $\frac{m^2}{m^2 K}$
cd18	17980	28.16	30.15	5.82	129.37	5.17	9600	6370
cd24	24300	27.24	29.27	6.75	172.19	6.89	12530	7940
cd30	30500	26.38	28.41	7.64	216.27	8.65	15440	9440
cd36	36670	25.46	27.53	8.64	253.83	10.15	17750	10630
cd16	15960	28.83	30.66	5.28	125.10	5.00	9410	6240
cd18	17910	28.26	30.25	5.81	129.40	5.18	9630	6380
cd20	19890	27.92	29.91	6.10	142.95	5.72	10550	6890
cd22	21990	27.62	29.63	6.41	157.67	6.31	11570	7430
cd24	24070	27.36	29.36	6.69	172.85	6.91	12610	7970
cd26	26070	27.01	29.01	6.99	187.45	7.50	13570	8470
cd28	28130	26.74	28.74	7.30	201.74	8.07	14510	8960
cd30	30570	26.39	28.43	7.67	215.23	8.61	15370	9410
cd32	32430	26.20	28.21	7.88	231.78	9.27	16470	9960
cd34	34420	25.88	27.90	8.22	244.69	9.79	17270	10370
cd36	36540	25.40	27.48	8.67	252.27	10.09	17620	10570

Table C.15: Row data for the G-SC geometry

run	row 1		row 2		row 3		row 4		row 5	
	$T_{w,out}$ °C	q'' W/m ²								
cd18	30.24	20890	30.13	19780	30.14	19880	30.20	20480	30.02	18680
cd24	29.35	28330	29.23	26730	29.27	27260	29.30	27660	29.09	24860
cd30	28.50	35590	28.36	33240	28.40	33910	28.43	34410	28.19	30380
cd36	27.63	42950	27.49	40190	27.52	40780	27.54	41180	27.27	35860
cd16	30.75	18930	30.65	17960	30.66	18060	30.70	18450	30.55	16990
cd18	30.34	21090	30.23	19990	30.24	20090	30.29	20590	30.12	18880
cd20	30.01	23300	29.89	21970	29.92	22300	29.96	22740	29.77	20640
cd22	29.71	25580	29.60	24230	29.63	24600	29.67	25090	29.47	22640
cd24	29.46	28170	29.34	26560	29.38	27100	29.41	27500	29.20	24690
cd26	29.11	30700	28.98	28810	29.01	29240	29.05	29830	28.82	26480
cd28	28.84	33040	28.72	31160	28.76	31790	28.79	32260	28.55	28500
cd30	28.52	35750	28.40	33750	28.43	34250	28.46	34750	28.21	30570
cd32	28.29	37780	28.17	35620	28.21	36340	28.22	36520	27.98	32200
cd34	27.99	40070	27.86	37610	27.90	38370	27.92	38750	27.65	33620
cd36	27.58	42690	27.44	39950	27.49	40930	27.50	41120	27.23	35830

Table C.16: Shell-side heat transfer coefficients and uncertainties for the G-SC geometry

run	bundle				row 1		row 2		row 3		row 4		row 5	
	q''	q'	h_o	w										
	W/m ²	W/m	$\frac{W}{m^2 K}$	± %										
cd18	20070	1190	13500	10.	16530	14.	12700	11.	12990	11.	14950	13.	10090	10.
cd24	27030	1610	13330	8.	16040	10.	12700	9.	13690	9.	14510	10.	9950	8.
cd30	33880	2020	12840	6.	15170	8.	12060	7.	12850	8.	13490	8.	9330	6.
cd36	40580	2410	12330	5.	14610	7.	11940	6.	12450	7.	12810	7.	8890	6.
cd16	17860	1060	13390	11.	17770	16.	13500	13.	13850	13.	15400	14.	10650	11.
cd18	20020	1190	13470	10.	17290	14.	13200	11.	13510	12.	15210	13.	10450	10.
cd20	22220	1320	13420	9.	16720	13.	12770	10.	13610	11.	14870	12.	10090	9.
cd22	24560	1460	13370	8.	15890	11.	12660	10.	13430	10.	14580	10.	9960	8.
cd24	26850	1600	13180	7.	16020	10.	12670	9.	13660	9.	14480	10.	9910	8.
cd26	29050	1730	13050	7.	16030	10.	12600	8.	13290	9.	14290	9.	9650	7.
cd28	31380	1870	12870	6.	15450	9.	12540	8.	13410	8.	14130	8.	9570	7.
cd30	33980	2020	12880	6.	15280	8.	12530	7.	13150	8.	13810	8.	9410	6.
cd32	35950	2140	12660	6.	14800	8.	12240	7.	13020	7.	13230	7.	9270	6.
cd34	38170	2270	12410	5.	14430	7.	11870	7.	12580	7.	12960	7.	8840	6.
cd36	40500	2410	12210	5.	14310	7.	11720	6.	12570	7.	12740	7.	8850	6.

APPENDIX D. TABULATED HCFC-123 CONDENSATION DATA

Table D.1: Refrigerant-side data for the 26-fpi geometry

run	q W	T_{sat} °C	inlet outlet		middle tube $T_{s,o}$					\dot{m} kg/min
			sh °C	sc °C	row 1 °C	row 2 °C	row 3 °C	row 4 °C	row 5 °C	
bf16	16080	35.02	3.43	.03	33.68	33.68	33.28	33.41	33.50	5.68
bf18	18060	35.03	4.14	.06	33.43	33.48	33.03	33.18	33.33	6.36
bf20	20250	35.06	5.03	.09	33.21	33.28	32.88	32.98	33.18	7.10
bf22	22070	35.05	4.07	.09	33.00	33.00	32.64	32.74	32.97	7.77
bf24	24160	35.07	5.81	.08	32.86	32.84	32.50	32.60	32.84	8.44
bf26	26150	35.04	4.65	.03	32.53	32.55	32.23	32.37	32.61	9.19
bf28	28360	35.02	5.73	.14	32.22	32.24	31.95	32.14	32.33	9.91
bf30	30450	34.97	6.31	.13	31.97	32.03	31.67	31.86	32.06	10.62
bf32	32370	35.00	7.04	.11	31.80	31.85	31.46	31.68	31.82	11.25
bf34	34070	34.99	7.58	.19	31.49	31.66	31.26	31.49	31.60	11.81
bf36	36170	35.01	8.03	.16	31.33	31.47	31.02	31.27	31.42	12.52
bf18	18180	34.91	5.32	-.09	33.37	33.39	32.95	33.07	33.22	6.37
bf24	24240	35.09	4.75	.05	32.77	32.74	32.40	32.53	32.82	8.51
bf30	30280	35.01	5.98	.20	31.94	32.02	31.66	31.91	32.07	10.57
bf36	36010	35.04	8.60	.24	31.24	31.41	30.99	31.24	31.39	12.43

Table D.2: Water-side data for the 26-fpi geometry

run	q W	$T_{bulk,in}$ °C	$T_{bulk,out}$ °C	LMTD °C	\dot{m}_{bulk} kg/min	\dot{m}_{tube} kg/min	Re	h_i
								$\frac{W}{m^2 K}$
bf16	15840	29.17	30.99	4.92	125.22	5.01	9330	6540
bf18	17840	28.55	30.52	5.47	130.28	5.21	9590	6710
bf20	20070	28.20	30.20	5.83	144.58	5.78	10570	7270
bf22	21930	27.88	29.88	6.14	157.86	6.31	11460	7780
bf24	24040	27.64	29.63	6.39	173.64	6.95	12540	8370
bf26	26110	27.28	29.28	6.72	187.21	7.49	13410	8860
bf28	28320	26.89	28.91	7.09	201.02	8.04	14280	9340
bf30	30550	26.50	28.54	7.42	215.41	8.62	15170	9830
bf32	32450	26.28	28.29	7.69	231.19	9.25	16200	10380
bf34	34290	25.99	28.01	7.97	243.70	9.75	16970	10790
bf36	36460	25.61	27.68	8.35	252.95	10.12	17470	11080
bf18	17950	28.41	30.40	5.49	129.63	5.19	9520	6680
bf24	24110	27.56	29.57	6.49	172.24	6.89	12420	8310
bf30	30350	26.53	28.56	7.44	215.06	8.60	15160	9820
bf36	36140	25.51	27.61	8.46	247.63	9.91	17070	10880

Table D.3: Row data for the 26-fpi geometry

run	row 1		row 2		row 3		row 4		row 5	
	$T_{w,out}$ °C	q'' W/m ²								
bf16	30.99	17830	30.99	17830	30.83	16260	30.88	16750	30.92	17150
bf18	30.50	19880	30.52	20080	30.34	18250	30.40	18860	30.46	19470
bf20	30.16	22170	30.19	22510	30.03	20700	30.07	21160	30.15	22060
bf22	29.85	24330	29.85	24330	29.71	22600	29.75	23100	29.84	24210
bf24	29.62	26770	29.61	26630	29.48	24860	29.52	25410	29.61	26630
bf26	29.23	28570	29.24	28710	29.12	26950	29.17	27690	29.26	29000
bf28	28.84	30670	28.85	30830	28.74	29100	28.81	30200	28.88	31300
bf30	28.48	33210	28.50	33540	28.37	31350	28.44	32530	28.51	33710
bf32	28.24	35460	28.26	35820	28.12	33290	28.20	34730	28.25	35640
bf34	27.92	36800	27.98	37950	27.84	35280	27.92	36800	27.96	37570
bf36	27.60	39390	27.65	40380	27.49	37210	27.58	39000	27.63	39980
bf18	30.39	20080	30.40	20180	30.22	18360	30.27	18870	30.33	19470
bf24	29.53	26550	29.52	26420	29.39	24660	29.44	25340	29.55	26820
bf30	28.48	32820	28.51	33320	28.38	31130	28.47	32650	28.53	33660
bf36	27.51	38760	27.57	39920	27.42	37010	27.51	38760	27.56	39730

Table D.4: Shell-side heat transfer coefficients and uncertainties for the 26-fpi geometry

run	bundle				row 1		row 2		row 3		row 4		row 5	
	q'' W/m ²	q' W/m	h_o W/m ² K	w ± %										
bf16	17940	1060	14090	16.	13780	17.	13780	17.	9580	13.	10660	14.	11660	15.
bf18	20170	1190	13660	14.	12870	15.	13440	15.	9350	12.	10480	13.	11820	14.
bf20	22650	1340	13350	13.	12280	13.	13030	13.	9660	11.	10380	11.	12050	13.
bf22	24720	1460	12860	11.	12140	12.	12140	12.	9530	10.	10190	10.	11920	12.
bf24	27080	1600	12850	10.	12400	11.	12190	11.	9820	10.	10470	10.	12190	11.
bf26	29360	1730	12590	9.	11530	10.	11710	10.	9710	9.	10480	9.	12100	10.
bf28	31840	1880	12430	9.	11100	9.	11270	9.	9570	8.	10610	9.	11800	9.
bf30	34270	2020	12270	8.	11200	8.	11530	9.	9580	8.	10580	8.	11700	9.
bf32	36420	2150	12070	7.	11200	8.	11520	8.	9490	7.	10590	8.	11360	8.
bf34	38400	2270	11900	7.	10610	7.	11510	8.	9540	7.	10610	7.	11200	8.
bf36	40800	2410	11860	7.	10790	7.	11520	7.	9380	7.	10510	7.	11220	7.
bf18	20300	1200	14050	15.	13450	15.	13750	16.	9530	12.	10490	13.	11830	14.
bf24	27160	1600	12570	10.	11650	10.	11450	10.	9290	9.	10050	10.	12050	11.
bf30	34060	2010	12030	8.	10790	8.	11270	8.	9380	8.	10640	8.	11600	9.
bf36	40530	2390	11590	7.	10290	7.	11110	7.	9200	7.	10290	7.	10970	7.

Table D.5: Refrigerant-side data for the 40-fpi geometry

run	q W	T_{sat} °C	inlet outlet		middle tube $T_{s,o}$					\dot{m} kg/min
			sh °C	sc °C	row 1 °C	row 2 °C	row 3 °C	row 4 °C	row 5 °C	
bg18	18130	34.99	3.50	.08	33.76	33.51	33.70	33.59	33.48	6.40
bg24	24090	34.96	4.55	.19	33.23	32.88	33.23	33.08	32.85	8.46
bg30	30160	35.01	6.34	.18	32.79	32.33	32.73	32.52	32.15	10.51
bg36	35970	35.02	9.88	.22	32.36	31.76	32.13	31.85	31.47	12.35
bg16	16110	34.93	4.24	.02	33.82	33.63	33.77	33.66	33.58	5.67
bg18	18080	34.97	2.94	.07	33.77	33.52	33.74	33.60	33.46	6.39
bg20	20130	34.96	5.68	.14	33.59	33.36	33.56	33.42	33.25	7.03
bg22	22150	34.95	5.30	.06	33.38	33.15	33.44	33.27	33.10	7.76
bg24	24170	34.97	5.94	.12	33.32	33.00	33.32	33.15	32.88	8.44
bg26	26160	35.02	6.11	.15	33.21	32.82	33.18	33.00	32.70	9.13
bg28	28160	35.00	5.24	.09	32.98	32.59	32.95	32.80	32.44	9.86
bg30	30250	35.03	6.32	.06	32.86	32.41	32.80	32.59	32.23	10.55
bg32	32330	35.00	7.72	.17	32.70	32.17	32.54	32.30	31.92	11.20
bg34	34220	34.96	7.49	.28	32.49	31.90	32.28	32.02	31.68	11.86
bg36	36170	34.99	8.68	.26	32.35	31.71	32.12	31.84	31.43	12.47

Table D.6: Water-side data for the 40-fpi geometry

run	q W	$T_{bulk,in}$ °C	$T_{bulk,out}$ °C	LMTD °C	\dot{m}_{bulk} kg/min	\dot{m}_{tube} kg/min	Re	h_i $\frac{W}{m^2 K}$
bg18	17940	28.21	30.20	5.78	129.36	5.17	8620	5340
bg24	23990	27.36	29.36	6.63	172.20	6.89	11260	6650
bg30	30170	26.52	28.53	7.54	215.76	8.63	13850	7900
bg36	36110	25.54	27.60	8.51	251.29	10.05	15790	8840
bg16	15890	28.82	30.63	5.19	125.75	5.03	8480	5250
bg18	17860	28.25	30.22	5.74	130.31	5.21	8690	5370
bg20	19950	27.90	29.90	6.06	143.22	5.73	9480	5770
bg22	21980	27.67	29.66	6.29	158.38	6.34	10430	6240
bg24	24010	27.43	29.43	6.58	172.93	6.92	11330	6680
bg26	25980	27.21	29.20	6.84	187.90	7.52	12250	7120
bg28	28030	26.89	28.89	7.16	201.62	8.06	13050	7510
bg30	30190	26.57	28.58	7.50	214.76	8.59	13800	7880
bg32	32360	26.24	28.25	7.82	231.26	9.25	14750	8330
bg34	34300	25.89	27.91	8.12	244.29	9.77	15460	8670
bg36	36310	25.52	27.58	8.51	253.00	10.12	15890	8880

Table D.7: Row data for the 40-fpi geometry

run	row 1		row 2		row 3		row 4		row 5	
	$T_{w,out}$ °C	q'' W/m ²								
bg18	30.21	20130	30.12	19230	30.19	19930	30.15	19530	30.11	19120
bg24	29.36	26800	29.24	25190	29.36	26800	29.31	26130	29.23	25060
bg30	28.56	34250	28.41	31730	28.54	33910	28.47	32740	28.35	30720
bg36	27.68	41850	27.49	38130	27.61	40480	27.52	38720	27.40	36370
bg16	30.64	17810	30.57	17120	30.62	17610	30.58	17220	30.55	16930
bg18	30.23	20180	30.14	19260	30.22	20080	30.17	19570	30.12	19060
bg20	29.91	22400	29.83	21510	29.90	22290	29.85	21730	29.79	21060
bg22	29.65	24400	29.57	23410	29.67	24650	29.61	23910	29.55	23170
bg24	29.43	27050	29.32	25570	29.43	27050	29.37	26240	29.28	25030
bg26	29.22	29390	29.09	27490	29.21	29240	29.15	28360	29.05	26900
bg28	28.90	31530	28.77	29490	28.89	31380	28.84	30590	28.72	28710
bg30	28.62	34260	28.47	31750	28.60	33920	28.53	32750	28.41	30750
bg32	28.31	37250	28.14	34190	28.26	36350	28.18	34910	28.06	32750
bg34	27.98	39730	27.79	36120	27.91	38400	27.83	36880	27.72	34790
bg36	27.66	42130	27.46	38190	27.59	40750	27.50	38980	27.37	36420

Table D.8: Shell-side heat transfer coefficients and uncertainties for the 40-fpi geometry

run	bundle				row 1		row 2		row 3		row 4		row 5	
	q'' W/m ²	q' W/m	h_o $\frac{W}{m^2 K}$	w $\pm \%$										
bg18	20150	1200	17110	18.	17110	20.	13450	16.	16160	19.	14510	17.	13120	16.
bg24	26860	1590	16010	13.	15880	14.	12330	12.	15880	14.	14230	13.	12090	12.
bg30	33700	2000	14810	10.	15730	11.	12010	10.	15150	11.	13330	10.	10870	9.
bg36	40270	2390	13980	8.	15960	10.	11810	8.	14220	9.	12360	8.	10340	8.
bg16	17880	1060	17170	20.	16930	22.	13730	18.	15900	21.	14130	19.	12990	18.
bg18	20080	1190	17130	18.	17570	20.	13740	17.	17060	20.	14850	18.	13070	16.
bg20	22390	1330	16920	16.	17040	18.	13930	15.	16590	17.	14620	16.	12700	14.
bg22	24650	1460	16860	15.	16090	16.	13380	14.	16910	16.	14640	15.	12820	13.
bg24	26920	1600	16620	13.	16900	15.	13270	13.	16900	15.	14750	14.	12240	12.
bg26	29130	1730	16030	12.	16670	14.	12760	11.	16310	13.	14370	12.	11830	11.
bg28	31390	1860	15620	11.	15910	12.	12400	11.	15590	12.	14130	11.	11340	10.
bg30	33760	2000	15240	10.	16170	12.	12290	10.	15560	11.	13660	10.	11110	9.
bg32	36140	2140	14710	9.	16460	11.	12230	9.	15020	10.	13070	10.	10750	9.
bg34	38280	2270	14380	8.	16400	11.	11940	9.	14520	10.	12720	9.	10710	8.
bg36	40490	2400	14110	8.	16180	10.	11770	8.	14410	9.	12510	8.	10310	8.

Table D.9: Refrigerant-side data for the Tu-Cii geometry

run	q W	T_{sat} °C	inlet outlet		middle tube $T_{s,o}$					\dot{m} kg/min
			sh °C	sc °C	row 1 °C	row 2 °C	row 3 °C	row 4 °C	row 5 °C	
bc18	18170	34.97	3.98	.15	34.09	34.21	33.95	33.86	33.83	6.39
bc24	24230	35.08	4.91	.29	33.91	34.06	33.76	33.58	33.56	8.49
bc30	30180	35.04	6.80	.37	33.57	33.67	33.44	33.21	33.10	10.48
bc36	36190	35.06	8.99	.53	33.16	33.24	33.00	32.65	32.49	12.45
bc16	16110	34.92	3.52	.08	34.20	34.34	34.10	34.01	33.96	5.68
bc18	18120	34.98	3.83	.10	34.16	34.33	34.09	34.00	33.93	6.38
bc20	20250	34.95	4.00	.14	34.04	34.19	33.95	33.83	33.75	7.13
bc22	22240	34.95	4.12	.17	33.93	34.08	33.86	33.69	33.66	7.82
bc24	24220	35.08	4.95	.23	33.98	34.13	33.85	33.68	33.63	8.49
bc26	26120	35.06	4.14	.26	33.84	33.99	33.74	33.53	33.48	9.18
bc28	28310	35.06	5.49	.31	33.70	33.83	33.57	33.37	33.29	9.89
bc30	30440	34.98	6.80	.36	33.49	33.64	33.38	33.13	33.02	10.58
bc32	32490	35.02	7.50	.45	33.36	33.46	33.23	32.94	32.83	11.25
bc34	34430	34.98	6.74	.50	33.20	33.28	33.06	32.74	32.58	11.95
bc36	36280	35.05	8.07	.53	33.13	33.21	32.97	32.62	32.44	12.53

Table D.10: Water-side data for the Tu-Cii geometry

run	q W	$T_{bulk,in}$ °C	$T_{bulk,out}$ °C	LMTD °C	\dot{m}_{bulk} kg/min	\dot{m}_{tube} kg/min	Re	h_i $\frac{W}{m^2 K}$
bc18	17900	29.39	31.38	4.59	129.05	5.16	8990	6600
bc24	23870	28.91	30.91	5.19	170.84	6.83	11780	8220
bc30	29900	28.37	30.35	5.72	216.80	8.67	14780	9890
bc36	35900	27.60	29.62	6.52	254.56	10.18	17070	11160
bc16	15630	29.98	31.77	4.04	125.24	5.01	8820	6470
bc18	17790	29.53	31.50	4.47	129.69	5.19	9060	6630
bc20	19950	29.29	31.27	4.68	145.24	5.81	10100	7240
bc22	21880	29.08	31.07	4.88	157.87	6.31	10930	7730
bc24	23850	29.00	30.99	5.10	172.81	6.91	11940	8300
bc26	25780	28.81	30.79	5.28	186.80	7.47	12850	8820
bc28	27770	28.57	30.55	5.53	201.53	8.06	13800	9350
bc30	30050	28.21	30.21	5.80	214.92	8.60	14600	9800
bc32	32140	28.02	30.02	6.04	231.30	9.25	15650	10380
bc34	33980	27.70	29.70	6.33	243.65	9.75	16370	10780
bc36	35630	27.56	29.56	6.55	255.29	10.21	17100	11180

Table D.11: Row data for the Tu-Cii geometry

run	row 1		row 2		row 3		row 4		row 5	
	$T_{w,out}$ °C	q'' W/m ²								
bc18	31.37	19880	31.42	20380	31.31	19280	31.27	18880	31.26	18780
bc24	30.91	26590	30.97	27380	30.85	25790	30.78	24860	30.77	24720
bc30	30.36	33570	30.40	34240	30.31	32730	30.22	31210	30.18	30530
bc36	29.65	40800	29.68	41400	29.59	39610	29.46	37040	29.40	35850
bc16	31.77	17440	31.83	18030	31.73	17050	31.69	16660	31.67	16470
bc18	31.48	19680	31.55	20380	31.45	19370	31.41	18970	31.38	18670
bc20	31.25	22150	31.31	22830	31.21	21700	31.16	21130	31.13	20790
bc22	31.05	24200	31.11	24940	31.02	23830	30.95	22970	30.94	22850
bc24	30.99	26760	31.05	27560	30.94	26090	30.87	25140	30.85	24880
bc26	30.79	28780	30.85	29650	30.75	28200	30.67	27030	30.65	26740
bc28	30.56	31200	30.61	31990	30.51	30420	30.43	29170	30.40	28690
bc30	30.23	33780	30.29	34780	30.19	33110	30.09	31440	30.05	30770
bc32	30.04	36170	30.08	36890	29.99	35280	29.88	33300	29.84	32580
bc34	29.75	38860	29.78	39430	29.70	37920	29.58	35640	29.52	34500
bc36	29.62	40920	29.65	41520	29.56	39730	29.43	37150	29.36	35750

Table D.12: Shell-side heat transfer coefficients and uncertainties for the Tu-Cii geometry

run	bundle				row 1		row 2		row 3		row 4		row 5	
	q'' W/m ²	q' W/m	h_o $\frac{W}{m^2 K}$	w ± %										
bc18	20150	1200	26510	27.	24380	27.	29380	32.	20050	23.	17830	21.	17340	20.
bc24	26880	1590	24960	19.	23730	20.	28300	23.	20250	18.	17130	16.	16740	15.
bc30	33560	1990	23500	15.	23610	16.	26030	17.	21050	15.	17410	13.	16080	12.
bc36	40270	2390	20970	11.	22060	13.	23430	13.	19680	12.	15640	10.	14160	10.
bc16	17730	1050	29000	34.	26210	33.	34640	42.	22370	29.	19400	25.	18150	24.
bc18	20060	1190	29620	30.	25910	29.	34620	37.	23270	26.	20400	24.	18620	22.
bc20	22460	1330	28590	26.	26080	26.	32600	31.	22880	23.	19710	21.	18130	19.
bc22	24650	1460	28020	24.	25150	23.	30740	27.	22970	21.	18930	18.	18450	18.
bc24	26860	1590	26090	20.	25630	21.	30930	25.	22260	19.	18620	17.	17760	16.
bc26	29000	1720	25370	18.	24530	19.	29120	22.	22090	18.	18230	15.	17420	15.
bc28	31330	1860	24030	16.	23750	17.	27040	19.	21050	16.	17630	14.	16560	13.
bc30	33800	2010	23270	15.	23400	16.	27080	18.	21360	15.	17320	13.	16020	12.
bc32	36100	2140	22010	13.	22370	14.	24440	15.	20140	13.	16270	12.	15130	11.
bc34	38220	2270	20770	12.	22350	13.	23790	14.	20230	13.	16200	11.	14600	10.
bc36	40170	2380	20230	11.	21870	13.	23210	13.	19520	12.	15540	10.	13850	9.

Table D.13: Refrigerant-side data for the G-SC geometry

run	q W	T_{sat} °C	inlet outlet		middle tube $T_{s,o}$					\dot{m} kg/min
			sh °C	sc °C	row 1 °C	row 2 °C	row 3 °C	row 4 °C	row 5 °C	
bd18	18210	35.08	3.87	.09	33.40	33.48	33.14	33.55	33.29	6.42
bd24	24270	35.04	4.02	.19	32.75	32.86	32.59	32.95	32.67	8.54
bd30	30200	35.02	5.91	.30	32.19	32.22	31.90	32.28	31.96	10.54
bd36	36180	35.07	7.20	.39	31.48	31.57	31.30	31.66	31.33	12.55
bd16	16120	34.96	5.47	.04	33.51	33.56	33.22	33.61	33.40	5.64
bd18	18170	35.03	4.60	.10	33.35	33.43	33.09	33.51	33.25	6.38
bd20	20210	35.00	6.06	.11	33.13	33.29	33.00	33.37	33.11	7.06
bd22	22130	35.01	4.46	.12	33.04	33.12	32.87	33.22	32.93	7.77
bd24	24190	35.01	3.70	.08	32.84	32.95	32.70	33.00	32.73	8.53
bd26	26090	35.02	4.35	.20	32.65	32.76	32.51	32.82	32.54	9.16
bd28	28270	35.01	4.77	.17	32.42	32.50	32.27	32.56	32.27	9.91
bd30	30230	35.07	5.98	.22	32.34	32.43	32.17	32.49	32.20	10.55
bd32	32180	34.98	5.83	.26	32.08	32.11	31.91	32.17	31.88	11.23
bd34	34320	34.94	7.70	.35	31.81	31.87	31.60	31.90	31.60	11.88
bd36	36290	35.06	8.36	.35	31.60	31.66	31.42	31.72	31.42	12.53

Table D.14: Water-side data for the G-SC geometry

run	q W	$T_{bulk,in}$ °C	$T_{bulk,out}$ °C	LMTD °C	\dot{m}_{bulk} kg/min	\dot{m}_{tube} kg/min	Re	h_i $\frac{W}{m^2 K}$
bd18	17730	28.26	30.23	5.82	129.28	5.17	9610	6380
bd24	23780	27.37	29.35	6.68	172.19	6.89	12560	7950
bd30	29970	26.49	28.48	7.56	215.51	8.62	15410	9420
bd36	36110	25.47	27.53	8.60	252.02	10.08	17630	10570
bd16	15850	28.85	30.67	5.19	125.25	5.01	9420	6250
bd18	17950	28.25	30.24	5.78	129.92	5.20	9660	6400
bd20	19990	28.03	30.00	5.98	145.38	5.82	10760	6990
bd22	21930	27.74	29.74	6.27	157.76	6.31	11600	7440
bd24	24000	27.47	29.45	6.55	173.24	6.93	12660	7990
bd26	25950	27.20	29.19	6.83	187.47	7.50	13620	8490
bd28	28150	26.83	28.83	7.20	201.59	8.06	14530	8970
bd30	30190	26.68	28.68	7.41	216.03	8.64	15520	9460
bd32	32240	26.33	28.33	7.68	231.78	9.27	16520	9970
bd34	34450	25.92	27.95	8.03	243.31	9.73	17190	10320
bd36	36350	25.56	27.62	8.49	253.06	10.12	17740	10620

Table D.15: Row data for the G-SC geometry

run	row 1		row 2		row 3		row 4		row 5	
	$T_{w,out}$ °C	q'' W/m ²								
bd18	30.21	19670	30.24	19970	30.11	18660	30.27	20270	30.17	19260
bd24	29.30	25930	29.34	26460	29.24	25130	29.37	26860	29.27	25530
bd30	28.44	32790	28.45	32950	28.34	31110	28.47	33290	28.36	31450
bd36	27.46	38930	27.49	39520	27.40	37760	27.52	40100	27.41	37950
bd16	30.64	17400	30.66	17600	30.53	16330	30.68	17790	30.60	17010
bd18	30.19	19560	30.22	19860	30.09	18550	30.25	20170	30.15	19160
bd20	29.93	21440	29.99	22120	29.88	20880	30.02	22450	29.92	21330
bd22	29.68	23750	29.71	24120	29.62	23020	29.75	24610	29.64	23260
bd24	29.40	25950	29.44	26490	29.35	25280	29.46	26760	29.36	25410
bd26	29.13	28080	29.17	28670	29.08	27360	29.19	28960	29.09	27500
bd28	28.77	30510	28.80	30980	28.72	29730	28.82	31290	28.72	29730
bd30	28.62	32700	28.65	33200	28.56	31690	28.67	33540	28.57	31860
bd32	28.27	35080	28.28	35260	28.21	34000	28.30	35620	28.20	33820
bd34	27.89	37210	27.91	37580	27.82	35880	27.92	37770	27.82	35880
bd36	27.56	39290	27.58	39680	27.50	38110	27.60	40070	27.50	38110

Table D.16: Shell-side heat transfer coefficients and uncertainties for the G-SC geometry

run	bundle				row 1		row 2		row 3		row 4		row 5	
	q'' W/m ²	q' W/m	h_o $\frac{W}{m^2 K}$	w ± %										
bd18	20030	1190	13060	14.	12100	14.	12920	15.	9860	12.	13830	16.	11120	13.
bd24	26770	1590	12950	11.	11560	11.	12420	11.	10420	10.	13130	12.	10970	10.
bd30	33530	1990	12650	8.	11780	9.	11970	9.	10120	8.	12350	9.	10420	8.
bd36	40290	2400	12060	7.	10960	7.	11420	8.	10110	7.	11910	8.	10250	7.
bd16	17820	1060	13790	16.	12440	16.	13080	17.	9670	14.	13760	18.	11310	15.
bd18	20130	1200	13640	14.	12070	14.	12890	15.	9830	12.	13810	16.	11090	13.
bd20	22410	1330	14090	13.	11810	13.	13390	14.	10700	12.	14300	15.	11580	13.
bd22	24550	1460	14100	12.	12380	12.	13140	13.	11040	11.	14260	14.	11460	12.
bd24	26860	1600	13790	11.	12200	11.	13150	12.	11150	11.	13660	12.	11350	11.
bd26	29000	1730	13560	10.	12120	11.	13020	11.	11120	10.	13500	11.	11310	10.
bd28	31440	1870	13260	9.	11980	10.	12590	10.	11040	9.	13030	10.	11040	9.
bd30	33670	2000	13440	9.	12200	9.	12810	10.	11100	9.	13240	10.	11270	9.
bd32	35900	2140	13280	8.	12310	9.	12500	9.	11220	8.	12900	9.	11060	8.
bd34	38320	2280	13200	8.	12070	8.	12440	9.	10900	8.	12630	9.	10900	8.
bd36	40480	2410	12520	7.	11490	8.	11820	8.	10580	7.	12150	8.	10580	7.

APPENDIX E. TABULATED CFC-11 CONDENSATION DATA

Table E.1: Refrigerant-side data for the 26-fpi geometry

run	q W	T_{sat} °C	inlet outlet		middle tube $T_{s,o}$					\dot{m} kg/min
			sh °C	sc °C	row 1 °C	row 2 °C	row 3 °C	row 4 °C	row 5 °C	
df18	18060	34.93	3.58	.43	33.01	32.98	32.43	32.61	32.78	6.07
df24	23870	34.99	2.91	.43	32.47	32.47	31.97	32.18	32.42	8.04
df30	29820	34.99	3.78	.44	31.77	31.83	31.42	31.72	31.80	10.01
df36	35920	35.07	5.32	.52	31.20	31.32	30.77	31.12	31.18	11.99
df16	16070	34.97	2.39	.51	33.18	33.08	32.54	32.73	32.91	5.42
df18	18020	34.98	4.77	.69	33.00	32.92	32.30	32.53	32.78	6.02
df20	20150	34.94	5.19	.41	32.81	32.76	32.17	32.38	32.61	6.73
df22	22080	35.02	4.06	.57	32.66	32.61	32.07	32.22	32.53	7.40
df24	24060	34.97	3.50	.38	32.36	32.36	31.89	32.10	32.34	8.09
df26	26030	35.03	4.42	.48	32.21	32.21	31.75	32.00	32.21	8.72
df28	27760	35.04	3.22	.51	31.98	32.01	31.62	31.90	32.06	9.34
df30	29910	35.07	2.69	.51	31.81	31.87	31.46	31.76	31.84	10.08
df32	32100	35.00	3.93	.50	31.52	31.57	31.15	31.46	31.52	10.77
df34	33960	35.09	4.65	.58	31.40	31.46	31.01	31.32	31.40	11.36
df36	36180	35.02	4.09	.43	31.18	31.27	30.72	31.07	31.12	12.13

Table E.2: Water-side data for the 26-fpi geometry

run	q W	$T_{bulk,in}$ °C	$T_{bulk,out}$ °C	LMTD °C	\dot{m}_{bulk} kg/min	\dot{m}_{tube} kg/min	Re	$\frac{h_i}{W}$ $\frac{1}{m^2 \cdot K}$
df18	18020	27.98	29.97	5.94	129.86	5.19	9450	6660
df24	23960	27.19	29.20	6.77	171.91	6.88	12290	8270
df30	30100	26.36	28.37	7.61	214.98	8.60	15090	9800
df36	36710	25.51	27.54	8.54	259.40	10.38	17860	11290
df16	16020	28.55	30.38	5.50	125.64	5.03	9240	6520
df18	18020	27.93	29.92	6.04	130.06	5.20	9450	6660
df20	20140	27.63	29.64	6.29	144.20	5.77	10410	7210
df22	22130	27.39	29.41	6.60	157.88	6.32	11340	7740
df24	24130	27.15	29.14	6.79	174.19	6.97	12440	8350
df26	26150	26.90	28.89	7.11	188.05	7.52	13360	8850
df28	28260	26.61	28.63	7.39	201.19	8.05	14200	9320
df30	30270	26.37	28.39	7.67	215.45	8.62	15130	9820
df32	32600	25.99	28.01	7.99	230.52	9.22	16050	10320
df34	34580	25.78	27.80	8.28	244.82	9.79	16960	10810
df36	36930	25.40	27.45	8.60	258.27	10.33	17750	11240

Table E.3: Row data for the 26-fpi geometry

run	row 1		row 2		row 3		row 4		row 5	
	$T_{w,out}$ °C	q'' W/m ²								
df18	29.98	20320	29.97	20220	29.75	17990	29.82	18700	29.89	19410
df24	29.18	26770	29.18	26770	28.99	24210	29.07	25290	29.16	26500
df30	28.31	32800	28.33	33140	28.18	30620	28.29	32470	28.32	32970
df36	27.48	39990	27.52	40800	27.33	36940	27.45	39380	27.47	39790
df16	30.41	18290	30.37	17890	30.15	15730	30.23	16520	30.30	17200
df18	29.94	20560	29.91	20250	29.66	17710	29.75	18620	29.85	19640
df20	29.65	22790	29.63	22570	29.40	19970	29.48	20870	29.57	21890
df22	29.41	24950	29.39	24710	29.18	22110	29.24	22850	29.36	24340
df24	29.11	26720	29.11	26720	28.93	24260	29.01	25350	29.10	26580
df26	28.86	28990	28.86	28990	28.69	26490	28.78	27810	28.86	28990
df28	28.57	30860	28.58	31010	28.44	28810	28.54	30380	28.60	31330
df30	28.33	33040	28.35	33380	28.20	30850	28.31	32710	28.34	33210
df32	27.95	35360	27.97	35720	27.82	33010	27.93	34990	27.95	35360
df34	27.75	37740	27.77	38120	27.61	35060	27.72	37170	27.75	37740
df36	27.40	40420	27.43	41030	27.24	37190	27.36	39610	27.38	40020

Table E.4: Shell-side heat transfer coefficients and uncertainties for the 26-fpi geometry

run	bundle				row 1		row 2		row 3		row 4		row 5	
	q'' W/m ²	q' W/m	h_o $\frac{W}{m^2 K}$	w $\pm \%$										
df18	20270	1200	10730	11.	10860	12.	10660	12.	7320	9.	8200	10.	9240	11.
df24	26870	1590	10930	8.	10770	9.	10770	9.	8090	8.	9100	8.	10440	9.
df30	33660	1990	11090	7.	10310	8.	10600	8.	8640	7.	10030	8.	10460	8.
df36	40810	2410	11000	6.	10420	7.	10970	7.	8650	6.	10040	7.	10290	7.
df16	18030	1060	9970	11.	10500	13.	9710	12.	6560	10.	7520	10.	8520	11.
df18	20250	1190	10160	10.	10670	12.	10110	11.	6710	9.	7730	9.	9110	10.
df20	22630	1340	10700	10.	10960	11.	10590	11.	7320	9.	8280	9.	9570	10.
df22	24840	1470	10640	9.	10780	10.	10430	10.	7570	8.	8270	8.	9940	9.
df24	27080	1600	10870	8.	10420	9.	10420	9.	7960	8.	8950	8.	10260	9.
df26	29310	1730	10790	8.	10410	8.	10410	8.	8160	8.	9260	8.	10410	8.
df28	31480	1860	10820	7.	10190	8.	10340	8.	8510	7.	9770	8.	10640	8.
df30	33810	1990	10950	7.	10260	8.	10550	8.	8610	7.	9980	7.	10400	8.
df32	36350	2140	11050	7.	10250	7.	10530	7.	8650	7.	9980	7.	10250	7.
df34	38510	2270	10900	6.	10330	7.	10600	7.	8650	6.	9940	7.	10330	7.
df36	41080	2420	11070	6.	10600	7.	11010	7.	8690	6.	10080	7.	10340	7.

Table E.5: Refrigerant-side data for the 40-fpi geometry

run	q W	T_{sat} °C	inlet outlet		middle tube $T_{s,o}$					\dot{m} kg/min
			sh °C	sc °C	row 1 °C	row 2 °C	row 3 °C	row 4 °C	row 5 °C	
d618	17970	35.02	3.41	.44	33.40	33.15	33.26	33.18	33.04	6.04
dg24	24020	34.95	4.26	.42	32.93	32.58	32.81	32.72	32.40	8.05
dg30	30070	34.99	3.22	.58	32.62	32.07	32.44	32.28	31.82	10.10
dg36	35920	35.11	.33	.57	32.36	31.72	32.07	31.79	31.37	12.20
dg16	16060	34.96	2.90	.41	33.52	33.24	33.35	33.30	33.19	5.41
dg18	18110	35.08	5.00	.77	33.55	33.28	33.39	33.28	33.14	6.05
dg20	20090	34.95	3.08	.60	33.25	32.97	33.14	33.02	32.83	6.75
dg22	22060	34.99	3.67	.53	33.13	32.85	33.07	32.93	32.70	7.41
dg24	24120	35.02	4.01	.59	33.01	32.72	32.95	32.84	32.51	8.08
dg26	26110	35.01	4.52	.61	32.85	32.47	32.79	32.68	32.29	8.74
dg28	27870	35.02	3.42	.79	32.80	32.34	32.65	32.52	32.07	9.35
dg30	30070	35.04	3.64	.61	32.67	32.12	32.49	32.34	31.88	10.09
dg32	32210	35.08	4.98	.62	32.52	31.93	32.30	32.08	31.68	10.76
dg34	34150	35.02	1.96	.59	32.29	31.60	32.04	31.79	31.38	11.53
dg36	36470	34.96	2.53	.81	32.08	31.41	31.82	31.54	31.19	11.99

Table E.6: Water-side data for the 40-fpi geometry

run	q W	$T_{bulk,in}$ °C	$T_{bulk,out}$ °C	LMTD °C	\dot{m}_{bulk} kg/min	\dot{m}_{tube} kg/min	Re	h_i $\frac{W}{m^2 K}$
d618	17920	27.82	29.81	6.21	129.29	5.17	8540	5320
dg24	24050	26.98	28.98	7.01	172.42	6.90	11180	6630
dg30	30390	26.13	28.15	7.94	215.53	8.62	13720	7860
dg36	36230	25.52	27.56	8.64	255.26	10.21	16030	8950
dg16	15980	28.40	30.23	5.66	125.07	5.00	8350	5200
dg18	18030	27.90	29.89	6.19	130.19	5.21	8620	5350
dg20	20130	27.48	29.49	6.48	143.66	5.75	9420	5760
dg22	22050	27.29	29.30	6.72	157.65	6.31	10300	6200
dg24	24190	27.07	29.07	6.99	173.42	6.94	11270	6670
dg26	26220	26.78	28.80	7.27	187.16	7.49	12090	7070
dg28	28070	26.60	28.60	7.49	202.02	8.08	12990	7500
dg30	30440	26.24	28.26	7.86	216.37	8.65	13810	7900
dg32	32510	25.94	27.96	8.21	230.45	9.22	14600	8280
dg34	34720	25.54	27.59	8.53	243.92	9.76	15320	8630
dg36	36470	25.28	27.32	8.73	257.68	10.31	16090	8990

Table E.7: Row data for the 40-fpi geometry

run	row 1		row 2		row 3		row 4		row 5	
	$T_{w,out}$ °C	q'' W/m ²								
d618	29.83	20120	29.74	19210	29.78	19620	29.75	19310	29.70	18810
dg24	29.00	27100	28.88	25490	28.96	26560	28.93	26160	28.82	24690
dg30	28.20	35550	28.02	32540	28.14	34550	28.09	33710	27.94	31190
dg36	27.66	42510	27.46	38540	27.57	40720	27.48	38930	27.35	36350
dg16	30.25	18100	30.15	17130	30.19	17520	30.17	17320	30.13	16930
dg18	29.93	20560	29.83	19550	29.87	19960	29.83	19550	29.78	19040
dg20	29.51	22690	29.41	21570	29.47	22240	29.43	21800	29.36	21010
dg22	29.31	24780	29.21	23550	29.29	24530	29.24	23920	29.16	22940
dg24	29.08	27260	28.98	25910	29.06	26990	29.02	26450	28.91	24960
dg26	28.81	29560	28.68	27670	28.79	29270	28.75	28690	28.62	26800
dg28	28.64	32070	28.49	29710	28.59	31280	28.55	30650	28.40	28300
dg30	28.32	35190	28.14	32160	28.26	34180	28.21	33340	28.06	30810
dg32	28.03	37840	27.84	34430	27.96	36580	27.89	35330	27.76	33000
dg34	27.67	40430	27.45	36250	27.59	38910	27.51	37390	27.38	34930
dg36	27.40	42510	27.19	38300	27.32	40910	27.23	39100	27.12	36900

Table E.8: Shell-side heat transfer coefficients and uncertainties for the 40-fpi geometry

run	bundle				row 1		row 2		row 3		row 4		row 5	
	q'' W/m ²	q' W/m	h_o $\frac{\ddot{w}}{m^2 K}$	w ± %										
d618	20050	1190	12520	13.	12810	14.	10530	12.	11460	13.	10750	13.	9710	12.
dg24	26860	1590	13250	10.	13740	12.	10950	10.	12710	11.	12000	11.	9850	10.
dg30	33770	2000	12980	8.	15310	10.	11290	9.	13770	10.	12650	9.	9970	8.
dg36	40310	2390	13160	7.	15660	9.	11490	8.	13560	8.	11830	8.	9800	7.
dg16	17900	1060	12360	14.	12970	16.	10230	13.	11200	14.	10700	14.	9780	13.
dg18	20190	1200	12770	13.	13940	15.	11130	13.	12140	14.	11130	13.	10030	12.
dg20	22470	1330	13140	12.	13740	14.	11130	12.	12590	13.	11590	12.	10090	11.
dg22	24640	1460	13350	11.	13660	13.	11190	11.	13110	12.	11850	12.	10190	10.
dg24	26990	1600	13400	10.	13880	12.	11460	10.	13340	12.	12350	11.	10110	10.
dg26	29230	1730	13430	10.	13970	11.	11040	10.	13450	11.	12490	10.	9970	9.
dg28	31250	1850	13360	9.	14670	11.	11240	9.	13380	10.	12460	10.	9690	9.
dg30	33810	2010	13200	8.	15160	10.	11170	9.	13630	10.	12520	9.	9850	8.
dg32	36160	2150	12930	8.	14990	10.	11030	8.	13330	9.	11920	8.	9790	8.
dg34	38480	2280	12800	7.	15030	9.	10690	8.	13210	9.	11690	8.	9670	7.
dg36	40750	2420	13040	7.	14940	9.	10880	7.	13180	8.	11520	8.	9850	7.

Table E.9: Refrigerant-side data for the Tu-Cii geometry

run	q W	T_{sat} °C	inlet outlet		middle tube $T_{s,o}$					\dot{m} kg/min
			sh °C	sc °C	row 1 °C	row 2 °C	row 3 °C	row 4 °C	row 5 °C	
dc18	18140	34.91	4.81	.55	33.69	33.81	33.50	33.43	33.41	6.06
dc24	24100	35.02	4.66	.50	33.56	33.69	33.39	33.22	33.19	8.07
dc30	30350	35.04	6.00	.69	33.25	33.33	33.04	32.78	32.75	10.10
dc36	35920	34.99	8.02	.99	32.83	32.88	32.61	32.23	32.18	11.86
dc16	16090	34.97	3.58	.43	33.88	33.98	33.69	33.65	33.65	5.41
dc18	18090	34.97	5.37	.53	33.79	33.91	33.62	33.55	33.53	6.04
dc20	20060	34.95	4.38	.54	33.73	33.87	33.61	33.51	33.49	6.72
dc22	22150	35.00	3.26	.52	33.71	33.89	33.59	33.49	33.42	7.45
dc24	24090	35.03	4.96	.49	33.62	33.77	33.47	33.35	33.30	8.05
dc26	26130	35.02	4.73	.52	33.53	33.68	33.37	33.22	33.17	8.74
dc28	28100	35.08	5.52	.56	33.44	33.57	33.29	33.11	33.06	9.38
dc30	30290	35.08	7.48	.59	33.34	33.47	33.18	32.95	32.95	10.03
dc32	31980	35.04	7.77	.65	33.17	33.28	33.01	32.72	32.72	10.58
dc34	34000	35.04	7.06	.79	33.02	33.10	32.84	32.52	32.49	11.27
dc36	35880	34.94	8.47	.97	32.82	32.90	32.63	32.28	32.25	11.82

Table E.10: Water-side data for the Tu-Cii geometry

run	q W	$T_{bulk,in}$ °C	$T_{bulk,out}$ °C	LMTD °C	\dot{m}_{bulk} kg/min	\dot{m}_{tube} kg/min	Re	h_i $\frac{W}{m^2 K}$
dc18	18040	28.95	30.94	4.98	130.31	5.21	9000	6620
dc24	24050	28.52	30.52	5.51	172.21	6.89	11780	8240
dc30	30410	27.92	29.92	6.15	217.77	8.71	14700	9880
dc36	36030	27.24	29.25	6.81	257.46	10.30	17120	11220
dc16	15950	29.58	31.40	4.48	125.77	5.03	8780	6470
dc18	17950	29.08	31.06	4.89	130.44	5.22	9030	6630
dc20	19950	28.94	30.92	5.02	144.79	5.79	9990	7200
dc22	22010	28.78	30.79	5.23	157.55	6.30	10840	7690
dc24	23960	28.63	30.62	5.42	172.81	6.91	11850	8270
dc26	26030	28.45	30.43	5.60	188.65	7.55	12880	8850
dc28	28070	28.30	30.28	5.81	202.58	8.10	13790	9360
dc30	30240	28.05	30.06	6.05	216.10	8.64	14630	9830
dc32	31840	27.85	29.83	6.23	230.59	9.22	15540	10330
dc34	34130	27.57	29.57	6.51	244.58	9.78	16380	10800
dc36	36120	27.27	29.27	6.71	258.44	10.34	17200	11250

Table E.11: Row data for the Tu-Cii geometry

run	row 1		row 2		row 3		row 4		row 5	
	$T_{w,out}$ °C	q'' W/m ²								
dc18	30.93	20180	30.98	20680	30.85	19370	30.82	19060	30.81	18960
dc24	30.53	26930	30.58	27600	30.46	25990	30.39	25060	30.38	24920
dc30	29.95	34400	29.98	34900	29.87	33040	29.77	31350	29.76	31180
dc36	29.29	41270	29.31	41670	29.21	39670	29.07	36860	29.05	36460
dc16	31.40	17810	31.44	18200	31.32	17030	31.30	16830	31.30	16830
dc18	31.06	19990	31.11	20500	30.99	19280	30.96	18980	30.95	18880
dc20	30.91	22190	30.97	22870	30.86	21630	30.82	21180	30.81	21070
dc22	30.78	24520	30.85	25370	30.73	23900	30.69	23410	30.66	23050
dc24	30.62	26760	30.68	27560	30.56	25950	30.51	25280	30.49	25010
dc26	30.44	29210	30.50	30090	30.38	28330	30.32	27450	30.30	27160
dc28	30.29	31370	30.34	32160	30.23	30420	30.16	29320	30.14	29000
dc30	30.07	33960	30.12	34810	30.01	32960	29.92	31440	29.92	31440
dc32	29.85	36060	29.89	36780	29.79	34990	29.68	33010	29.68	33010
dc34	29.60	38630	29.63	39200	29.53	37300	29.41	35020	29.40	34830
dc36	29.31	41020	29.34	41630	29.24	39620	29.11	37000	29.10	36800

Table E.12: Shell-side heat transfer coefficients and uncertainties for the Tu-Cii geometry

run	bundle				row 1		row 2		row 3		row 4		row 5	
	q'' W/m ²	q' W/m	h_o W/m ² K	w ± %										
dc18	20210	1200	17600	17.	17340	18.	19860	20.	14250	16.	13310	15.	13020	15.
dc24	26900	1600	19100	14.	19260	15.	21720	17.	16480	14.	14270	13.	13990	12.
dc30	33940	2010	18690	11.	19730	13.	20980	13.	16890	11.	14110	10.	13860	10.
dc36	40200	2390	17860	9.	19510	11.	20230	11.	16990	10.	13560	9.	13150	9.
dc16	17900	1060	17580	19.	17200	20.	19390	22.	13860	17.	13180	17.	13180	17.
dc18	20130	1190	18350	18.	17870	19.	20570	21.	14960	16.	13930	16.	13610	15.
dc20	22360	1330	19720	17.	19010	18.	22450	21.	16750	17.	15230	15.	14880	15.
dc22	24670	1460	20520	16.	19900	17.	24030	20.	17610	16.	16060	15.	15030	14.
dc24	26840	1590	19980	15.	19730	16.	22920	18.	17200	14.	15450	13.	14820	13.
dc26	29140	1730	19950	14.	20220	15.	23340	17.	17700	14.	15630	13.	15020	12.
dc28	31380	1860	19690	13.	19730	14.	22040	15.	17410	13.	15190	12.	14630	11.
dc30	33820	2010	19720	12.	20090	13.	22340	14.	17810	12.	15050	11.	15050	11.
dc32	35650	2120	18990	11.	19800	12.	21460	13.	17650	11.	14490	10.	14490	10.
dc34	38060	2260	18560	10.	19610	11.	20760	12.	17270	11.	14090	9.	13860	9.
dc36	40220	2390	18390	9.	19740	11.	20860	11.	17450	10.	14080	9.	13860	9.

Table E.13: Refrigerant-side data for the G-SC geometry

run	q W	T_{sat} °C	inlet outlet		middle tube $T_{s,o}$					\dot{m} kg/min
			sh °C	sc °C	row 1 °C	row 2 °C	row 3 °C	row 4 °C	row 5 °C	
dd16	16060	34.96	2.69	.46	33.04	33.12	33.06	33.17	32.91	5.41
dd18	18010	35.01	5.08	.37	32.77	32.98	32.92	33.03	32.77	6.02
dd20	20180	34.96	6.93	.49	32.52	32.76	32.71	32.82	32.52	6.70
dd22	22120	35.05	3.93	.45	32.35	32.68	32.62	32.76	32.40	7.42
dd24	24130	35.04	4.75	.57	32.06	32.45	32.40	32.54	32.18	8.07
dd26	26030	35.00	5.14	.51	31.85	32.24	32.21	32.33	31.96	8.70
dd28	28090	35.09	6.17	.55	31.75	32.15	32.10	32.21	31.84	9.35
dd30	30140	35.03	5.42	.63	31.52	31.87	31.87	31.98	31.55	10.05
dd32	31840	35.14	4.84	.66	31.54	31.84	31.78	31.92	31.48	10.64
dd34	33810	34.99	7.33	.68	31.27	31.45	31.45	31.57	31.15	11.20
dd36	35910	35.00	7.53	.75	30.98	31.31	31.28	31.40	30.92	11.88
dd18	18080	34.96	3.83	.52	32.79	32.89	32.84	33.00	32.68	6.07
dd24	24080	35.05	4.35	.60	32.33	32.46	32.44	32.58	32.22	8.06
dd30	30290	35.08	5.69	.52	31.81	31.98	31.98	32.12	31.69	10.10
dd36	36060	35.08	5.48	.60	31.24	31.36	31.33	31.51	31.03	12.03

Table E.14: Water-side data for the G-SC geometry

run	q W	$T_{bulk,in}$ °C	$T_{bulk,out}$ °C	LMTD °C	\dot{m}_{bulk} kg/min	\dot{m}_{tube} kg/min	Re	$\frac{h_i}{W}$ $\frac{m^2}{K}$
dd16	15940	28.36	30.19	5.69	125.42	5.02	9330	6220
dd18	17910	27.78	29.77	6.24	129.53	5.18	9530	6360
dd20	20110	27.40	29.40	6.57	144.05	5.76	10520	6890
dd22	22090	27.22	29.23	6.84	158.13	6.33	11500	7410
dd24	24170	26.90	28.92	7.16	172.23	6.89	12440	7910
dd26	26090	26.66	28.65	7.37	187.78	7.51	13480	8460
dd28	28240	26.45	28.46	7.66	202.14	8.09	14450	8950
dd30	30350	26.08	28.10	7.98	216.16	8.65	15320	9410
dd32	32250	26.00	27.99	8.18	232.07	9.28	16420	9950
dd34	33950	25.63	27.61	8.41	246.13	9.85	17260	10380
dd36	36270	25.21	27.25	8.82	254.75	10.19	17710	10630
dd18	17840	27.65	29.63	6.31	129.34	5.17	9490	6340
dd24	23920	26.94	28.93	7.12	172.62	6.90	12470	7930
dd30	30220	26.14	28.16	7.95	215.21	8.61	15280	9380
dd36	36610	25.34	27.36	8.78	260.03	10.40	18130	10820

Table E.15: Row data for the G-SC geometry

run	row 1		row 2		row 3		row 4		row 5	
	$T_{w,out}$ °C	q'' W/m ²								
dd16	30.15	17420	30.18	17720	30.16	17520	30.20	17910	30.10	16940
dd18	29.67	19000	29.75	19800	29.73	19600	29.77	20010	29.67	19000
dd20	29.30	21240	29.39	22250	29.37	22030	29.41	22470	29.30	21240
dd22	29.09	22950	29.21	24420	29.19	24180	29.24	24790	29.11	23200
dd24	28.75	24730	28.89	26600	28.87	26340	28.92	27000	28.79	25270
dd26	28.48	26670	28.62	28710	28.61	28570	28.65	29150	28.52	27260
dd28	28.29	28870	28.43	31070	28.41	30750	28.45	31380	28.32	29340
dd30	27.94	31210	28.06	33220	28.06	33220	28.10	33890	27.95	31380
dd32	27.87	33680	27.97	35490	27.95	35130	28.00	36030	27.85	33320
dd34	27.50	35920	27.56	37060	27.56	37060	27.60	37830	27.46	35150
dd36	27.11	37570	27.22	39750	27.21	39550	27.25	40340	27.09	37180
dd18	29.59	19580	29.63	19980	29.61	19780	29.67	20380	29.55	19170
dd24	28.87	25860	28.92	26530	28.91	26390	28.96	27060	28.83	25320
dd30	28.08	32410	28.14	33410	28.14	33410	28.19	34240	28.04	31740
dd36	27.28	39160	27.32	39970	27.31	39760	27.37	40970	27.21	37750

Table E.16: Shell-side heat transfer coefficients and uncertainties for the G-SC geometry

run	bundle				row 1		row 2		row 3		row 4		row 5	
	q'' W/m ²	q' W/m	h_o $\frac{W}{m^2 K}$	w ± %										
dd16	17830	1060	10100	11.	9290	12.	9860	12.	9470	12.	10270	13.	8430	11.
dd18	20020	1190	10400	11.	8660	10.	10000	11.	9640	11.	10390	12.	8660	10.
dd20	22450	1340	10670	10.	8880	10.	10360	11.	10000	10.	10740	11.	8880	10.
dd22	24640	1470	10830	9.	8640	9.	10510	10.	10160	10.	11070	10.	8920	9.
dd24	26920	1600	10890	8.	8420	8.	10470	9.	10140	9.	10990	10.	8950	8.
dd26	29050	1730	11020	8.	8580	8.	10600	9.	10430	9.	11110	9.	9100	8.
dd28	31390	1870	11120	8.	8760	8.	10760	8.	10440	8.	11090	9.	9150	8.
dd30	33710	2010	11140	7.	9000	7.	10660	8.	10660	8.	11300	8.	9120	7.
dd32	35710	2120	11090	7.	9460	7.	10880	8.	10580	8.	11360	8.	9210	7.
dd34	37760	2250	11180	6.	9760	7.	10590	7.	10590	7.	11200	7.	9250	7.
dd36	40220	2390	11230	6.	9410	7.	10870	7.	10730	7.	11320	7.	9170	7.
dd18	20020	1190	10030	10.	9250	11.	9950	11.	9590	11.	10720	12.	8630	10.
dd24	26750	1590	10730	8.	9660	9.	10460	9.	10290	9.	11170	10.	9080	9.
dd30	33720	2010	11250	7.	10040	8.	10950	8.	10950	8.	11790	8.	9490	7.
dd36	40490	2410	11260	6.	10290	7.	10850	7.	10710	7.	11600	7.	9390	7.